Modelling acoustic propagation in modern turbofan intakes using a multimodal method

Bruno Mangin

DOCTORAT BRETAGNE SCIENCES LOIRE POUR L'INGENIEUR

Le Mans Université

THÈSE DE DOCTORAT

LE MANS UNIVERSITÉ

ÉCOLE DOCTORALE N° 602
Sciences pour l'Ingénieur
Spécialité : *Acoustique*

Par
Bruno MANGIN

Modelling acoustic propagation in modern turbofan intakes using a multimodal method

Thèse présentée et soutenue à ONERA Châtillon, le 29/11/2023
Unité de recherche : LAUM - UMR 6613, CNRS
Thèse N° : 2023LEMA1020

Composition du Jury :

Président :	—	
Rapporteurs :	Michel ROGER	Professeur d'aéroacoustique, LMFA (UMR 5509, CNRS)
	Edward James BRAMBLEY	Professeur de mathématiques, University of Warwick
Examinateurs :	Jean-François MERCIER	Directeur de recherche, POEMS (UMR 7231, CNRS)
	Simon FELIX	Directeur de recherche, LAUM (UMR 6613, CNRS)
	Estelle PIOT	Directrice de recherche HDR, ONERA Toulouse
Dir. de thèse :	Gwenaël GABARD	Professeur d'aéroacoustique, LAUM (UMR 6613, CNRS),
Encadrant de thèse :	Majd DAROUKH	Ingénieur de Recherche, ONERA Châtillon

ACKNOWLEDGEMENT

I would like to begin by thanking all the members of the jury, and in particular the reviewers Michel Roger and Edward James Brambley, for agreeing to review this work and for their constructive comments.

Je tiens aussi, bien évidemment, à remercier Majd Daroukh et Gwénaël Gabard d'avoir encadré cette thèse pendant ces trois années. Ce manuscrit n'aurait jamais vu le jour sans vous deux. Merci à Majd d'avoir supporté la tête de mule que tu avais comme doctorant. C'est une chance d'avoir eu un encadrant avec une telle capacité d'écoute et un tel amour de la rigueur, ces qualités ont plus que grandement participé à la réussite de cette thèse. J'espère que l'on continuera à se voir après ça, et à grimper ensemble (je n'ai peut-être pas passé de noire à Rungis pendant ma thèse mais ça ne saurait tarder). Merci à Gwénaël pour ta capacité à me sortir des situations les plus complexes grâce à une compréhension folle du sujet. Deux choses sont infinies : l'Univers et les connaissances de Gwénaël. Mais en ce qui concerne l'Univers, personne n'en a encore acquis la certitude.

J'ai passé ces trois dernières années à l'ONERA, et quelle chance! J'y ai trouvé une ambiance incroyable et des gens fascinants par leur intelligence et leur sagacité. Je n'aurais pas pu rêver d'un meilleur endroit où faire ma thèse. La liste des personnes que je dois remercier va être longue, et je m'excuse déjà si j'en ai oublié certaines. Tout d'abord, merci à Éric, l'infatigable, de m'avoir accueilli au sein de l'équipe. Ensuite, merci à Thomas, le dieu de sAbrinA. Tu m'as sauvé la vie plus d'une fois quand je n'arrivais pas à faire converger mes calculs, et même si une question de cinq minutes se transforme souvent en discussion d'une heure, ces échanges en valaient toujours la peine. Merci à Cyril, l'émerveillé, qui, quand je doutais de la pertinence de mes résultats, trouvait toujours une manière de les présenter de manière à les mettre en valeur. Les résultats SPID étaient toujours supers, incroyables, précis, et cela mettait du baume au cœur. Merci d'ailleurs à mes utilisateurs de SPID préférés : Majd, Cyril, Benjamin, Sandrine et Ingrid. Vous m'avez montré que cette thèse avait une utilité, et vous m'avez permis de corriger plus d'un bug dans mon code. Enfin, merci à Xavier, le magicien de l'algèbre, sans qui la stabilisation des schémas de Magnus n'aurait pas été possible. D'un point de vue moins scientifique, merci pour les parties de jeux de société pendant nos pauses déjeuner, en particulier à Martin, le joueur acharné. Merci pour les super sessions acoufoot (et oui, sans "k"), qui, malgré leurs violences

légendaires, étaient toujours un bon moment, surtout pour les bières et les pizzas qui suivaient. Merci en particulier à notre maître organisateur, Benjamin, le marathonien. Merci aux autres membres de l'équipe : Vincent, le puits de connaissances infini, Jules, le politicien, Antoine, le révolutionnaire, Smaïl, la force tranquille, Yves et Laurent C., les rugbymen qui s'ignorent, Patrick, le meneur d'hommes, Fafa, le bidouilleur, Laurent S., notre barista et Hugo, notre hipster. Merci aussi à Elise, la passionnante, pour nos sorties escalade, musée et théâtre. C'est une grande joie de t'avoir rencontrée et j'espère pouvoir continuer à te compter parmi mes amis dans les prochaines années. Enfin, un grand merci à Mathieu, le collègue parfait, sans qui ma thèse se serait arrêtée en fin de première année. Quand la thèse n'avançait pas et que le moral était au plus bas, au doux temps du Covid, tu as été celui de l'équipe qui m'a écouté quand j'en avais le plus besoin et qui a su trouver les mots justes pour me pousser à persévérer. Quand ce manuscrit sortira, je te devrai une boîte de lego de ton choix. J'en profite pour glisser un petit message à Marie : sache que tu as fait un excellent choix et que tu as trouvé une vraie perle. Je vous souhaite tout le bonheur possible à tous les deux.

En dehors de l'Onera, je tiens tout d'abord à remercier mes amis avec qui nous nous sommes lancés ensemble dans la grande aventure qu'est la thèse. Merci à Jeanne, la machine, à Cyril, le sosie, et à Théodore, le bricolo. Vous êtes une source d'inspiration, et votre motivation sans faille est un véritable exemple. Nous avons eu des thèses très différentes, et l'aventure a parfois pu être difficile, mais j'ai été heureux de pouvoir la vivre avec vous. Merci ensuite à tous mes amis parisiens qui ont fait de ces trois années parmi les plus belles de ma vie : Delphine et nos sorties musée et resto, Arnaud pour les soirées de folie, Ethan et nos sorties escalade, Ruben, l'homme parfait, Hugues & Palmyre pour nos après-midis jeux de société, Paul et tes 800 articles de journaux à lire, JB, le yes-man, Clothilde et Antoine, les confrères du T6, et Camille et Mathilde, les chefs cuistots. Vous êtes des gens en or, et je suis désolé de vous consacrer si peu de place dans ces remerciements. Nous fêterons la thèse ensemble pour compenser ça. Merci aussi à mes amis non-parisiens, Paul et Félix de la meilleure des colocations (le nom n'a toujours pas changé au moment où j'écris ces remerciements, en espérant que ça le sera bientôt), Olivier, le sportif fou, Grégoire, le modèle de droiture et de sérieux, Florent, le calme parmi les calmes, et tous les autres que j'oublie.

Merci aussi à Étrog, un professeur de prépa exceptionnel à qui je me dois d'adresser une partie de ces remerciements. Vous avez su me donner le goût des mathématiques, et vous avez toujours cru en moi. Je vous dois la réussite de mes années de prépa, et cette thèse ne se serait jamais faite sans le soutien que vous m'avez apporté à l'époque. Les MPSI et PCSI ne savent pas la chance qu'ils ont de vous avoir comme professeur.

Enfin, un immense merci à ma famille, sans laquelle je ne serais jamais arrivé jusqu'ici. Mes parents, qui, avec mes sœurs, nous ont toujours poussés à aller de l'avant, ont toujours insisté pour que nous cultivions nos talents et qui sont un rocher sans faille sur lequel on peut toujours compter. Merci à Ben et Malix. Vous êtes pour moi des modèles de sérieux et d'intelligence, et j'espère un jour pouvoir rattraper votre niveau (même s'il reste beaucoup de chemin à parcourir). Ben, merci en particulier pour les sorties au musée avec toi, qui étaient toujours passionnantes et qui m'ont permis de sortir "un peu" de mon inculture. Et Malix, merci pour ton sens de l'écoute et ton soutien.

Qn xxzow d SAUX wx uqwolpgl ox baiv lpe wzwme.

TABLE OF CONTENTS

INTRODUCTION

0.1 General context

Aviation has become an integral part of modern society, with millions of people traveling by air every day. However, this has come at a significant environmental cost. The environmental impacts of aviation are diverse, ranging from greenhouse gas emissions to degradation of air quality. In fact, aviation alone is responsible for 4.8% of the estimated anthropogenic contribution to effective radiative forcing between 2000 and 2018 [1]. Furthermore, aircraft noise pollution is a major source of nuisance and has significant implications for human health [2].

High levels of aircraft noise have been linked to various adverse health effects, including sleep disturbances and cardiovascular diseases. In the Paris region alone, millions of people are affected by aircraft noise and have developed health problems leading to a reduction in life expectancy ranging from several months to several years. This highlights the need for effective measures to mitigate aircraft noise and its impacts on human health.

The International Civil Aviation Organization (ICAO) has established norms and standards to regulate aircraft pollution to address this issue. In particular, it has defined the maximum noise levels an aircraft can generate at specific certification points. This represents the disturbance caused to airport neighbours. These norms motivate aircraft manufacturers to develop innovative engine architectures and technologies that can reduce fuel consumption and the noise generated by an aircraft. Among these technologies are engines with a very high bypass ratio (ratio of the mass flow rate in the bypass stream to the mass flow rate entering the core) or semi-buried engines, which are widely studied for their potential to reduce engine consumption.

Acousticians are continuously striving to develop new and improved models that can accurately predict and quantify the noise generated by these new engine concepts. This is essential to support the development of quieter and more environmentally friendly aircraft engines.

0.2 Acoustic certification points

Let us first recall the noise certification points that have been previously mentioned [3]. There are three of them:

— Take-off sideline configuration: This condition represents the loudest noise experienced during take-off, typically very close to the airport. It involves engines at full power.

— Take-off cutback configuration: This scenario represents the minimum noise perceived during a take-off operation, especially close to the flight path. In this case, the aircraft is in take-off configuration but with reduced power.

— Approach configuration: This condition represents the noise perceived during the final approach phase. During the approach, the aircraft is in its noisiest landing configuration. It maintains stabilized thrust on a standard glide path.

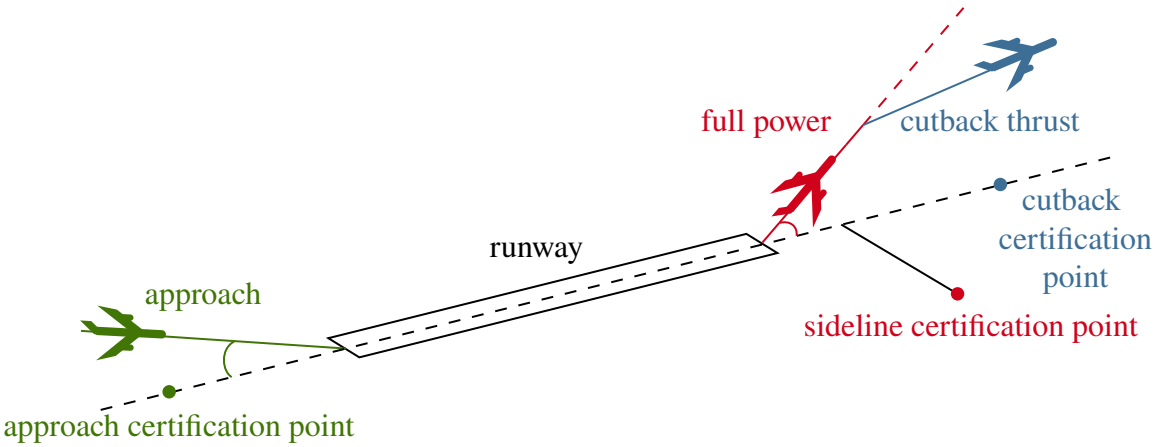

Figure 1 – Acoustic certification points.

0.3 Aircraft noise

The noise produced by an aircraft results from two major contributors: the engine and the airframe. The airframe noise mainly comes from the slats, flaps, and landing gears, while the engine noise mainly arises from the jet and the fan. The relative importance of these contributors varies depending on the aircraft type and engine configuration.

In this thesis, we focus on engine noise, which is a main contributor to noise during certification points for long-range carriers. Jet noise is the noise generated by the high-velocity exhaust gases exiting the engine nozzle. This noise contribution to the overall noise level is important for the sideline certification point. Fan noise, on the other hand, is caused by complex interactions between the engine blades, vanes and the turbulent air flow. It is an important noise source to the sideline and cutback phases.

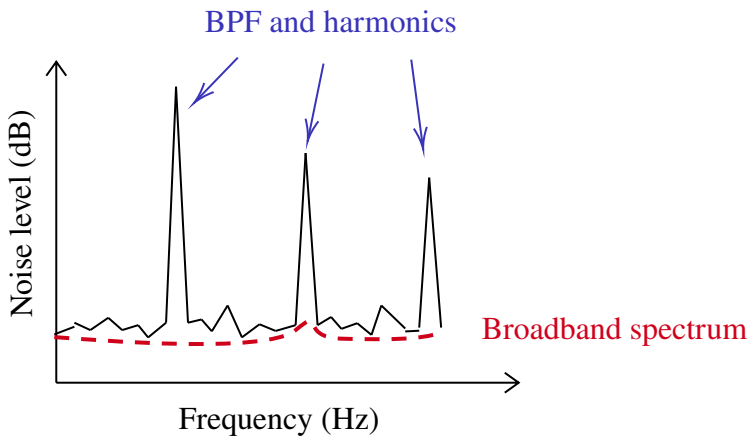

Figure 2 – Example of noise spectrum from a subsonic fan.

Until recently, aircraft manufacturers have largely relied on increasing the ByPass Ratio (BPR) of engines to reduce fuel consumption. In the same way, higher BPR decreases jet velocity, and therefore reduces jet noise, which was the dominant noise source. This approach has been the easiest way to comply with the noise reduction regulations set by the ICAO. However, since the jet noise level is now equivalent to the fan contribution, further noise reduction requires all noise sources to be addressed. Concerning the jet noise, future engine designs, such as the High Bypass Ratio (HBR) and Ultra High Bypass Ratio (UHBR) engines, will continue to decrease it. However, the evolution of fan noise is not straightforward. In fact, fan noise is more complicated as it has multiple origins, making it challenging to estimate a priori [4]. To address this challenge, it is necessary to understand the involved noise mechanisms and how they will be affected by the new engine geometries.

0.4 Fan noise

Figure 2 shows a schematic noise spectrum generated by a fan operating at subsonic conditions. The noise generated by the fan includes both tonal and broadband components [5]. The broadband noise has a continuous distribution of frequencies and is typically caused by turbulence in the flow and its interaction with the blades and vanes. The tonal noise, on the other hand, emerges at frequencies that are multiple of the Blade Passing Frequency (BPF). The main mechanisms involved in tonal noise are detailed hereafter.

Rotor self-noise

Rotor Self-Noise (RSN) is generated by the steady pressure on the rotor blades as they rotate

through the air. Shocks can also develop over blade suction sides at transonic speeds and also contribute to the acoustic field because of their rotation. The rotor self-noise is characterized by tonal components at multiples of the BPF and generates the so-called rotor-locked modes characterized by their azimuthal order $m = nB$, with n the order of the considered BPF harmonic and B the number of rotor blades.

Rotor-stator interaction noise

Rotor-Stator Interaction (RSI) noise is generated by the interaction between the wakes of the rotor blades and the stator blades located downstream. When the stator blades see the wakes generated by the rotor blades, they experience unsteady flow conditions that result in periodic variations in pressure. In ideal conditions (homogeneous rows and uniform flow), the sound field is characterized by azimuthal Fourier components of order $m = nB - kV$, where k is any integer, and V is the number of stator vanes. These modes are classically refered to as Tyler & Sofrin modes. When the flow is heterogeneous, the rotor blade wakes become heterogeneous and cause the appearance of the neighbouring modes.

Distortion-Rotor interaction noise

Distortion-Rotor Interaction (DRI) noise is generated by the interaction between the rotor blades and the steady azimuthal heterogeneity, or distortion, of the incoming flow. This distortion causes the flow to contain azimuthal Fourier components of order l. This interaction leads to periodic fluctuations of the pressure distribution over the blades. The associated sound field is then characterized by azimuthal harmonics of order $m = nB + l$. In classical turbofan engines, these modes are generally considered to be negligible [6].

0.5 Modelling challenges in modern turbofan engines

0.5.1 New acoustic sources caused by azimuthal flow distortion

In modern aero engines, the nacelle is designed so that the flow is uniform during straight and level cruise flights (with a low angle of incidence) to maximize engine efficiency. However, during take off, the plane is under high incidence, which means that the engine axis and the external flow are not aligned. Consequently, the flow that enters the engine is no longer axisymmetric [7], as illustrated in Figure 3. There is an azimuthal heterogeneity of the flow. The air inlet reduces this inhomogeneity, and the distortion levels decrease sharply. Therefore, this distortion can usually be considered negligible almost everywhere for long air inlets, and the interaction of this distortion with the rotating fan can be neglected. However, the air-inlet

length tends to be shortened for new engine geometries, and part of this effect is lost. Typically for UHBR engines, strong azimuthal distortions are expected in the most significant part of the air inlet [8]. Therefore, for UHBR engines, the impact of distortion on source generation is anticipated to increase.

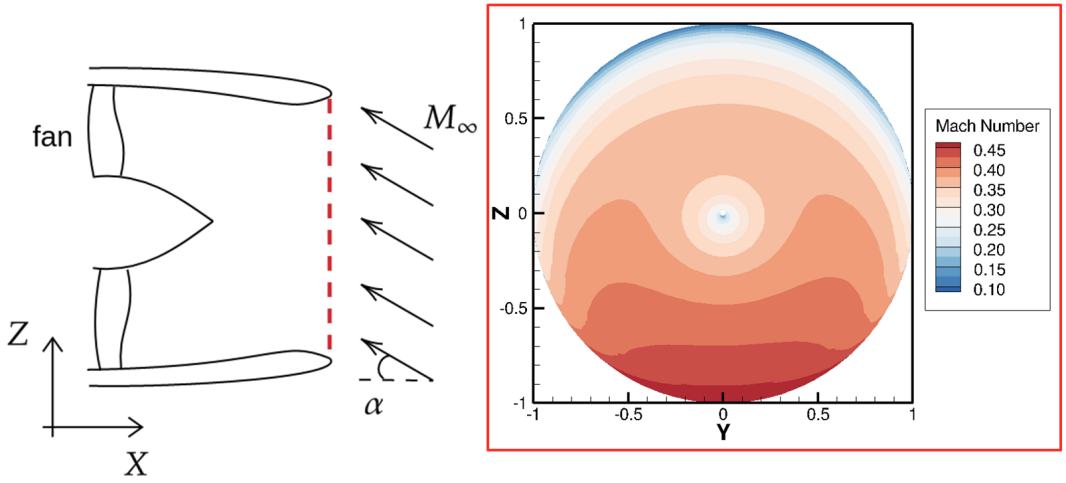

Figure 3 – An engine inlet with an incoming flow of incidence α.

Figure 4 provides an example of an angular mode spectra of the fan sources for such an engine. A mode distribution at the second BPF for an UHBR engine with twenty-two fan blades and thirty-four stator vanes is represented. In this figure, the blue modes correspond to the case without azimuthal flow distortion, while the modes that emerge when azimuthal flow distortion is present are shown in red. These modes will then propagate in the intake before radiating outside the nacelle. In the intake, the duct plays a high-pass filter role on the frequency. This means that some of the modes generated by the fan naturally vanish inside the duct and will only weakly contribute to the radiated sound field [9]. For the sideline and cutback certification points, the rotor-locked mode tends to be close to cut-off. As a consequence, some of the new modes created by the distortion-rotor interaction mechanism can be cut-on. As for the approach certification point, these modes should be cut-off.

0.5.2 On the increased importance of capturing modal transitions

Another consequence of shortening the engine intake in HBR and UHBR configurations, is that some modes are evanescent on only a small distance. In this context, the modes that are only weakly cut-off (cut-off but close to the cut-off limit) can impact the radiated acoustic field, and they need to be accounted for in the predictions [10]. Note that the modes are either cut-on or

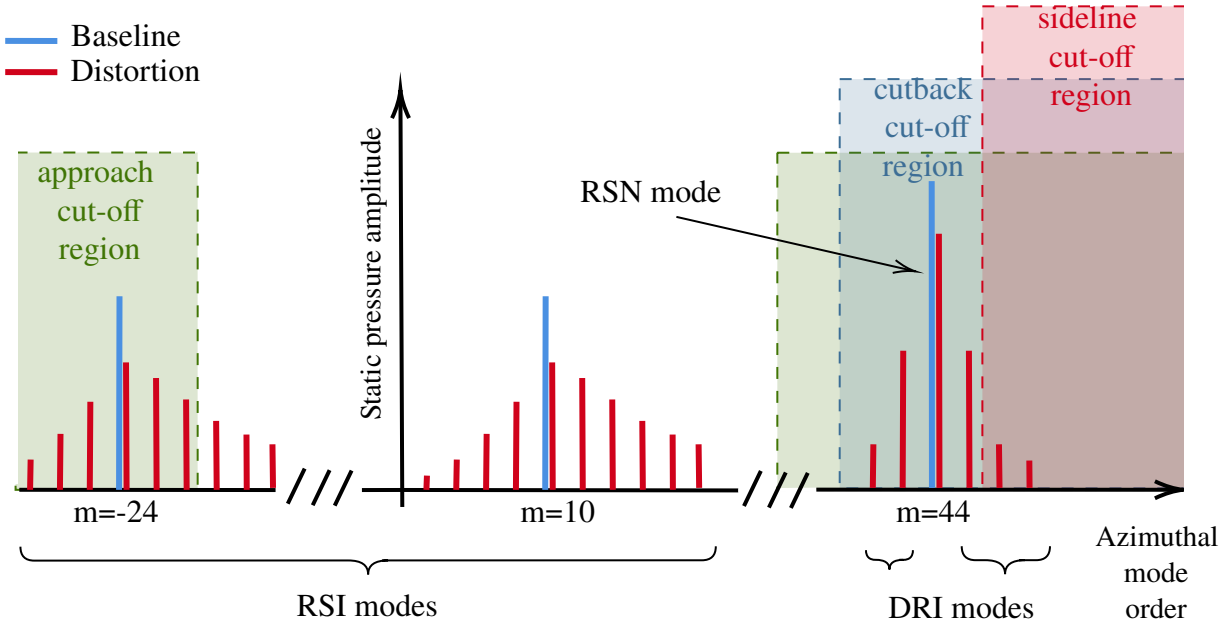

Figure 4 – Example of the azimuthal mode distribution at BPF2, with the cut-off region associated with each certification point.

cut-off for a constant duct with uniform flow. However, in real geometries, the situation is more complex because the geometry varies. Because of this variation, some cut-off modes become cut-on and vice-versa. The evolution of these modes is more difficult to predict since transitions are highly sensitive to geometry or flow changes and are generally associated with important reflections inside the duct [11, 12, 13] that can even cause amplification phenomena [14, 15, 16, 17] or blade vibration instabilities [18, 19]. It is worth noting that for modes that encounter a transition, models used for predicting the sound radiated from an engine can struggle to predict the directivity pattern accurately [20].

One of the focuses of this work is on these transition phenomena, as their contribution to the overall radiated sound is expected to become more important. Because, at first, the distortion-rotor interaction will generate modes close to transition during the take-off. In addition, the appearance of Tyler & Sofrin neighbouring modes in the presence of distortion makes more likely the appearance of modes close to their cut-off frequency (see Figure 4).

0.5.3 Azimuthal diffusion caused by propagation in a disorted flow

It has been mentioned that the flow distortion can significantly impact the acoustic sources, with the appearance of new modes generated in the presence of distortion [21]. Moreover, it also

has a major impact on the propagation with a strong modification of the acoustic field inside the intake [22, 23].

Furthermore, the shortening of the air inlet reduces the available space within the duct where acoustic treatment can be applied [24]. Consequently, acoustic liners must now be applied in sections of the intake characterized by high distortion levels. Hence, it becomes imperative to model the interaction between the flow distortion and the liner.

Finally, it is critical to incorporate radiation calculations for short air inlets due to the increased occurrence of modes near transition or weakly cut-off. For such calculations, distortion must be considered, as it significantly affects the acoustic radiation [25].

0.6 Scope and contributions of the thesis

The main focus of this thesis is to address the challenges in modelling acoustic propagation and radiation in modern turbofan engines, with a specific emphasis on the air inlet of UHBR designs. By considering the effects of mode transition phenomena, distortion caused by an angle of incidence, and the reflection and attenuation caused by liners, the aim is to develop fast and accurate models that can capture the propagation and radiation of acoustic waves in these engines. The need for improvements in the modelling and physical comprehension can be declined into three objectives:

— Investigating the impact of multiple acoustic transitions governed by the geometry.

— Evaluating and addressing the limitations of performing only in-duct calculations.

— Examining the consequences of flow distortion on the acoustic field and incorporating these into the models.

Through these analyses, this thesis aims to provide insights, into the influence of modern turbofan engine geometries on fan noise propagation and to give simplified models that enhance its understanding.

0.7 Outline

In the first chapter, the fundamental equations of aero-acoustics are introduced, along with an examination of the models currently used. Following this, the main chapter of the thesis delves into the presentation of the full admittance multimodal method. Once this work is established,

the subsequent chapters are dedicated to addressing modal transitions, radiation from the intake and the impact of azimuthal flow distortion on the propagation.

Chapter 1 – Acoustic propagation in turbofan intakes

Chapter 1 establishes the theoretical foundation for acoustic propagation within turbofan intakes and introduces the notations employed throughout this thesis. In Section 1.1, the governing equations of acoustic propagation within a turbofan intake are presented. These equations are derived, starting from the Navier-Stokes equations, through simplifications that eventually yield the Goldstein propagation equation. Section 1.2 provides an overview of the numerical methods used in aero-acoustics for solving the previously discussed equations. Advancing from simpler to more detailed models, Section 1.3 presents semi-analytical methods used in aero-acoustics. First, it presents the analytical modes propagating in ducts characterized by constant cross-sections and homogeneous flows. Then, it explores more elaborate mode representations that consider non-homogeneous flows within ducts of constant cross-section. Following this, models based on the WKB ansatz capable of computing the modal amplitude evolution in slowly varying geometries are presented. Finally, multimodal methods are introduced, enabling the consideration of interaction between modes but in cases without flow or with constant flow only.

Chapter 2 – General multimodal method for flow and acoustic calculation

The main objective of Chapter 2 is to present the general multimodal method developed in the thesis. This involves developing a method that accurately computes the mean flow at a low computational cost and then computing the acoustic propagation with this base flow. In Section 2.1, we introduce a multimodal method that computes the acoustic variables for an already-known base flow. Outside of the extension of the initial multimodal method to potential heterogeneous flow, two improvements are given by the thesis. The first one consists of rewriting the Magnus–Möbius scheme to avoid conditioning issues generally observed when using polynomial bases. The other one is the introduction of a formulation to deal with liner discontinuities. Next, in Section 2.2, we modify this method to perform flow calculations. This modification involves using the multimodal method at a zero frequency without convective effects and rewriting the boundary conditions. Validations are then performed for in-duct calculations in Section 2.3 to ensure the method's accuracy. This validation confirms the ability of the method to predict the flow and acoustic fields accurately.

This chapter is partly based on a paper submitted to a peer-reviewed journal [26].

Chapter 3 – Formulation with a multiple-scale flow and the study of modal transition

Chapter 3 aims to address the challenges posed by transition phenomena as well as to explore their effects on in-duct propagation. The impact of modal scattering near these transition phenomena is also investigated. To tackle this problem, in the case of slowly varying geometries, we present a modified multimodal method that uses a multiple-scale flow in Section 3.1. This development includes the rewriting of the equations to account for the new flow. It allows to separate the mode propagation from scattering phenomena. The validity of this method is assessed on various academic test cases and the model is shown to behave well near transitions phenomena. The method is then specifically used to study double transition phenomena in Section 3.2. An improved model formulation based on the WKB ansatz that does not incorporate scattering phenomena, is also presented to further validate the model. This study gives us insights into phenomena such as tunnelling and trapped modes. Additionally, we investigate the impact of neglecting the scattering, an assumption generally used for single-mode calculations. This chapter is constructed using two peer-reviewed publications: one where the multimodal formulation with a multiple-scale flow is presented [27] and the other where double transition phenomena are investigated [28].

Chapter 4 – Formulation with multiple ducts and free-field acoustic radiation

The main objective of Chapter 4 is to develop a multimodal method that allows the computation of the radiated sound from an intake. In Section 4.1, the general multimodal method is modified to perform radiation calculations. This modification involves considering an isolated duct surrounded by a notational one with a larger radius and a perfectly matched layer on its outer wall. This layer simulates an infinite domain by damping the waves that propagate outwards. Validations are performed in Section 4.2 to assess the method's accuracy. This confirm that the method can be used to predict the external flow and the radiated field accurately. Finally, we conduct a parametric study to analyse acoustic parameters' impact on the radiated field and to further validate the method.

This chapter is constructed using a conference publication [29].

Chapter 5 – Three-dimensional formulation: the impact of flow distortion

Chapter 5 aims to investigate the influence of azimuthal flow distortion caused by an angle of incidence and its integration into the developed multimodal method. In Section 5.1, we begin by analyzing the nature and characteristics of the flow distortion. Based on these findings, we

propose modifying the existing multimodal method to account for the flow distortion effectively in Section 5.2. This involves using multiple Fourier components in the basis and modifying the flow boundary conditions. Next, in Section 5.3, we validate the modified method by examining its performance for both flow and acoustic computations. This validation process helps us to better understand the flow distortion's impact on the acoustic field. Finally, in Section 5.4, we begin by analyzing the influence of a liner on the acoustic field when distortion is present. Then, we examine the impact of reducing the length of the intake on both in-duct propagation and free-field radiation.

The first part of this chapter is based on a conference publication [30] where the impact of the distortion on in-duct computations is studied.

Chapter 6 – Conclusion

The conclusions of this thesis are given in Chapter 6. This chapter also includes proposals of future work.

0.8 Chronological sequence

This thesis has been organised for clarity but does not follow the chronological order. Initially, the research was dedicated to the study of flow distortion, with significant efforts directed towards creating a WKB model that could effectively compute acoustic propagation in such a flow. However, the initial model struggled to accurately capture the main propagation effects in distorted flows because of the strong hypothesis used to derive the analytical solution. This prompted a shift in the study of transition phenomena. Then, a new WKB model was proposed to investigate double transitions, demonstrating promising results. Nevertheless, discrepancies between this model and numerical computations persisted. To better understand the model's limitations, an admittance multimodal method with a multiple scale flow was introduced. This method enabled the separation of mode propagation from modal scattering phenomena and provided favourable results. Nonetheless, it was observed that its accuracy was poor at high velocities and frequencies. Further work was conducted to explore the potential applicability of the admittance multimodal to perform acoustic calculation for arbitrary potential flows. These investigations demonstrated good performances, but the computational demands for flow calculations remained high compared to the acoustic calculation. Subsequently, some tests showed that the method could be adapted to perform also the flow calculations. This was a significant shift in the thesis. A complete multimodal method became available, and effective

in studying in-duct computations. The method then continued to evolve, addressing free-field computations, liner discontinuities, and flow distortion calculations.

Chapter 1

Acoustic propagation in turbofan intakes

This chapter delves into the fundamental aspects of acoustic propagation within turbofan intakes. We begin by examining in Section 1.1 the essential governing equations that form the foundation for understanding how acoustics interact with fluid dynamics. Starting with the conservation laws in fluid dynamics, we specifically present the Navier-Stokes equations in Section 1.1.1. From there, we explore how simplifications of these equations lead to the definition of the Euler equations. These equations are commonly employed in acoustic propagation, as discussed in Section 1.1.2. In this section, we also introduce the concept of linearized Euler equations, built on the assumption that acoustic waves are minor perturbations compared to the mean flow. Additionally, as we address aero-engine intakes, the Goldstein propagation equation is presented in Section 1.1.3. This section concludes by introducing duct acoustic boundary conditions (Section 1.1.4) and the conservation equation related to acoustic energy (Section 1.1.5).

Moving forward, we explore some numerical techniques employed to solve aeroacoustic equations in Section 1.2. We look into common methods used to tackle the Helmholtz equation in Section 1.2.1, as well as the Goldstein propagation equation in Section 1.2.2. Additionally, we provide a brief overview of methods used to solve the non-linearized and linearized Euler equations in Section 1.2.3.

Finally, we present in Section 1.3 semi-analytical methods that offer a computationally efficient way of solving the propagation problem when restricting to in-duct propagation. They are given by increasing complexity. At first, the case where the engine intake is modelled as a constant duct is introduced. This case with uniform flow is detailed in Section 1.3.1 and allows us to introduce the concept of modes and transitions. The extension to non-uniform flows, with models based on eigenvalues analyses, is presented in Section 1.3.2. Then, the geometry is allowed to vary slowly, and we present multiple-scale models in Section 1.3.3, where the propagation of a single mode whose amplitude and axial wave number vary is solved. Lastly, we

present in Section 1.3.4 methods where the propagation of multiple modes is solved along with their interactions.

1.1 Governing equations

1.1.1 Conservation laws in fluid dynamics

Aeroacoustics involves the study of sound generated by a flow and is described by the equations of fluid dynamics. When the fluid is treated as a continuum, we can apply the conservation laws of physics to an infinitesimal volume element fixed in space and time. Solving these conservation equations typically requires calculating how certain flow properties change within that element. Specifically, when considering properties such as density ($\tilde{\rho}$), momentum ($\tilde{\rho}\tilde{\mathbf{v}}$), and total energy ($\tilde{\rho}\tilde{e}$), we arrive to the Navier-Stokes equations in their differential form:

— the mass conservation law:

$$\frac{\partial \tilde{\rho}}{\partial t} + \nabla \cdot (\tilde{\rho}\tilde{\mathbf{v}}) = 0, \tag{1.1}$$

— the momentum conservation law:

$$\frac{\partial (\tilde{\rho}\tilde{\mathbf{v}})}{\partial t} + \nabla \cdot (\tilde{\rho}\tilde{\mathbf{v}} \otimes \tilde{\mathbf{v}}) = -\nabla \tilde{p} + \nabla \cdot \tau + \tilde{\rho}\tilde{\mathbf{f}}, \tag{1.2}$$

— the energy conservation law:

$$\frac{\partial (\tilde{\rho}\tilde{e})}{\partial t} + \nabla \cdot (\tilde{\rho}\tilde{e}\tilde{\mathbf{v}}) = \nabla \cdot (\tau \cdot \tilde{\mathbf{v}} - \tilde{p}\tilde{\mathbf{v}} + \tilde{\mathbf{q}}) + \tilde{\rho}\tilde{\mathbf{f}} \cdot \tilde{\mathbf{v}}. \tag{1.3}$$

In these equations, $\tilde{\mathbf{v}}$ represents the Eulerian velocity, τ the viscous stress tensor, $\tilde{p}$ the pressure, $\tilde{\mathbf{f}}$ a force density and $\tilde{\mathbf{q}}$ the heat flux, ∇ is the nabla operator and $\otimes$ the outer product. To complete the system, it is necessary to describe $\tilde{p}$, $\tilde{\tau}$, and $\tilde{\mathbf{q}}$ based on assumptions about the considered fluid.

First, we focus on the way to find $\tilde{p}$. We start by breaking down $\tilde{e}$ into two components: the internal energy per unit mass $\tilde{e}_i$ and the kinetic energy. This gives:

$$\tilde{e} = \tilde{e}_i + \frac{\|\tilde{\mathbf{v}}\|^2}{2}.$$

Next, we introduce the system's entropy $\tilde{s}$, which depends on the internal energy and density. These two variables are related by the fundamental thermodynamic relation, $T d\tilde{s} = d\tilde{e}_i + \tilde{p} d\tilde{\rho}^{-1}$

with T the temperature, assuming reversibility of the process. When neglecting heat conduction and viscosity, the flow becomes isentropic, implying the conservation of energy law taking the form:

$$\frac{\partial \tilde{s}}{\partial t} + \tilde{\mathbf{v}} \cdot \nabla \tilde{s} = 0. \tag{1.4}$$

Then, we can express $\tilde{s}$ as a function of two other variables, which allow to write $\tilde{\rho} = \tilde{\rho}(\tilde{p}, \tilde{s})$. Consequently, we have:

$$d\tilde{\rho} = \frac{1}{\tilde{c}^2} d\tilde{p} + \left(\frac{\partial \tilde{\rho}}{\partial \tilde{s}}\right)_{\tilde{p}} d\tilde{s}, \tag{1.5}$$

where:

$$\tilde{c} = \sqrt{\left(\frac{\partial \tilde{p}}{\partial \tilde{\rho}}\right)_{\tilde{s}}}, \tag{1.6}$$

represents the speed of sound. If we consider in addition a homentropic perfect gas (homogeneous flow and entropy uniform) we have access to the condition on $\tilde{p}$ we wanted to close the previous equations:

$$\tilde{p} = K\tilde{\rho}^{\gamma}, \ \tilde{c}^2 = \frac{\gamma \tilde{p}}{\tilde{\rho}}, \tag{1.7}$$

where γ is the ratio of specific heats and K is a constant [31].

Using Navier-Stokes equations directly for acoustic computations offers several advantages. It can represent the complex fluid dynamics interactions contributing to both sound generation and sound propagation. However, solving these equations can be particularly complex and costly, and it is interesting to introduce some simplifications when the focus is on acoustic propagation only.

1.1.2 Euler equations

For acoustic propagation, is it reasonable to make the hypothesis that the viscosity and heat conduction can be neglected. Then, Navier-Stokes equations can be simplified into the Euler equation [32]. Here, we will also assume that the external force density is equal to zero, which is a resealable hypothesis in the inlet of a turbofan when only the propagation is considered. These assumptions give the Euler equations:

$$\begin{aligned} \frac{\partial \tilde{\rho}}{\partial t} + \nabla \cdot (\tilde{\rho}\tilde{\mathbf{v}}) &= 0, \\ \frac{\partial (\tilde{\rho}\tilde{\mathbf{v}})}{\partial t} + \nabla \cdot (\tilde{\rho}\tilde{\mathbf{v}} \otimes \tilde{\mathbf{v}}) &= -\nabla \tilde{p}, \end{aligned} \tag{1.8}$$

$$\frac{\partial \tilde{s}}{\partial t} + \tilde{\mathbf{v}} \cdot \nabla \tilde{s} = 0.$$

These equations can be further simplified if the acoustic perturbations are assumed to be small compared to the mean flow variables. Any flow variables $\tilde{a}$ can then be decomposed as $\tilde{a} = A + a$, with a associated with a perturbation, A associated with a mean flow variable and $a \ll A$ for scalar variables and $|\mathbf{a}| \ll |\mathbf{A}|$ for vector variables. The mean flow variables satisfy the steady Euler equations when there is no perturbations, which write:

$$\begin{aligned} \nabla \cdot (D\mathbf{V}) &= 0, \\ D(\mathbf{V} \cdot \nabla)\mathbf{V} &= -\nabla P, \\ \mathbf{V} \cdot \nabla S &= 0. \end{aligned} \tag{1.9}$$

Nevertheless, when the perturbations are accounted for, the Euler equations should still be respected. When injecting the perturbed variables in the previous equations and neglecting second and third-order terms, the Linearized Euler Equations (LEE) are obtained:

$$\begin{aligned} \frac{\partial \rho}{\partial t} + \nabla \cdot (\rho \mathbf{V} + D\mathbf{v}) &= 0, \\ D\left(\frac{\partial}{\partial t} + \mathbf{V} \cdot \nabla\right)\mathbf{v} + D(\mathbf{v} \cdot \nabla)\mathbf{V} + \rho(\mathbf{V} \cdot \nabla)\mathbf{V} &= -\nabla p, \\ \frac{\partial s}{\partial t} + \mathbf{V} \cdot \nabla s + \mathbf{v} \cdot \nabla S &= 0. \end{aligned} \tag{1.10}$$

With these two sets of equations, we distinguish the mean flow and the perturbation resolution, and the mean flow is only seen as a medium through which sound can propagate. If the base flow is known, this second set of equations is the only one to solve when only propagation is accounted for. This simplification reduces the complexity of the problem by going from a non-linear to a linear problem. However, these equations are only valid for small perturbations and cannot capture non-linear effects. This makes them not applicable to scenarios where non-linear phenomena play a significant role, as would be the case for shock waves [33].

1.1.3 Irrotational formulation

It is useful to split the perturbation velocity $\mathbf{v}$ into a rotational $\mathbf{v}^R$ and an irrotational part $\nabla\phi$ such that $\mathbf{v} = \mathbf{v}^R + \nabla\phi$, with ϕ the velocity potential and $\nabla \cdot \mathbf{v}^R = 0$ [34]. Then, by considering an isentropic flow and by imposing that the acoustic pressure only depends on the acoustic potential $p = -D\ (\partial/\partial t + \mathbf{V} \cdot \nabla)\phi$ (second equation of the LEE), we can dissociate the hydrodynamic

fluctuations from the acoustic ones, which gives [9]:

$$\begin{gathered}\nabla\cdot(D\nabla\phi)-D\left(\frac{\partial}{\partial t}+\mathbf{V}\cdot\nabla\right)\left[\frac{1}{C^2}\left(\frac{\partial}{\partial t}+\mathbf{V}\cdot\nabla\right)\phi\right]=-\nabla\cdot(D\mathbf{v}^R),\\ \left(\frac{\partial}{\partial t}+\mathbf{V}\cdot\nabla\right)\mathbf{v}^R+(\mathbf{v}^R\cdot\nabla)\mathbf{V}=-\xi\times\nabla\phi,\end{gathered}\tag{1.11}$$

where $\xi=\nabla\times\mathbf{V}$ is the mean vorticity.

The potential part of the velocity follows a wave equation, whereas the rotational part follows a transport equation. Therefore, the first part can be associated with acoustic propagation, when the second can be associated with hydrodynamic convection. The two equations are coupled by the mean vorticity ξ.

The intake of an aero-engine is generally designed such that the flow is as uniform as possible to maximize engine efficency and no flow separations are to be expected. Therefore, it is reasonable to assume that the steady flow can be approximated by a potential flow [7]. When the flow is considered potential, the mean vorticity is equal to zero. Therefore, a clear separation between the two equations is obtained and the acoustic problem reduces to the resolution of the following equation for the acoustic potential:

$$\nabla\cdot(D\nabla\phi)-D\left(\frac{\partial}{\partial t}+\mathbf{V}\cdot\nabla\right)\left[\frac{1}{C^2}\left(\frac{\partial}{\partial t}+\mathbf{V}\cdot\nabla\right)\phi\right]=0.\tag{1.12}$$

This equation can also be obtained in the frequency domain by rewriting each variable in terms of a mean part and a complex perturbated part as: $\tilde{a}=A+\mathrm{Re}(a\,\mathrm{e}^{i\omega t})$, with ω the characteristic pulsation of the source (the same variable name a as used for time-depending variable is used again in order not to introduce unecessary complex notations). The Equation (1.12) then becomes the Goldstein propagation equation:

$$\nabla\cdot(D\nabla\phi)-D(i\omega+\mathbf{V}\cdot\nabla)\left[\frac{1}{C^2}(i\omega+\mathbf{V}\cdot\nabla)\phi\right]=0.\tag{1.13}$$

This representation allows to separate the acoustic fluctuations related to the potential part, which propagate, from other hydrodynamic perturbations that are convected with the mean flow. When this is done, the set of equations on the perturbations variables simplifies to a single equation on the acoustic potential. Note that even if this equation represents well the acoustic propagation in the intake of the engine, its domain of applicability is limited. For example, the mean vorticity cannot be neglected for the jet, with the presence of a shear layer, or in the

interstage region, with the swirling flow behind the rotating fan.

When the medium is at rest, this equation reduces to the Helmholtz equation:

$$\Delta\phi + \frac{\omega^2}{C^2}\phi = 0, \tag{1.14}$$

where Δ is the Laplacian operator.

1.1.4 Acoustic boundary condition

The previous equations are not confined solely to duct acoustics, and they hold validity for broader problem domains. However, to provide a precise distinction for duct acoustics, it becomes essential to introduce the pertinent boundary conditions. When the sound waves propagate within the duct without being absorbed or attenuated, the boundary equation is $\mathbf{v} \cdot \mathbf{n} = 0$, where $\mathbf{n}$ represents the normal vector to the wall. Walls with these properties are referred to as "hard walled".

However, when there is a wall treatment that is locally reacting, the duct walls are specified by a complex impedance Z. These walls are referred to as "lined walls" in this manuscript. At a point along the wall with zero mean flow, this impedance links the acoustic pressure and velocity such that:

$$p = Z(\mathbf{v} \cdot \mathbf{n}).$$

However, for models in which the boundary layer along the wall has a vanishing thickness and the mean flow does not tend to zero (as in solvers for Euler or Goldstein's equations), an alternative boundary condition is required. This condition must be valid for a point near the wall but still within the mean flow. In the case of arbitrary mean flow, Myers [35] derived the following expression:

$$\mathrm{i}\omega(\mathbf{v} \cdot \mathbf{n}) = \left[\frac{\mathrm{D}}{\mathrm{D}t} - \mathbf{n} \cdot (\mathbf{n} \cdot \nabla\mathbf{V})\right]\left(\frac{1}{Z}p\right), \tag{1.15}$$

with $\mathrm{D}/\mathrm{D}t = \mathrm{i}\omega + \mathbf{V} \cdot \nabla$ the convective derivative. Note that when the impedance is infinite ($Z = \infty$), the previous equation simplifies to the hard walled boundary condition $\mathbf{v} \cdot \mathbf{n} = 0$.

1.1.5 Acoustic power

With the introduction of liners, it becomes important to define the acoustic power. Indeed, acoustic power remains constant in the context of a homentropic and irrotational flow with hard

walled boundary conditions, while it is attenuated in the presence of a lined wall. Consequently, it facilitates the comprehension of liner's impact on the acoustics.

This notion has first been derived by starting from the linearized equations [36] but can also be directly defined in a general context using the Euler equations for a homentropic flow [37]. At first, an exact equation governing the transport of energy associated with disturbances is derived and writes:

$$\frac{\partial \tilde{H}}{\partial t} + \nabla \cdot \tilde{\mathbf{I}} = -\tilde{D_v}, \tag{1.16}$$

where $\tilde{H}$ is the perturbation density of energy, $\tilde{\mathbf{I}}$ is the perturbation energy flux, and $\tilde{D_v}$ is the perturbation dissipation. With the same linearized decomposition as the one used in Section 1.1.2, up to the second order, these terms are written:

$$\begin{aligned} \tilde{H} &= \frac{C^2\rho^2}{2D} + \frac{D\mathbf{v}\cdot\mathbf{v}}{2} + \rho\mathbf{V}\cdot\mathbf{v}, \\ \tilde{\mathbf{I}} &= (D\mathbf{v} + \rho\mathbf{V})\left(\frac{C^2\rho}{D} + \mathbf{v}\cdot\mathbf{V}\right), \\ \tilde{D_v} &= -D\mathbf{V}\cdot(\boldsymbol{\omega}_r \times \mathbf{v}) - \rho\mathbf{v}\cdot(\boldsymbol{\xi}\times\mathbf{V}) - \left(\mathbf{v} + \frac{\rho}{D}\mathbf{V}\right)\cdot\left(\mathbf{f} + \frac{\rho}{D}\mathbf{F}\right), \end{aligned} \tag{1.17}$$

where $\boldsymbol{\omega}_r = \nabla \times \mathbf{v}_R$.

In the case of a homentropic and irrotational flow, the dissipation term vanishes, and the energy is conserved. In that case, the time-averaged value of the energy flux writes (see also [38]):

$$\mathbf{I} = \frac{1}{2}\mathrm{Re}\left[\left(\frac{p}{D} + \mathbf{V}\cdot\nabla\phi\right)(D\nabla\phi + \rho\,\mathbf{V})^*\right], \tag{1.18}$$

in which $*$ denotes the complex conjugate. We define the acoustic power for a given transverse section S as [36]:

$$\mathcal{P} = \int_S \mathbf{I}\cdot\mathbf{n}\,\mathrm{d}S, \tag{1.19}$$

where $\mathbf{n}$ represents the normal to the surface. The acoustic power quantifies the energy carried by sound waves and its variation allows us to quantify the effect of an acoustic treatment. Finally, as it must be conserved for a hard walled duct, evaluating this value at different positions permits the assessment of the validity of an analytical or numerical method.

1.2 Numerical propagation methods

The fundamental theories described above provide diverse strategies to represent acoustic propagation inside a duct. The most direct approach involves solving the Navier-Stokes Equations (1.1)–(1.3), which govern both fluid dynamics and acoustics. However, the numerical resolution of these equations can be computationally demanding.

An alternative method, known as the hybrid approach, is employed when source generation and propagation can be decoupled, assuming a limited spatial extent of the source (Lighthill's analogy [39]). In such cases, the Euler equations (1.8) or the LEE (1.10) are typically solved. These equations can be addressed using numerical or analytical techniques, given certain assumptions. In the present study, we adopt this hybrid approach. In this case, the problem can be splitted into three components:

1. A source model defining the modal composition of the sound field coming from the fan module.
2. A propagation model predicting the propagation in the intake that accounts for liner absorption.
3. A radiation model radiating acoustic disturbances to the far field.

When using an hybrid approach, various numerical method can be used. Most of the time, they are adapted to solve one type of equations. The methods are therefore presented by increasing the complexity of the solved equations. The following list provides an overview of some existing methodology but is not meant to be exhaustive.

1.2.1 Helmholtz solver

When the medium is at rest, the Helmholtz equation governs sound propagation. In this case, the three-dimensional (3D) problem, represented by volume integral equation, can be simplified as a two-dimensional (2D) problem, into a surface integral equation, thus reducing the problem's dimensionality. This idea is the basis of the Boundary Element Method (BEM) [40, 41], which stands as the method of choice for acoustic problems in the absence of flow [42].

1.2.2 Goldstein propagation solver

When there is a need to incorporate a flow, it is first of interest to limit to irrotational flows. In this case the equation to solve is the Goldstein propagation equation (1.13). The

potential nature of the flow allows to reduce the complexity of the problem by modelling it by a single scalar equation. In this context, the Finite Element Method (FEM) has found substantial application in intake propagation problems (see for example [43, 4, 24, 8]), where the Goldstein propagation equation describes well the acoustic propagation. Based on a weak formulation of Equations (1.13), such methods solve the acoustic propagation equation by discretizing the complex domain into smaller sub-domains. The equation's solution on each sub-domain is approximated using simple basis functions. Aggregating the solutions across all sub-domains provides an approximation of the global solution. For boundary conditions involving liners, Eversman [44] has reformulated the weak form of Equation (1.15) to facilitate handling of impedance step changes.

1.2.3 Linearized Euler or Euler solvers

In regions where the potential flow hypothesis does not hold, it is necessary to account for the coupling between the hydrodynamic and acoustic modes and to solve the Euler equations. When it is the case, no method appears to stand apart. Outside from problems associated with instabilities [45], these methods are generally time-domain. Therefore, these methods focus on having a numerically precise solution over extended time periods. They use high-order spatial discretization schemes and time integration strategies that ensure accuracy over extended temporal domains [46, 47, 48]. Some of the main existing methods are Finite Differences Methods (FDMs), Finite Volume Methods (FVMs) and once again FEMs. More details on this kind of methods can be found in [24].

1.3 Semi-analytical propagation methods

In many instances, aeroengine geometries undergo relatively minor variations along the axial direction, allowing for the derivation of simplified formulations. Although these formulations offer less precise acoustic representations, they are computationally much less expensive compared to the aforementioned methods and are useful tools for optimization processes (see, for example [49, 50]). Here, we present some of these models, gradually increasing in complexity. Initially, the geometry is approximated as an infinite cylindrical duct with a constant and axial cross-sectional flow. In this scenario, an analytical solution for the acoustic problem is obtained, enabling to explain the concept of transverse acoustic modes.

Subsequently, we extend the notion of transverse modes to cases where analytical solutions

are not easily available. To achieve this, we introduce eigenvalue methods. However, restricting the geometry to a cylindrical duct is a limiting approximation. Hence, we explore the potential to introduce geometric variations. When these variations occur gradually, the application of perturbation methods becomes attractive. Multiple-Scales (MS) methods exemplify this, where the transverse modes found earlier are considered to evolve in accordance with duct variations. Both amplitude and wavenumbers are treated as slowly varying functions.

It is important to note that these methods do not consider any interaction between the modes. While this approximation holds promise for low-frequency cases, its accuracy decreases for high-frequencies. In such instances, methods that allow multiple modes to propagate within the duct become valuable. These methods are referred to as multimodal techniques. The underlying concept involves computing both how the mode proprieties evolve due to the duct variations and how the modes interact while they propagate.

In this section, all the parameters are scaled to be dimensionless: the density is normalized by a reference density ρ_∞, velocities by a reference sound speed c_∞, spatial dimensions by the typical duct radius R_∞, velocity potential by $R_\infty c_\infty$, and pressure by $\rho_\infty c_\infty^2$. We consider a cylindrical coordinate system (x, r, θ), with the associated basis vectors $(\mathbf{e}_x, \mathbf{e}_r, \mathbf{e}_\theta)$. The hub and tip radii of the annular cross section are written R_1 and R_2.

1.3.1 Analytical solution in a constant infinite duct with a uniform axial flow

The analysis of sound propagation within a duct can be significantly facilitated by making certain assumptions on its geometry and flow proprieties. Specifically, assuming a circular or annular and infinite duct, represented in Figure 1.1, with constant hub and tip radii, along with axial and uniform cross-flow $\mathbf{V} = (U, 0, 0)$, facilitates the analysis. In that case, an analytical solution of the modes that can propagate can be found analytically [36].

1.3.1.1 Solving the eigenmodes

In the current case, the equation to solve is the Goldstein propagation Equation (1.13). Using the fact that the flow is uniform, this equation simplifies to the convected Helmholtz equation:

$$-k^2\phi + 2\mathrm{i}kM\frac{\partial\phi}{\partial x} + M^2\frac{\partial^2\phi}{\partial x^2} = \Delta\phi, \tag{1.20}$$

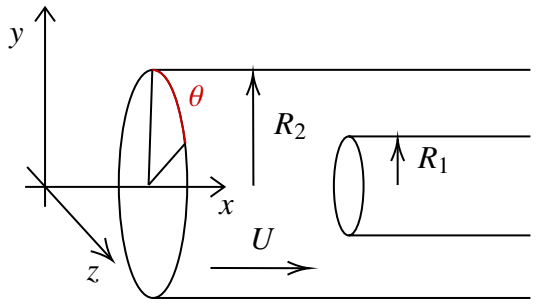

Figure 1.1 – Representation of the engine inlet.

where $k = \omega/C$ and $M = U/C$. To solve the Equation (1.20), a separation of variables in the cylindrical coordinate system (x, r, θ) is introduced: $\phi = R(r)\Theta(\theta)X(x)$. This gives the following equations:

$$\frac{1}{X}\left(k^2X - 2ikM\frac{\mathrm{d}X}{\mathrm{d}x} - (M^2-1)\frac{\mathrm{d}^2X}{\mathrm{d}x^2}\right) = \alpha^2, \tag{1.21a}$$

$$\frac{1}{R}r\frac{\mathrm{d}}{\mathrm{d}r}\left(r\frac{\mathrm{d}R}{\mathrm{d}r}\right) + \alpha^2r^2 = m^2, \tag{1.21b}$$

$$\frac{1}{\Theta}\frac{\mathrm{d}^2\Theta}{\mathrm{d}\theta^2} = -m^2, \tag{1.21c}$$

where α^2 and m^2 are constants. As the geometry imposes a 2π-periodicity, the only way for the previous equations to be valid is for m to be an integer. The solutions of the previous set of equations are written $N_m\left(\mathrm{J}_m(\alpha_m r) + \Gamma_m \mathrm{Y}_m(\alpha_m r)\right)\mathrm{e}^{i(-m\theta-\mu x)}$, where J_m and Y_m are the Bessel functions of the first and second kind of order m, N_m is the mode amplitude and α_m is the radial wavenumber. The axial wavenumber μ is determined from the dispersion relation:

$$(k - \mu M)^2 = \alpha^2 + \mu^2. \tag{1.22}$$

The possible values of α are finally obtained using the boundary conditions. A loss of generality is made here by imposing hard walled boundary conditions, which impose that the acoustic radial velocity equals zero at the wall:

$$\begin{cases} \left.\dfrac{\partial\phi}{\partial r}\right|_{R1} = 0 \\ \left.\dfrac{\partial\phi}{\partial r}\right|_{R2} = 0. \end{cases}$$

For $N_m \neq 0$, it gives:

$$\Gamma_m = -\frac{\mathrm{J}'_m(\alpha_{mn}R_2)}{\mathrm{Y}'_m(\alpha_{mn}R_2)} = -\frac{\mathrm{J}'_m(\alpha_{mn}R_1)}{\mathrm{Y}'_m(\alpha_{mn}R_1)}. \tag{1.23}$$

This equation has an infinite number of solutions written α_{mn}, with n an integer. As they are real, they can be sorted such as α_{mn} will corresponds to the n^{th} zero of the equation $\mathrm{J}'_m(\alpha_{mn}R_2)\mathrm{Y}'_m(\alpha_{mn}R_1) - \mathrm{Y}'_m(\alpha_{mn}R_2)\mathrm{J}'_m(\alpha_{mn}R_1) = 0$, for Bessel functions of order m.

An interesting property of modes is that they form an orthogonal basis and each variable of this basis is a solution of the linearized acoustic equations [9]. As a result, for a given frequency, the acoustic potential inside the duct can be written as the sum of all the modes found above:

$$\phi(r,\theta,x,t) = \sum_{m\in\mathbb{Z}}\sum_{n\in\mathbb{N}} \psi_{mn}(r)(A_{mn}\,\mathrm{e}^{i(-m\theta-\mu_+ x)} + B_{mn}\,\mathrm{e}^{i(-m\theta-\mu_- x)}), \tag{1.24}$$

with $\psi_{mn}(r) = N_m\left[\mathrm{J}_m(\alpha_{m,n}r) + \Gamma_{mn}\mathrm{Y}_m(\alpha_{m,n}r)\right]$, $\mu_\pm = (-kM \pm \sqrt{k^2-(1-M^2)\alpha^2})/(1-M^2)$ the two solutions of the dispersion relation (1.22) and (A_{mn}, B_{mn}) two constants defined by the source.

Due to the formulation of the Θ function, the sound field for a given azimuthal mode m presents m angular lobes (periodicity of $2\pi/m$). Regarding the radial direction, the fact that α_{mn} is the n^{th} zero on the real axis of the hard walled boundary condition means that n lobes appear. An acoustic mode $(m,n) = (5,2)$ propagating in an axisymmetric duct is shown in Figure 1.2 over the transverse plane and over the duct walls to illustrate this. This figure shows that the mode has five lobes in the azimuthal direction and two in the radial direction. It is important to note that this mode can also be viewed as a helicoidal wave since it appears to be rolled along the propagation axis when looking at a constant phase.

1.3.1.2 Focus on mode transition

Let us now focus on the two solutions of the dispersion relation (1.22):

$$\mu_\pm = \frac{-kM \pm \sqrt{k^2-(1-M^2)\alpha^2}}{1-M^2}. \tag{1.25}$$

The wavenumber k is imposed by the frequency and the radial wavenumber α by the boundary condition, so this relation gives the axial wavelength μ. If the discriminant $4(k^2-\alpha^2+\alpha^2M^2)$ is positive, the axial wavenumber μ is real, and the wave is propagative. Such modes are said to be cut-on. On the contrary, when this term is negative, the wave becomes evanescent, and modes are said to be cut-off. A transition corresponds to the case where this term is equal to zero. It can also

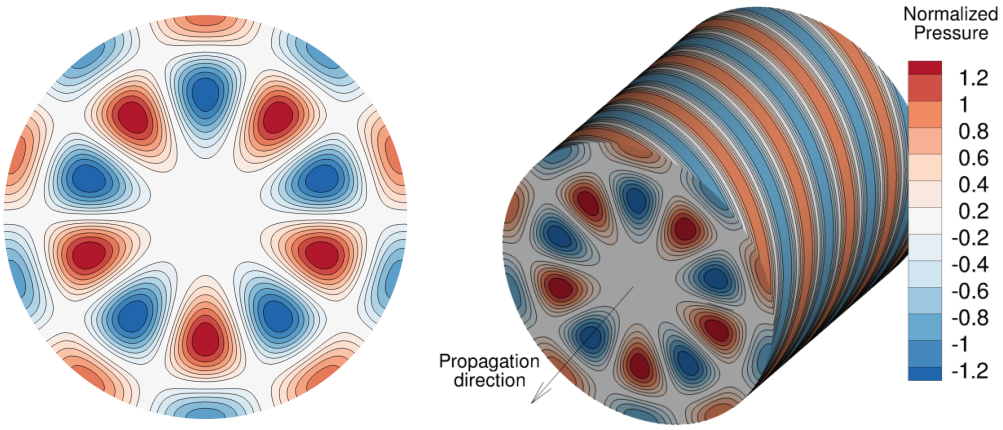

Figure 1.2 – Example of an acoustic pressure field for a mode $(m, n) = (5, 2)$: transverse slice (left), outer duct wall (right).

be noted that this transition depends on the non-dimensionalized pulsation $k = \omega/C$ for a given flow, geometry and mode. The acoustic waves go from purely evanescent to propagative when the frequency increases. This means that the duct works as a high-pass filter on the frequency. The transition also depends on the value of α. When the azimuthal wavenumber m increases for a given frequency, the acoustic waves go from purely propagative to evanescent. This means that the duct works as a low-pass filter on m. Evaluating the frequency at which the transition occurs allows for limiting the number of modes to calculate. In fact, evanescent ones will have little influence on the acoustic field far from the source and can be ignored. This enables to truncate the infinite basis in theory to a reduced mode basis of finite dimension, constituted by only the cut-on modes. All the phenomena described here take place in the case of hard walled boundary conditions. This concept breaks down in the case of a lined wall since the radial wavenumber α becomes a complex number.

In order to illustrate these behaviours, the same acoustic mode $(m, n) = (5, 2)$, as shown in Figure 1.2 is considered, but the frequency is decreased such that the mode becomes cut-off. A cut at $\theta = 0$ is shown in Figure 1.3. The exponential decrease for the cut-off mode is clearly visible and low pressure values are obtained away from the source.

1.3.2 Semi-analytical methods in a constant duct with a non-uniform flow

1.3.2.1 Brief review

The previous model provides analytical solutions for duct modes under uniform flow conditions, which helps to understand the acoustic structure in more complex duct and serve as a

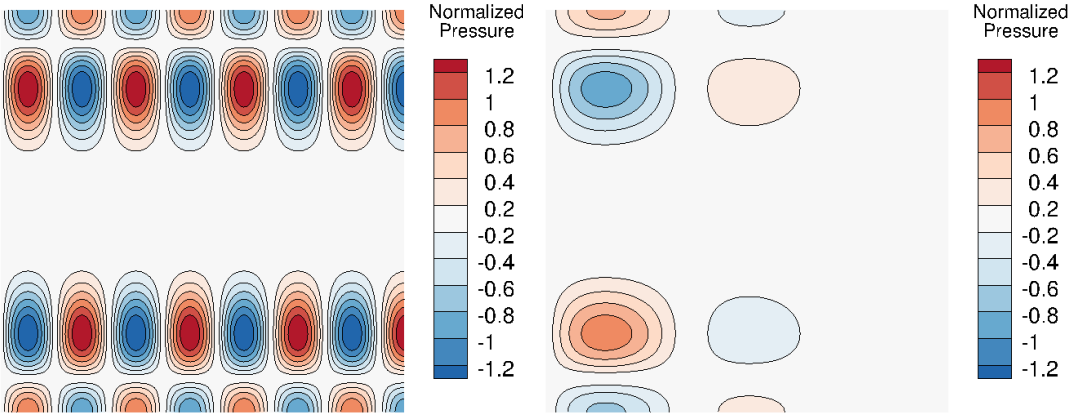

Figure 1.3 – Example of an acoustic pressure field shape, y-slice, for a mode $(5, 2)$ with a cut-on (left) and cut-off (right) behaviour.

basis for advanced modelling. However, real-world geometries often involve non-uniform flows within the engine. Thus, an extension of the previous methodology is required to accommodate this complexity. These modes are associated with eigensolutions of a propagation equation on a cross-sectional plane, thus the dimensionality has shifted from three dimensions to two dimensions.

When assumptions about the shape of the mean flow are made, this problem can be solved analytically and the mode can still be derived. This has been done for ducts with sheared flows [51, 52] to understand hydrodynamic instability that may occur above a liner, and in cases involving a distorted mean flow by assuming a simple cosine-shaped distortion and a thin annular duct [53, 54].

If no assumptions, about the mean flow is made, the problem is rewritten as an eigenproblem that needs to be solved numerically. Different methods are available, among them some categories stand out: spectral methods [55, 56, 57] and finite-element methods [58, 59]. The distinction between these methods comes from the selection of basis functions. Spectral methods employ infinitely differentiable global functions as basis functions. Conversely, finite-element methods partition the domain into smaller elements and define a trial function within each element. As such, the trial functions adopt a local character.

1.3.2.2 Mathematical description of the problem

Here, all the variables are considered to be independent of the axial direction, and the mean density and speed of sound are assumed constant. The base flow is taken parallel and of the form $\mathbf{V} = (U(r, \theta), 0, 0)$.

As no hypothesis on the nature of the flow is made, it is necessary to fall back on the linearized Euler equations (1.10). The acoustic field is written in terms of modal solutions by assuming an expression of the form:

$$(p, u, v, w) = (p_j, u_j, v_j, w_j) \exp(-\mathrm{i}\mu_j x),$$

where the velocity vector (u_j, v_j, w_j) and the pressure p_j transverse modes are unknown functions of the transverse coordinates. These modes represent the shape taken by these variables in the transverse direction. The LEE can be written:

$$\mathcal{L}(\mathcal{X}_j) = 0, \tag{1.26}$$

where $\mathcal{X} = (p_j, u_j, v_j, w_j)^T$ and:

$$\mathcal{L} = \begin{pmatrix} \mathrm{i}(k - \mu_j M) & -\mathrm{i}\mu_j & \dfrac{\partial}{\partial r} + \dfrac{1}{r} & \dfrac{1}{r}\dfrac{\partial}{\partial \theta} \\ -\mathrm{i}\mu_j & \mathrm{i}(k - \mu_j M) & \dfrac{\partial M}{\partial r} & \dfrac{1}{r}\dfrac{\partial M}{\partial \theta} \\ \dfrac{\partial}{\partial r} & 0 & \mathrm{i}(k - \mu_j M) & 0 \\ \dfrac{1}{r}\dfrac{\partial}{\partial \theta} & 0 & 0 & \mathrm{i}(k - \mu_j M) \end{pmatrix}. \tag{1.27}$$

The liner boundary condition defined in Equation (1.15) becomes $kZu_j = (k - \mu_j M)p_j$.

Solving the above linear problem for a known mean velocity profile and impedance involves solving a dispersion relation. If certain hypotheses are made on the shape of the flow, this relation can be solved analytically. However in most cases, this relation remains implicit, necessitating numerical solution through the discretization of the problem.

1.3.3 Single mode propagation in slowly varying ducts

1.3.3.1 Brief review

The previous models give us insight into the shape that the acoustic can take over the transverse plane. Yet, they are not able to account for the engine geometry variations.

New methodologies are needed to account for ducts with varying radii. If the acoustic perturbations vary rapidly compared to the duct geometry and flow length scales, a leading-order approximation of the exact solution to the propagation problem can be found using the Wentzel–Kramers–Brillouin (WKB) method [60, 61] which is a special case of the multiple-

scale methods. This approach has been applied by Nayfeh & Telionis [62] and Nayfeh *et al.* [63] for modes propagating in lined ducts with slowly varying geometries of rectangular or circular cross-sections. It has been afterward improved in the circular case by Rienstra, who found an adiabatic invariant of the slowly varying mode in the case of an irrotational mean flow [64]. The flow is given by a multiple-scale approach while the acoustic field is represented by a summation of WKB modes, whose amplitudes vary slowly and are determined using a solvability condition. This combined MS/WKB method has been extended to more complex flows and geometries, for instance by taking into account swirling flows [65], arbitrary cross-sections [66], strongly curved ducts [67] and sheared flows [68]. However, one of the drawbacks of this technique is that it is only valid as long as there is no transition inside the duct. Where this happens, the incident mode becomes partly transmitted and partly reflected, which is not accounted for in the previous formulations. A composite solution that accounts for this behaviour and removes the singularity has been proposed in the case where there is a single turning point [11, 69, 12, 13]. This solution, governed by Airy's equation, is valid in the surrounding of the turning point and matches the slowly varying modal solution far from it.

These models have the advantage of extending classical straight duct model to duct with an axial variation of the geometry and their computational cost is the same as the previous analytical models. In order to understand more precisely how this is possible, the application of this methodology proposed by Rienstra, and its extension to the presence of a single transition, for ducts of arbitrary cross-section [66] and for a potential flow is briefly presented here for hard walled boundaries.

1.3.3.2 WKB solution for ducts of varying arbitrary cross-section

We begin by defining the slowly varying axial coordinate $X = \epsilon x$, where ϵ is a small parameter. As the duct geometry is assumed to vary slowly, the hub and tip variation are written $R_1(X, \theta)$ and $R_2(X, \theta)$.

The objective is to find a formulation of the flow in the varying duct. The mean flow equations are solved by assuming that the axial mean flow varies slowly with the axial coordinate X. Noting that $\partial A/\partial x = \epsilon \partial A/\partial X + O(\epsilon^2)$ for any slowly varying variable A, a reasoning on orders of magnitude then shows that the flow variables take the form:

$$\begin{aligned} \mathbf{V}(X, r, \theta; \epsilon) &= U_0(X)\mathbf{e}_x + \epsilon \mathbf{V}_\perp(X, r, \theta) + O(\epsilon^2), \\ [D, P, C](X, r; \epsilon) &= [D_0, P_0, C_0](X) + O(\epsilon^2), \end{aligned} \tag{1.28}$$

with $\mathbf{V}_\perp$ the transverse mean flow velocity. Injecting these expressions into Equation (1.9) gives:

$$\begin{aligned} \frac{1}{2}U_0^2 + \frac{1}{\gamma-1}D_0^{\gamma-1} &= E + O(\epsilon^2), \\ U_0 &= \frac{F}{D_0 S} + O(\epsilon^2), \\ P_0 &= \frac{1}{\gamma}D_0^{\gamma} + O(\epsilon^2), \\ C_0 &= D_0^{(\gamma-1)/2} + O(\epsilon^2), \end{aligned} \tag{1.29}$$

where E and F are two constants (Bernoulli's constant and cross-sectional mass flow, respectively) and S is the transverse cross-section area. Solving numerically (e.g. with a Newton algorithm) the leading-order of the density gives access all other mean flow variables [68].

For the acoustic field, if no modal transition is present inside the duct, and if the acoustic wavelength is of the order of the duct diameter, then the WKB approximation yields a solution of the form:

$$\phi(x, r, \theta; \epsilon) = \Phi(X, r, \theta; \epsilon) \exp\left(-\mathrm{i}\epsilon^{-1} \int^X \mu(\xi) d\xi\right), \tag{1.30}$$

where the axial wavenumber μ varies in the axial direction.

By assuming $\Phi(X, r, \theta; \epsilon) = \Phi_0(X, r, \theta) + \epsilon\Phi_1(X, r, \theta) + O(\epsilon^2)$ and gathering the $O(1)$ terms of the Goldstein propagation Equation (1.13), it gives at each axial location X an eigenvalue problem for Φ_0 of the form:

$$-\Delta_\perp \Phi_0 = \alpha^2 \Phi_0, \quad \mathbf{n}_\perp \cdot \nabla\Phi_0 = 0, \tag{1.31}$$

where $\Delta_\perp$ is the transverse Laplacian operator. The vector $\mathbf{n}_\perp$ is the component of the vector normal to the surface in the transverse cross-section and $\alpha = \sqrt{(k_0 - \mu M_0)^2 - \mu^2}$ is defined as the radial wavenumber with $k_0 = \omega/C_0$ the free-field wavenumber and $M_0 = U_0/C_0$ the axial Mach number.

Let us consider the n^{th} eigenvalue α_n and the associated eigenmode ψ_n of this eigenproblem, with ψ_n normalized such that:

$$\iint_S \psi_n^2 \mathrm{d}S = 1. \tag{1.32}$$

Then, we have $\Phi_0 = N(X)\psi_n$ with N a slowly varying modal amplitude. In the following, we drop the n subscript for concision. The amplitude N is obtained by a development to the second

order ($o(\epsilon^2)$) of the perturbation equations (1.13) to get a solvability condition. It yields:

$$\left(\frac{Q_0}{N}\right)^2 = \frac{\omega\sigma D_0}{C_0}, \tag{1.33}$$

with $\sigma^2 = 1 - (C_0^2 - U_0^2)\alpha^2/\omega^2$ and Q_0 a constant associated to the source amplitude. The term σ is the reduced axial wavenumber and is linked to the axial wavenumber by the relation $\mu = \omega(C_0\sigma - U_0)/(C_0^2 - U_0^2)$.

As a result, the acoustic field associated with a single mode n is written:

$$\begin{aligned}\phi = Q_0\sqrt{\frac{C_0}{\omega D_0\sigma}}\psi\ \exp\left[\frac{\mathrm{i}}{\epsilon}\int_X \frac{\omega U_0}{C_0^2 - U_0^2}\mathrm{d}X\right] \\ \left[\mathcal{D}\ \exp\left[\frac{-\mathrm{i}}{\epsilon}\int_X \frac{\omega C_0\sigma}{C_0^2 - U_0^2}\mathrm{d}X\right] + \mathcal{U}\ \exp\left[\frac{\mathrm{i}}{\epsilon}\int_X \frac{\omega C_0\sigma}{C_0^2 - U_0^2}\mathrm{d}X\right]\right],\end{aligned} \tag{1.34}$$

where $\mathcal{D}$ stands for the modal amplitude associated with the mode propagating in one direction, while $\mathcal{U}$ is used for the mode going in the opposite direction.

The acoustic fluctuations are represented with a summation of slowly varying modes for ducts with an axial geometry variation. However, near modal transition, the axial wavenumber does not vary slowly and this formulation cannot be used [11].

1.3.3.3 Solution in the presence of a transition

When there is a modal transition, the situation is more complex than in the constant case scenario (Section 1.3.3.2) because a cut-off mode can become cut-on and vice-versa. The evolution of these modes is more difficult to predict because the WKB formulation is not valid in the vicinity of a turning point as the axial wavenumber does not vary slowly. Several methods exist to model the transition phenomenon, and both a physical explanation and a mathematical expression for modes undergoing such transitions have been proposed [11, 12, 13]. Ovenden dealt with this issue by introducing a uniformly valid solution that can be used both in the neighbourhood of the transition point (inner region of size $|X - X_t| = O(\epsilon^{2/3}\omega^{-2/3})$ [1] with X_t the location of the transition) and in the region far upstream and far downstream from it (outer region of size $|X - X_t| = O(1)$).

The uniformly valid solution derived by Ovenden, valid for an arbitrary cross-section, is

1. In the literature, the inner boundary layer thickness is generally defined as $|X - X_t| = O(\epsilon^{2/3})$, but we prefer here to highlight the frequency scaling.

based on Airy functions (Ai, Bi) and writes [12]:

$$\phi = Q_0 \sqrt{\frac{C_0}{\omega D_0}} \psi \left[-\frac{3}{2\epsilon\sigma^3} \int_{X_t}^{X} \frac{\omega C_0 \sigma}{C_0^2 - U_0^2} \mathrm{d}X \right]^{1/6} [a\,\mathrm{Ai}(s_t) + b\,\mathrm{Bi}(s_t)] \exp\left[\frac{\mathrm{i}}{\epsilon} \int_{X_t}^{X} \frac{\omega U_0}{C_0^2 - U_0^2} \mathrm{d}X \right], \quad \text{with } s_t = \left(\frac{3\mathrm{i}}{2\epsilon} \int_{X_t}^{X} \frac{\omega C_0 \sigma}{C_0^2 - U_0^2} \mathrm{d}X \right)^{2/3}, \tag{1.35}$$

where ψ is the normalized transverse mode shape and a and b are two constants to be determined. The coefficients a and b are obtained by matching the asymptotic form of the previous uniformly valid formulation (1.35) and the slowly varying WKB solution (1.34) far upstream and far downstream of the transition. For a cut-on/cut-off transition, it yields:

$$a = 2\sqrt{\pi}\mathrm{e}^{\mathrm{i}\pi/4},\ b = 0, \tag{1.36}$$

and for a cut-off/cut-on transition:

$$a = -\sqrt{\pi}\mathrm{e}^{\mathrm{i}\pi/4},\ b = \sqrt{\pi}\mathrm{e}^{-\mathrm{i}\pi/4}. \tag{1.37}$$

This allows to predict the transmission and reflection near transitions and is therefore of great use. In practice, in the context of total noise prediction, it could be argued that the interest of the study of transition is limited since only a very small number of modes will encounter a transition. However, in some cases, the study of these modes is of major interest since they are responsible for important reflections inside the duct which can cause blade vibration instabilities [18, 19]. Moreover, when more than one transition is present, more complex phenomena can appear, such as amplifications [14, 15, 16, 17], and have major implication on the noise source emission. Note that these multiple transition phenomena have been studied when the geometry present some symmetric properties [70], but there is a lack of models to tackle these phenomena in more complex cases.

1.3.4 Multiple mode propagation in varying geometries and their interaction

1.3.4.1 Brief review

The WKB models previously presented are of great interest for slowly varying geometries but are not valid when the geometry variations are not small compared to the acoustic wavelength. When this happens, a single mode cannot accurately represent the acoustic field.

As the injected wave propagates in the presence of significant geometric variations or flow changes, the acoustic wave is modified and more and more modes are required to represent the acoustic field. This energy transfer from the injected mode to the neighbouring modes is referred to as modal scattering. In order to account for this diffusion phenomenon, it is possible to use an eigenmode decomposition in the transverse plane and to solve numerically the axial evolution of modes and their interaction.

To do this, three types of methodology are often used:

— **One-way calculations** are very efficient but are grounded in the assumption that reflections from both the geometry and the mean flow can be ignored [71, 72]. This approach enables a direct path from the source to the exit, yet it falls short in capturing transition phenomena or flow-induced reflections, such as those observed in scenarios involving distorted flows [20].

— **Iterative Bremmer** [73] or **iterative one-way** calculations [74, 59] involve an iterative process to obtain the successive reflections that occur. This iterative procedure is repeated until a converged solution is obtained. While these methods can incorporate transition phenomena, they are not suited for addressing significant amplification phenomena coming from trapped modes. Furthermore, the iterative nature of the process can introduce computational time overhead.

— **Admittance multimodal** method use an admittance matrix to account for the reflection and scattering that can occur inside the domain. A first calculation of this matrix is performed before computing the acoustic field. This method can accommodate a great number of reflection phenomena [75]. However, the method is limited to the solving of the Helmholtz equation or of the convected Helmholtz equation.

The last method is particularly appealing in the scope of this thesis since one of the focuses is on transition phenomena. However, an adaptation of the method to solve the Goldstein propagation equation will be needed (i.e. to account for a complete potential flow). Below is a more detailed description of the method.

Admittance Multimodal Methods (MM) are first based on a rewriting of the propagation problem into initial value problems consisting of two coupled first-order equations. These equations describe the modal evolution of an acoustic quantity (generally the pressure) and its derivative. The approach involves projecting the acoustic problem onto an orthogonal and complete local basis, generally the local transverse eigenmodes. This basis (Fourier Bessel functions for the circular case) serves as a representation space for the acoustic field, enabling decomposing the problem into modal components. However, the previous studies show that two problems emerge when this type of method is used. First, the acoustic equation with evanescent modes is unstable, making it particularly difficult to solve. Then, the problem is not just an initial value problem since there is a strong coupling between the duct inlet and outlet. For two-dimensional ducts with varying cross-section, Pagneux *et al.* [75] overcame these difficulties by introducing an admittance matrix representing the medium's refraction and reflection index (Dirichlet-to-Neumann operator). They showed that the evolution of the admittance satisfies a Riccati equation which can be solved using a Magnus–Möbius scheme [76]. This method is appealing, as it does not encounter any problem even if a important number of reflections are to be expected in the duct, however its convergence rate can be slow [77]. A new modal expansion of pressure can be introduced to enhance the convergence regarding the number of transverse modes. The same local transverse modes are used but a supplementary mode is added. This mode is a chosen transverse function orthogonal to the initial modes. Incorporating this supplementary mode significantly improves convergence, making the solution more robust and accurate. A large amount of work has been devoted to finding these supplementary modes in a circular case [78] and for a waveguide with varying cross-section and curvature [79, 49]. However, these solutions were limited to solving the Helmholtz equation until recently. But studies have started to incorporate more complex phenomena, with, for example, nonlinear sound propagation [80] or ducts with inhomogeneous sound-speed profiles [81].

In order to understand more precisely how the method works, an application of this methodology to compute the propagation inside a duct of axially varying annular cross-section without flow is presented. The formulation is taken from [78].

1.3.4.2 Admittance multimodal solution for ducts of axially varying annular cross-section without flow

The Helmholtz Equation (1.14) for the pressure writes:

$$(\Delta + k^2)p = 0 \tag{1.38}$$

and the boundary condition is $\nabla p \cdot \mathbf{n} = 0$.

Let us denote the acoustic pressure derivative $\partial p/\partial x$ as q. The first step is to discretize the acoustic field on the transverse basis function ψ_n. These basis functions are solutions at the axial location x of the eigenvalue problem (1.31) previously defined. As a remainder, the eigenvalue problem writes:

$$(\Delta_\perp + \alpha_n^2)\psi_n = 0,\ \mathbf{n}_\perp \cdot \nabla_\perp \psi_n = 0, \tag{1.39}$$

where S is the transverse surface and $\int_S \psi_i^* \psi_j \mathrm{d}S = \delta_{ij}$.

This allows to define the acoustic pressure and its axial derivative using the basis function amplitudes $(\mathbf{p}, \mathbf{q}) = (p_n, q_n)_{n\in[0,N]}$:

$$\begin{aligned} p &= \sum_{n=0}^{N} p_n(x)\psi_n(x,r), \\ q &= \sum_{n=0}^{N} q_n(x)\psi_n(x,r). \end{aligned} \tag{1.40}$$

By substituting the acoustic variables with their discretized expression, and projecting the Helmholtz equation on the $N+1$ modes $\psi_n(x,r)$, the following coupled mode equations are obtained:

$$\frac{\mathrm{d}}{\mathrm{d}x}\begin{pmatrix} \mathbf{p} \\ \mathbf{q} \end{pmatrix} = \begin{pmatrix} M_{11} & M_{12} \\ M_{21} & M_{22} \end{pmatrix}\begin{pmatrix} \mathbf{p} \\ \mathbf{q} \end{pmatrix}, \tag{1.41}$$

with:

$$\begin{aligned} (M_{11})_{ij} = -\int_S \phi_i^* \frac{\partial \phi_j}{\partial x}\mathrm{d}S,\ (M_{12})_{ij} = -\delta_{ij}, \\ (M_{21})_{ij} = (\alpha_j^2 - k^2)\delta_{ij},\ M_{22} = -M_{11}^H, \end{aligned} \tag{1.42}$$

and where ^{H} denotes the adjoint transpose.

The next step in the admittance multimodal method consists in defining an admittance matrix Y such that $\mathbf{q} = Y\mathbf{p}$. This matrix is governed by the following Riccati equation:

$$\frac{\mathrm{d}Y}{\mathrm{d}x} = -YM_{11} - YM_{12}Y + M_{21} + M_{22}Y \tag{1.43}$$

which is solved using a Magnus–Möbius scheme [76, 82] and an initial value Y^e. For the initial value, one possibility to define it, is to consider a constant cross-section duct termination with only outgoing waves. Then, as in such a duct the axial wavenumber is known analytically, an

analytical expression of the admittance is obtained $Y^e_{i,j} = \mathrm{i}\sqrt{k^2 - \alpha_j^2}\delta_{ij}$. The admittance is then calculated from the exit to the source by integrating Equation (1.43).

Injecting the expression of the admittance into the modal matrix equation gives the following equation for the acoustic pressure:

$$\frac{\mathrm{d}}{\mathrm{d}x}(\mathbf{p}) = (M_{11} + M_{12}Y)\,\mathbf{p}. \tag{1.44}$$

It can be integrated from the source to the exit given an initial value $\mathbf{p}_i = (I_d + R)\mathbf{p}_+$, where $\mathbf{p}_+$ is the incoming acoustic wave, R is the local reflection matrix $R = (Y_i + Y)^{-1}(Y_i - Y)$, and Y_i is the constant cross-section duct admittance at the injection plane [75].

The incorporation of an additional mode substantially enhances the convergence of the basis. This mode is designed orthogonal to the other transverse modes, and such that $\mathbf{n}_\perp \cdot \nabla_\perp \psi_{-1} \neq 0$, to better account for the non-zero derivative of the potential gradient for a curved wall that cannot be satisfied by the local transverse modes (which satisfy $\mathbf{n}_\perp \cdot \nabla_\perp \psi_n = 0$ at the wall). Various techniques exist to define this supplementary mode. Nonetheless, it's worth noting that in the scope of this thesis, although it has shown significant improvements when solving the Helmholtz equation, this extension has not been implemented. Therefore, we will not go deeper into details. The reasons behind its exclusion in this study will be detailed in subsequent manuscript sections.

1.4 Conclusion

Aeroacoustics involves the study of sound generated by fluid flows, which fluid dynamics equations can describe. By neglecting the viscosity and heat conduction, the acoustic propagation can be described using the Euler equations. Furthermore, if the acoustic fluctuations are considered to be orders of magnitude smaller than the aerodynamic ones, these equations can be simplified to the linearized Euler equations. Finally, by introducing an irrotational flow hypothesis, a last simplification can be made to obtain the Goldstein propagation equation. When this equation is to be solved, only a single variable, the potential, gives access to the overall acoustic field. Moreover, this equation is linear, making it much easier to solve than Navier-Stokes equations.

While source computation can be computationally expensive, propagation can be achieved more efficiently using various methods. These methods can be broadly classified as numerical or semi-analytical. Numerical methods, such as finite difference, boundary element, and finite element methods, offer great versatility but come with high computational costs. When sound

propagation occurs within a duct, it is possible to employ faster methodologies by using some of the acoustic properties in this region. These characteristic forms, known as modes, enable faster calculations. In the context of evaluating various engine geometries, semi-analytical methods, based on the concept of modes, are particularly valuable.

Nevertheless, the emergence of new engine geometries, such as those with high bypass ratios and semi-buried engines, poses challenges to the underlying assumptions of existing models. These modelling challenges necessitate the development of new approaches. Two important aspects are the shorter air inlet length, requiring models to consider cut-off and transition modes, and significant inflow distortion. To address these challenges, two promising approaches have emerged: the WKB method and the multimodal method. The WKB method offers cost-effective calculations and has been modified to incorporate phenomena like transitions or complex flows such as sheared flows. However, it cannot incorporate scattering phenomena. On the other hand, the multimodal method can accurately compute modes' evolution and interactions within the duct. However, it is limited to cases without or with a constant mean flow.

CHAPTER 2

GENERAL MULTIMODAL METHOD FOR FLOW AND ACOUSTIC CALCULATION

As stressed out in Chapter 1, the admittance multimodal method is very efficient in solving the Helmholtz equation, being both fast and accurate. The extension of this method to solve the Goldstein propagation equation, developed during this PhD thesis, is detailed in the present chapter.

The method, presented in Section 2.1, is initially designed to compute the acoustic field in the presence of an already-known potential base flow. The first step is to transform the Goldstein propagation equation into a set of coupled one-dimensional equations, with only first-order derivatives in the axial direction, that governs the evolution of the acoustic potential and acoustic axial velocity. Contrary to the the original multimodal method, the basis is composed of Fourier components (in azimuthal direction) and Chebyshev polynomials (in radial direction). This polynomial basis offers excellent convergence properties for smooth geometries. However, with this basis, high-order modes (not well captured by the polynomial basis) are present in the calculation and must be handled with care [59, 49]. A modification of the Magnus–Möbius scheme [76, 82] traditionally used for the axial integration is proposed. This modification is based on an eigendecomposition of the Magnus matrix. A procedure is also added to deal with liner discontinuity.

This method provides fast predictions if the base flow is known. But in order to obtain fast predictions on the whole, the multimodal method is here also used to compute the base flow by analogy with an acoustic field at a zero frequency and without convective effects. This is done in Section 2.2.

Finally, the developed method is validated for both flow and acoustic calculations against a FEM code in Section 2.3, for axisymmetric cases. The focus is on the accuracy and stability of predictions for various modes and frequencies.

2.1 Acoustic multimodal formulation

2.1.1 Governing equations

In the standard multimodal formulation, the Helmholtz equation is solved using the acoustic pressure and axial velocity as primary variables. Solving the equation for pressure can be particularly cumbersome in cases with flow, therefore we work here with the acoustic velocity potential ϕ such that $\mathbf{v} = \nabla\phi$. The flow is assumed to be a potential perfect gas flow. Therefore, the mean flow velocity also derive from a scalar potential, denoted Φ.

With these hypotheses, the steady Euler equations (1.9) simplifies to:

$$\nabla \cdot (D\nabla\Phi) = 0 \,, \tag{2.1a}$$

$$\frac{D^{\gamma-1}}{\gamma-1} + \frac{1}{2}\nabla\Phi \cdot \nabla\Phi = E \,, \tag{2.1b}$$

with E a Bernoulli constant. As stated in Section 1.1.3, the acoustic velocity potential is governed by the Goldstein propagation equation:

$$\nabla \cdot (D\nabla\phi) - D\frac{\mathrm{D}}{\mathrm{D}t}\left(\frac{1}{C^2}\frac{\mathrm{D}\phi}{\mathrm{D}t}\right) = 0 \,, \tag{2.2a}$$

$$p = -D\frac{\mathrm{D}\phi}{\mathrm{D}t}. \tag{2.2b}$$

The walls of the duct are considered to be impermeable to the mean flow:

$$\mathbf{V} \cdot \mathbf{n} = 0. \tag{2.3}$$

For acoustic boundary conditions, they are considered to be lined with an impedance Z. The Ingard–Myers impedance condition (1.15) is used for this purpose:

$$\mathrm{i}\omega(\mathbf{v} \cdot \mathbf{n}) = \left[\frac{\mathrm{D}}{\mathrm{D}t} - \mathbf{n} \cdot (\mathbf{n} \cdot \nabla\mathbf{V})\right]\left(\frac{1}{Z}p\right). \tag{2.4}$$

To apply the multimodal method, the governing equation must be rearranged into a system with only first-order derivatives in the axial direction x. The chosen variables are the acoustic potential ϕ and its axial derivative u. The system then writes:

$$\frac{\partial\phi}{\partial x} = u, \tag{2.5a}$$

$$D\frac{\partial}{\partial x}\left(\left(1-M^2\right)u\right) = D\frac{\mathrm{D}}{\mathrm{D}t}\left(\frac{1}{C^2}\frac{\mathrm{D}_\perp\phi}{\mathrm{D}t}\right) + D\frac{\mathrm{D}_\perp}{\mathrm{D}t}\left(\frac{Uu}{C^2}\right) + \frac{D}{2C^2}\frac{\partial}{\partial x}\left(\mathbf{V}_\perp\cdot\mathbf{V}_\perp\right)u - \nabla_\perp\cdot\left(D\nabla_\perp\phi\right), \tag{2.5b}$$

in which $M = U/C$ is the axial Mach number and $\mathrm{D}_\perp/\mathrm{D}t = \mathrm{i}\omega + \mathbf{V}_\perp\cdot\nabla$.

2.1.2 Variational formulation

The weak formulation of Equations (2.5) is obtained by multiplying them by a test function g^* and by integrating over the duct cross-section, denoted S, whose boundary is the contour Λ. After some manipulations, one can write [1]:

$$\int_S D(1-M^2)\frac{\partial\phi}{\partial x}g^*\mathrm{d}S = \int_S D(1-M^2)ug^*\mathrm{d}S \tag{2.6a}$$

$$\begin{aligned}\frac{\mathrm{d}}{\mathrm{d}x}\left(\int_S D(1-M^2)ug^* - \frac{DU}{C^2}\frac{\mathrm{D}_\perp\phi}{\mathrm{D}t}g^*\mathrm{d}S\right) &= \int_S D(1-M^2)u\frac{\partial g^*}{\partial x} + D\nabla_\perp g^*\cdot\nabla_\perp\phi \\ -\frac{D}{C^2}\left(\frac{\mathrm{D}_\perp\phi}{\mathrm{D}t}\left(\frac{\mathrm{D}_\perp g}{\mathrm{D}t}\right)^* + Uu\left(\frac{\mathrm{D}_\perp g}{\mathrm{D}t}\right)^* + U\frac{\mathrm{D}_\perp\phi}{\mathrm{D}t}\frac{\partial g^*}{\partial x}\right)\mathrm{d}S &- \int_\Lambda Dg^*\nabla\phi\cdot\mathbf{n}\mathrm{d}\Lambda.\end{aligned} \tag{2.6b}$$

Note that, even if not necessary in theory, we multiply the first equation by $D(1-M^2)$ before the integration.

For the impedance condition (1.15), and following Eversmann [83], we use Stokes' theorem to rewrite the last term in Equation (2.6):

$$\begin{aligned}\int_\Lambda Dg^*\nabla\phi\cdot\mathbf{n}\,\mathrm{d}\Lambda = \frac{1}{\mathrm{i}\omega}\int_\Lambda\frac{D^2}{Z}\left(Uu\left(\frac{\mathrm{D}g}{\mathrm{D}t}\right)^* + \frac{\mathrm{D}_\perp\phi}{\mathrm{D}t}\left(\frac{\mathrm{D}g}{\mathrm{D}t}\right)^*\right)\mathrm{d}\Lambda - \\ \frac{1}{\mathrm{i}\omega}\frac{\mathrm{d}}{\mathrm{d}x}\left[\int_\Lambda\frac{D^2}{Z}\left(Uu + \frac{\mathrm{D}_\perp\phi}{\mathrm{D}t}\right)g^*(\mathbf{V}\cdot\boldsymbol{\tau})\mathrm{d}\Lambda\right],\end{aligned} \tag{2.7}$$

where $\boldsymbol{\tau}$ is the unit vector tangential to the duct wall. In the remaining of the manuscript, $\mathbf{V}\cdot\boldsymbol{\tau}$ is simply denoted V_τ.

1. This step involves an integration by parts. There are many ways to perform it. Here, it was chosen to maximize the symmetries since this gave us the best numerical proprieties.

2.1.3 Modal decomposition

The acoustic variables are represented using a set of linearly independent transverse cross-section functions, denoted $(\varphi_j)_{j\in\mathbb{N}}$. Using this basis, the acoustic potential and its axial derivative are written:

$$\phi = \sum_j \phi_j(x)\varphi_j(x,r,\theta)\ , \quad \text{and } u = \sum_j u_j(x)\varphi_j(x,r,\theta). \tag{2.8}$$

The same basis is used for the test functions associated to ϕ and u. The Equation (2.6) then becomes:

$$\int_S D(1-M^2)\varphi_i^*\varphi_j \mathrm{d}S\frac{\mathrm{d}\phi_j}{\mathrm{d}x} = -\int_S D(1-M^2)\varphi_i^*\frac{\partial\varphi_j}{\partial x}\mathrm{d}S\phi_j + \int_S D(1-M^2)\varphi_i^*\varphi_j\mathrm{d}Su_j, \tag{2.9}$$

$$\begin{aligned}
&\frac{\mathrm{d}}{\mathrm{d}x}\left(\int_S D(1-M^2)\varphi_j\varphi_i^*\mathrm{d}Su_j - \int_S \frac{DU}{C^2}\frac{\mathrm{D}_\perp\varphi_j}{\mathrm{D}t}\varphi_i^*\mathrm{d}S\phi_j\right) = \\
&+\left(\int_S D\nabla_\perp\varphi_i^*\cdot\nabla_\perp\varphi_j - \frac{D}{C^2}\frac{\mathrm{D}_\perp\varphi_j}{\mathrm{D}t}\left(\frac{\mathrm{D}\varphi_i}{\mathrm{D}t}\right)^*\mathrm{d}S - \frac{1}{\mathrm{i}\omega}\int_\Lambda \frac{D^2}{Z}\frac{\mathrm{D}_\perp\varphi_j}{\mathrm{D}t}\left(\frac{\mathrm{D}\varphi_i}{\mathrm{D}t}\right)^*\mathrm{d}\Lambda\right)\phi_j \\
&+\left(\int_S D(1-M^2)\varphi_j\frac{\partial\varphi_i^*}{\partial x} - \frac{DU}{C^2}\varphi_j\left(\frac{\mathrm{D}_\perp\varphi_i}{\mathrm{D}t}\right)^*\mathrm{d}S - \frac{1}{\mathrm{i}\omega}\int_\Lambda\frac{D^2U}{Z}\varphi_j\left(\frac{\mathrm{D}\varphi_i}{\mathrm{D}t}\right)^*\mathrm{d}\Lambda\right)u_j \\
&+\frac{1}{\mathrm{i}\omega}\frac{\mathrm{d}}{\mathrm{d}x}\left(\int_\Lambda\frac{D^2V_\tau}{Z}\frac{\mathrm{D}_\perp\varphi_j}{\mathrm{D}t}\varphi_i^*\mathrm{d}\Lambda\phi_j + \int_\Lambda\frac{D^2V_\tau U}{Z}U\varphi_j\varphi_i^*\mathrm{d}\Lambda u_j\right).
\end{aligned} \tag{2.10}$$

Equations (2.9) and (2.10) can be written in vector form by introducing the vectors $\boldsymbol{\phi}$ and $\mathbf{u}$ containing the unknowns $\phi_j(x)$ and $u_j(x)$. The equations governing the axial variation of these vectors are:

$$\begin{pmatrix} A_{11} & A_{12} \\ A_{21} & A_{22} \end{pmatrix}\frac{\mathrm{d}}{\mathrm{d}x}\begin{pmatrix} \boldsymbol{\phi} \\ \mathbf{u} \end{pmatrix} = \begin{pmatrix} M_{11} & M_{12} \\ M_{21} & M_{22} \end{pmatrix}\begin{pmatrix} \boldsymbol{\phi} \\ \mathbf{u} \end{pmatrix}. \tag{2.11}$$

The detailed expressions for the matrices A_{11}, A_{12}, A_{21}, A_{22}, M_{11}, M_{12}, M_{21} and M_{22} are given in Appendix A.

2.1.4 Overview of the calculation

Equation (2.11) is unstable and cannot be integrated directly because of the presence of evanescent modes [82]. The multimodal method allows to solve this issue by defining an admittance matrix Y that links the two vectors $\boldsymbol{\phi}(x)$ and $\mathbf{u}(x)$ through the relation $\mathbf{u}(x) = Y(x)\boldsymbol{\phi}(x)$. It then becomes necessary to integrate this matrix before computing the acoustic potential. But before going deeper into the numerical details of the method, an overview of the procedure to

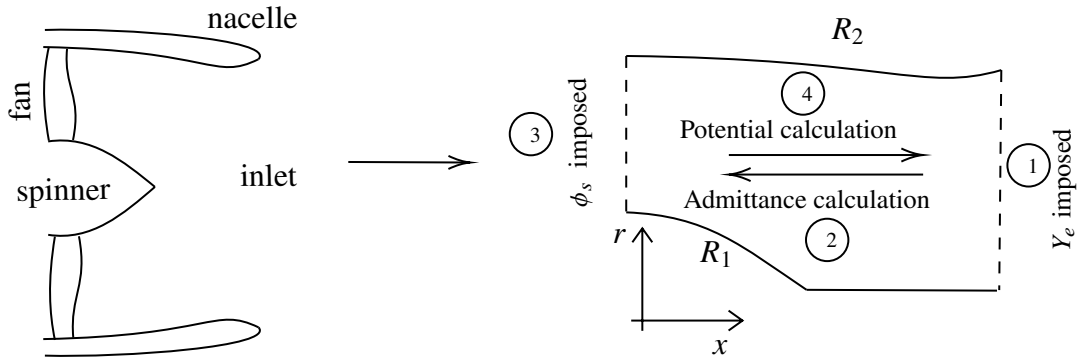

Figure 2.1 – Schematic of the calculation performed.

perform a multimodal computation is given in the following and is depicted in Figure 2.1. Let us suppose that we want to compute the acoustic propagation inside the intake of an aero-engine. This region is considered to be a duct whose cross-section varies axially. In the following, the source denotes the fan plane location while the exit refers to the inlet plane. First, the admittance Y_e at the exit is computed (step 1). Using this initial value, the admittance Y is calculated from the exit to the source using a Magnus–Möbius scheme (step 2). Next, the potential at the source $\boldsymbol{\phi}_s$ is calculated using the specified injected wave and the previously obtained admittance (step 3). Finally, the Magnus–Möbius scheme is once more employed to obtain the potential throughout the entire engine (step 4).

2.1.5 Transverse mode basis

To overcome the limitations of standard hard walled modes which struggle to satisfy the wall boundary conditions (see discussion in Section 1.3.4), a new type of basis function is employed. A Fourier series still represents the acoustic field in the circumferential direction, while a set of Chebyshev polynomials is used in the radial direction to take advantage of their good convergence properties [55, 67, 57]. A first choice would be to take:

$$\varphi_j = \varphi_p^m = T_p\left(\frac{r - R_1}{R_2 - R_1}\right) e^{-\mathrm{i}m\theta}, \tag{2.12}$$

with T_p the shifted Chebyshev polynomial of the first kind of order $p \in \mathbb{N}$. However in the case of circular ducts ($R_1 = 0$), some integrals are not defined when $m \neq 0$ ($\lim_{\delta\to 0} \int_\delta^{R_2} r^{-1}\mathrm{d}r = \infty$). One solution is to replace R_1 by a small, non-zero value in the case of a circular duct, typically the spacing between two central collocation points. Due to the properties of the duct modes (behaviour as $r^{|m|}$ when $r \to 0$, [84]) some of the previous matrices are then poorly conditioned.

A better solution is to add a constraint on the coefficients of Fourier expansions to have basis functions of the form $rf(r)e^{-\mathrm{i}m\theta}$ when $m \neq 0$. We therefore choose, for all m:

$$\varphi_p^m = \left(\frac{r}{R_2 - R_1}\right)^{\min(|m|,1)} T_p\left(\frac{r - R_1}{R_2 - R_1}\right) e^{-\mathrm{i}m\theta}. \tag{2.13}$$

With this basis, the physical behaviour is better captured in the case of circular ducts.

When the flow is axisymmetric, there is no possible coupling between different circumferential Fourier modes, so that no distinction is made between φ_p^m and T_p. The case with non-axisymmetric flow will be specifically studied in Chapter 5.

2.1.6 Admittance calculation

Introducing the definition of the admittance matrix in Equation (2.11), it is possible to show that this matrix satisfies a Riccati equation of the form:

$$\frac{\mathrm{d}Y}{\mathrm{d}x} = -YA_{11}^{-1}M_{11} - YA_{11}^{-1}M_{12}Y - A_{22}^{-1}A_{21}A_{11}^{-1}(M_{11} + M_{12}Y) + A_{22}^{-1}M_{21} + A_{22}^{-1}M_{22}Y \ . \tag{2.14}$$

This equation is solved numerically using a Magnus–Möbius scheme [76, 82], starting from an initial value Y_e.

We use the same procedure as in References [80, 27] to define the matrix Y_e. We assume an infinite duct termination with constant cross-section, with only forward waves at the exit. To determine the admittance there, the acoustic variables are expressed as a summation of modes. By doing so, the problem simplifies to an eigenvalue problem where the solutions correspond to the eigenvalues λ_i and eigenvectors associated with the acoustic potential $\mathbf{w}_i^\phi$ and axial velocity $\mathbf{w}_i^u$ waves. These waves are separated into the forward (+) and backward (−) directions based on the sign of $\mathrm{Re}(\lambda_i) - \omega/\overline{C}\ \overline{M}/(1 - \overline{M}^2)$ for cut-on modes and $\mathrm{Im}(\lambda_i)$ for cut-off modes, where the overline denotes the mean value of the flow variable over the cross-section. The resulting forward admittance matrix is given by:

$$Y_e = W_+^u(W_+^\phi)^{-1} = W_+^\phi \Lambda_+^e (W_+^\phi)^{-1}, \tag{2.15}$$

where $\Lambda_+^e = \mathrm{diag}(\lambda_0, \lambda_1, \lambda_2, ...)$ is the matrix of eigenvalues, and $W_+^\phi = \left(\mathbf{w}_0^\phi, \mathbf{w}_1^\phi, ...\right)$ and $W_+^u = \left(\mathbf{w}_0^u, \mathbf{w}_1^u, ...\right)$ are the matrices of potential and axial velocity eigenvectors associated with forward waves. Note that W_+^ϕ represents the transfer matrix from the transverse eigenmode basis to the polynomial basis.

The admittance is calculated from the exit to the source by integrating the Equation (2.14) (details of this axial integration will be addressed in Section 2.1.8).

2.1.7 Potential calculation

Injecting the expression of the admittance into Equation (2.11) gives the following equation for the acoustic potential:

$$A_{11}\frac{\mathrm{d}\boldsymbol{\phi}}{\mathrm{d}x} = M_{11}\boldsymbol{\phi} + M_{12}Y\boldsymbol{\phi}. \tag{2.16}$$

It can then be calculated from the source to the exit given an initial value $\boldsymbol{\phi}_s$ (more details are given in Section 2.1.8).

Let us assume that we want to specify an incoming acoustic wave represented by its potential distribution $\boldsymbol{\phi}_s^+$. It is necessary to find the waves travelling in the opposite direction, noted $\boldsymbol{\phi}_s^-$, that emerge due to geometrical or flow reflections, to have $\boldsymbol{\phi}_s = \boldsymbol{\phi}_s^+ + \boldsymbol{\phi}_s^-$.

Let us define the reflection matrix R such as $\boldsymbol{\phi}_s^- = R\boldsymbol{\phi}_s^+$. To obtain this matrix R from the admittance matrix Y, the acoustic potential and its axial derivative are decomposed at the source location into right and left propagating waves as:

$$\boldsymbol{\phi}_s = \boldsymbol{\phi}_s^+ + \boldsymbol{\phi}_s^- \text{ and } \mathbf{u}_s = \mathbf{u}_s^+ + \mathbf{u}_s^-. \tag{2.17}$$

Using the value of the admittance at the source plane and continuity conditions for the acoustic and its axial derivative, the following relation is obtained:

$$Y(\boldsymbol{\phi}_s^+ + \boldsymbol{\phi}_s^-) = Y_s^+\boldsymbol{\phi}_s^+ + Y_s^-\boldsymbol{\phi}_s^-, \tag{2.18}$$

with $Y_s^\pm$ the local forward/backward admittance matrix. Since the previous relation is true for any injected field $\boldsymbol{\phi}_s^+$, we obtain $R = (Y - Y_s^-)^{-1}(Y_s^+ - Y)$ and the potential at the source is $\boldsymbol{\phi}_s = (I_d + R)\boldsymbol{\phi}_s^+$, with I_d the identity matrix.

2.1.8 Modification of the Magnus–Möbius scheme

High-order modes, that are not well captured by the polynomial basis, are present in the calculations, as reported by Wilson *et al.* [59] and Guennoc [49]. Their axial wavenumbers are far from the ones associated with physical modes, and they tend to be strongly cut-off. It will be shown later that the matrices involved in the Magnus–Möbius scheme are directly related to these wavenumbers. While the physical eigenvalues (obtained when using the hard walled duct modes

as an approximation basis) do not pose a problem, the non-physical eigenvalues obtained when using a polynomial basis lead to poorly conditioned matrices due to their strongly cut-off nature. To avoid this conditioning issue, we propose a modified formulation of the Magnus–Möbius scheme.

Firstly, the classical Magnus–Möbius scheme is described below. We introduce the exit location x_e and the source position x_s. Considering an axial discretization $(x_n)_{n\in[\![0,N]\!]}$ such that $x_N = x_s$ and $x_0 = x_e$ (note the decreasing evolution, as the admittance is solved from the exit plane to the source plane), the potential and acoustic velocity at positions x_n and x_{n+1} are linked using the following equation:

$$\begin{pmatrix} \boldsymbol{\phi}_{n+1} \\ \mathbf{u}_{n+1} \end{pmatrix} = \mathrm{e}^{\Omega_n} \begin{pmatrix} \boldsymbol{\phi}_n \\ \mathbf{u}_n \end{pmatrix}, \tag{2.19}$$

where the matrix Ω_n is the Magnus matrix, the expression of which can be found using the matrices defined in Section 2.1.3 [82]. After splitting the matrix exponential into four blocks:

$$\mathrm{e}^{\Omega_n} = \begin{pmatrix} E_1 & E_2 \\ E_3 & E_4 \end{pmatrix}, \tag{2.20}$$

the evolution of the admittance and the potential are written:

$$\begin{aligned} Y_{n+1} &= (E_3 + E_4 Y_n)(E_1 + E_2 Y_n)^{-1} \\ \boldsymbol{\phi}_n &= (E_1 + E_2 Y_n)^{-1} \boldsymbol{\phi}_{n+1}. \end{aligned} \tag{2.21}$$

The difficulty is that the matrix $(E_1 + E_2 Y_n)$ can be ill-conditioned [49], which makes the scheme not robust for high frequencies or flow variations. We use an eigen decomposition of the matrix Ω_n to avoid using these matrices. Since the transfer matrix $\exp(\Omega_n)$ represents the transfer of information from the axial location x_n to its neighbouring value x_{n+1}, the eigenvalues (Λ_+, Λ_-) of Ω_n, are characteristic of the evolution of right-running $(\boldsymbol{\phi}_+, \mathbf{u}_+)$ and left-running $(\boldsymbol{\phi}_-, \mathbf{u}_-)$ eigenvectors. The exponential matrix can be rewritten as:

$$\mathrm{e}^{\Omega_n} = \begin{pmatrix} \boldsymbol{\phi}_+ & \boldsymbol{\phi}_- \\ \mathbf{u}_+ & \mathbf{u}_- \end{pmatrix} \begin{pmatrix} \mathrm{e}^{\Lambda_+} & 0 \\ 0 & \mathrm{e}^{\Lambda_-} \end{pmatrix} \begin{pmatrix} \boldsymbol{\phi}_+ & \boldsymbol{\phi}_- \\ \mathbf{u}_+ & \mathbf{u}_- \end{pmatrix}^{-1}. \tag{2.22}$$

In addition, by assuming that all the sub-matrices are invertible, the last matrix can be rewritten:

$$\begin{pmatrix} \boldsymbol{\phi}_+ & \boldsymbol{\phi}_- \\ \mathbf{u}_+ & \mathbf{u}_- \end{pmatrix}^{-1} = \begin{pmatrix} (\boldsymbol{\phi}_+ - \boldsymbol{\phi}_- \mathbf{u}_-^{-1}\mathbf{u}_+)^{-1} & 0 \\ 0 & (\mathbf{u}_- - \mathbf{u}_+ \boldsymbol{\phi}_+^{-1}\boldsymbol{\phi}_-)^{-1} \end{pmatrix} \begin{pmatrix} I_d & -\boldsymbol{\phi}_- \mathbf{u}_-^{-1} \\ -\mathbf{u}_+ \boldsymbol{\phi}_+^{-1} & I_d \end{pmatrix}. \tag{2.23}$$

By noting $Y_\pm = \mathbf{u}_\pm \boldsymbol{\phi}_\pm^{-1}$ the admittance matrix associated to respectively right (upper sign) or left (lower sign) running modes, the blocks of the matrix exponential can be written:

$$\begin{aligned}
E_1 &= \boldsymbol{\phi}_+ \mathrm{e}^{\Lambda_+} \boldsymbol{\phi}_+^{-1} (I_d - Y_-^{-1} Y_+)^{-1} + \boldsymbol{\phi}_- \mathrm{e}^{\Lambda_-} \boldsymbol{\phi}_-^{-1} (I_d - Y_+^{-1} Y_-)^{-1}, \\
E_2 &= \boldsymbol{\phi}_+ \mathrm{e}^{\Lambda_+} \boldsymbol{\phi}_+^{-1} (Y_+ - Y_-)^{-1} + \boldsymbol{\phi}_- \mathrm{e}^{\Lambda_-} \boldsymbol{\phi}_-^{-1} (Y_- - Y_+)^{-1}, \\
E_3 &= \mathbf{u}_+ \mathrm{e}^{\Lambda_+} \mathbf{u}_+^{-1} (Y_+^{-1} - Y_-^{-1})^{-1} + \mathbf{u}_- \mathrm{e}^{\Lambda_-} \mathbf{u}_-^{-1} (Y_-^{-1} - Y_+^{-1})^{-1}, \\
E_4 &= \mathbf{u}_+ \mathrm{e}^{\Lambda_+} \mathbf{u}_+^{-1} (I_d - Y_- Y_+^{-1})^{-1} + \mathbf{u}_- \mathrm{e}^{\Lambda_-} \mathbf{u}_-^{-1} (I_d - Y_+ Y_-^{-1})^{-1}.
\end{aligned} \tag{2.24}$$

This formulation highlights the problem that arises when high-order modes are present. As these modes are strongly cut-off, the matrices E_1, E_2, E_3, E_4 involve adding terms in e^{Λ_+} to other terms in e^{Λ_-} while these two exponentials have entirely different orders of magnitudes. Depending on the direction of the axial integration, one of those two always corresponds to exponentially increasing terms, say here e^{Λ_+}, while the other is linked to exponentially decreasing terms, say here e^{Λ_-}. This means that the terms in e^{Λ_+} are very large while the ones in e^{Λ_-} are very small, leading to round-off errors. The goal is to reformulate this expression so as to avoid this summation, which is difficult to compute accurately.

The previous expressions are therefore inserted into the Equation (2.21) to give:

$$\begin{aligned}
Y_{n+1} &= Y_+ + (Y_- - Y_+) P_- R P_+^{-1} (I_d + P_- R P_+^{-1})^{-1} \\
\boldsymbol{\phi}_n &= (I_d + R) P_+^{-1} (I_d + P_- R P_+^{-1})^{-1} \boldsymbol{\phi}_{n+1}.
\end{aligned} \tag{2.25}$$

where $P_- = \boldsymbol{\phi}_- \mathrm{e}^{\Lambda_-} \boldsymbol{\phi}_-^{-1}$, $P_+^{-1} = \boldsymbol{\phi}_+ \mathrm{e}^{-\Lambda_+} \boldsymbol{\phi}_+^{-1}$ and $R = (Y_n - Y_-)^{-1}(Y_+ - Y_n)$.

Note that with these expressions, contrary to the ones in (2.24), there is no summation of the term e^{Λ_+} and e^{Λ_-}. The impact of the high-order mode interaction is included in the term $P_- R P_+^{-1}$, with the high-order modes which are small in both $\mathrm{e}^{-\Lambda_+}$ and e^{Λ_-}.

A quick analysis of Y_{n+1} can give us a better understanding of the role of each of the previous matrices. The terms $\boldsymbol{\phi}_\pm \mathrm{e}^{\Lambda_\pm} \boldsymbol{\phi}_\pm^{-1}$ are characteristic of the propagation of the left and right running modes between the axial position x_n and x_{n+1}. By analogy to the reflection matrix found when deriving the expression for the potential at the source, the matrix R can be associated with the local reflection between left- and right-running modes. When $Y_n = Y_+$ (constant cross-section duct), $R = 0$ and the formulation reduces to $Y_{n+1} = Y_+$. This is expected because the admittance is constant inside a duct when there is no geometry or flow variation. In such a duct $\boldsymbol{\phi}_n = \boldsymbol{\phi}_+ \mathrm{e}^{-\Lambda_+} \boldsymbol{\phi}_+^{-1} \boldsymbol{\phi}_{n+1}$ which means that there is also no possible modal scattering.

Note that the expression obtained for the potential in Equation (2.25) is similar to the ones derived by Wilson [59] or Félix & Pagneux [77], but here we have not neglected the contribution

of high-order modes.

Although this methodology is useful, it has two drawbacks. First, computing the eigenvalues of the matrix Ω_n can be numerically costly compared to the matrix exponential. Secondly, as explained previously, it is necessary to distinguish between left and right-running modes. Failing to sort these modes correctly can cause some numerical difficulties. In theory, it would be possible to use the group velocity to differentiate between them, but evaluating this quantity can be challenging in practice. As an alternative, the "transverse-mode criteria", defined in Section 2.1.6, can be used to classify these modes. This method for ordering the different categories of eigenmodes is used here and reliably distinguishes left and right-running modes for the studied cases.

2.1.9 Impedance discontinuities

The equations previously derived are valid as long as the impedance is represented by a differentiable function. However, in practice, the liner is only applied on a finite portion of the duct, which induces impedance discontinuities. That results in a non-defined matrices M_{21} and M_{22}, making the Magnus–Möbius scheme impossible to use. To solve this issue, several solutions are available. The first option is to impose a continuity of the acoustic potential and acoustic axial velocity (or the acoustic pressure and acoustic axial velocity) at both sides of a discontinuity, which is equivalent to impose a continuity of the admittance. The second option is to consider the duct as completely treated, but with an impedance that is smoothly varying along the axial coordinate. The third option is to use the conservation equations of mass and momentum to determine an admittance connection formula [85].

The first option is incomplete, as it ignores reflections that occur at the axial location of the discontinuities [85]. The second option requires significant over-mesh of the "discontinuity" regions in order to correctly represent the rapidly varying impedance. Here, the third option is therefore preferred. The formula for the admittance across such a discontinuity is obtained by deriving the admittance jump using the weak formulation of the acoustic equation over a vanishingly small control volume.

2.1.9.1 Formulation of the problem

The case of a duct with at least one impedance discontinuity, which can be located either on the hub or the tip, is studied. Let us consider one of these discontinuities, where the impedance

varies from Z^l to Z^r, by defining a thin volume V_l that surrounds it. We assume that the impedance Z varies continuously from Z^l to Z^r over a transition region of size 2δ, as sketched in Figure 2.2. Note that the original problem is recovered when taking the limit $\delta \to 0$. The computational domain V_l is enclosed by the surfaces S_w, S_r, and S_l. S_r and S_l are located respectively at $x = x_d + \delta$ and $x = x_d - \delta$, where x_d is the axial location of the discontinuity, and S_w corresponds to the duct wall surfaces. Finally, $\Lambda_{l/r}$ denote the contours along the perimeter of the duct at $x = x_d \pm \delta$.

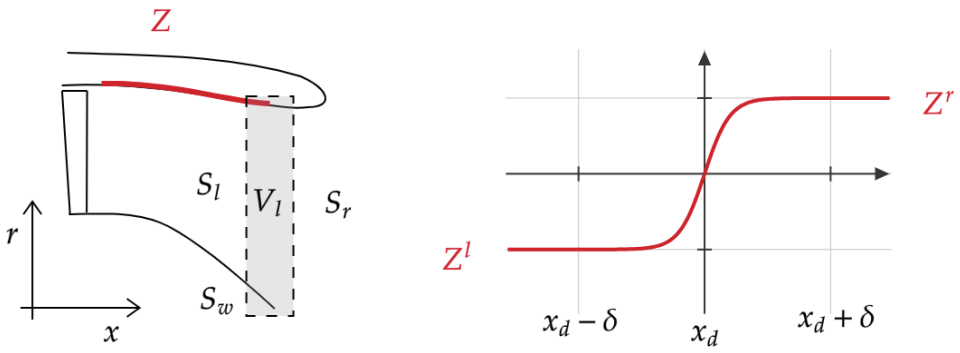

Figure 2.2 – Sketch of a generic liner discontinuity.

2.1.9.2 Governing equations

Let us start by recalling the continuity equation and the mass equation for the perturbation variables:

$$\begin{aligned} \mathrm{i}\omega D\phi + D\mathbf{V}\cdot\nabla\phi + p = 0, \\ \nabla\cdot(D\nabla\phi) - D(\mathrm{i}\omega + \mathbf{V}\cdot\nabla)\left[\frac{1}{C^2}(\mathrm{i}\omega + \mathbf{V}\cdot\nabla)\phi\right] = 0. \end{aligned} \tag{2.26}$$

The weak formulation of these equations obtained through partial integration over the domain V_l writes:

$$\begin{aligned} \int_{V_l} \mathrm{i}\omega D\phi\varphi_i^* + D\mathbf{V}\cdot\nabla\phi\varphi_i^* + p\varphi_i^*\,\mathrm{d}V_l = 0, \\ \int_{V_l} \nabla\cdot(D\nabla\phi)\varphi_i^* - D(\mathrm{i}\omega + \mathbf{V}\cdot\nabla)\left[\frac{1}{C^2}(\mathrm{i}\omega + \mathbf{V}\cdot\nabla)\phi\right]\varphi_i^*\mathrm{d}V_l = 0, \end{aligned} \tag{2.27}$$

for a test function φ_i^* defined on V_l. The mass flow conservation, $\nabla\cdot(D\mathbf{V}) = 0$, is used to write $D\mathbf{V}\cdot\nabla\phi = \nabla\cdot\phi D\mathbf{V}$. Then, by applying the divergence theorem, it is straightforward to show

that:

$$\begin{aligned}
&\int_{V_l} \mathrm{i}\omega D\phi\varphi_i^* - D\mathbf{V}\phi\cdot\nabla\varphi_i^* + p\varphi_i^* \,\mathrm{d}V_l = -\int_S D\mathbf{V}\phi\varphi_i^*\cdot\mathbf{n}\,\mathrm{d}S,\\
&\int_{V_l} D\nabla\varphi_i^*\cdot\nabla\phi - \frac{D}{C^2}(\mathbf{V}\cdot\nabla\phi+\mathrm{i}\omega\phi)(\mathbf{V}\cdot\nabla\varphi_i^*-\mathrm{i}\omega\varphi_i^*)\,\mathrm{d}V_l = \\
&\qquad\int_S D\varphi_i^*\left(\nabla\phi-\frac{1}{C^2}\left(\mathbf{V}\cdot\nabla\phi+\mathrm{i}\omega\phi\right)\mathbf{V}\right)\cdot\mathbf{n}\,\mathrm{d}S,
\end{aligned} \tag{2.28}$$

with $\mathbf{n}$ the unit outgoing normal vector. By reminding that a hard walled boundary condition is used for the mean flow, $\mathbf{V}\cdot\mathbf{n}=0$, the right-hand side of both equations can be developed as:

$$\begin{aligned}
&\int_S D\mathbf{V}\phi\varphi_i^*\cdot\mathbf{n}\,\mathrm{d}S = \int_{S_r} DU\varphi_i^*\phi\,\mathrm{d}S - \int_{S_l} DU\varphi_i^*\phi\,\mathrm{d}S,\\
&\int_S D\varphi_i^*\left(\nabla\phi-\frac{1}{C^2}\left(\mathbf{V}\cdot\nabla\phi+\mathrm{i}\omega\phi\right)\mathbf{V}\right)\cdot\mathbf{n}\,\mathrm{d}S = \int_{S_w} D\varphi_i^*\frac{\partial\phi}{\partial n}\,\mathrm{d}S+\\
&\int_{S_r} D\varphi_i^* u\,\mathrm{d}S - \int_{S_l} D\varphi_i^* u\,\mathrm{d}S + \int_{S_l}\frac{UD}{C^2}\left(\mathbf{V}\cdot\nabla\phi+\mathrm{i}\omega\phi\right)\varphi_i^*\,\mathrm{d}S-\\
&\qquad\int_{S_r}\frac{UD}{C^2}\left(\mathbf{V}\cdot\nabla\phi+\mathrm{i}\omega\phi\right)\varphi_i^*\,\mathrm{d}S.
\end{aligned} \tag{2.29}$$

Further simplification can be done using Stokes' theorem to write (see Eversmann's paper [83] for more details):

$$\begin{aligned}
\int_{S_w} D\varphi_i^*\frac{\partial\phi}{\partial n}\,\mathrm{d}S =& \frac{\mathrm{i}}{\omega}\int_{S_w}\frac{D^2}{Z}(\mathbf{V}\cdot\nabla\phi+\mathrm{i}\omega\phi)(\mathbf{V}\cdot\nabla\varphi_i^*-\mathrm{i}\omega\varphi_i^*)\,\mathrm{d}S+\\
&\frac{\mathrm{i}}{\omega}\int_{\Lambda_r}\frac{D^2}{Z}\left(\mathbf{V}\cdot\nabla\phi+\mathrm{i}\omega\phi\right)\varphi_i^*(\mathbf{n}\times\mathbf{V})\cdot\mathrm{d}\mathbf{\Lambda}+\\
&\frac{\mathrm{i}}{\omega}\int_{\Lambda_l}\frac{D^2}{Z}\left(\mathbf{V}\cdot\nabla\phi+\mathrm{i}\omega\phi\right)\varphi_i^*(\mathbf{n}\times\mathbf{V})\cdot\mathrm{d}\mathbf{\Lambda}.
\end{aligned} \tag{2.30}$$

2.1.9.3 Matching procedure

To obtain a matching condition, we take the limit of the above expressions when $\delta\to 0$, which represents a liner discontinuity. We assume that the acoustic potential axial derivative has finite singularities (i.e., it is well-behaved and does not have infinite discontinuities), ensuring that the volume integrals of expression (2.28) vanish when the volume vanishes. By combining

all of the previous equations, we obtain:

$$\int_{S_r} DU\varphi_i^*\phi \,\mathrm{d}S - \int_{S_l} DU\varphi_i^*\phi \,\mathrm{d}S = 0.$$
$$\int_{S_r} D(1-M^2)\varphi_i^* u \,\mathrm{d}S - \int_{S_l} D(1-M^2)\varphi_i^* u \,\mathrm{d}S = \frac{\mathrm{i}}{\omega}\int_{\Lambda_r} \frac{D^2}{Z}\left(\mathbf{V}\cdot\nabla\phi + \mathrm{i}\omega\phi\right)\varphi_i^*(\mathbf{n}\times\mathbf{V})\cdot\mathrm{d}\mathbf{\Lambda} + \frac{\mathrm{i}}{\omega}\int_{\Lambda_l} \frac{D^2}{Z}\left(\mathbf{V}\cdot\nabla\phi + \mathrm{i}\omega\phi\right)\varphi_i^*(\mathbf{n}\times\mathbf{V})\cdot\mathrm{d}\mathbf{\Lambda}. \tag{2.31}$$

The previous general equation shows that the acoustic potential is continuous across the liner discontinuity by noting that the radius, the mean axial velocity, and the mean density are continuous. When there is no mean flow, it shows that the admittance (and, therefore, the acoustic axial velocity) is also continuous across the liner discontinuity. Otherwise, it indicates that its axial derivative is not continuous if Z is not, which confirms that the admittance is not continuous across the discontinuity. To find its variation across the transition region, we expand the velocity potential and its axial derivative in terms of the basis functions $(\varphi_j)_{j\in\mathbb{N}}$. It yields:

$$\int_S D(1-M^2)\varphi_i^*\varphi_j \mathrm{d}S\left[u_j^r - u_j^l\right] = \frac{\mathrm{i}}{\omega}\int_\Lambda \frac{D^2}{Z^r}\left(U\varphi_j u_j^r + \left(V\frac{\partial\varphi_j}{\partial r} + \mathrm{i}\omega\varphi_j\right)\phi_j^r\right)\varphi_i^*(\mathbf{n}\times\mathbf{V})\cdot\mathrm{d}\mathbf{\Lambda} + \frac{\mathrm{i}}{\omega}\int_\Lambda \frac{D^2}{Z^l}\left(U\varphi_j u_j^l + \left(V\frac{\partial\varphi_j}{\partial r} + \mathrm{i}\omega\varphi_j\right)\phi_j^l\right)\varphi_i^*(\mathbf{n}\times\mathbf{V})\cdot\mathrm{d}\mathbf{\Lambda}. \tag{2.32}$$

Finally, the admittance jump across the impedance discontinuity can be found:

$$Y^l = \left(\mathcal{A} - \mathcal{N}^l\right)^{-1}\left(\mathcal{P}^l - \mathcal{P}^r + \left(\mathcal{A} - \mathcal{N}^r\right)Y^r\right), \tag{2.33}$$

with

$$\begin{aligned}\mathcal{A}_{ij} &= \int_S D(1-M^2)\varphi_j\varphi_i^*\mathrm{d}S,\\ (\mathcal{N}^{r/l})_{ij} &= \frac{1}{\mathrm{i}\omega}\int_\Lambda \frac{D^2V_\tau}{Z^{r/l}}U\varphi_j\varphi_i^*\mathrm{d}\Lambda,\\ (\mathcal{P}^{r/l})_{ij} &= \frac{1}{\mathrm{i}\omega}\int_\Lambda \frac{D^2V_\tau}{Z^{r/l}}\left(\mathrm{i}\omega\varphi_j + V\frac{\partial\varphi_j}{\partial r}\right)\varphi_i^*\mathrm{d}\Lambda,\end{aligned} \tag{2.34}$$

and where $\boldsymbol{\phi}^{r/l}$ and $\mathbf{u}^{r/l}$ refer to the amplitudes of the acoustic potential and the acoustic axial

velocity at $x_d \pm \delta$, $\mathbf{u}^r = Y^r \boldsymbol{\phi}^r$ and $\mathbf{u}^l = Y^l \boldsymbol{\phi}^l$.

2.1.9.4 Computation

In practice, when a liner is applied from an axial position x_1 to x_2 three multimodal computations are done for the admittance: one after the liner $x \in [x_2, x_e]$, one in the liner region $x \in [x_1, x_2]$ and the last one before the liner $x \in [x_s, x_1]$. The admittance jump condition of Equation (2.33) is used between each part. Then, the potential is computed in the opposite direction as previously.

2.2 Flow multimodal formulation

It is interesting to note that solving the acoustic propagation Equation (2.2a) for $\omega \to 0, m = 0$ and $\mathbf{V} = \mathbf{0}$ amounts to solving Equation (2.1a) for the potential mean flow, with ϕ replaced by Φ. In this section, we show how to apply the multimodal method developed for acoustic propagation to calculate the mean flow. The same procedure as for the acoustic calculation is followed, but with two important differences, described in the next sections.

2.2.1 Iterative procedure

An iterative procedure is required because Equation (2.1a) is non-linear due to the dependence of the mean density D on the velocity potential Φ, as defined by (2.1b). Starting from an initial value for the density, we solve Equation (2.2a) using the same multimodal method as above to calculate the mean velocity potential and axial velocity. A new density field D is then calculated using (2.1b). This process is repeated until the change in D between two iterations is smaller than a chosen threshold.

2.2.2 Inflow condition

The other specificity for using the multimodal method for computing the mean flow lies in the definition of the inflow condition. Indeed, a problem arises when we need to define an admittance at the exit where we consider a constant cross-section duct end. The analogy with the acoustics shows that the first eigenvalue associated with the mean flow potential and mean flow axial velocity is $\lambda = 0$. Equation (2.15) then indicates that the mean flow potential is not

proportional to the mean flow axial velocity. Consequently, the Equation (2.15) cannot be used as such anymore.

To address this limitation, we propose representing the mean flow in the constant duct end as a combination of a mean value U_0 and perturbations that vary exponentially. In such a duct, the vector of mean flow axial velocity coefficients is therefore written:

$$\mathbf{U}(x) = U_0 \mathbf{w}_0^U + \sum_{i \neq 0} \alpha_i \mathbf{w}_i^U e^{\lambda_i x}, \tag{2.35}$$

where $\lambda_i \in \mathbb{R}^*$. The term of $\mathbf{w}_0^U$ associated with φ_0 is 1 and all the other ones are equal to zero. This implies that Φ writes:

$$\mathbf{\Phi}(x) = U_0 \mathbf{w}_0^\Phi + \sum_{i \neq 0} \alpha_i \mathbf{w}_i^\Phi e^{\lambda_i x}, \tag{2.36}$$

where the term of $\mathbf{w}_0^\Phi$ associated with the mode φ_0 is $x + c^\Phi$, with c^Φ a constant. At the exit, this term equals $x_e + c^\Phi$.

By noting that the flow perturbations cannot increase in a constant cross-section duct, and therefore by only selecting the eigenvalues associated with exponentially decreasing perturbations, the exit boundary condition for the admittance is:

$$Y_e = W_+^U (W_+^\Phi)^{-1}. \tag{2.37}$$

When the method is used to compute the mean flow, the admittance matrix plays a double role at the duct exit. On the one hand, it sets the potential constant c^Φ, and on the other hand, it avoids spurious reflections.

With this value, it is possible to find the admittance everywhere inside the duct using the standard Magnus–Möbius scheme. Unfortunately, the technique to stabilize this scheme for high-order modes (see Section 2.1.8) cannot be used for the flow since the matrix Ω_n is not diagonalizable.

2.3 Validation for axisymmetric cases

2.3.1 Engine geometry

Within the framework of this thesis, our focus is directed towards the engine's intake. Initially, the plan was to adopt an UHBR engine, aligning with the thesis's aim to develop models applicable to this type of geometry. However, the novelty of these configurations has

limited their availability in existing literature. As a result, an alternative choice has been made, and a geometry that has undergone extensive study is taken: the CFM56 engine [64, 14, 83, 86, 69, 12].

Throughout the whole thesis, we consider the engine to be axisymmetric, so its geometry is entirely defined by the spinner radius R_1 and the nacelle radius R_2. A representation of the engine inlet walls variation can be found in [12]:

$$\begin{aligned} R_1(x) &= \max\left(0, 0.64212 - \left(0.04777 + 0.98234(x/L)^2\right)^{0.5}\right), \\ R_2(x) &= 1 - 0.18453(x/L)^2 + 0.10158\frac{\mathrm{e}^{-11(L-x)/L} - \mathrm{e}^{-11}}{1 - \mathrm{e}^{-11}}, \\ &0 \leq x \leq L, \text{ and } L = 2. \end{aligned} \tag{2.38}$$

The fan is located at the axial position $x = 0$ and the duct exit is at $x = L$. For test cases with a liner, a constant impedance $Z_2 = 2 - \mathrm{i}$ is applied between $x = 0.2$ and $x = 1.8$ at the tip.

2.3.2 Two dimensional validation tool

In this thesis, we used the Python Finite Elements (PFE) [87] code developed by Gwénaël Gabard for validation purposes. This code computes both the steady potential flow and the acoustic field. The solver is based on a weak formulation of Equations (1.9) and (1.13) over a volume V_l bounded by a surface S. In this solver, the lined wall boundary condition is also implemented using the Myers formulation [35]. For the injection/exit boundary conditions, a representation over transverse hard walled modes is used, which allows to specify the incoming mode and to avoid any spurious reflection on the source/exit plane. Quadratic elements (6-node triangles) are used to represent the solutions.

The acoustic potential field is interpolated on an unstructured, triangular mesh generated using Gmsh [88]. The terminal plane needs to be located far enough from regions of non-uniformities. Therefore, the duct is extended by 0.5 to have an exit condition where the flow can be assumed uniform. When using the FEM solver, there is also a need to refine the sharp edges and the liner discontinuities to have an accurate solution. For all presented test cases, a mesh convergence study is performed to evaluate if the acoustic field is accurately represented. An example mesh is shown in Figure 2.3.

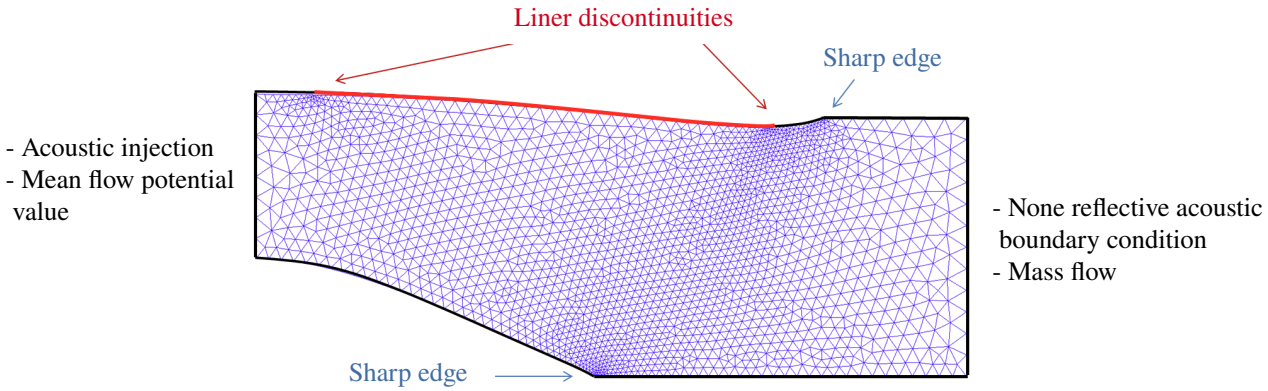

Figure 2.3 – Example of mesh used for computations with the PFE solver (under-meshed for the sake of visibility).

2.3.3 Validation methodology

2.3.3.1 Convergence computation

For a given two-dimensional variable $f(x,r)$, we define the variable f_p referring to the approximation obtained using the multimodal method with p polynomials. The error of the method is defined as:

$$\epsilon_p = \left(\frac{2\pi \int_{R_1}^{R_2} \int_0^L |f_\mathrm{p} - f_\mathrm{ref}|^2 r \mathrm{d}x\mathrm{d}r}{2\pi \int_{R_1}^{R_2} \int_0^L |f_\mathrm{ref}|^2 r \mathrm{d}x\mathrm{d}r} \right)^{1/2}, \tag{2.39}$$

where f_ref is the reference solution obtained using the FEM solver [87] with a fine grid and where the integration is performed over the meridional plane (see geometry definition in Section 2.3.1). For the flow calculations, the error is calculated for the axial velocity, and for the acoustic results, the error is calculated for the pressure amplitude.

2.3.3.2 Axial discretization

The multimodal method involves a numerical integration along the x axis to calculate both the admittance matrix and the potential field. Identifying a robust criterion to define the number of points in the axial direction is important to achieve a trade-off between accuracy and computational efficiency. For this purpose, we define a density, D_{ex}, as the number of points per acoustic wavelength of the highest-order cut-on mode. In the case where no cut-on mode is present inside the duct, D_{ex} is the number of points per characteristic length of decay of the most evanescent mode. However, we have to ignore non-physical high-order modes since they are highly evanescent and would lead to a dramatically oversampled mesh. Therefore, we only

consider the first two-thirds of the modes, which is considered a good criterion for physical modes [65].

The eigenvalues computed at the duct exit are chosen to define the number of axial grid points N_x:

$$N_x = D_{ex}\lambda_{chosen}L, \tag{2.40}$$

where λ_{chosen} corresponds to the chosen eigenvalue. In the rest of this chapter, we use $D_{ex} = 1$ and a second order modified Magnus–Möbius scheme [76, 82].

2.3.4 Flow results

To validate the computation of the mean flow, three test cases are considered, with a low, medium and high velocity defined at the fan face by $M_s = -0.2$, -0.4 and -0.6, respectively. For each of these cases, the number of Chebyshev polynomials is varied: $p = 3$, 6 or 9. The results are shown in Figure 2.4. While three polynomials are not sufficient to accurately represent the mean flow, a good representation of the flow can already be achieved with only six polynomials. With nine polynomials, the agreement is excellent. The areas where the accuracy is reduced are near the sharp corners along the duct walls, which are located at the transition from the spinner to the duct axis near ($x = 1.25$), and at the exit of the duct ($x_e = 2$), where a straight duct is used for the exit condition. At these points, the flow velocity tends to zero to satisfy the wall boundary condition, which results in strong local gradients in the solution. Yet, these localized losses of accuracy do not impact the rest of the solution, and the method is able to compute the mean flow accurately even with a limited number of polynomials. The results in Figure 2.4 also indicate that the required number of polynomials does not depend on the specified Mach number value, since there is no visible loss of accuracy when increasing it. The difference, which is not visible in the graph, is the number of iterations required to converge to the solution of the non-linear Equation (2.1a). For the low-velocity case, only three steps are required to reach a converged solution (with a tolerance of 10^{-5}), while five steps are needed for the medium-velocity case and seven for the high-velocity case. This is expected, since compressible effects become more significant as the Mach number increases.

Figure 2.5 presents a convergence analysis using the FEM computations as the reference solutions. The number of polynomials used in the multimodal method is varied between 1 and 50. The results confirm the qualitative observations based on Figure 2.4. Firstly, an accurate representation of the flow can be obtained even with a small number of polynomials. For example, with just nine polynomials, the relative error is only $\epsilon_p \simeq 6\times10^{-4}$. Secondly, the specified Mach

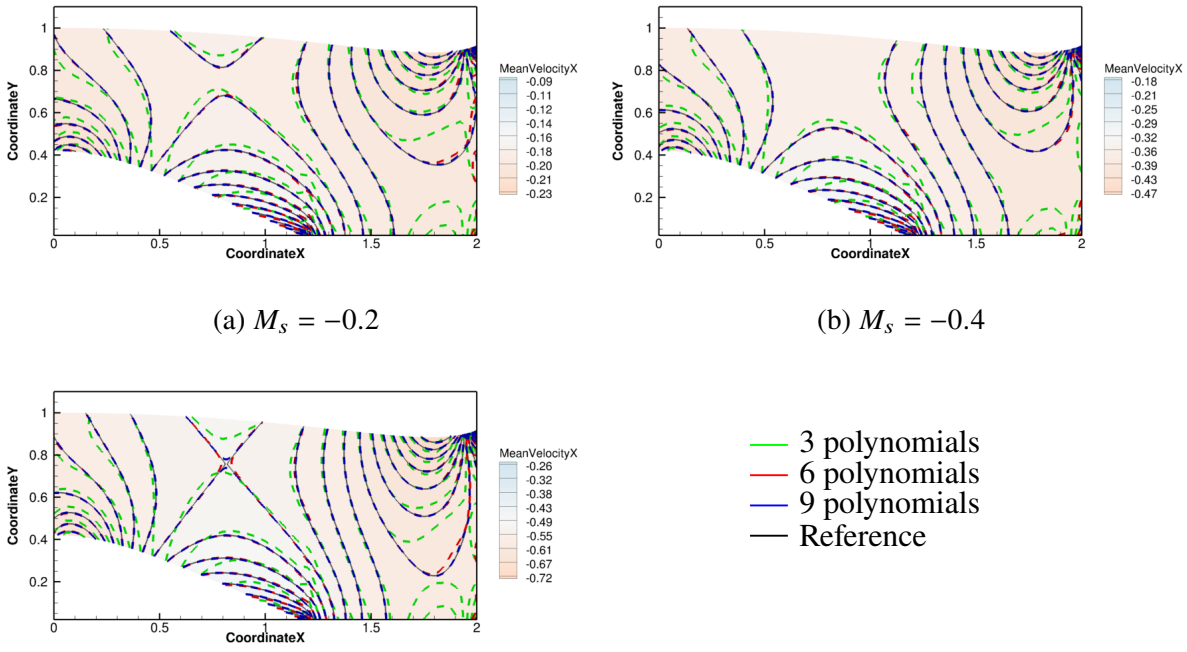

(a) $M_s = -0.2$

(b) $M_s = -0.4$

(c) $M_s = -0.6$

Figure 2.4 – Contours of normalized axial velocity, overlaid on the reference FEM solution, for varying numbers of polynomials.

number only has a small influence on the accuracy.

To provide an indication of the computational cost of the flow calculations with the multimodal method (based on the Python implementation), we report the CPU time for a single iteration needed to solve Equation (2.1a). With five polynomials, the time is 0.09 seconds, with ten polynomials it is 0.25 seconds, with twenty polynomials it is 0.97 seconds, and it is 7.2 seconds with fifty polynomials. While the method is advantageous with a small number of polynomials, the calculation time increases rapidly as the number of polynomials increases. Still, the multimodal method can provide useful results with reasonably low computational times.

2.3.5 Hard walled acoustic results

For the acoustic computation, the higher the velocity, the worse the conditioning of the Magnus. Therefore, the high-velocity calculation ($M_s = -0.6$) is used for the acoustic calculations. Forty polynomials are used for the flow computations to prevent the numerical error on the flow from affecting the acoustic calculations. Note that axial grid points used in the multimodal

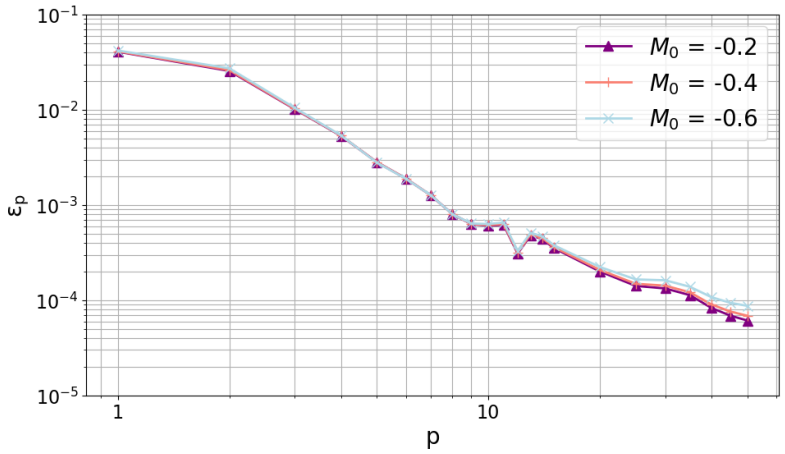

Figure 2.5 – Relative error on the axial velocity field as a function of the number of polynomials used in the multimodal method for three specified velocities.

calculations of the mean flow might differ from those used in the multimodal calculation of the sound field. For this purpose, it is preferable to interpolate the vectors $\mathbf{\Phi}(x)$ and $\mathbf{U}(x)$ introduced in Section 2.2 for the mean flow calculation onto the axial grid points needed for the acoustic calculation (instead of interpolating directly the flow fields such as $U(x,r)$).

To analyse the acoustic response, we first perform a qualitative test by analyzing contour maps of the sound pressure levels (SPL) defined as:

$$SPL = 20\log_{10}\left(\frac{p_{RMS}}{2\times 10^{-5}}\right), \tag{2.41}$$

where p_{RMS} is the root mean square pressure. In the case of a single frequency signal, $p_{RMS} = \sqrt{2}|p|$, where $|p|$ is the pressure amplitude. This is done for a mode $(m,n) = (13,1)$ at $\omega = 20$ and $\omega = 30$, and for the modes $(m,n) = (1,1)$ and $(m,n) = (13,3)$ at $\omega = 20$. These modes include a case where the injected mode encounters a transition from cut-on to cut-off inside the duct ($(m,n) = (13,3)$) and cases where the injected modes are far from modal transitions (all other modes). A unit value is specified for the outer wall pressure of the incoming wave at the source location for all cases. The SPL contours inside the duct are calculated for each case with the FEM, in order to have a reference solution, and with the multimodal method with various numbers of polynomials $p = 10$, 15 and 25. The results are shown in Figure 2.6.

When the mode $(13,1)$ is injected at $\omega = 20$, even with 10 polynomials, the agreement is already good for SPL between 50 and 110 dB, but the agreement remains poor for low SPL. With 15 or 25 polynomials, the agreement is excellent for all SPL shown in the graph. It should be noted that it is in the regions where the flow speed is higher ($x \in [1.8, 2]$) that the precision is

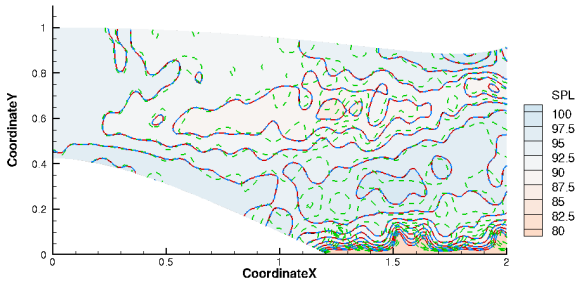

(a) $(m, n) = (1, 1)$ at $\omega = 20$

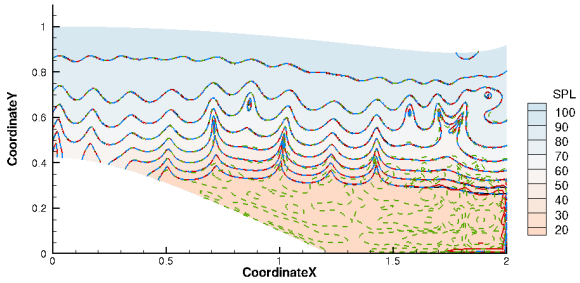

(b) $(m, n) = (13, 1)$ at $\omega = 20$

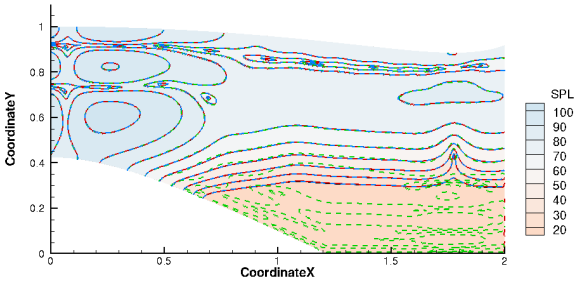

(c) $(m, n) = (13, 3)$ at $\omega = 20$

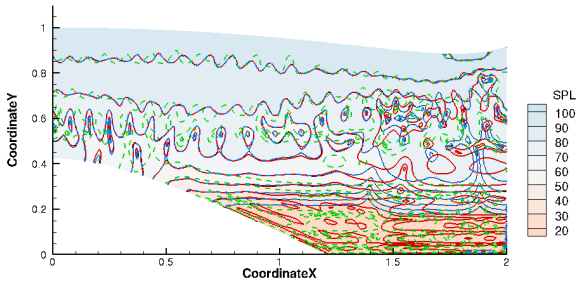

(d) $(m, n) = (13, 1)$ at $\omega = 30$

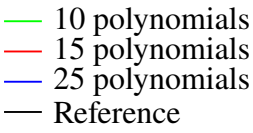

Figure 2.6 – Contours on sound pressure levels, overlaid on the reference FEM solution, for different numbers of polynomials.

the lowest. Similar conclusions can be made for the higher radial order mode $(13, 3)$. When the frequency is increased for the azimuthal mode $(m, n) = (13, 1)$, the agreement is degraded. With 10 polynomials, the pressure field is inaccurate everywhere in the duct. With 15 polynomials, the agreement improves markedly, and for high SPL values, the agreement is acceptable. With 25 polynomials, the agreement is once again excellent. As expected, more polynomials are needed when increasing the frequency since the number of cut-on modes also increases.

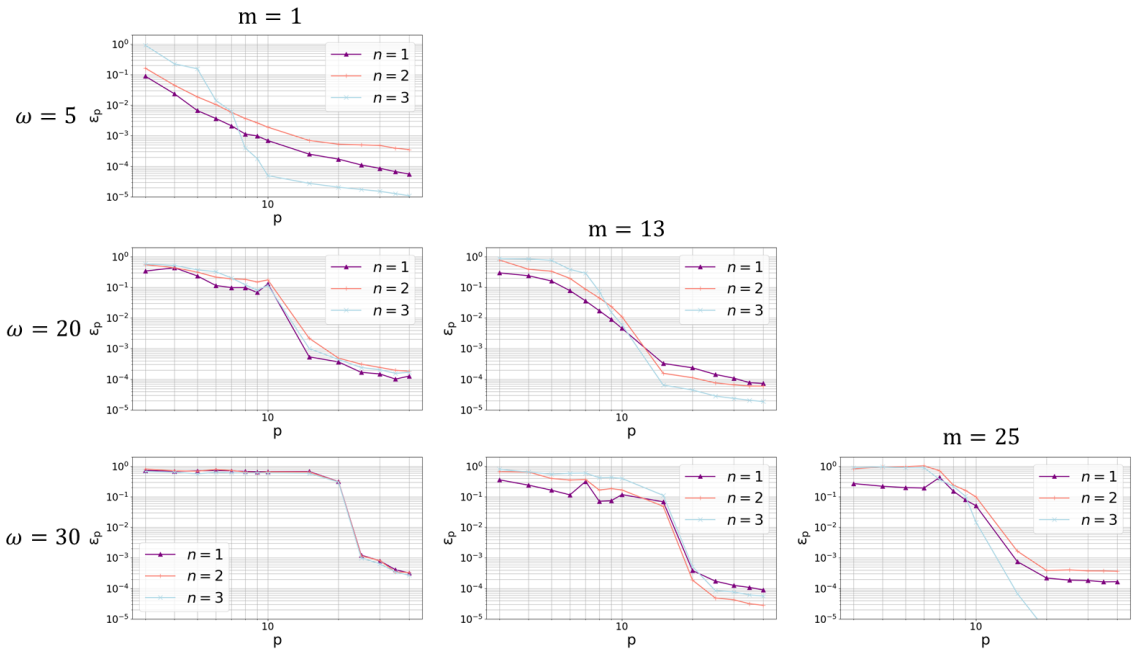

Figure 2.7 – Error of the acoustic pressure field as a function of the number of polynomials used.

To further confirm these qualitative observations, we perform a convergence analysis by plotting, in Figure 2.7, the relative error on the amplitude of acoustic pressure as a function of the number of polynomials. We consider the influence of the azimuthal mode order, the frequency, as well as the first three radial orders. It is important to note that we exclude cases in which the mode is strongly cut-off at the source plane since their strong decay is hard to compute accurately using the FEM. We first consider the azimuthal mode $m = 1$ for a wide range of polynomials. We observe that the convergence graphs can be divided into three parts for this mode. First, a pre-asymptotic region where the error is almost equal to 100% and where including further polynomials does not modify the error. Then a sharp decay region, where the convergence is almost exponential (typical of a spectral method), is obtained. Lastly, a slower convergence is observed. The authors assume that this last region is linked to the axial discretization, and that the observed convergence rate is related to the order of the Magnus–Möbius scheme. Note that for the frequency $\omega = 5$, the pre-asymptotic behaviour is not observed mainly because very few polynomials are necessary to accurately represent the acoustic field. For the radial order $n = 3$ at the same frequency, the error decreases more sharply than for the other radial orders for a low number of polynomials $p < 10$, before converging again with the previously observed convergence rates. One explanation for this behaviour is that the Magnus–Möbius scheme is highly adapted to compute cut-off modes. Therefore the convergence rate at the beginning

corresponds to the improvement in the representation of the radial mode $n = 3$. After that, the convergence is more linked to the representation of the radial modes $n = 1, 2$ (which are cut-on). In fact, the $n = 3$ will create radial modes $n = 1, 2$ by modal scattering. Therefore, the convergence rate after the strong decay is the one of these newly created modes. When the azimuthal mode order increases ($m = 13$ and $m = 25$), all the observations made before remain true except for the size of the pre-asymptotic region. The decrease starts further (compared to the distance to a modal transition) in the graph since a higher azimuthal mode means that the acoustic field is mainly concentrated near the tip wall, and higher-order polynomials are necessary to represent it. However, the error remains small even with a limited number of polynomials. In fact, for all frequencies and radial orders, the error is less than 0.1% with 30 polynomials.

Next, to assess the effectiveness of the stabilization proposed for the Magnus–Möbius scheme in Section 2.1.8, we compare the conditioning of the matrices that need to be inverted for both the standard and improved schemes: namely, $(E_1 + E_2 Y)$ for the standard scheme and $(I_d + P_- R P_+^{-1})$ for the improved scheme. We consider two cases: the mode $(m, n) = (13, 1)$ at $\omega = 20$ and the mode $(m, n) = (1, 1)$ at $\omega = 30$ (both cases use 40 polynomials). The conditioning does not depend on the axial discretization with the modified scheme, while it is highly sensitive to it in the standard scheme. Therefore, to evaluate the improvement brought by the new formulation, four axial integration steps are used with the standard scheme: $D_{\text{ex}} = 0.5$, 1, 2, 10. The results are shown in Figure 2.8. As expected, the conditioning of the improved scheme is better than the one of the standard scheme almost everywhere. Some peaks appear in both formulations near axial positions where modal transitions occur (cut-on to cut-off, or vice versa). The conditioning of the matrix $(E_1 + E_2 Y)$ is the worst near the exit region ($x = 2$) where the duct radius varies rapidly. In this region, the proposed stabilized scheme improves the conditioning by several orders of magnitudes.

Finally, we report the computational time required for each calculation. These are measured using a Python implementation of the multimodal method running on a desktop computer. The CPU time is not given for each calculation, but instead we provide a range of runtimes, from the shortest to the longest runtimes for a fixed number of polynomials. With five polynomials, the runtime ranges from 0.02 to 0.9 seconds, while with ten polynomials, it ranges from 0.09 to 3 seconds. Similarly, with twenty polynomials, the runtime ranges from 0.5 to 7 seconds, and with forty polynomials, it ranges from 1.5 to 33 seconds. It is important to note that unlike for the flow calculations in Section 2.3.4, the computational time for a given number of polynomials varies significantly depending on the studied mode and frequency since they influence the number of points in the axial direction. Note that the criterion defined for D_{ex} is rather conservative, and

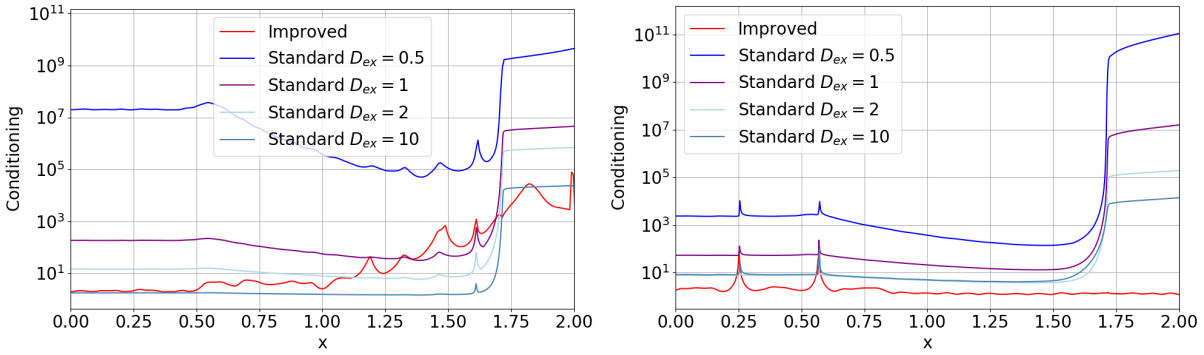

(a) $m = 1$ (b) $m = 13$

Figure 2.8 – Conditioning of the matrix to invert in the Magnus–Möbius scheme with the standard and improved formulation.

sufficiently accurate results can be obtained with smaller values of D_{ex}.

2.3.6 Lined acoustic results

Test cases with a liner are now performed to validate the developed method for such cases. The same flow is considered as for the hard walled test cases. It should be recalled that when there is an impedance discontinuity along the wall, the jump condition derived in Section 2.1.9 is used. For the three multimodal computations (see Section 2.1.9) the density criterion D_{ex} is used in each region, leading to different axial discretizations. Contours of the sound pressure levels in the duct are given in Figure 2.9. All the conclusions made for the hard walled cases remain valid, and an additional observation can be noted. At the junctions between hard and lined walls, the jump in surface impedance induces sharp gradients in the acoustic velocity potential, and hence large jumps in the acoustic pressure. This type of weak singularity is difficult to capture with a spectral method [89] such as the multimodal method. It is therefore expected that the rate of convergence of the numerical model will be reduced when compared to the hard walled test cases. To mitigate this, in the presence of a liner, high-order polynomials are required to accurately represent the large pressure gradients near the end points of the liner. This effect is relatively weak for the first liner discontinuity at $x = 0.2$, but is clearly visible at $x = 1.8$.

Once again, a convergence study is performed, and the same flow condition and acoustic modes as the ones used for the hard walled validation are taken. Figure 2.10 presents the results. As expected, achieving a precision of 10^{-3} requires more polynomials than for the hard walled case, and the convergence rate is lower. This slower convergence rate makes the method less appealing for lined wall computations. It would be necessary to add supplementary modes to

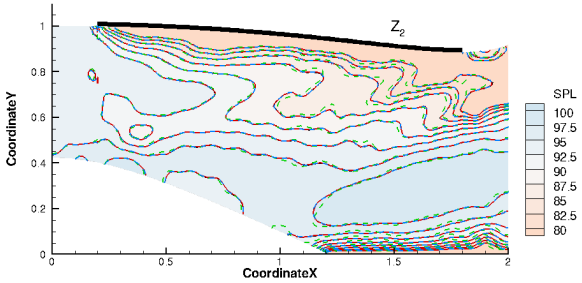

(a) $(m, n) = (1, 1)$ at $\omega = 20$

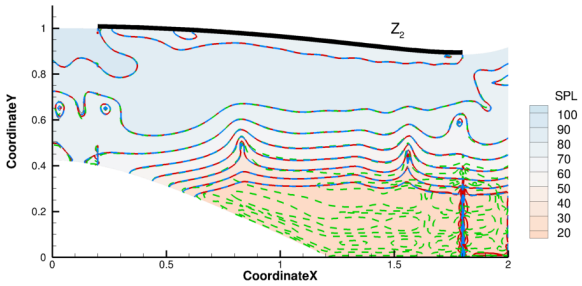

(b) $(m, n) = (13, 1)$ at $\omega = 20$

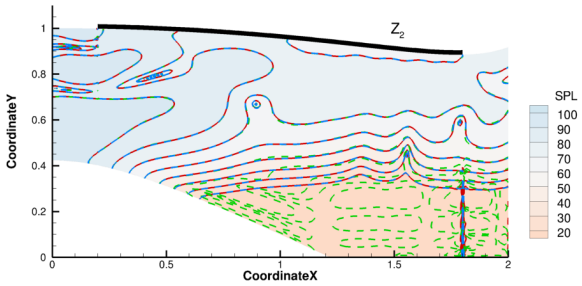

(c) $(m, n) = (13, 3)$ at $\omega = 20$

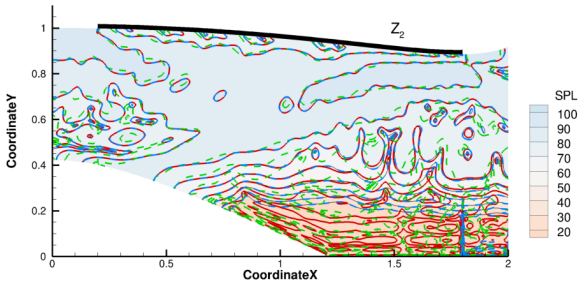

(d) $(m, n) = (13, 1)$ at $\omega = 30$

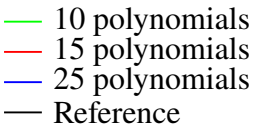

Figure 2.9 – Contours of the sound pressure level in the lined duct, overlaid on the reference FEM solution, for different numbers of polynomials.

address the singularities in the pressure field and avoid this slow convergence. Another key observation is that the liner tends to smooth the convergence plots by decreasing the size of the pre-asymptotic region, and for the most difficult hard walled cases ($\omega = 30$), the error goes faster to a value of 10^{-2}. This could be due to the fact that the method captures well the attenuation of the liner with few polynomials ($p < 20$), even if the prediction of the pressure singularity is erroneous. These singularities also pose problems with finite element methods, where it is

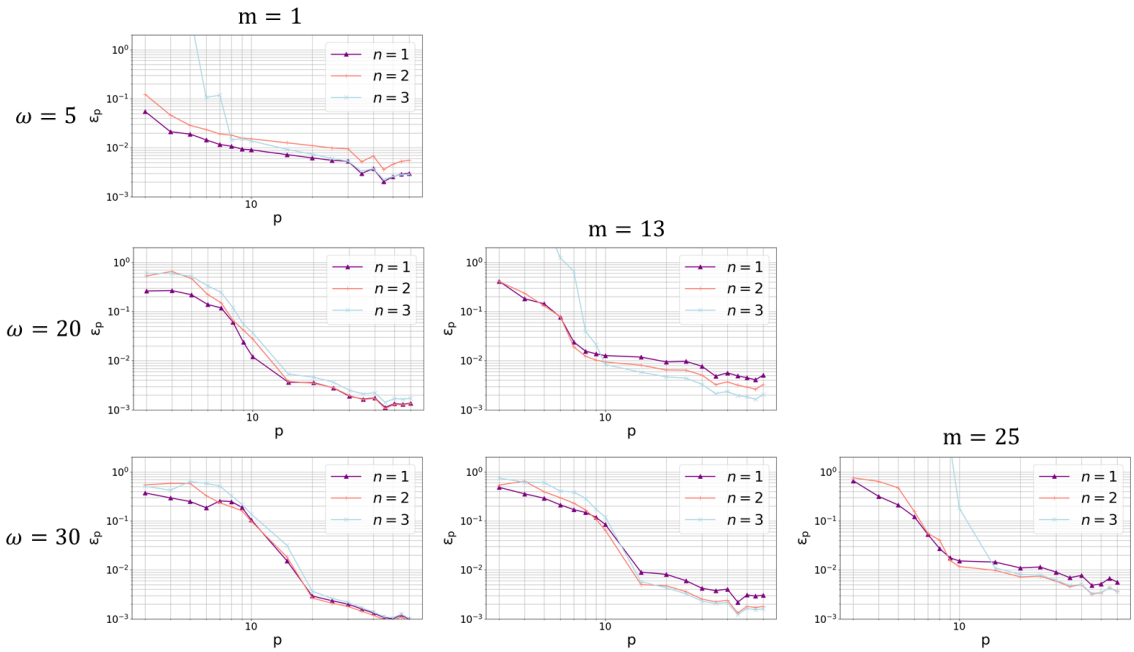

Figure 2.10 – Error on the acoustic pressure field as a function of the number of polynomials used with a lined wall boundary condition.

necessary to refine the region around them. Note that the calculation times required by the multimodal method are similar to the ones obtained for the hard walled test cases.

2.3.7 Criteria for defining the numerical parameters

In the previous section, we used a criteria $D_{ex} = 1$ for the computations. This induced over-meshed computations, but it was taken to achieve accurate comparisons with the FEM results. Now, the question arises as to how the multimodal parameters can be adjusted to obtain less accurate but computationally less demanding calculations. Hence, the objective of this section is to identify appropriate values of D_{ex} (mesh discretization) and p (polynomial order) for a specific geometry. By determining optimal values of these parameters, we can have a balance between computational efficiency and acceptable accuracy in the calculations. In order to evaluate the effect of the number of polynomials independently from the axial discretization, the duct is intentionally over-meshed at first while the number of polynomials is varied. For this purpose, a range of azimuthal mode orders ($m = 5, 10, 20, 40, 75, 100$) and frequency bands are considered, and the evolution of the number of polynomials required to achieve a precision of 10^{-2} is analyzed. The evolution of the number of polynomials with respect to frequency and the

highest cut-on radial order is plotted in Figure 2.11. It is observed that the error varies linearly with frequency. For a given azimuthal mode order, the higher the frequency, the greater the number of polynomials required. This is due to the fact that higher radial modes are cut-on, and they need more polynomials to be accurately represented as they exhibit greater radial variation. Similarly, when increasing the azimuthal order the energy is shifted towards the tip, and higher polynomial orders are necessary for accurate representation. The second graph indicates that the variation with the highest radial cut-on mode order n_{max} is also linear, and seems to follow the dashed curves defined by $p_{needed} = 2 \times (n_{max} + 2) + 0.1 \times m$.

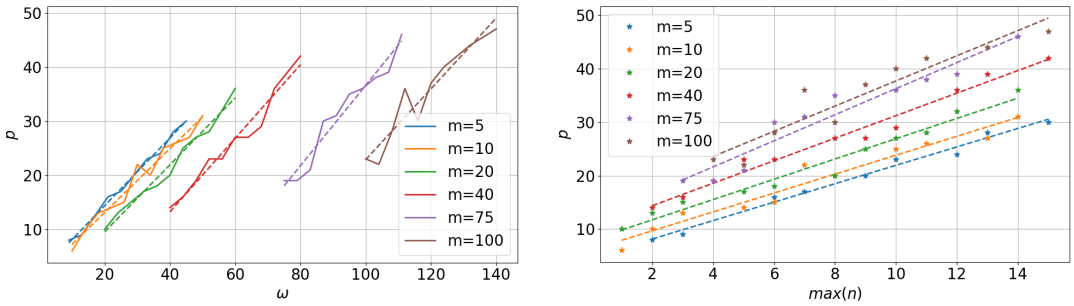

(a) Frequency evolution

(b) Radial order evolution

Figure 2.11 – Number of polynomials needed to reach an error of 1% on the pressure field.

The same procedure can be applied to the axial density parameter D_{ex}. However, since this parameter is continuous, the error can be analyzed as a function of the axial density chosen. For this purpose, four azimuthal modes are considered ($m = 5, 40, 75, 100$) over a range of frequencies, and the axial density is varied from 10^{-2} to 2. The resulting evolution of the error with respect to the axial density is shown in Figure 2.12. Unlike the number of polynomials in the radial direction, there is little impact from the frequency or azimuthal mode order. In almost all cases, an axial density of $D_{ex} = 0.25$ is sufficient to achieve an error of 1%, while an axial density of $D_{ex} = 1$ is sufficient to achieve an error of 0.1%. Note that the blue curve exhibits a different behaviour. It is due to the fact that no cut-on modes are present at this frequency, so the mesh discretization criterion is not the same as for the other cases (see Section 2.3.3.2).

To assess the effectiveness of the Magnus scheme modification, we replicate the previous graph using the original Magnus method instead of the proposed one. In cases where the method failed, we assigned a value of 100% to the error. The results are presented in Figure 2.13. For the mode $m = 5$, the interest of the proposed method is not obvious since the convergence graph exhibits almost the same behaviour as the one obtained before. Moreover, when the computation

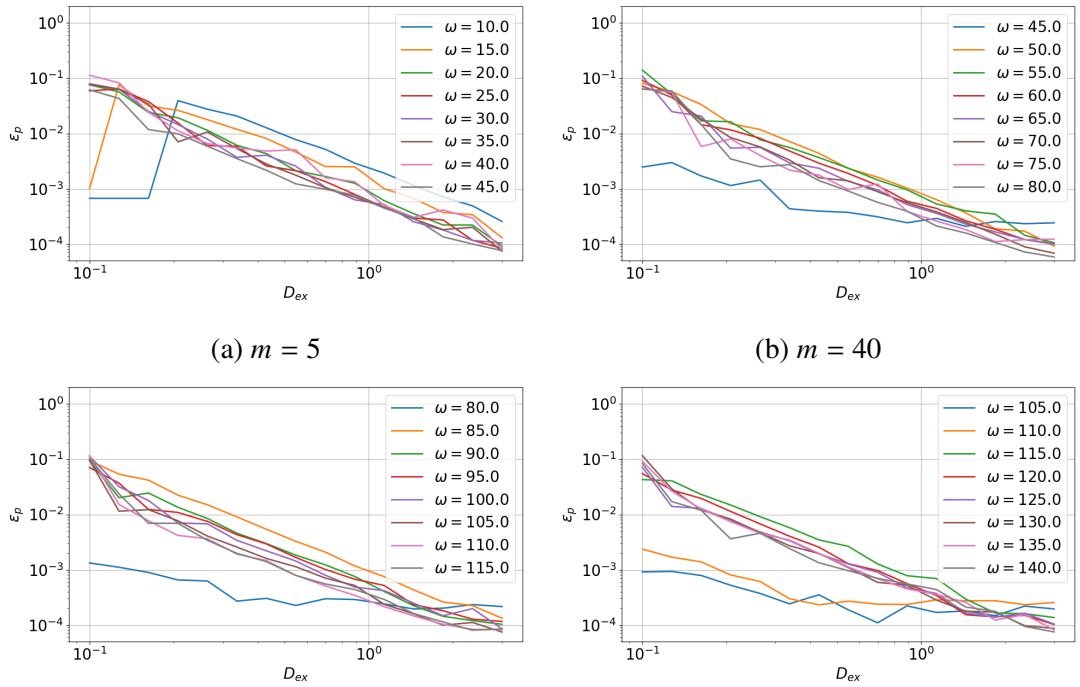

(a) $m = 5$ (b) $m = 40$

(c) $m = 75$ (d) $m = 100$

Figure 2.12 – Error on the pressure field as a function of the axial density using the improved Magnus scheme.

works, the standard scheme is almost 1.5 times faster than the proposed method since it does not require costly eigenvalue calculations. However, for the mode $m = 40$, the standard scheme fails almost everywhere, and the convergence is recovered only from $D_{ex} = 2$. Finally, for the last two modes, $m = 75$ and $m = 100$, the standard scheme fails again everywhere for these discretizations, and higher D_{ex} are needed to recover acceptable results. This highlights the benefits of the proposed scheme, which had no trouble performing those calculations.

2.4 Conclusion

A novel multimodal method for computing the acoustic field in a duct with a general potential mean flow has been formulated. The acoustic field is solved by representing the acoustic variables onto Fourier functions and Chebyshev polynomials. However, this representation introduces non-physical modes that can lead to stability issues. To address this, a modification of the Magnus–Möbius scheme has been proposed. This modification successfully avoids the stability problems associated with the non-physical modes and allows for a more relaxed axial discretization. A

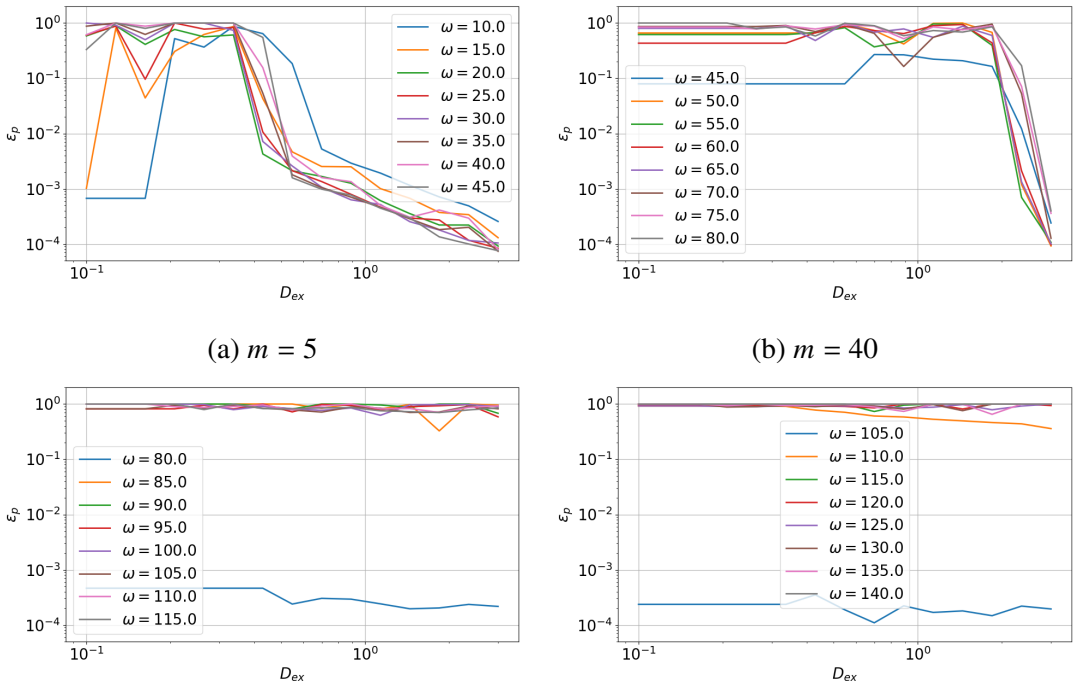

(a) $m = 5$ (b) $m = 40$

(c) $m = 75$ (d) $m = 100$

Figure 2.13 – Error on the pressure field as a function of the axial density using the standard Magnus scheme.

procedure has also been added to deal with liner discontinuity. In addition, the method has been adapted to compute the mean flow in the duct by modifying the multimodal boundaries and performing an iterative process on the density. Finally, the proposed method has been compared against a finite-element solution on a model of a turbofan inlet duct without and with lined walls over a wide range of frequencies. The results show excellent agreement between the multimodal method and the FEM reference solution, indicating the high efficiency of the proposed method for in-duct flow and acoustic computations. It is worth noting that the method's accuracy is good even with a limited number of polynomials which makes it very fast. For example, the computations generally take few seconds to reach an error of 1%.

Chapter 3

Formulation with a multiple-scale flow and the study of modal transition

The previously introduced admittance multimodal method proves efficient for performing in-duct flow and acoustic calculations. However, it is hard to distinguish the 1D mode propagation from the 2D modal scattering. Making such a distinction becomes particularly attractive in investigating transition phenomena. Transition phenomena are inherently 1D and intricately linked to the propagation of a single mode.

Considering the computation of in-duct acoustic propagation in the presence of mean flow, it is possible to introduce simplifications into the flow analysis, especially when dealing with slowly varying geometries. In this context, employing multiple-scale assumptions, as done in WKB methods [64], to establish a simplified flow can be interesting. It is shown that with this flow, it becomes possible to separate the mode propagation effect from modal scattering phenomena within the multimodal method. As a result, this flow appears appealing to study transition phenomena.

Therefore, we use the previous acoustic multimodal formulation but with a multiple-scale flow. This formulation is developed in Section 3.1. With this simplification, all the integrals are known analytically. This method is then evaluated against WKB results and validated using FEM computations. The model is shown to behave well near transition phenomena and is used to study the case where the injected mode encounters multiple turning points in a duct with slowly varying geometry and in the presence of mean flow. The case where two of such turning points arise in the duct due to radius variations is studied in Section 3.2. In order to further validate the model and to gain insights on the impact of neglecting modal scattering, an extension to WKB's approach to address acoustic propagation in ducts with multiple transitions is also presented.

3.1 Multimodal formulation with a multiple scale potential flow

3.1.1 Development of the formulation

The present section uses the admittance multimodal method previously developed to calculate acoustic fields in axisymmetric ducts, considering a multiple scale flow. This extension allows for the incorporation of first-order effects related to both convection and flow-induced scattering mechanisms at a lower computation cost.

3.1.1.1 Multiple-scale flow

The multiple-scale flow has already been presented in the Section 1.3.3 but the main idea to construct this flow is recalled here and adapted to the ciruclar/annular case. The objective is to find a formulation of the flow in the slowly varying duct. We begin by defining the slowly varying axial coordinate $X = \epsilon x$, where ϵ is a small parameter. The mean flow equations are solved by assuming that the geometry and axial mean flow vary slowly with the axial coordinate X. Noting that $\partial A/\partial x = \epsilon \partial A/\partial X + O(\epsilon^2)$ for any slowly-varying variable A, a reasoning on orders of magnitude then shows that the flow variables take the form [64]:

$$\begin{aligned} \mathbf{V}(X, r, \theta; \epsilon) &= U_0(X)\mathbf{e}_x + \epsilon V_1(X, r, \theta)\mathbf{e}_r + O(\epsilon^2), \\ [D, P, C](X, r; \epsilon) &= [D_0, P_0, C_0](X) + O(\epsilon^2), \end{aligned} \tag{3.1}$$

where:

$$\begin{aligned} &\frac{1}{2}\left(\frac{F}{D_0(R_2^2 - R_1^2)}\right)^2 + \frac{1}{\gamma - 1} D_0^{\gamma-1} = E + O(\epsilon^2), \\ &U_0 = \frac{F}{D_0(R_2^2 - R_1^2)} + O(\epsilon^2), \\ &P_0 = \frac{1}{\gamma} D_0^{\gamma}, \\ &C_0 = D_0^{(\gamma-1)/2}, \\ &V_1 = V_1^a(X) r + V_1^b(X)\frac{1}{r} = -\frac{F}{2D_0}\frac{\partial}{\partial X}\left(\frac{1}{R_2^2 - R_1^2}\right) r + \frac{F}{2D_0}\frac{\partial}{\partial X}\left(\frac{R_1^2}{R_2^2 - R_1^2}\right)\frac{1}{r} + O(\epsilon), \end{aligned} \tag{3.2}$$

with E and F two constants (Bernoulli's constant and the cross-sectional mass flow rate, respectively).

3.1.1.2 Modified wave equation

The goal is here to find expressions of the matrices A_{11}, A_{12}, A_{21}, A_{22}, M_{11}, M_{12}, M_{21} and M_{22} of Equation (2.11) in this simplified case. A first idea would be to start from these matrices and inject the previous flow expressions into our equations. But we prefer here to start again from the Goldstein propagation Equation (1.13) and to use the flow expressions of Equation (3.2) to write all the matrices in such a way that we can distinguish the modal scattering from the mode self-propagation. Using the flow expressions and keeping only the first-order terms in the Goldstein propagation Equation (1.13) yields [1]:

$$\begin{aligned}\frac{\partial}{\partial x}\left((1-M_0^2)u\right) = &\left(-\Delta_\perp - \left(\frac{\omega}{C_0}\right)^2 - \frac{2\mathrm{i}\epsilon}{C_0^3}\frac{\mathrm{d}C_0}{\mathrm{d}X}\omega U_0 + 2\mathrm{i}\omega\frac{\epsilon V_1}{C_0^2}\frac{\partial}{\partial r}\right)\phi \\ &+ \left(2\mathrm{i}\frac{\omega U_0}{C_0^2} + 2\frac{\epsilon U_0 V_1}{C_0^2}\frac{\partial}{\partial r}\right)u + O(\epsilon^2\omega^2 U_0)\end{aligned} \tag{3.3}$$

As for the boundary condition (1.15) it can be written:

$$\begin{aligned}\mathrm{i}\omega(\nabla\phi\cdot\mathbf{n}_i) = &-\left(-\omega^2\frac{D_0}{Z_i} + \mathrm{i}\omega U_0\epsilon\frac{\mathrm{d}}{\mathrm{d}X}\left(\frac{D_0}{Z_i}\right) + 2\mathrm{i}\epsilon V_1\frac{D_0}{Z_i}\omega\frac{\partial}{\partial r} - \mathrm{i}\omega\frac{D_0}{Z_i}\frac{\partial\epsilon V_1}{\partial r}\right)\phi \\ &-\left(2\mathrm{i}\omega U_0\frac{D_0}{Z_i} + U_0\epsilon\frac{\mathrm{d}}{\mathrm{d}X}\left(\frac{D_0U_0}{Z_i}\right) + 2\epsilon U_0V_1\frac{D_0}{Z_i}\frac{\partial}{\partial r} - \frac{D_0}{Z_i}\frac{\partial\epsilon V_1}{\partial r}U_0\right)u \\ &-\frac{D_0}{Z_i}U_0^2\frac{\partial u}{\partial x} + O(\epsilon^2\omega^2U_0).\end{aligned} \tag{3.4}$$

3.1.1.3 Multimodal approach

The acoustic potential and its derivative are projected on basis functions, but they are considered to vary slowly in the duct such that $\phi = \sum_j \phi_j(x)\varphi_j(X,r,\theta)$ and $u = \sum_j u_j(x)\varphi_j(X,r,\theta)$ respectively. The weak formulation of Equation (3.3) is written:

$$\int_S \varphi_i^*\frac{\partial}{\partial x}\left((1-M_0^2)u\right)\mathrm{d}S =$$

1. The remaining terms are of order ϵ^2, but we want to highlight the mean flow velocity and the frequency scaling (valid for $\omega > 1$).

$$\int_S \left[\nabla_\perp \varphi_i^* \nabla_\perp \phi + \varphi_i^* \left(-k_0^2 - \frac{2\mathrm{i}\epsilon}{C_0} \frac{\mathrm{d}C_0}{\mathrm{d}X} k_0 M_0 + 2\mathrm{i}k_0 \frac{\epsilon V_1}{C_0} \frac{\partial}{\partial r} \right) \phi + \varphi_i^* \left(2\mathrm{i}k_0 M_0 + 2\frac{\epsilon V_1}{C_0} M_0 \frac{\partial}{\partial r} \right) u \right] \mathrm{d}S$$
$$- \int_\Lambda \varphi_i^* \nabla_\perp \phi \cdot \mathrm{d}\mathbf{\Lambda} + O(\epsilon^2 \omega^2 U_0), \tag{3.5}$$

with $k_0 = \omega / C_0$. The equation is transformed by using the mass conservation equation and the projection of ϕ and u over the basis $(\varphi_j)_{j \in \mathbb{N}}$ and becomes:

$$\begin{aligned} \frac{\mathrm{d}}{\mathrm{d}x} \left((1 - M_0^2) \int_S \varphi_i^* \varphi_j dS u_j \right) = & \left[\int_S \nabla_\perp \varphi_i^* \nabla_\perp \varphi_j - k_0^2 \varphi_i^* \varphi_j + \mathrm{i}k_0 \epsilon \left(-M_0 \left(\frac{1}{S} \frac{\mathrm{d}S}{\mathrm{d}X} + \frac{2}{C_0} \frac{\mathrm{d}C_0}{\mathrm{d}X} \right) \varphi_i^* \varphi_j \right. \right. \\ & - M_0 \frac{\partial}{\partial X} (\varphi_i^* \varphi_j) + \frac{V_1}{C_0} \left(\varphi_i^* \frac{\partial}{\partial r} (\varphi_j) - \varphi_j \frac{\partial}{\partial r} (\varphi_i^*) \right) \mathrm{d}S + M_0 \frac{\mathrm{d}}{\mathrm{d}X} \left(\int_S \varphi_i^* \varphi_j \mathrm{d}S \right) \Big) \Big] \phi_j \\ & + \left[\int_S 2\mathrm{i}k_0 M_0 \varphi_i^* \varphi_j + \epsilon \left(\frac{V_1 M_0}{C_0} \left(\varphi_i^* \frac{\partial}{\partial r} (\varphi_j) - \varphi_j \frac{\partial}{\partial r} (\varphi_i^*) \right) - M_0^2 \frac{1}{S} \frac{\mathrm{d}S}{\mathrm{d}X} \varphi_i^* \varphi_j \mathrm{d}S \right. \right. \\ & \left. \left. + (1 - M_0^2) \frac{\partial}{\partial X} (\varphi_i^*) \varphi_j \right) \mathrm{d}S \right] u_j - \int_\Lambda \varphi_i^* \nabla \phi \cdot \mathrm{d}\mathbf{\Lambda} + O(\epsilon^2 \omega^2 U_0). \end{aligned} \tag{3.6}$$

Then, the second Equation (2.9) of the multimodal formulation becomes:

$$\int_S (1 - M_0^2) \varphi_i^* \varphi_j \mathrm{d}S \frac{\mathrm{d}\phi_j}{\mathrm{d}x} = - \int_S \epsilon (1 - M_0^2) \varphi_i^* \frac{\partial \varphi_j}{\partial X} \mathrm{d}S \phi_j + \int_S (1 - M_0) \varphi_i^* \varphi_j \mathrm{d}S u_j. \tag{3.7}$$

This leads to new equations governing the axial variation of the vectors $(\boldsymbol{\phi}, \mathbf{u})$:

$$\begin{pmatrix} A_{11} & 0 \\ 0 & A_{22} \end{pmatrix} \frac{\mathrm{d}}{\mathrm{d}x} \begin{pmatrix} \boldsymbol{\phi} \\ \mathbf{u} \end{pmatrix} = \begin{pmatrix} M_{11} & M_{12} \\ M_{21} & M_{22} \end{pmatrix} \begin{pmatrix} \boldsymbol{\phi} \\ \mathbf{u} \end{pmatrix} + O(\epsilon^2 \omega^2 U_0), \tag{3.8}$$

with:

$$\begin{aligned} A_{11} &= M_{12} = (1 - M_0^2) G_0, \\ A_{22} &= (1 - M_0^2) G_0 + \frac{\mathrm{i}D_0}{\omega} U_0^2 L_0, \\ M_{11} &= -\epsilon (1 - M_0^2) S_0, \\ M_{21} &= G_1 - k_0^2 G_0 + \mathrm{i}k_0 \epsilon \left(-M_0 \left(\left(\frac{1}{S} \frac{\mathrm{d}S}{\mathrm{d}X} + \frac{2}{C_0} \frac{\mathrm{d}C_0}{\mathrm{d}X} \right) G_0 - \frac{\mathrm{d}}{\mathrm{d}X} (G_0) \right) + ((S_1 - S_1^*) - M_0 (S_0 + S_0^*)) \right) \\ &\quad - \frac{\mathrm{i}D_0}{\omega} \left(-\omega^2 L_0 + \epsilon \left(\mathrm{i} \frac{U_0}{D_0} \frac{\mathrm{d}D_0}{\mathrm{d}X} \omega L_0 + \mathrm{i}U_0 \omega L_1 + 2\mathrm{i}\omega L_2 - \mathrm{i}\omega L_3 \right) \right), \\ M_{22} &= 2\mathrm{i}k_0 M_0 G_0 + \epsilon \left((1 - M_0^2) S_0^* - \frac{\mathrm{d}}{\mathrm{d}X} \left((1 - M_0^2) G_0 \right) + M_0 (S_1 - S_1^*) - \frac{M_0^2}{S} \frac{\mathrm{d}S}{\mathrm{d}X} G_0 \right) \end{aligned} \tag{3.9}$$

$$-\frac{\mathrm{i}D_0}{\omega}\left(2\mathrm{i}\omega U_0 L_0+\epsilon\left(U_0^2 L_4-\frac{U_0^2}{S}\frac{\mathrm{d}(S)}{\mathrm{d}X}L_0+U_0^2 L_1+2U_0 L_2-U_0 L_3\right)\right).$$

The matrices $(G_0, S_0, S_1, G_1, L_0, L_1, L_2, L_3, L_4)$ are defined by:

$$\begin{aligned}
(G_0)_{ij} &= \int_S \varphi_i^* \varphi_j \mathrm{d}S, \qquad (S_0)_{ij} = \int_S \varphi_i^* \frac{\partial \varphi_j}{\partial X}\mathrm{d}S,\\
(S_1)_{ij} &= \int_S \frac{V_1}{C_0}\varphi_i^* \frac{\partial \varphi_j}{\partial r}\mathrm{d}S, \quad (G_1)_{ij} = \int_S \nabla_\perp \varphi_i^* \nabla_\perp \varphi_j \mathrm{d}S,\\
(L_0)_{ij} &= \int_0^{2\pi}\left(R_2/Z_2\ \left(\varphi_i^*\varphi_j\right)\big|_{r=R_2} + R_1/Z_1\ \left(\varphi_i^*\varphi_j\right)\big|_{r=R_1}\right)\mathrm{d}\theta,\\
(L_1)_{ij} &= \int_0^{2\pi}\left(R_2\frac{\mathrm{d}[1/Z_2]}{\mathrm{d}X}\ \left(\varphi_i^*\varphi_j\right)\big|_{r=R_2} + R_1\frac{\mathrm{d}[1/Z_1]}{\mathrm{d}X}\ \left(\varphi_i^*\varphi_j\right)\big|_{r=R_1}\right)\mathrm{d}\theta,\\
(L_2)_{ij} &= \int_0^{2\pi}\left(R_2/Z_2\left(V_1\varphi_i^*\frac{\partial \varphi_j}{\partial r}\right)\bigg|_{r=R_2} + R_1/Z_1\left(V_1\varphi_i^*\frac{\partial \varphi_j}{\partial r}\right)\bigg|_{r=R_1}\right)\mathrm{d}\theta,\\
(L_3)_{ij} &= \int_0^{2\pi}\left(R_2/Z_2\left(\frac{\partial V_1}{\partial r}\varphi_i^*\varphi_j\right)\bigg|_{r=R_2} + R_1/Z_1\left(\frac{\partial V_1}{\partial r}\varphi_i^*\varphi_j\right)\bigg|_{r=R_1}\right)\mathrm{d}\theta,\\
(L_4)_{ij} &= \int_0^{2\pi}\left(R_2/Z_2\left(\varphi_i^*\frac{\partial \varphi_j}{\partial X}\right)\bigg|_{r=R_2} + R_1/Z_1\left(\varphi_i^*\frac{\partial \varphi_j}{\partial X}\right)\bigg|_{r=R_1}\right)\mathrm{d}\theta.
\end{aligned} \tag{3.10}$$

The matrices $(L_0, L_1, L_2, L_3, L_4)$ are associated with the radial boundary conditions and characterize the attenuation due to the liner. In the case of a hard walled duct, all these matrices vanish. It is important to note that the terms that have been neglected scale like $U_0\omega^2$. This means that the higher the mean velocity and the frequency, the worse the expected results.

3.1.1.4 Multimodal calculation

For the axial integration, the classical procedure of Chapter 2 is used with our improved Magnus–Möbius scheme. The only difference stands in the exit boundary condition where the eigenvalue problem is simplified. It writes:

$$\mathrm{i}\lambda_i\begin{pmatrix} A_{11} & 0\\ 0 & A_{22}\end{pmatrix}\begin{pmatrix}\mathbf{w}_i^\phi\\ \mathbf{w}_i^u\end{pmatrix} = \begin{pmatrix} 0 & M_{12}\\ M_{21} & M_{22}\end{pmatrix}\begin{pmatrix}\mathbf{w}_i^\phi\\ \mathbf{w}_i^u\end{pmatrix}, \tag{3.11}$$

with:

$$A_{11} = M_{12} = (1-M_0^2)G_0, \qquad M_{21} = G_1 - k_0^2 G_0 + \mathrm{i}D_0\omega L_0, \tag{3.12}$$

$$A_{22} = (1 - M_0^2)G_0 + \frac{\mathrm{i}D_0}{\omega}U_0^2 L_0, \qquad M_{22} = 2\mathrm{i}k_0 M_0 G_0 + 2D_0 U_0 L_0.$$

3.1.1.5 Transverse mode basis

If an arbitrary basis is chosen for φ_j, computing the matrices in Equation (3.8) is time-consuming and the method would not bring a significant benefit compared to the general multimodal method of Chapter 2. Therefore, it is important to use a basis leading to analytical expressions for integrals in Equation (3.10).

Standard hard walled modes - Fourier-Bessel basis

Most multimodal studies [75, 77, 82, 80] use standard basis functions composed of local hard walled transverse eigenmodes. For axisymmetric ducts, if we associate a pair $(m, n) \in (\mathbb{Z}, \mathbb{N})$ to each index j (such that the basis functions $\varphi_j = \varphi_{mn}$), these eigenmodes write:

$$\varphi_{mn} = N_{mn} \left[\mathrm{J}_m(\alpha_{mn} r) + \Gamma_{mn} \mathrm{Y}_m(\alpha_{mn} r)\right] \mathrm{e}^{-\mathrm{i}m\theta}, \tag{3.13}$$

with α_{mn} and Γ_{mn} defined in Section 1.3.1.1. The normalisation factor N_{mn} is:

$$N_{mn} = \left(2\pi \int_{R_1}^{R_2} \left[\mathrm{J}_m(\alpha_{mn} r) + \Gamma_{mn} \mathrm{Y}_m(\alpha_{mn} r)\right]^2 r \mathrm{d}r\right)^{-0.5}. \tag{3.14}$$

Using the integral properties of Bessel functions, the normalization factor can be found analytically:

$$\begin{aligned}\int_{R_1}^{R_2} \left[\mathrm{J}_m(\alpha_{mn} r) + \Gamma \mathrm{Y}_m(\alpha_{mn} r)\right]^2 r \mathrm{d}r = &\frac{1}{2}\left(R_2^2 - \frac{m^2}{\alpha_{mn}^2}\right)\left[\mathrm{J}_m(\alpha_{mn} R_2) + \Gamma \mathrm{Y}_m(\alpha_{mn} R_2)\right]^2 - \\ &\frac{1}{2}\left(R_1^2 - \frac{m^2}{\alpha_{mn}^2}\right)\left[\mathrm{J}_m(\alpha_{mn} R_1) + \Gamma \mathrm{Y}_m(\alpha_{mn} R_1)\right]^2.\end{aligned} \tag{3.15}$$

For a hard walled duct, this basis has four major advantages:

1. analytical expressions for both $(G_0)_{ij} = \delta_{ij}$ and $(G_1)_{ij} = \alpha_i^2 \delta_{ij}$ are available;
2. it gives an analytical solution for the acoustic field in regions without scattering;
3. it is a complete basis [9], which means that any transverse shape can be recovered if a sufficient number of modes is used;
4. the matrix W_1^ϕ is the identity matrix and the exit admittance matrix is a diagonal matrix with the axial wavenumbers on the diagonal.

However, this basis presents a major weakness which leads to slow convergence for hard walled ducts: the derivatives of all the basis functions are equal to zero at the wall, whereas the acoustic boundary condition imposes a non-zero derivative for the potential gradient for a curved wall. Adding a non-physical supplementary Dirichlet mode (see Section 1.3.4) inside the modal basis [79] allows to overcome this issue, but this is case-dependent.

With such a basis, the matrices defined above have a clear physical meaning. The matrices G_0 and G_1 are diagonal and represent the propagation in the straight parts of the duct (isolated mode propagation). The matrices S_0 and S_1 have non-diagonal terms that are equal to zero only when there is no wall variation and can therefore be related to geometrical/flow scattering. The modal scattering can be artificially turned off by imposing that S_0 and S_1 are equal to zero. In this case, all the matrices are diagonal and the modes do not interact (the method can thus be referred to as multimodal without scattering).

It is worth noting that the multiple-scales approximation weakly impacts the self-propagation terms since the neglected terms ($O(\epsilon^2\omega^2 U_0)$ related to scattering, referred to as flow-scattering terms, are only present when there is a mean flow.

Fourier-Chebyshev basis

To overcome the limitations of standard hard walled modes, we can still use the polynomial basis of the general admittance multimodal method of Chapter 2. When this is done, the expressions of the matrices given in Equation (3.10) can be developed (see Appendix B) such that all the integrals that remain are independent of frequency, flow, geometry and azimuthal order, which is a major benefit of the chosen basis. These integrals only need to be computed once and can then be stored, thus allowing for fast computations. Note that there is again no possible coupling between different circumferential Fourier modes. Therefore we consider that the value of the azimuthal order m is fixed, and no distinction is made between φ_p^m and φ_p. For convenience, this basis is called Chebyshev basis in the following.

3.1.1.6 Impedance discontinuities

With the same methodology as the one used in Section 2.1.9, it is possible to find the jump in the admittance matrix:

$$Y(x_d^l) = \left(\left(1 - M_0^2\right) G_0 - \frac{D_0 U_0^2}{\mathrm{i}\omega} L_0^l\right)^{-1} \left(\frac{D_0 U_0}{\mathrm{i}\omega}\left(\mathrm{i}\omega L_0^l - \mathrm{i}\omega L_0^r + \epsilon\left(L_2^l - L_2^r\right)\right)\right. \tag{3.16}$$

$$+\left(\left(1-M_0^2\right)G_0-\frac{D_0U_0^2}{\mathrm{i}\omega}L_0^r\right)Y(x_d^r)\Bigg)+O(\epsilon^2\omega^2U_0),$$

where G_0, L_0, L_2 are the matrices defined in Section 3.1.1.3.

3.1.2 Comparison between the Bessel and Chebyshev bases for an infinite uniform duct

For an infinite annular uniform duct with lined walls, the propagation problem reduces to the eigenvalue problem given in Equation (3.11).

In order to evaluate the interest of each basis on this simplified case, this problem is solved for parameters representative of a modern engine inlet, with a unit nacelle radius R_2, a spinner radius R_1 equal to 0.3 and a wall impedance Z_2 equal to $2 - \mathrm{i}$. The flow is uniform, D_0 and C_0 equal to 1 and M_0 equal to -0.5. The acoustic variables are computed at $\omega = 25$ and for an azimuthal mode $m = 24$ [58].

At first, both the distribution of the upstream eigenvalues in the complex plane and the shape of an upstream transverse function for the radial order $n = 5$ are computed using a Chebyshev basis. The results are plotted in Figures 3.1a and 3.1b, showing this basis's ability to represent the duct modes correctly. Excellent agreement is obtained when fifteen or twenty polynomials are used. However, with fewer polynomials, the solution quickly deteriorates, and with ten polynomials, the radial distribution of the mode is lost. When enough basis functions are used, there are only minor differences between the eigenvalues obtained numerically and the analytical ones.

Then, to evaluate the benefit of the Chebyshev basis over a standard hard walled transverse basis, the reduction of the error with the increase of the number of basis functions is investigated. The evolution of the error on the radial eigenmode is defined by:

$$\epsilon_p = \left(\frac{\int |\phi_p - \phi_\infty|^2 r\mathrm{d}r}{\int |\phi_\infty|^2 r\mathrm{d}r}\right)^{1/2}, \tag{3.17}$$

with ϕ_p the potential obtained with p basis functions and ϕ_∞ the reference semi-analytical solution (computed as in [64]). The convergence of the Chebyshev and hard walled Bessel bases is assessed in Figure 3.1c. As expected, for a lined duct, the Chebyshev basis outperforms the Bessel basis when many polynomials are used, with an exponential convergence rate. However, when few basis functions are used, the Bessel basis better represents the eigenmodes. These

results confirm that the method has excellent convergence and accuracy if enough Chebyshev polynomials are used. Note that for this case, the use of a supplementary mode for the Bessel basis could drastically improve the convergence observed [90].

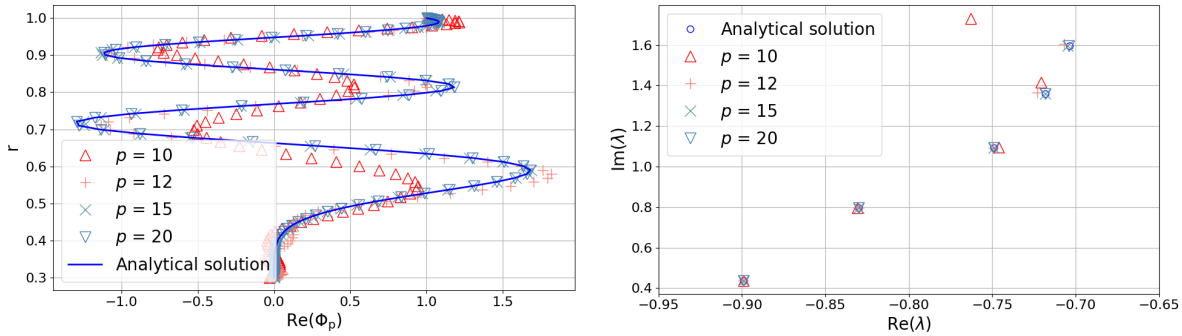

(a) Radial evolution of the eigenmode $n = 5$ (real part)

(b) First five radial computed eigenvalues in the complex plane

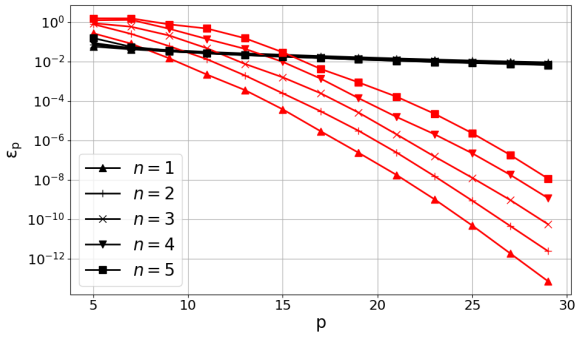

(c) Evolution of the error with the number of basis functions, red lines for the Chebyshev basis and black ones for the Bessel basis

Figure 3.1 – Validation of the eigenvalue resolution inside a constant waveguide with $(R_1, R_2) = (0.3, 1)$, $M_0 = 0.5$, $\omega = 25$, $m = 24$ and $Z_2 = 2 - \mathrm{i}$.

3.1.3 Validation for a slowly-varying duct

3.1.3.1 Validation methodology

- **Numerical procedure**

The CFM56 geometry defined in Section 2.3.1 is used for the validation. The small parameter ϵ is defined by the maximum slope of the nacelle radius, which gives $\epsilon \approx 0.3$. This can be

considered as strong, but the radius variation is particularly important near the exit and remains limited elsewhere.

The multiple-scale multimodal formulation is first evaluated against a method where the axial variation of the acoustic variables is determined analytically. Here, the WKB models defined in Section 1.3.3 are used. These first comparisons aim to evaluate the benefit from using the present method instead of an analytical model, noting that the calculation time is similar.

Then, the validation is pursued using the FEM solver for Goldstein propagation equation described in Section 2.3.2. When the FEM is used, two cases can be distinguished. FEM computations are performed using the flow computed with the MS approximation (referred to as FEM/MS) to check that our method is correctly implemented and that the $O(\epsilon^2\omega^2 U_0)$ terms neglected in Equation (3.3) do not impact the solution. Then, FEM solutions that use the complete flow (referred to as FEM/CFD) are compared to the multimodal results. This allows to assess the limitation brought by the use of a MS flow and the impact of the neglected $O(\epsilon^2\omega^2 U_0)$ terms. It is unlikely that these terms can be neglected at high frequencies when a high-velocity mean flow is used. Typically for frequencies $\omega \sim \epsilon^{-1}$ and high velocities $M_0 \sim 1$, the neglected scattering terms could be, in theory, of the same order of magnitude as one of the computed scattering terms. Note that the error is expected to be equal to numerical precision in all the cases without flow ($M_0 = 0$), since all the neglected terms are scaled by the velocity.

For the multimodal calculations, two different bases can be applied (see Section 3.1.1.5). The Chebyshev one is preferred since it gives shorter calculation times than the Bessel functions. Nevertheless, the admittance multimodal method is also used with the Bessel basis since the modal scattering can be artificially turn-off. In that case, there is no interaction between modes and their resolution can be separated. Therefore, the problem reduces to a scalar integration, which drastically decreases the calculation time. This admittance multimodal method without scattering is referred to as MMWS in the following. Comparisons with the multimodal results (with Chebyshev basis) allow understanding the improvement brought by a formulation that captures the scattering mechanisms.

Details about the numerical resolution are defined here and will be applied to all the test cases. A unit value is specified for the outer wall pressure of the incoming wave at the source location. For the multimodal method, the criterion defined in Section 2.3.7 for the number of polynomials is used, and an axial density $D_{ex} = 0.5$ is chosen. Note that the discretization does not need to be refined near a liner discontinuity since the admittance jump is given analytically by the expression (2.33). With these criteria, all the test cases that are presented took less than one second to run with the developed multiple-scale multimodal method.

● **Flow computation**

For cases with flow, M_0, C_0 and D_0 values are specified at the axial location of the fan (with $C_s = 1$ and $D_s = 1$ in all case). The steady axial velocity and the velocity streamlines obtained with the FEM are represented in Figure 3.2a for a specified Mach number $M_s = -0.4$. The axial velocity averaged over successive cross-sections is also shown and is compared with the flow computed with the multiple-scales (MS) method in Figure 3.2b. Even if the averaged axial velocity obtained with both methods is almost identical, there are important radial variations that are not predicted by the MS method ($U = U_0(x) + O(\epsilon^2)$). This is particularly true near the exit ($x = L$) of the duct where the geometry is not slowly-varying ($\epsilon \approx \mathrm{d}R_2/\mathrm{d}x \approx 0.3$).

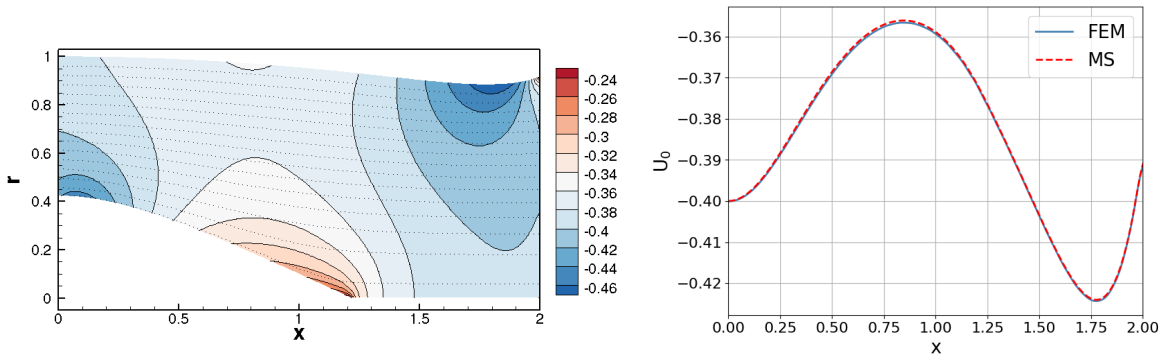

(a) Contours of normalized axial velocity, with the streamlines plotted as dotted black lines

(b) Cross-averaged axial velocity obtained with the FEM solver (solid line) and with the MS approximation (dotted line)

Figure 3.2 – Flow computed for a specified Mach number $M_s = -0.4$ at $x = 0$.

3.1.3.2 Hard walled results

The intention here is to explore the model's ability to represent the physics for cases without wall acoustic treatment.

● **Cut-on mode**

First, the benefit of using the model is shown at a low frequency ($\omega = 3$) by computing the propagation of the mode $(m, n) = (1, 1)$ for a specified Mach number $M_s = -0.4$ at the fan level. This is illustrated in Figure 3.3 by comparing the pressure contours over the meridional (x, r) plane given by the WKB, the multimodal, the multimodal without scattering and the FEM results.

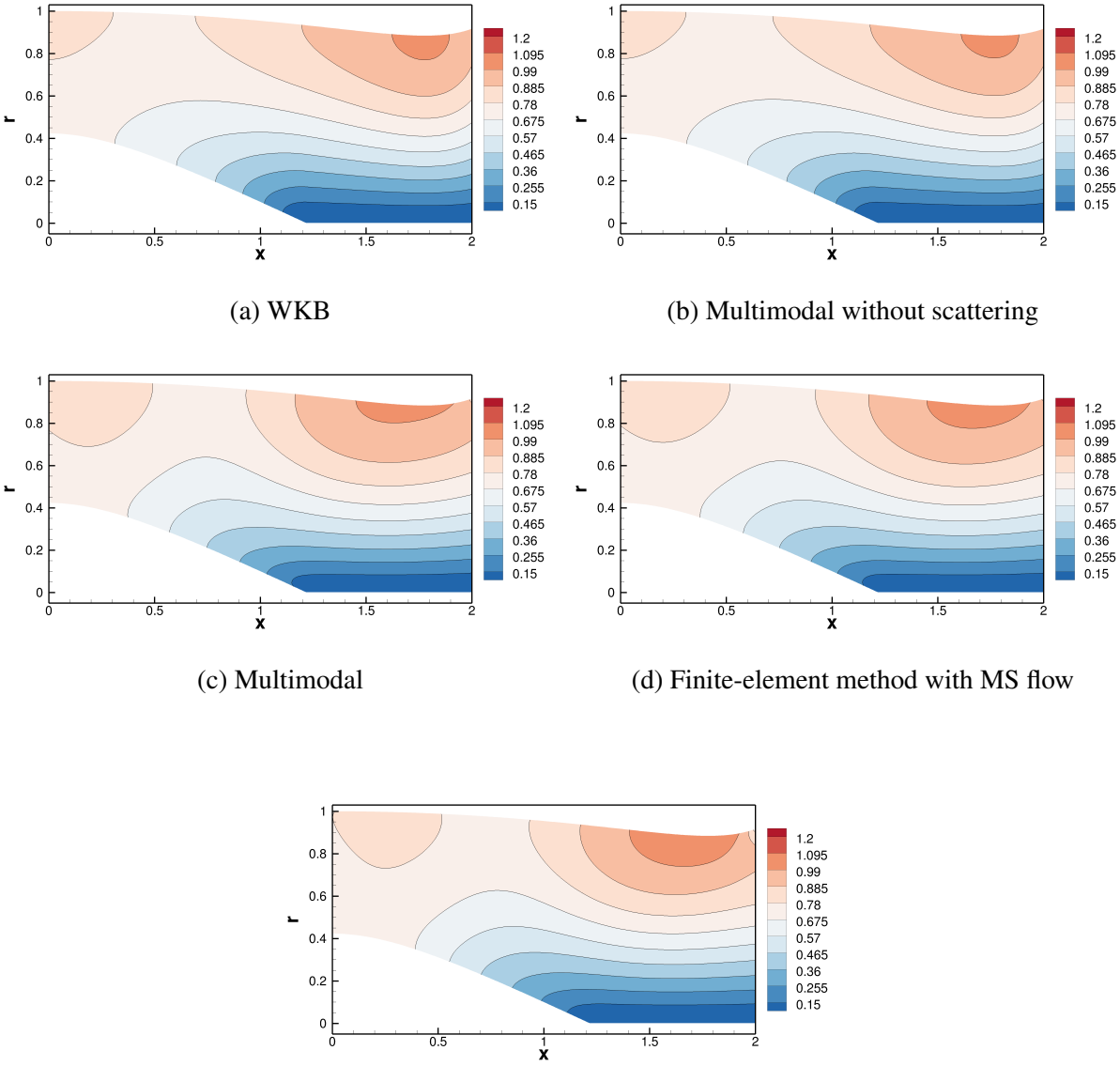

(a) WKB

(b) Multimodal without scattering

(c) Multimodal

(d) Finite-element method with MS flow

(e) Finite-element method with CFD flow

Figure 3.3 – Pressure magnitude associated to the mode (1,1) at $\omega = 3$ and $M_s = -0.4$.

The WKB and the multimodal method without scattering results are in excellent agreement. In cases where few reflections are expected inside the duct, the two methods give similar results. However, the results of both methods differ from the cases where modal scattering is accounted for. The agreement between the multimodal method and the FEM/MS is excellent, and the minor differences that can be observed come from the neglected $O(\epsilon^2)$ flow terms in the equation governing the acoustics. The multimodal method results slightly differ from the FEM/CFD ones, and this is due to the $O(\epsilon^2\omega^2 U_0)$ scattering terms that have been neglected. The fact that the CFD flow considers a constant duct at the outlet also tends to artificially reduce the radial flow velocity near the exit, increasing the discrepancies between methods.

- **Transition mode (cut-on/cut-off)**

The stability close to a transition (change of mode behaviour from cut-on to cut-off or vice-versa), which corresponds to a singularity in the admittance matrix [82], is evaluated by performing the same analysis but at a frequency $\omega = 31.0$ and for a mode $(m, n) = (20, 3)$. This mode is weakly cut-on at the injection plane, it encounters a turning point at $X_t = 0.84$ and becomes cut-off. The results are plotted in Figure 3.4. The multimodal method without scattering and the WKB are in good agreement, the Magnus–Möbius scheme avoids numerical instability despite the singularity of the admittance matrix and is adapted to capture total reflection phenomena. Note that this means that any number of transition and near transition phenomena can be captured without the need to modify the model. This makes the multimodal method without scattering typically suited to study phenomena where multiple transitions are present inside the duct. Once again, the FEM and multimodal are in good agreement. In this case, the inclusion of modal scattering and of a complete flow is not significant as all the methods give similar results.

- **Frequency evolution**

In order to evaluate more precisely the accuracy of all the methods, we compute the evolution of the error as the frequency and flow velocity increase for three different modes: $(m, n) = (1, 1)$, $(m, n) = (20, 1)$ and $(m, n) = (20, 3)$. The error is evaluated using the L^2 norm:

$$\epsilon_p = \left(\frac{\int_0^L \int_{R_1}^{R_2} |\phi - \phi_\infty|^2 r \mathrm{d}r\mathrm{d}x}{\int_0^L \int_{R_1}^{R_2} |\phi_\infty|^2 r \mathrm{d}r\mathrm{d}x} \right)^{1/2}, \tag{3.18}$$

with ϕ the potential obtained with the multimodal method, the multimodal method without scattering and the WKB method, and ϕ_∞ the reference FEM solution.

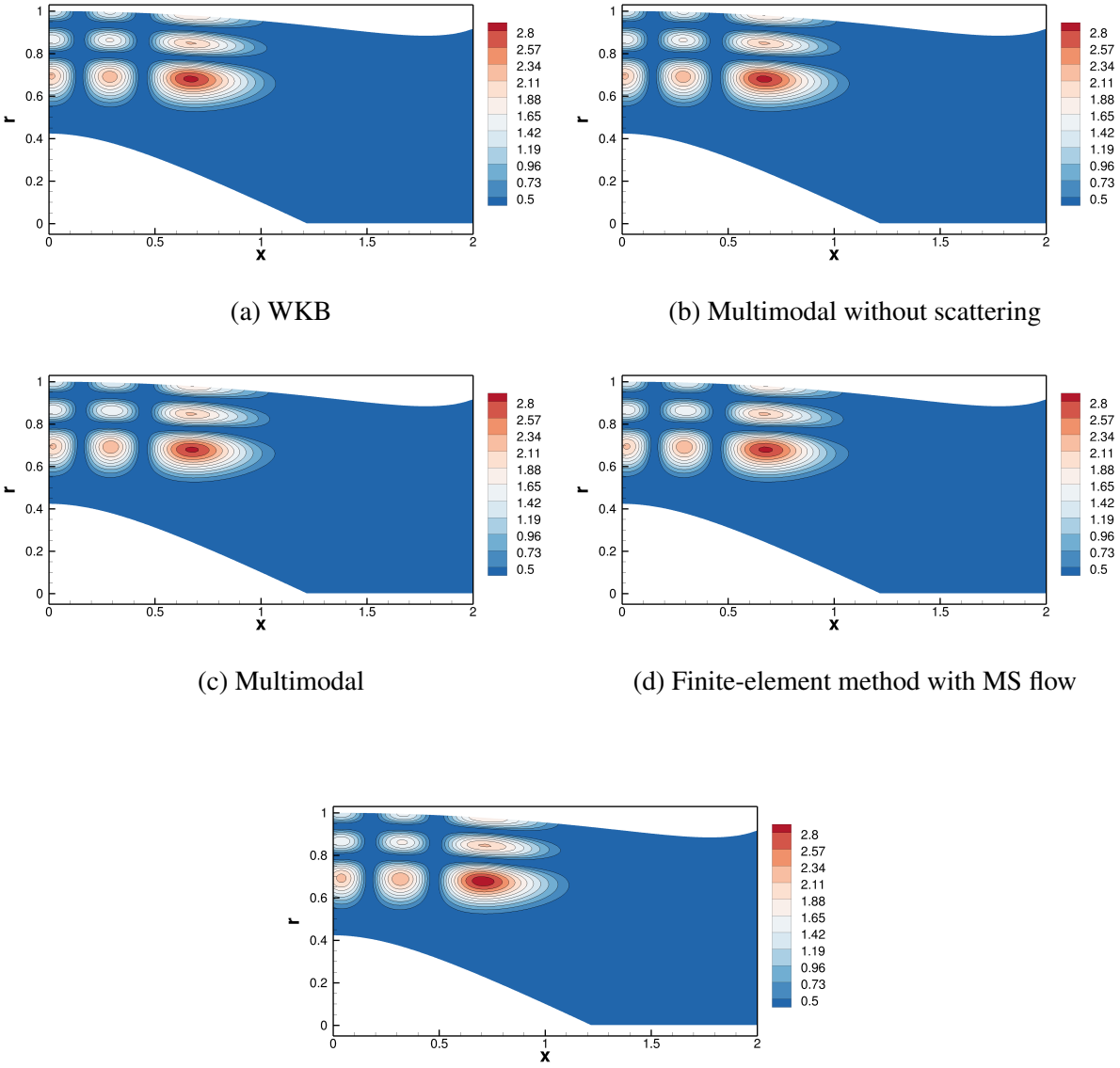

(a) WKB

(b) Multimodal without scattering

(c) Multimodal

(d) Finite-element method with MS flow

(e) Finite-element method with CFD flow

Figure 3.4 – Pressure magnitude associated to the mode (20,3) at $\omega = 31$ and $M = -0.4$.

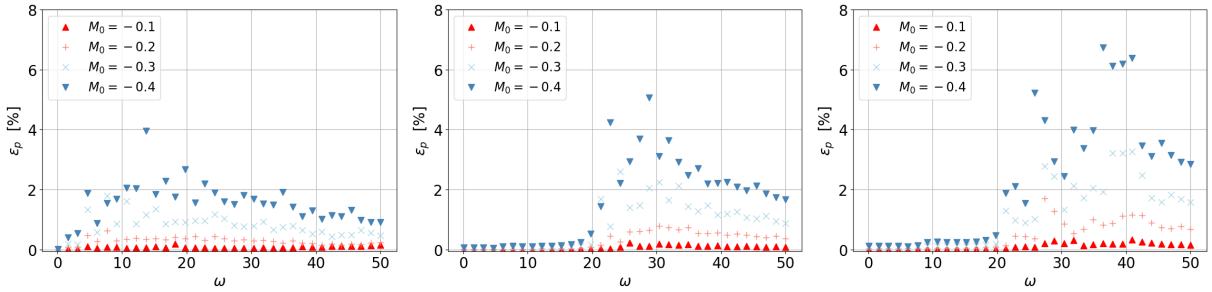

(a) $(m, n) = (1, 1)$ (b) $(m, n) = (20, 1)$ (c) $(m, n) = (20, 3)$

Figure 3.5 – Relative error between the FEM/MS as the reference solution and the multimodal method method, for various flow velocities and frequencies.

The results obtained when using the FEM/MS as reference solution are given in Figure 3.5.

Given the approximations of the method, there is a good quantitative agreement between the multimodal formulation and the FEM/MS, with discrepancies always inferior to 10% (of order $O(\epsilon^2)$). If the expected flow is close to the multiple-scale flow, the multimodal method will give accurate results in a calculation time almost identical to the WKB model. The modal scattering and convection effects of this flow are captured without deteriorating the computational efficiency of multimodal methods without flow.

The results obtained when the FEM/CFD is used as the reference solution and compared to the multimodal method, the multimodal method without scattering and the WKB method are now plotted in Figure 3.6. A key observation from the comparison between the multimodal method without scattering and WKB results is that the methods are equivalent in both cut-off and cut-on regions. The only region where the two methods differ is where reflection phenomena can occur typically near transition regions [70]. When the FEM/CFD results are compared to the multimodal results, the agreement is still excellent for low flow velocities where the multimodal model is particularly well suited. However with high flow velocities, the agreement deteriorates, especially for high frequencies. Even if the evolution of the errors is strongly dependent on the mode injected, some general trends are visible for the three computed cases:

- In regions where the mode is cut-on (approximately $\omega > m$), the error increases with the frequency and flow velocity. The distance to the transition region is the main driver of this error. Therefore the increase of the azimuthal mode order is favourable to the model.
- In regions where the mode is cut-off, the multimodal results perfectly fit the FEM results. The model captures the high attenuation of the mode. For this case, there is little modal

scattering, which explains the observed agreement.

- The results deteriorate when the mode encounters at least one transition in the duct. This is due to a small shift in the axial wavenumber that artificially increases the error rather than an erroneous pressure field representation. More details will be given in Section 3.2.

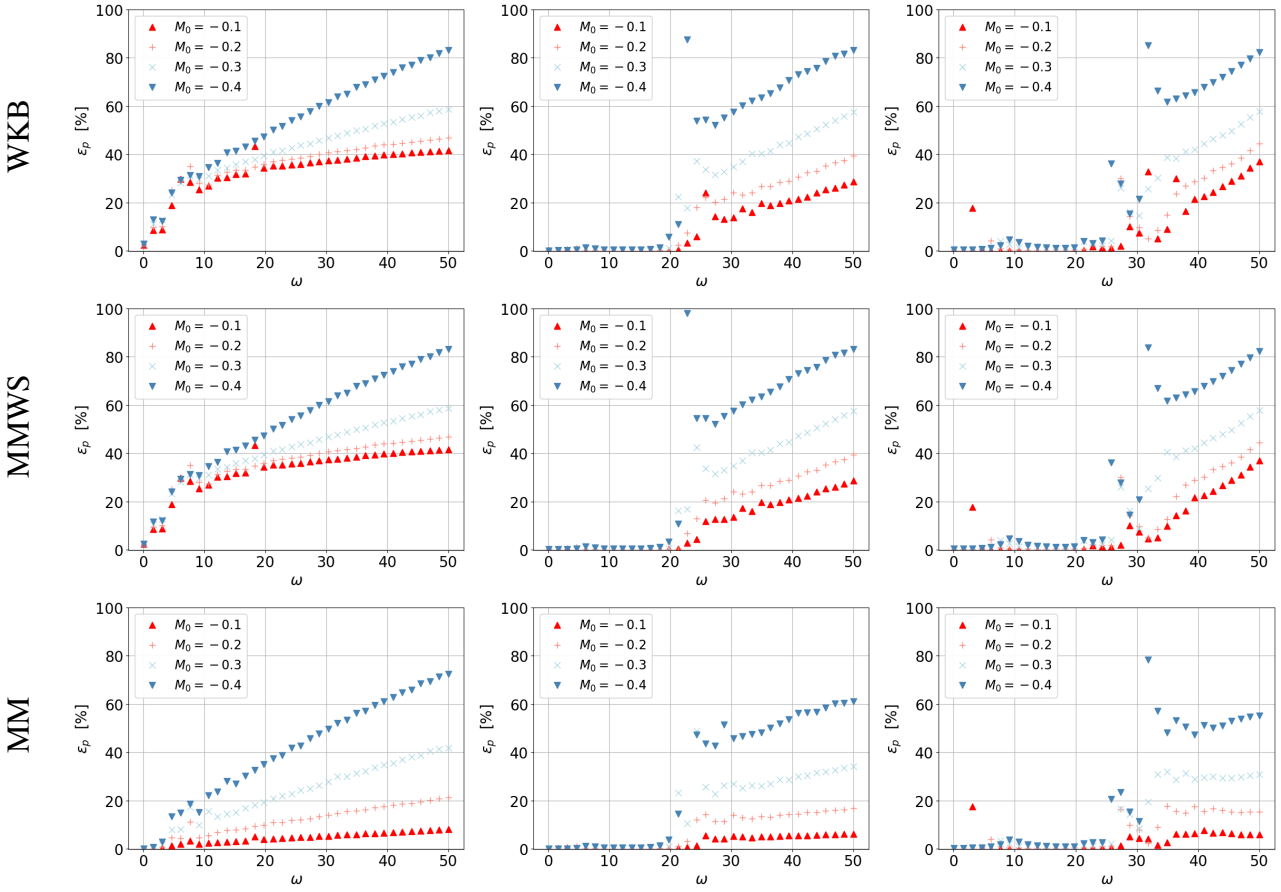

(a) $(m, n) = (1, 1)$ (b) $(m, n) = (20, 1)$ (c) $(m, n) = (20, 3)$

Figure 3.6 – Relative error between the FEM/CFD as the reference solution and the multimodal method, the multimodal method without scattering, and the WKB method, for various flows and frequencies.

3.1.3.3 Lined wall results

Eight test cases are used to validate the capability of the model to predict sound attenuation in lined turbofan inlets. Since the transverse mode differs before and after the liner, the models that neglect the scattering cannot be used here. Therefore only the multimodal method and the FEM can represent the propagation in such a duct.

The validation is shown in terms of the power attenuation predicted by each method, defined by:

$$\Delta P = 10 \log_{10} \left(\frac{P_{source}}{P_{exit}} \right), \tag{3.19}$$

where P_{source} and P_{exit} refer to the acoustic power (see Section 1.1.5) at the source plane and the exit plane respectively.

- **No-flow cases**

The first test cases are done without flow where we expect the multimodal model to be perfectly accurate. The attenuation obtained with our method and the FEM computations is given for all the test cases in Table 3.1. Both methods agree and the model appears to be a powerful tool to compute an estimated attenuation.

Case	(m, n)	ω	MM	FEM	Δ (MM - FEM)
1	(10,1)	16	44.1 dB	44.1 dB	0.0 dB
2	(12,1)	20	47.5 dB	47.5 dB	0.0 dB
3	(20,7)	44.5	24.5 dB	24.5 dB	0.0 dB
4	(30,2)	50	21.8 dB	21.8 dB	0.0 dB

Table 3.1 – Summary of the lined test case parameters and results for $M_s = 0$.

- **Flow cases**

Then test cases are considered with a Mach number $M_s = -0.4$. Here the model should give approximate results. The attenuations obtained are summarised in table 3.2. Discrepancies appear between all methods (even the FEM/MS and multimodal results differ) and no global trend appears. Nevertheless, the multimodal method still estimates the expected attenuation correctly and the prediction rarely differs by more than 1dB from the reference FEM/CFD results.

Case	(m,n)	ω	MM	FEM/MS	FEM/CFD	$\Delta(MM-FEM/CFD)$
1	(10,1)	16	49.7 dB	50.1 dB	49.0 dB	0.7dB
2	(12,1)	20	25.3 dB	25.1 dB	24.8 dB	0.5dB
3	(20,7)	44.5	30.7 dB	28.9 dB	31.9 dB	-1.2dB
4	(30,2)	50	14.3 dB	15.5 dB	14.0 dB	0.3dB

Table 3.2 – Summary of the lined test case parameters and results for $M_s = -0.4$.

To understand the slight difference between all the methods, pressure plots associated with test case 4 are shown in Figure 3.7. There is a good agreement for pressure contours and that the jump condition (3.16) proposed for the admittance gives consistent results. As expected by the formulation derived in Section 3.1.1.6, there is a reflection at the axial location of the liner discontinuity (visible at $x = 0.2$). Even if the attenuation of the liner is overestimated with the

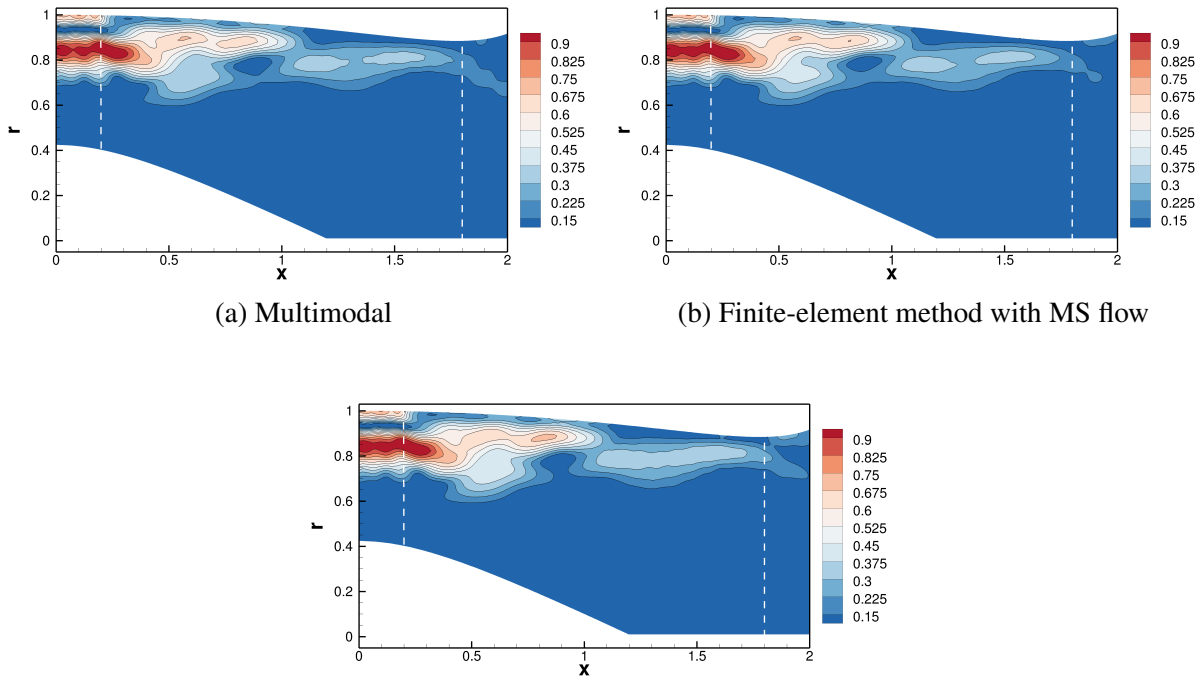

(a) Multimodal

(b) Finite-element method with MS flow

(c) Finite-element method with CFD flow

Figure 3.7 – Pressure magnitude associated to the mode (30,2) at $\omega = 50$ for $M = -0.4$ and $Z_2 = 2 - \mathrm{i}$.

multimodal method, no major differences are observed. The flow-induced scattering phenomena are of an order of magnitude smaller than the impact of the liner, and the attenuation predicted

by the proposed model is accurate.

3.1.4 Summary

The admittance multimodal method can be simplified when a multiple-scale potential mean flow is used. This simplified formulation has been implemented using two types of approximation bases: one is the same Chebyshev polynomials as used for the general multimodal method of Chapter 2, and the other one is composed of Fourier-Bessel functions. The latter presents the advantage of separating the propagation of modes from the scattering phenomenon and of providing analytical expressions of the multimodal matrices. When a Chebyshev basis is used, the method is very efficient because all the constitutive matrices of the multimodal formulation are independent of the frequency, the flow, the geometry and the azimuthal order.

Comparisons with a WKB method, a finite-element method using the same approximate flow, and one using a complete flow, have been carried out for the model of turbofan inlet over a large range of flows and frequencies. They are made on pressure contours for the hard walled test cases, and on power attenuation for the lined-wall ones. The agreement between the proposed multimodal method and the FEM that uses a MS flow is excellent in most cases, but it deteriorates for high frequencies and Mach numbers when compared to the FEM that uses a complete flow. Therefore, when high Mach numbers are expected, the general multimodal should be used. Still, the present simplified multimodal formulation appears very efficient for studying first-order effects of propagation. In particular, the error made by our model is always inferior to the one made by the WKB method which neglects the modal scattering. Note that the method behaves particularly well near transition phenomena. This demonstrates the efficiency of the simplified multimodal method which allows to compute acoustic propagation inside lined ducts with simplified potential flows without additional cost when compared to no-flow multimodal methods. Finally, it should be noted that the method applied by artificially turning off the scattering terms is in excellent agreement with standard WKB methods, especially in cases not involving transition phenomena.

3.2 Analysis of double transitions

The previous method effectively solves the Goldstein propagation equation with acceptable precision near a single modal transition. Test cases where two such transitions are encountered inside the duct will be considered here. Double transitions are of particular interest as they

can potentially lead to resonance [16] or tunnelling [70] phenomena, which can be challenging to compute accurately. Therefore, the focus is on cases where two turning points are present for the injected mode within the duct. These cases are studied to further validate the method and provide valuable insights to understand the impact of modal scattering on tunnelling and resonance phenomena.

In order to enhance the understanding of these mechanisms, a simplified WKB model is also developed to deal with the case where two transitions are present inside the duct. It will serve to validate the simplified multimodal formulation without modal scattering.

3.2.1 Extension of the WKB theory to acoustic double transition in ducts with flow

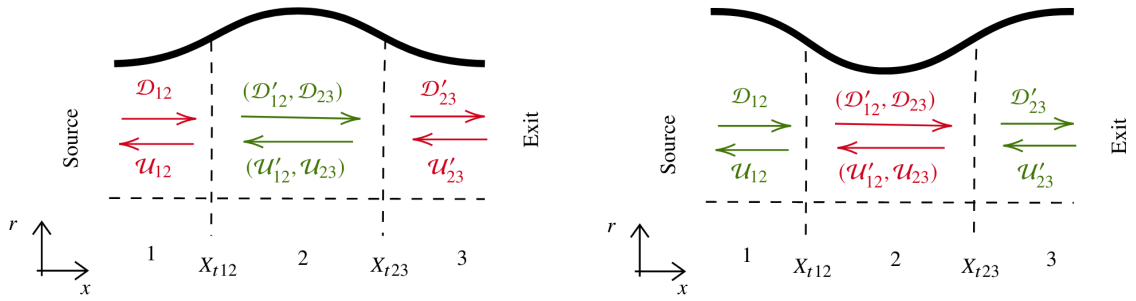

(a) Cut-off/cut-on/cut-off transition

(b) Cut-on/cut-off/cut-on transition

Figure 3.8 – Representation of a double transition configuration, with X_{t12} and X_{t23} the location of the two turning points. The green lines correspond to cut-on waves while the red ones correspond to cut-off ones.

3.2.1.1 Cut-off/cut-on/cut-off transition

Derivation of the solution

Let us consider a slowly varying duct which presents two turning points, with a mode undergoing a change from cut-off to cut-on and again to cut-off. Figure 3.8a illustrates the waves associated with such a mode inside a geometry with a local enlargement of the tip radius. The two turning points are denoted 12 and 23 and are seen as boundaries to distinguish the three regions 1, 2 and 3, where the mode is respectively cut-off, cut-on and cut-off. The prime indicates the modal amplitudes after each transition. The coefficients $\mathcal{D}$ and $\mathcal{U}$ can be used to write the slowly varying solutions of Equation (1.34) in the three regions, provided that the two turning

points are not in each other's inner boundary layer in order to have a valid outer solution in region 2 (referred to as distant turning points here). With this hypothesis, the uniformly valid solution based on Airy functions (see Section (1.35)) is written:

$$\begin{aligned}\phi = Q_0\sqrt{\frac{C_0}{\omega D_0}}\psi \left[-\frac{3}{2\epsilon\sigma^3}\int_{X_{t_i}}^{X}\frac{\omega C_0\sigma}{C_0^2-U_0^2}\mathrm{d}X\right]^{1/6} [a_i\,\mathrm{Ai}(s_t)+b_i\,\mathrm{Bi}(s_t)] \\ \exp\left[\frac{\mathrm{i}}{\epsilon}\int_{X_{t_i}}^{X}\frac{\omega U_0}{C_0^2-U_0^2}\mathrm{d}X\right], \\ \text{with } s_t = \left(\frac{3\mathrm{i}}{2\epsilon}\int_{X_{t_i}}^{X}\frac{\omega C_0\sigma}{C_0^2-U_0^2}\mathrm{d}X\right)^{2/3},\end{aligned} \tag{3.20}$$

where (a_i, b_i) are two unknown coefficients associated to the transition i. In practice, if $|s_t| > 1$ for each turning point, the hypothesis is respected and the asymptotic behaviour of Airy functions is reasonably recovered [11].

Before a transition ($X < X_{ti}$), the slowly varying formulation (see Equation (1.34)) writes:

$$\begin{aligned}\phi = Q_0\sqrt{\frac{C_0}{\omega D_0\sigma}}\psi\ \exp\left[\frac{\mathrm{i}}{\epsilon}\int_{X_{ti}}^{X}\frac{\omega U_0}{C_0^2-U_0^2}\mathrm{d}X\right] \\ \left[\mathcal{D}_i\ \exp\left[\frac{-\mathrm{i}}{\epsilon}\int_{X_{ti}}^{X}\frac{\omega C_0\sigma}{C_0^2-U_0^2}\mathrm{d}X\right]+\mathcal{U}_i\ \exp\left[\frac{\mathrm{i}}{\epsilon}\int_{X_{ti}}^{X}\frac{\omega C_0\sigma}{C_0^2-U_0^2}\mathrm{d}X\right]\right],\end{aligned} \tag{3.21}$$

and after a transition ($X > X_{ti}$):

$$\begin{aligned}\phi = Q_0\sqrt{\frac{C_0}{\omega D_0\sigma}}\psi\ \exp\left[\frac{\mathrm{i}}{\epsilon}\int_{X_{ti}}^{X}\frac{\omega U_0}{C_0^2-U_0^2}\mathrm{d}X\right] \\ \left[\mathcal{D}_i'\ \exp\left[-\frac{\mathrm{i}}{\epsilon}\int_{X_{ti}}^{X}\frac{\omega C_0\sigma}{C_0^2-U_0^2}\mathrm{d}X\right]+\mathcal{U}_i'\ \exp\left[\frac{\mathrm{i}}{\epsilon}\int_{X_{ti}}^{X}\frac{\omega C_0\sigma}{C_0^2-U_0^2}\mathrm{d}X\right]\right],\end{aligned} \tag{3.22}$$

with $i \in [12, 23]$ referring to a transition. The coefficient $\mathcal{D}_{12}$ is set equal to 1 without loss of generality, and the coefficient $\mathcal{U}_{23}'$ is set to zero by assuming that there is no reflection at the exit (note that a non-zero value can be prescribed to represent any other outlet condition). As for the single transition case, the asymptotic matching between Equations (3.20) and (3.21)–(3.22)

allows to find relations between the coefficients. Here, we obtain:

$$\begin{aligned}
\frac{a_{12}}{2\sqrt{\pi}\mathrm{e}^{-\mathrm{i}\pi/4}} &= \mathcal{U}_{12}, & \frac{a_{23}\mathrm{e}^{-\mathrm{i}\pi/4}+b_{23}\mathrm{e}^{\mathrm{i}\pi/4}}{2\sqrt{\pi}} &= \mathcal{D}_{23},\\
\frac{b_{12}}{\sqrt{\pi}\mathrm{e}^{-\mathrm{i}\pi/4}} &= 1, & \frac{a_{23}\mathrm{e}^{\mathrm{i}\pi/4}+b_{23}\mathrm{e}^{-\mathrm{i}\pi/4}}{2\sqrt{\pi}} &= \mathcal{U}_{23},\\
\frac{a_{12}\mathrm{e}^{\mathrm{i}\pi/4}+b_{12}\mathrm{e}^{-\mathrm{i}\pi/4}}{2\sqrt{\pi}\mathrm{e}^{-\mathrm{i}\pi/2}} &= \mathcal{D}'_{12}, & \frac{a_{23}}{2\sqrt{\pi}\mathrm{e}^{\mathrm{i}\pi/4}} &= \mathcal{D}'_{23},\\
\frac{a_{12}\mathrm{e}^{-\mathrm{i}\pi/4}+b_{12}\mathrm{e}^{\mathrm{i}\pi/4}}{2\sqrt{\pi}\mathrm{e}^{-\mathrm{i}\pi/2}} &= \mathcal{U}'_{12}, & \frac{b_{23}}{\sqrt{\pi}\mathrm{e}^{\mathrm{i}\pi/4}} &= 0.
\end{aligned} \tag{3.23}$$

In the second region, Equation (3.22) applied to the first transition and Equation (3.21) applied to the second transition give two expressions for ϕ. Matching these gives:

$$\mathcal{D}'_{12} = \mathcal{D}_{23}\mathrm{e}^{\mathrm{i}\zeta}, \mathcal{U}'_{12} = \mathcal{U}_{23}\mathrm{e}^{\mathrm{i}(\zeta-2\varphi)}, \tag{3.24}$$

with:

$$\varphi = \frac{1}{\epsilon}\int_{X_{t12}}^{X_{t23}} \frac{\omega\sigma C_0}{C_0^2-U_0^2}\mathrm{d}X, \zeta = -\frac{1}{\epsilon}\int_{X_{t12}}^{X_{t23}} \frac{\omega(U_0-\sigma C_0)}{C_0^2-U_0^2}\mathrm{d}X. \tag{3.25}$$

The mode is cut-on in the central region so that σ, φ and ζ are real numbers. By combining the previous equations, all the unknown coefficients can be determined:

$$\begin{aligned}
a_{12} &= \sqrt{\pi}\mathrm{e}^{\mathrm{i}\pi/4}\left(1-\frac{2}{1+\mathrm{e}^{-\mathrm{i}2\varphi}}\right), & b_{12} &= \sqrt{\pi}\mathrm{e}^{-\mathrm{i}\pi/4},\\
a_{23} &= 2\sqrt{\pi}\mathrm{e}^{\mathrm{i}\pi/4}\frac{\mathrm{e}^{-\mathrm{i}\zeta}}{1+\mathrm{e}^{-\mathrm{i}2\varphi}}, & b_{23} &= 0,\\
\mathcal{D}_{12} &= 1, & \mathcal{U}_{12} &= \frac{\mathrm{i}}{2}\left(1-\frac{2}{1+\mathrm{e}^{-\mathrm{i}2\varphi}}\right),\\
\mathcal{D}_{23} &= \frac{\mathrm{e}^{-\mathrm{i}\zeta}}{1+\mathrm{e}^{-\mathrm{i}2\varphi}}, & \mathcal{U}_{23} &= \frac{\mathrm{i}\mathrm{e}^{-\mathrm{i}\zeta}}{1+\mathrm{e}^{-\mathrm{i}2\varphi}},\\
\mathcal{D}'_{23} &= \frac{\mathrm{e}^{-\mathrm{i}\zeta}}{1+\mathrm{e}^{-\mathrm{i}2\varphi}}, & \mathcal{U}'_{23} &= 0.
\end{aligned} \tag{3.26}$$

The above solution is based on asymptotic matching between two distinct solutions in the central region. Consequently, a discontinuous potential can be obtained at the junction between the two formulations. To obtain a continuous solution, a correction can be applied on the coefficients (a_{23}, b_{23}) by performing a match directly on Airy functions in the central region. Therefore, the matching is done at the axial location X_c defined such that $-1/\epsilon\int_{X_{t12}}^{X_c}\omega C_0\sigma/(C_0^2-$

$U_0^2)\mathrm{d}X = 1/\epsilon \int_{X_{t23}}^{X_c} \omega C_0 \sigma/(C_0^2 - U_0^2)\mathrm{d}X = \varphi/2$ and writes:

$$[a_{23}\,\mathrm{Ai}(s_c) + b_{23}\,\mathrm{Bi}(s_c)] = \mathrm{i}\,[a_{12}\,\mathrm{Ai}(s_c) + b_{12}\,\mathrm{Bi}(s_c)]\;\mathrm{e}^{-\mathrm{i}(\zeta-\varphi)}, \tag{3.27}$$

where $s_c = s_{t12} = s_{t23} = \left(\frac{3\mathrm{i}}{2}\varphi/2\right)^{2/3}$. Note that this correction of the coefficient a_{23} ($b_{23} = 0$ here) does not extend the region of validity of the method (applicable when $|s_c| > 1$), and another equation is to be solved when the turning points are close (see for example the work of Nielsen and Peake for symmetric turning points [70]).

Transmission and reflection coefficients

The transmission and reflection coefficients $(\mathcal{T}_i, \mathcal{R}_i)$ associated with each transition $i \in [12, 23]$ are defined as follows:

$$\mathcal{T}_i = \frac{\mathcal{D}_i'}{\mathcal{D}_i},\ \mathcal{R}_i = \frac{\mathcal{U}_i}{\mathcal{D}_i}. \tag{3.28}$$

For the second transition, the expressions of a single transition obtained by Ovenden are recovered: $\mathcal{T}_{23} = 1$ and $\mathcal{R}_{23} = \mathrm{i}$ [12]. For the first transition, the following expressions are obtained:

$$\mathcal{T}_{12} = \frac{1}{1+\mathrm{e}^{-\mathrm{i}2\varphi}},\ \mathcal{R}_{12} = \frac{\mathrm{i}}{2}\left(1 - \frac{2}{1+\mathrm{e}^{-\mathrm{i}2\varphi}}\right). \tag{3.29}$$

These expressions illustrate that the incident wave can be amplified during its propagation ($|\mathcal{T}_{12}| \geq 1$) when $\varphi \in [\pi/3, 2\pi/3] \pmod{\pi}$. A resonance phenomena can even occur ($|\mathcal{T}_{12}| \to +\infty$) when $\mathrm{e}^{-\mathrm{i}2\varphi} \to -1$ i.e. $\varphi \to \pi/2 \pmod{\pi}$. An infinity of reflections (without energy loss) occurs in the region between two turning points. The resonance happens when the incident and the reflected waves overlap to form constructive interference in that region.

Acoustic power

Using the expressions given in Appendix C, the power can be evaluated inside each region using the Equations (3.21) and (3.22). For each region, the power writes:

$$\begin{aligned}
\mathcal{P}_1 &\propto 2\mathrm{Im}(\mathcal{D}_{12}\overline{\mathcal{U}_{12}}) = 2\mathrm{Im}\left(\frac{\sin(2\varphi)}{|\cos(2\varphi)+1+\mathrm{i}\sin(2\varphi)|^2}\right) = 0,\\
\mathcal{P}_2 &\propto |\mathcal{D}_{23}|^2 - |\mathcal{U}_{23}|^2 = 0,\\
\mathcal{P}_3 &\propto 2\mathrm{Im}(\mathcal{D}_{23}'\overline{\mathcal{U}_{23}'}) = 0.
\end{aligned} \tag{3.30}$$

The power is conserved in the model and is equal to zero everywhere inside the duct. However, this is because no modal scattering is considered. When added, energy can leak to neighbouring

modes, which gives a non-zero acoustic power if one of them is cut-on. This could be significant near resonance phenomena where high amplitudes are involved.

3.2.1.2 Cut-on/cut-off/cut-on transition

Derivation of the solution

Figure 3.8b illustrates the waves associated with a double transition mode inside a geometry with a local contraction. The regions are denoted using the same notation as in section 3.2.1.1. With the same methodology, it is possible to find the coefficients $\mathcal{U}_i, \mathcal{D}_i, \mathcal{U}'_i, \mathcal{D}'_i, a_i, b_i$ for $i \in [12, 23]$ in the case of cut-on/cut-off/cut-on transition. The results are:

$$\begin{aligned}
a_{12} &= \frac{2\sqrt{\pi}\mathrm{e}^{\mathrm{i}\pi/4}}{1+\mathrm{e}^{-\mathrm{i}2\varphi}/4}, & b_{12} &= \frac{2\sqrt{\pi}\mathrm{e}^{-\mathrm{i}\pi/4}\mathrm{e}^{-\mathrm{i}2\varphi}}{4+\mathrm{e}^{-\mathrm{i}2\varphi}}, \\
a_{23} &= -\sqrt{\pi}\mathrm{e}^{\mathrm{i}\pi/4}\frac{\mathrm{e}^{-\mathrm{i}\zeta}}{1+\mathrm{e}^{-\mathrm{i}2\varphi}/4}, & b_{23} &= \sqrt{\pi}\mathrm{e}^{-\mathrm{i}\pi/4}\frac{\mathrm{e}^{-\mathrm{i}\zeta}}{1+\mathrm{e}^{-\mathrm{i}2\varphi}/4}, \\
\mathcal{D}_{12} &= 1, & \mathcal{U}_{12} &= \mathrm{i}\frac{1-\mathrm{e}^{-\mathrm{i}2\varphi}/4}{1+\mathrm{e}^{-\mathrm{i}2\varphi}/4}, \\
\mathcal{D}_{23} &= \frac{\mathrm{e}^{-\mathrm{i}\zeta}}{1+\mathrm{e}^{-\mathrm{i}2\varphi}/4}, & \mathcal{U}_{23} &= -\frac{\mathrm{i}}{2}\frac{\mathrm{e}^{-\mathrm{i}\zeta}}{1+\mathrm{e}^{-\mathrm{i}2\varphi}/4}, \\
\mathcal{D}'_{23} &= \frac{\mathrm{e}^{-\mathrm{i}\zeta}}{1+\mathrm{e}^{-\mathrm{i}2\varphi}/4}, & \mathcal{U}'_{23} &= 0.
\end{aligned} \tag{3.31}$$

In the central region, the mode is cut-off so that σ and φ are imaginary numbers and ζ is a complex number.

Transmission and reflection coefficients

Here, the transmission and reflection coefficients $(\mathcal{T}, \mathcal{R})$ associated with the entire system are defined by:

$$\mathcal{T} = \frac{\mathcal{D}'_{23}}{\mathcal{D}_{12}} = \frac{\mathrm{e}^{-\mathrm{i}\zeta}}{1+\mathrm{e}^{-\mathrm{i}2\varphi}/4}, \; \mathcal{R} = \frac{\mathcal{U}_{12}}{\mathcal{D}_{12}} = \mathrm{i}\frac{1-\mathrm{e}^{-\mathrm{i}2\varphi}/4}{1+\mathrm{e}^{-\mathrm{i}2\varphi}/4}. \tag{3.32}$$

Since φ is imaginary here, $\mathrm{e}^{-\mathrm{i}2\varphi}$ is a real number. The greater the distance between the transitions, the smaller this value becomes. Therefore, if the two transitions are infinitely far from each other, the coefficients become: $\mathcal{T} = 0$ and $\mathcal{R} = \mathrm{i}$. The behaviour of a single cut-on/cut-off transition is recovered: the reflected wave has a phase-shift of $\pi/2$ and no energy leaks towards the exit of the duct [12]. In the particular case of symmetric transitions, this result had already been found by Nielsen and Peake [70].

Power consideration

Using the expressions given in Appendix C, the power can again be evaluated inside each region using the Equations (3.21)/(3.22) for the expression of ϕ. For each region, the power writes:

$$\begin{aligned} \mathcal{P}_1 &\propto |\mathcal{D}_{12}|^2 - |\mathcal{U}_{12}|^2 = 1 - |\mathcal{R}|^2, \\ \mathcal{P}_2 &\propto 2\mathrm{Im}(\mathcal{D}_{23}\overline{\mathcal{U}_{23}}) = |\mathcal{T}|^2, \\ \mathcal{P}_3 &\propto |\mathcal{D}'_{23}|^2 - |\mathcal{U}'_{23}|^2 = |\mathcal{T}|^2. \end{aligned} \tag{3.33}$$

The conservation of acoustic power is correctly recovered with the present model as $|\mathcal{T}|^2+|\mathcal{R}|^2 = 1$. As no modal scattering is considered, $|\mathcal{R}|^2$ and $|\mathcal{T}|^2$ represent the normalized reflected and transmitted powers respectively.

3.2.2 Cut-off/cut-on/cut-off transition

The developed multimodal model is validated against two methods for cases with cut-off/cut-on/cut-off transitions: a finite element method to see if the hypothesis of the multiple scale flow does not impact the overall results too much, and the WKB method presented above to validate our multimodal model in cases without modal scattering when the transitions are far. These analyses will also help to understand the impact of modal scattering on the pressure field.

3.2.2.1 Description of the test case

In order to evaluate the interest of the multimodal method to study double transitions, the first series of presented test cases are for modes undergoing a cut-off/cut-on/cut-off transition inside the duct. Therefore, a weakly cut-off mode is injected at the duct inlet. This mode encounters a first turning point and becomes cut-on before reaching a second one and returning to its initial state. The azimuthal mode order is chosen to be small in order to avoid that most of the acoustics is concentrated near the tip. The radial mode order is then chosen to ensure that there is at least one cut-on mode in the whole duct in order to evaluate the impact of the modal scattering over these modes. A no-flow and a flow case are studied to assess the effect of the flow on the propagation. For the flow case, the azimuthal and radial mode orders and the position of the turning points are kept constant to isolate the impact of the flow. For this purpose, the frequency is adjusted and therefore differs from the no-flow case.

Therefore, we consider a waveguide radius defined by $R_1 = 0,\ R_2 = 0.8+0.1\cos((x-2)\pi/2)$

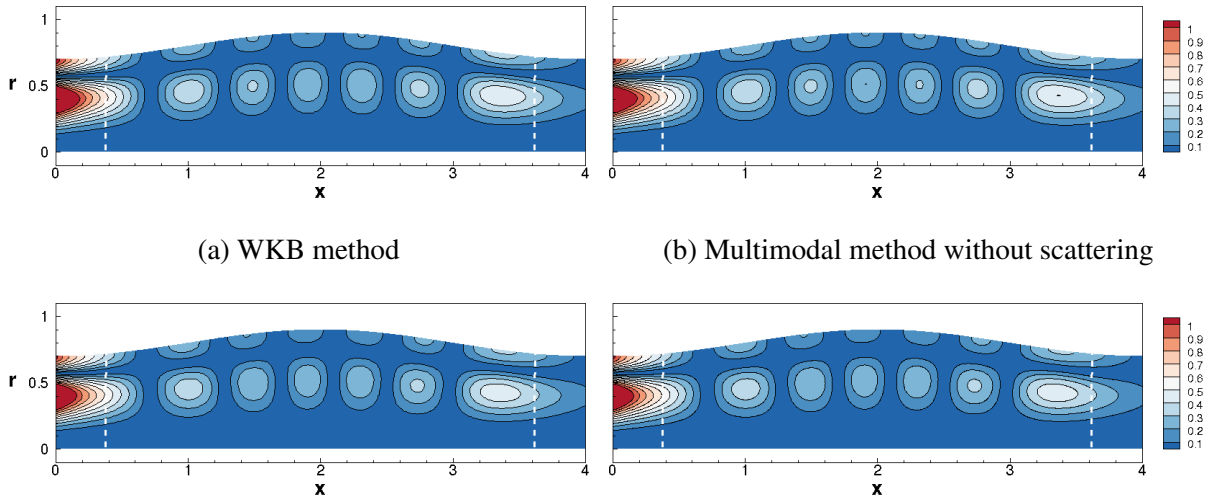

(a) WKB method

(b) Multimodal method without scattering

(c) Multimodal method

(d) Finite element method

Figure 3.9 – Maps of pressure magnitude associated to the mode (4,2) at $\omega = 12.94$ and $M_s = 0$. Turning points at $X_{t12} = 0.38$ and $X_{t23} = 3.62$.

for $x \in [0, 4]$. The right-running mode $(m, n) = (4, 2)$ is injected at $x = 0$ for $\omega = 12.94$ in the zero-flow case and at $\omega = 12.71$ in the flow case. For both cases, the turning points are located at $X_{t12} = 0.38$ and $X_{t23} = 3.62$. The behaviour of this mode is then investigated over a wide range of frequencies.

An estimate of the small parameter ϵ can be obtained based on the maximum slope of the wall ($R_2' = O(\epsilon)$) and gives $\epsilon \approx 0.16$. This yields an estimate of the inner-boundary layer thickness [13] (size of the region where the WKB ansatz is not valid) of $\epsilon^{-1/3}\omega^{-2/3} \approx 0.34$ for the single frequency cases.

3.2.2.2 Single frequency - without flow

We first consider the no-flow case for the mode (4, 2) at $\omega = 12.94$. The pressure amplitude over the meridional plane obtained using the WKB model, the mulitmodal method, the multimodal without scattering and the FEM are plotted in Figure 3.9.

There is a good qualitative agreement between the different methods. However, a difference is noticeable close to the wall between the models that neglect modal scattering and the other numerical methods. The first ones give vertical pressure isolines near the wall, whereas the other ones give wall normal isolines. This comes from the fact that the derivative of the transverse function is set to zero, which introduces an error of order ϵ.

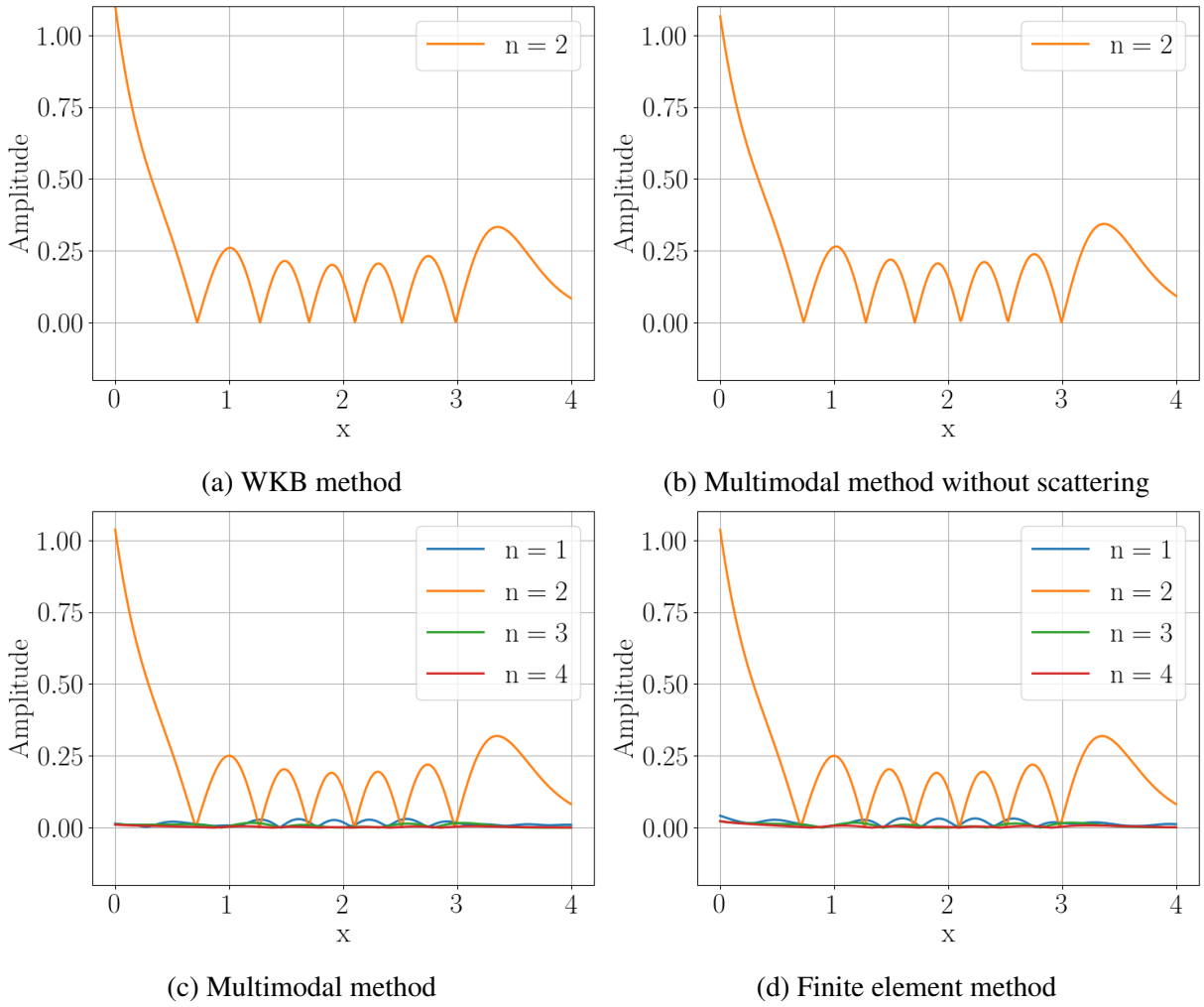

(a) WKB method

(b) Multimodal method without scattering

(c) Multimodal method

(d) Finite element method

Figure 3.10 – Projection over the first four Bessel functions of pressure associated to the injected mode (4,2) at $\omega = 12.94$ and $M_s = 0$. Turning points at $X_{t12} = 0.38$ and $X_{t23} = 3.62$.

The information brought by the pressure maps comparison is limited because the WKB method and the multimodal method without scattering only compute the axial variation associated with the main mode in the waveguide, whereas the FEM and multimodal method codes also compute the scattering on adjacent radial modes. A more detailed comparison is thus performed by projecting the acoustic field over the Bessel functions to separate the amplitude variations of the main mode from the modal scattering it produces. The results of this projection are given in Figure 3.10. For the FEM and multimodal methods, the projection values are limited to the first four radial modes.

There is excellent agreement between all methods for the main mode, which can be explained by a limited modal scattering over adjacent modes in addition to few reflections apart from the

transitions. However, the ratio of the amplitude associated with the cut-on mode $n = 1$ to the one of the injected mode increases between the inlet and the outlet, and the hypothesis made by the models that neglect scattering that the injected mode is dominant in the duct turns out to be less accurate near the exit. Otherwise, interaction lobes are observed for the mode $n = 1$, which does not encounter any transition. This is not an expected result since the associated maximum axial pressure variations should be located where the geometry change is more pronounced [82, 74, 79]. This is due to the fact that both the left- and right-running main modes produce scattered waves propagating in their direction. Therefore cut-on waves associated to the mode $n = 1$ propagate in both directions in the central region.

Even if the agreement looks excellent between all methods for the main mode, small differences in the predicted reflection at the inlet are observed. These are evaluated using the reflection coefficient defined as $\mathcal{R}_2 = p_2^-/p_2^+$ with p_2^- and p_2^+ the modal amplitudes associated with the left-running mode and right-running mode $n = 2$ respectively. We obtain $|\mathcal{R}_2| = 0.10$ with both the WKB method and the multimodal method without scattering, and $|\mathcal{R}_2| = 0.04$ with the multimodal method and the FEM. The differences are small compared to the modal amplitude of the injected mode. The reflection is overestimated when the scattering is not accounted for since the modal scattering tends to extract energy from the dominant mode.

3.2.2.3 Single frequency - with flow

We now consider the same mode but with a normalized frequency of $\omega = 12.71$ (to keep the same position of the turning points as in the case without flow) and in the presence of a mean flow such that $M_s = -0.2$ at the inlet plane.

The contour maps of pressure amplitude over the meridional plane are given in Figure 3.11. There is again a good qualitative agreement in terms of pressure magnitude with regard to the position of the interaction lobes.

As previously, a more quantitative evaluation is obtained by projecting the acoustic field over Bessel functions. The result is shown in Figure 3.12 and exhibits an excellent agreement. The projection confirms that there is no significant modal scattering, making the models without scattering particularly suitable here. The impact of the flow can be seen in the amplitudes of the lobes in the central cut-on region. The reflection coefficient is evaluated again for a more precise comparison. We obtain once more the same value with the WKB and the multimodal method without scattering: $|\mathcal{R}_2| = 0.046$. With the multimodal method and the FEM, we obtain $|\mathcal{R}_2| = 0.025$. Note that, once more the methods which accounts for the modal scattering agree on the value of the reflection coefficient despite the use of a MS flow for the multimodal method

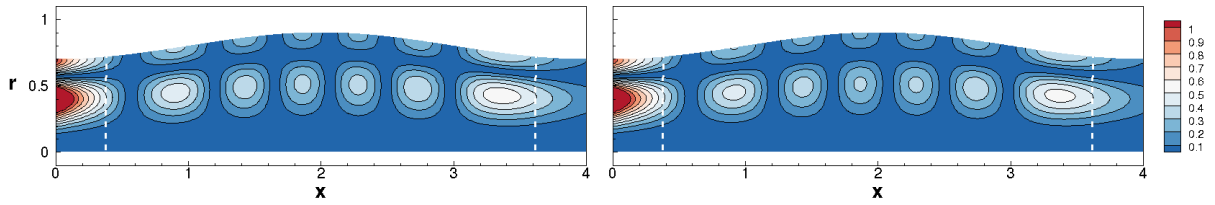

(a) WKB method

(b) Multimodal method without scattering

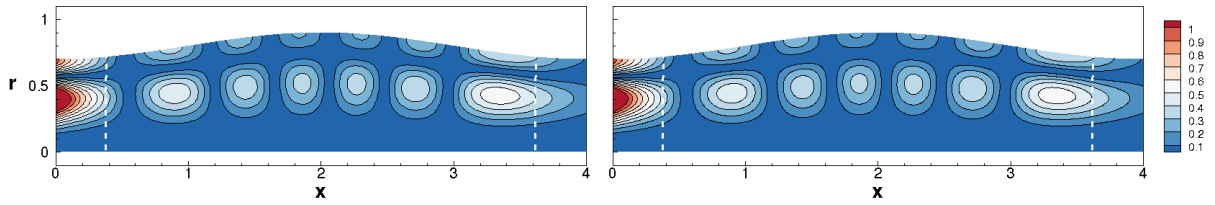

(c) Multimodal method

(d) Finite element method

Figure 3.11 – Maps of pressure magnitude associated to the mode (4,2) at $\omega = 12.71$ and $M_s = -0.2$. Turning points at $X_{t12} = 0.38$ and $X_{t23} = 3.62$.

calculations. However, when the scattering is not accounted for, the reflection is overestimated.

3.2.2.4 Frequency variation - the case of the acoustic resonator

The case of the resonance predicted by the WKB model (see Equation (3.29) when $\varphi \rightarrow \pi/2 \pmod{\pi}$) is now investigated by applying the methods over a wide range of frequencies for a case with and without flow. It will serve as validation for the multimodal method without scattering to see if it can encompass such phenomenon and it will allow us to understand the importance of modal scattering in such cases. The amplification inside the duct ($A = p_{\max}/p_0$ with $p_{\max}$ the maximum pressure inside the duct and p_0 the pressure at the source plane) is computed at each frequency with the multimodal method, the multimodal method without scattering, the FEM and the WKB method. The results are shown in Figures 3.13 and 3.14 for the case without flow and with flow respectively. The gray area corresponds to a region where the error caused by the matching assumptions becomes important because $|s_c| < 1$. Outside from this region, the agreement between the multimodal method without scattering and the WKB model is excellent for both the flow and the no flow cases. This means that the transitions are the main cause of reflections that occur inside the duct and that the multimodal method without scattering can capture this high amplification. However, when modal scattering is accounted for, the modal energy transfer tends to impact the frequencies of the amplification peaks. This difference is

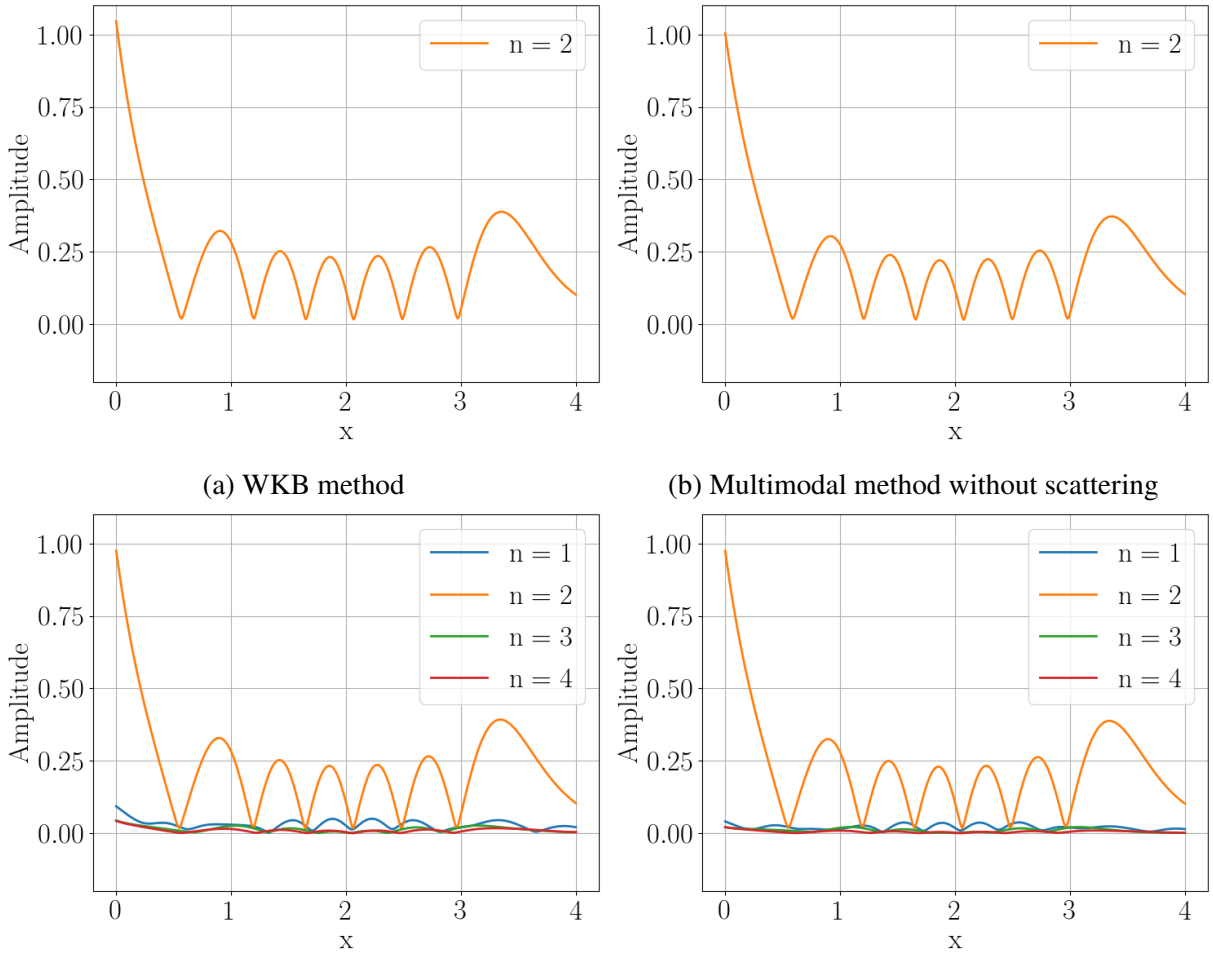

(a) WKB method

(b) Multimodal method without scattering

(c) Multimodal method

(d) Finite element method

Figure 3.12 – Projection over the first four Bessel functions of pressure associated to the injected mode (4,2) at $\omega = 12.71$ and $M_s = -0.2$. Turning points at $X_{t12} = 0.38$ and $X_{t23} = 3.62$.

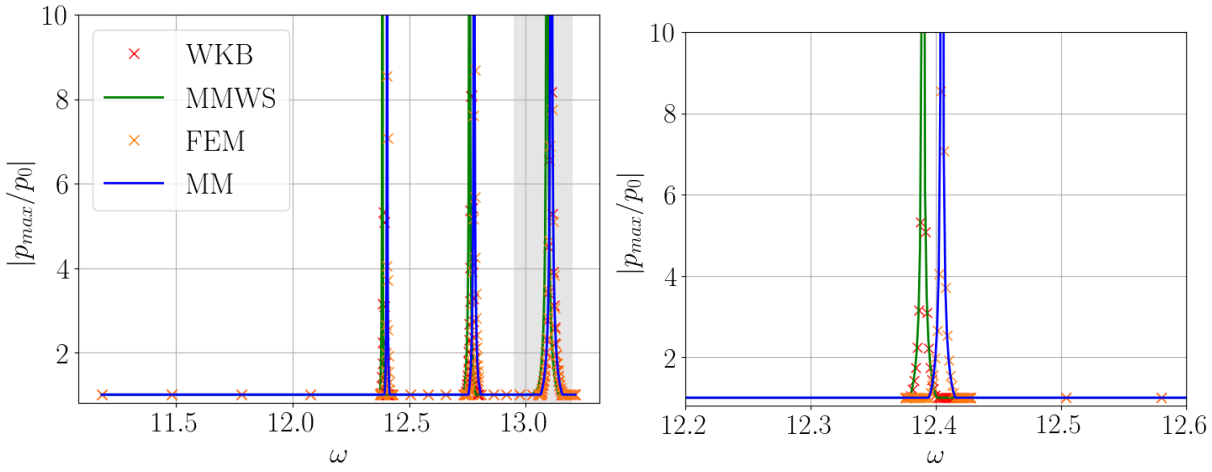

(a) Full frequency range

(b) Zoom on the resonance phenomena

Figure 3.13 – Variation of the amplification with frequency for the mode (4,2) for the case $M_s = 0$. The gray region correspond to a location where the WKB model errors are important.

minor and would imply only a few Hertz shift on the non-normalized frequencies. This shows one of the drawbacks of methods that neglect the impact of the modal scattering: they can provide an estimate of the frequency of the amplification peaks but not their exact values. On the other hand, the agreement between the multimodal method and the FEM solution is excellent. It shows that the simplified multimodal method can capture high amplification caused by trapped modes without difficulty, and it confirms the guess that using a multiple-scale flow for studying transitions is relevant. Note that the conclusions are the same for the no-flow and flow cases. In practice, this is because the flow-induced scattering mechanisms are weak and do not impact the overall results too much.

3.2.3 Cut-on/cut-off/cut-on transition

3.2.3.1 Description of the test case

We now consider the cut-on/cut-off/cut-on transition case. An incident cut-on mode is chosen at the duct inlet in such a way that it will quickly transition into a cut-off mode before returning to its initial state. In the central cut-off region, the wave decreases exponentially. Since this region is of limited length (tunnelling distance), there is a possibility for the wave not to vanish completely. This phenomena is referred to as tunnelling.

We consider a waveguide defined by the radii $R_1 = 0,\ R_2 = 0.8 - 0.1\cos((x-2)\pi/2)$ for $x \in [0, 4]$. The mode $(m, n) = (4, 2)$ is again injected at $x = 0$ at $\omega = 12.94$ for the no-flow case

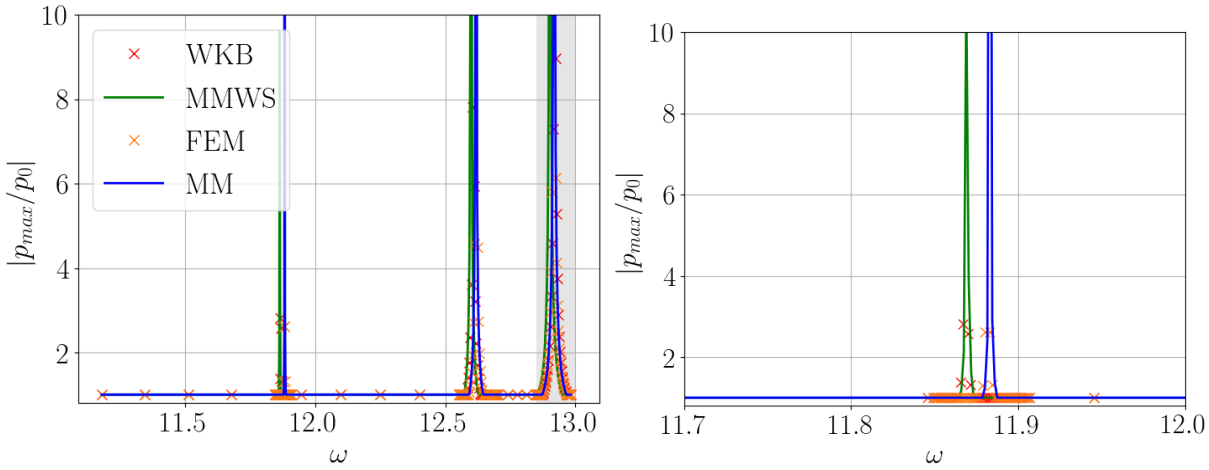

(a) Full frequency range

(b) Zoom on the resonance phenomena

Figure 3.14 – Variation of the amplification with frequency for the mode (4,2) for the case $M_s = -0.2$. The gray region correspond to a location where the WKB model errors are important.

and $\omega = 12.01$ for the flow case. For both cases, the turning points are located at $X_{t12} = 1.62$ and $X_{t23} = 2.38$. The behaviour of this mode for a wide range of frequencies is then investigated to study the tunnelling effect. The reasons behind these parameter choices are similar to those detailed in Section 3.2.2.1.

As previously, an estimate of the small parameter and the turning point boundary layer thickness can be given by $\epsilon \approx 0.16$ and $\epsilon^{-1/3}\omega^{-2/3} \approx 0.34$ respectively.

3.2.3.2 Single frequency - without flow

We first consider the no-flow case for the mode (4, 2) at $\omega = 12.94$. The pressure amplitude over the meridional plane obtained using the WKB model, the multimodal method without scattering, the multimodal method and the FEM is plotted in Figure 3.15.

There is a good qualitative agreement between the different methods. Most of the observations made for a single cut-on/cut-off transition [12] remain valid: there are interference pressure lobes before the first transition (interaction between the left- and right-running waves), and there is an increased pressure amplitude at the location of the transition.

As previously, a more quantitative evaluation can be obtained by projecting the acoustic field over the Bessel functions. The results are shown in Figure 3.16. For the case of a cut-on/cut-off/cut-on transition, the agreement between the formulations that neglect scattering is excellent and the concerned methods appear to be still accurate when compared to the multimodal method

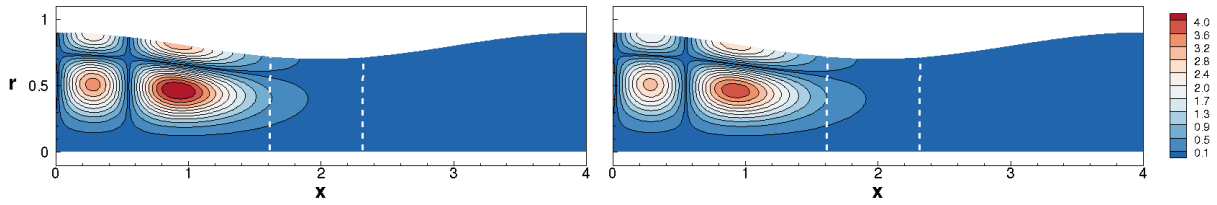

(a) WKB method

(b) Multimodal method without scattering

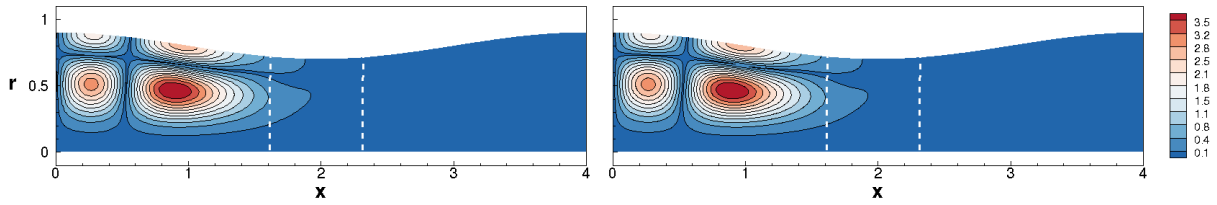

(c) Multimodal method

(d) Finite element method

Figure 3.15 – Maps of pressure magnitude associated to the mode (4,2) at $\omega = 12.94$ and $M_s = 0$. Turning points at $X_{t12} = 1.62$ and $X_{t23} = 2.38$.

and the FEM. This is due to a limited modal scattering over the adjacent modes. The behaviour of the cut-on mode $n = 1$ in the first cut-on region is similar to what has been obtained for the cut-off/cut-on/cut-off test cases, with interaction lobes between the upstream and downstream scattered waves. To quantify the difference from a single transition model, the amplitude of the reflection coefficient is again introduced as $\mathcal{R}_2 = p_2^-/p_2^+ = \mathcal{R}$. The amplitude of this coefficient is equal to one in the single-transition case. We obtain here with all the methods $|\mathcal{R}_2| = 0.99$, which shows that the second transition has only a little effect. Moreover, the good agreement between all the methods means that the modal scattering phenomena are of negligible impact. This is caused by attenuated reflected waves in the central region, which makes the first wave the main contributor to the modal scattering.

3.2.3.3 Single frequency - with flow

We now consider the same mode but at $\omega = 12.01$ (to keep the same position of the turning points as in the case without flow) and in the presence of a mean flow such that $M_s = -0.2$ at the inlet plane. The comparison is made between the WKB model, the multimodal method without scattering, the multimodal method and FEM. The pressure amplitude over the meridional plane obtained using the WKB model, the multimodal method, the multimodal method without scattering and the FEM are plotted in Figure 3.17. Once more, there is a good qualitative

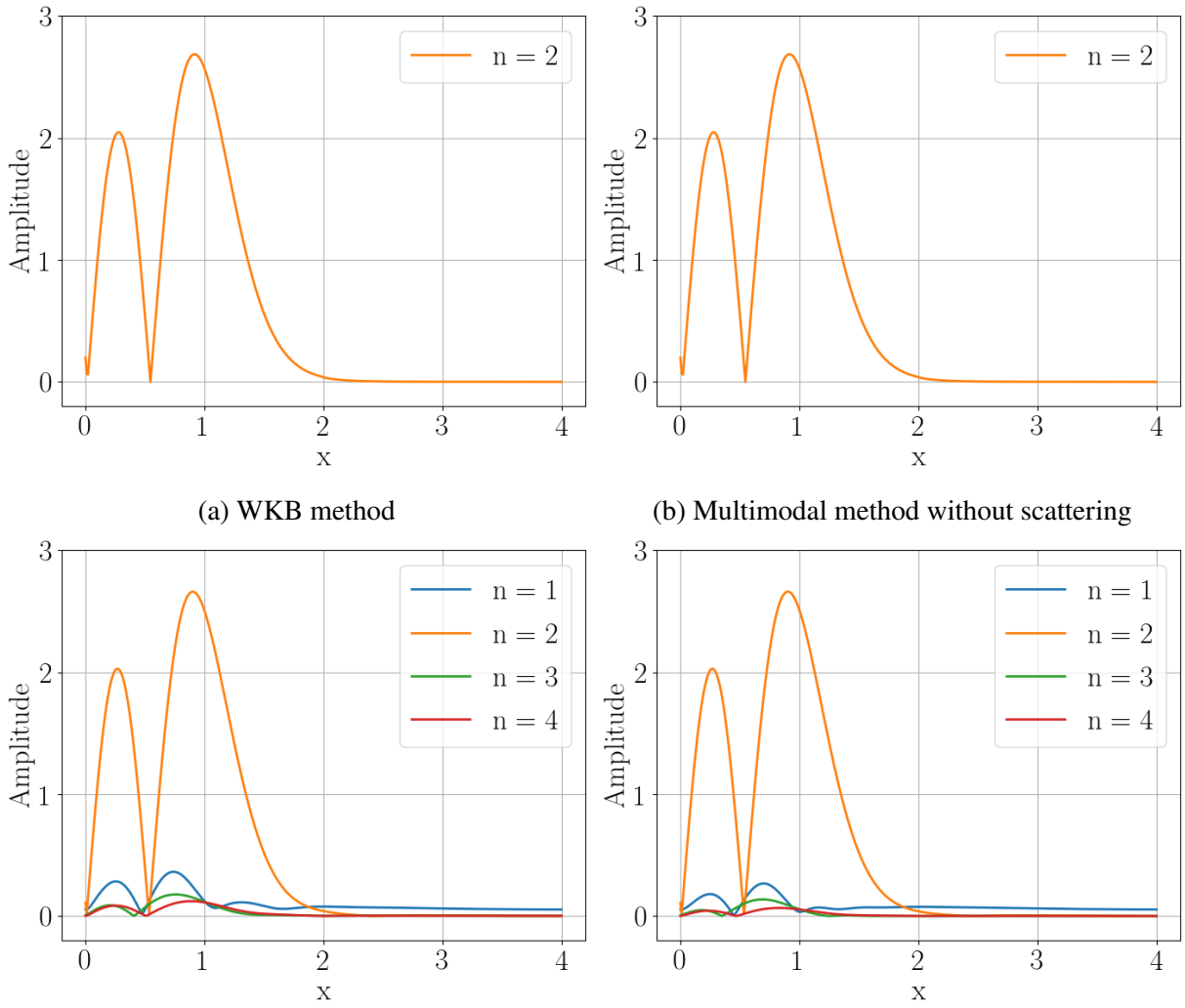

(a) WKB method

(b) Multimodal method without scattering

(c) Multimodal method

(d) Finite element method

Figure 3.16 – Projection over the first four Bessel functions of pressure associated to the injected mode (4,2) at $\omega = 12.94$ and $M_s = 0$. Turning points at $X_{t12} = 1.62$ and $X_{t23} = 2.38$.

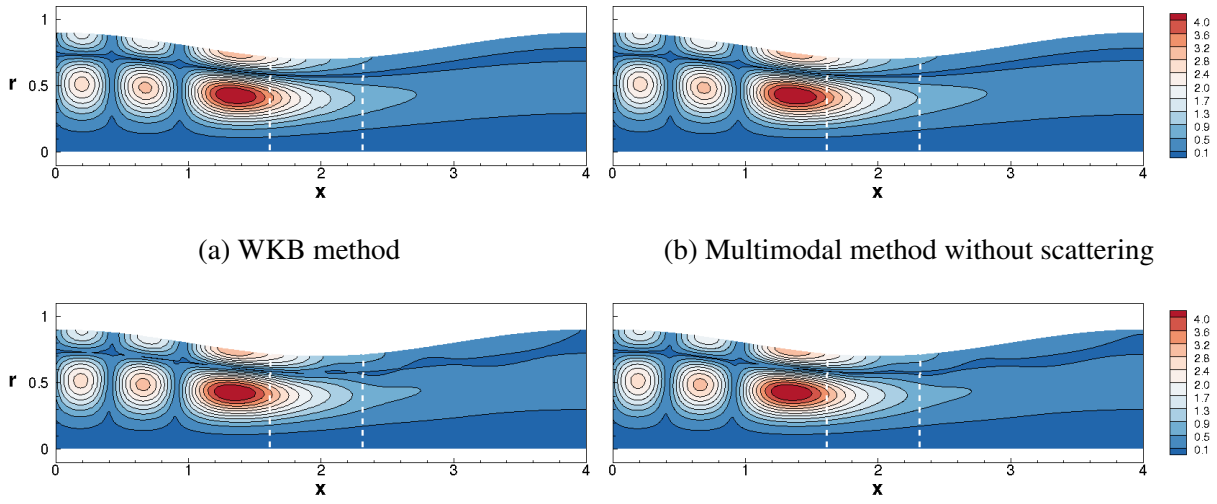

(a) WKB method

(b) Multimodal method without scattering

(c) Multimodal method

(d) Finite element method

Figure 3.17 – Maps of pressure magnitude associated to the mode (4,2) at $\omega = 12.01$ and $M_s = -0.2$. Turning points at $X_{t12} = 1.62$ and $X_{t23} = 2.38$

agreement regarding the shape and amplitude of the pressure magnitude, and most of the no-flow case observations remain valid. The agreement between the multimodal method without scattering and the WKB agreement is again excellent, which means that our multimodal method with artificial turning off of the scattering correctly predicts the multiple reflections that occurred.

As previously, a more quantitative evaluation can be obtained by projecting the acoustic field over Bessel's functions. The results of these projections are shown in Figure 3.18. The methods are in good agreement on both the shape and the amplitude of the pressure lobes. The reason is, as previously, a limited modal scattering over adjacent modes and a few reflections except from the ones due to transition phenomena. The comparison of the reflection coefficients gives similar conclusions as in the no-flow case, with a perfect match between all methodologies ($|\mathcal{R}_2| = 0.98$). Small differences are observed on the higher radial orders ($n > 1$) between the multimodal method and the FEM, but they are limited, and overall the two methods agree on the shape of the acoustic field.

3.2.3.4 Frequency variation - Tunneling effect

The two previous test cases were mainly used such that the WKB model could be used to validate the multimodal method without scattering, and therefore, the transitions were set to be distant. They have shown the simplified multimodal method's ability to evaluate the impact of the

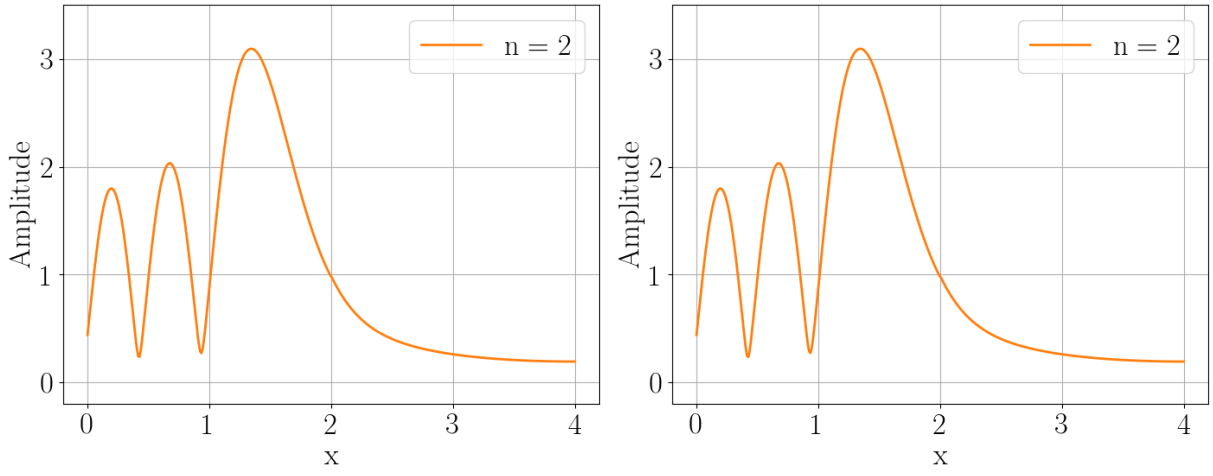

(a) WKB method

(b) Multimodal method without scattering

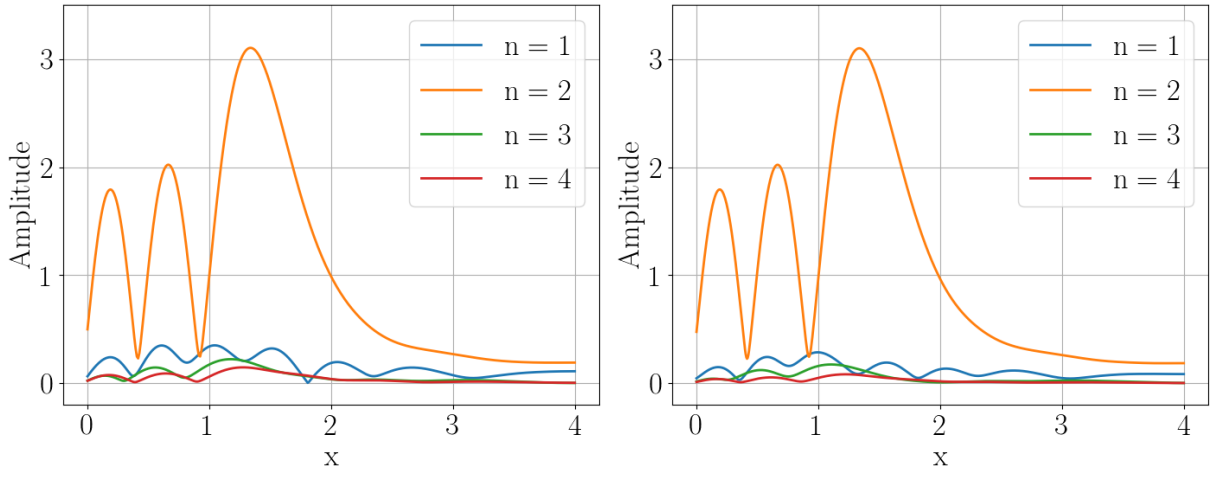

(c) Multimodal method

(d) Finite element method

Figure 3.18 – Projection over the first four Bessel functions of pressure associated to the injected mode (4,2) at $\omega = 12.01$ and $M_s = -0.2$. Turning points at $X_{t12} = 1.62$ and $X_{t23} = 2.38$.

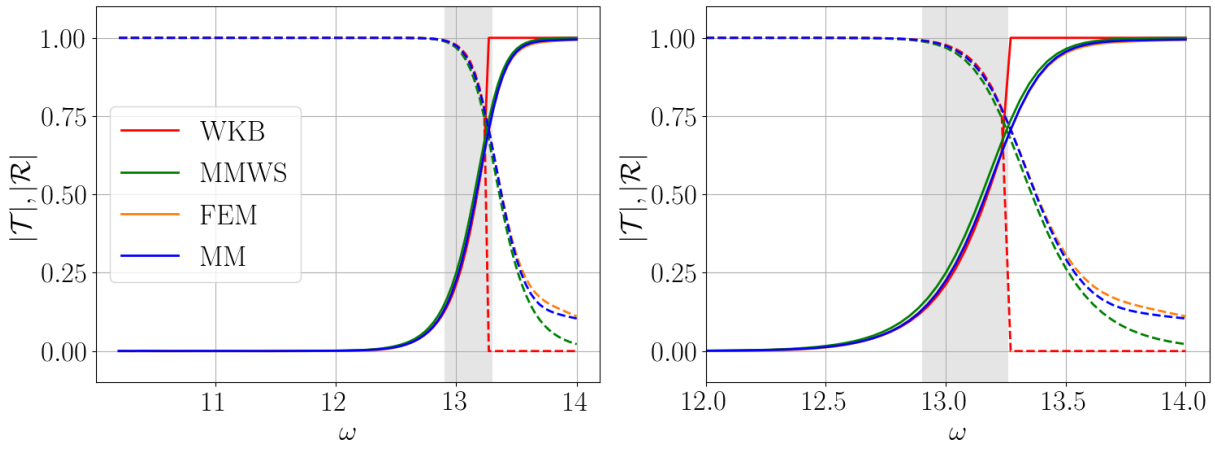

(a) Full frequency range

(b) Zoom on the collapsing transitions region

Figure 3.19 – Variation of the amplitude of the reflection (dashed line) and transmission (solid line) coefficients with frequency for the mode (4,2) for the case $M_s = 0$. The gray region correspond to a location where the WKB model errors are important.

tunnelling distance on the propagation. Nevertheless, the results are close to the ones of isolated transition, and the interest appears limited. In order to evaluate how the multimodal method behaves for close transitions and to understand its improvement when compared to simplified WKB models, we will perform computations outside of the area of validity of the WKB model ($|s_c| < 1$). In particular, we will see how the different methods behave near the tunnelling phenomenon for close transitions. For this purpose, the transmission and reflection coefficients of a mode undergoing a double cut-on/cut-off/cut-on transition are computed over a wide range of frequencies. The results for the case without and with flow are plotted in Figures 3.19 and 3.20 respectively.

The gray area corresponds to a region where the error caused by the matching assumptions becomes important in the improved WKB model because $|s_c| < 1$. For the analysis, the frequency plot is separated into three distinct regions. The main mode encounters two distant transitions in the first frequency range ($\omega < 12.9$ for the case without flow and $\omega < 12.1$ for the case with flow). In the second one ($12.90 < \omega < 13.3$ for the case without flow and $12.1 < \omega < 12.3$ for the case with flow), it experiences collapsing transitions. Finally, the main mode is fully cut-on in the last frequency range ($\omega > 13.3$ for the case without flow and $\omega > 12.3$ for the case with flow). There is an excellent quantitative agreement between all the methods in the first region, as expected from the single frequency cases. The modal scattering has a few impact on the propagation. In the second region, the WKB model is outside of its area of validity, but an analysis is still carried out. Where the two transitions merge, the coefficients $|\mathcal{T}|$ and $|\mathcal{R}|$

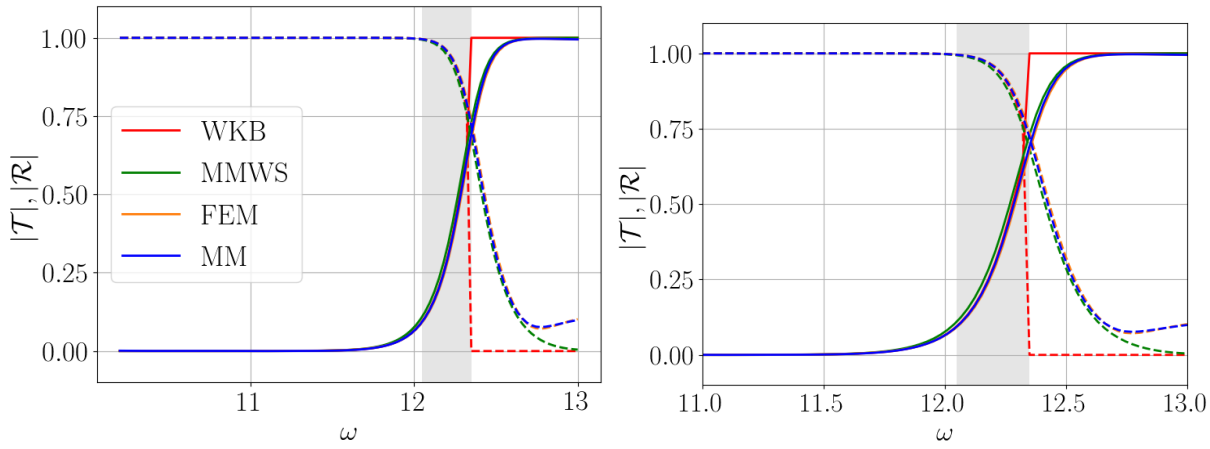

(a) Full frequency range

(b) Zoom on the collapsing transitions region

Figure 3.20 – Variation of the amplitude of the reflection (dashed line) and transmission (solid line) coefficients with frequency for the mode (4,2) for the case $M_s = -0.2$. The gray region correspond to a location where the WKB model errors are important.

should be equal to $1/\sqrt{2}$ in theory [70]. This is the case with the FEM, the multimodal method and the multimodal method without scattering but not with the WKB model. As observed for the amplification phenomena, there seems to be a frequency shift near this region with the model presented. However, this is not related here to the modal scattering, as the multimodal method without scattering gives the right solution. In the last region, the mode is cut-on, and no transition occurs inside the duct so that the reflection coefficient is expected to be equal to 0. It is not the case with the multimodal method and multimodal method without scattering which means that other reflections, not caused by a change of mode behaviour, occur. To solve this issue, the notion of complex turning points should be added to the WKB analysis [70]. It can be noted that the relation $|\mathcal{T}|^2 + |\mathcal{R}|^2 = 1$ is only valid for the multimodal method without scattering and WKB method, where the single injected mode carries out the overall energy. With the multimodal method, energy leaks on the adjacent modes and the previous relation is lost ($|\mathcal{T}|^2 + |\mathcal{R}|^2 < 1$). Despite this observation, note that as the scattering is limited, the multimodal method without scattering gives excellent results and closely matches the multimodal results. Finally, a reflection is observed in the last cut-on region when the FEM and multimodal method are used ($|\mathcal{R}| \approx 0.1$). It is linked to the scattering mechanism as it is not observed with the multimodal method without scattering. Still, its value is low, and the transmission coefficient is close to the one obtained with the multimodal method without scattering.

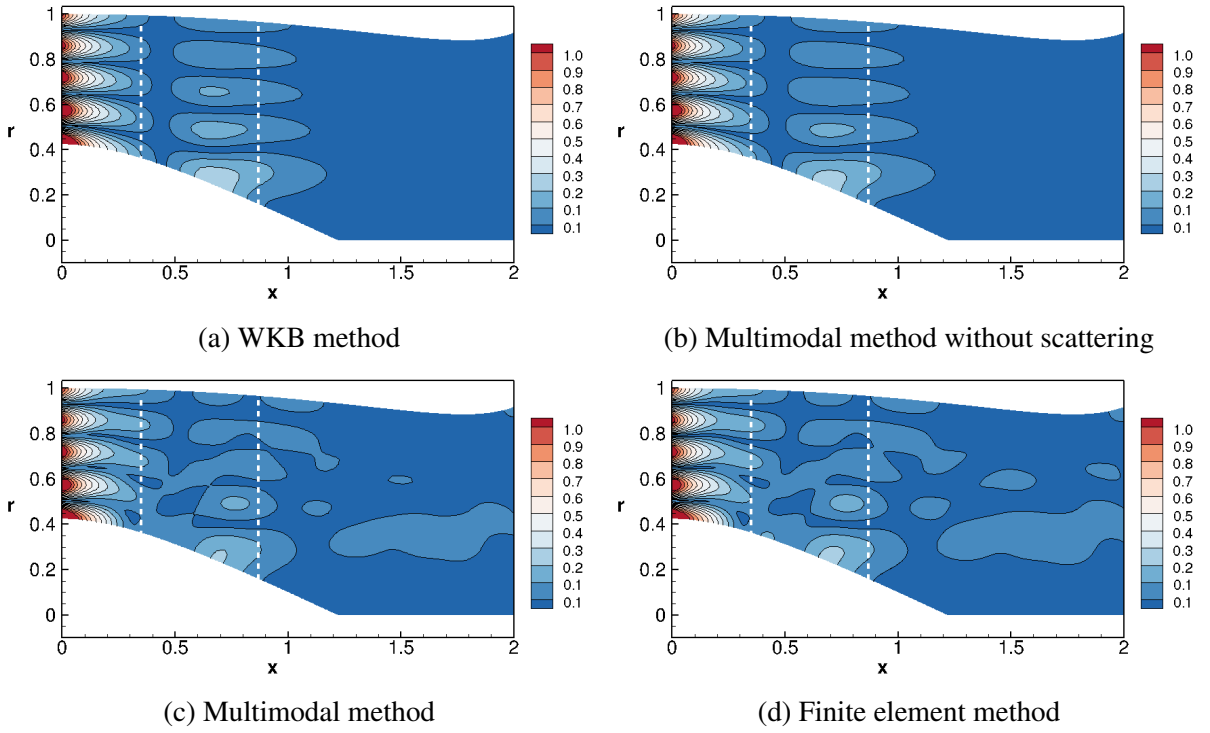

(a) WKB method

(b) Multimodal method without scattering

(c) Multimodal method

(d) Finite element method

Figure 3.21 – Maps of pressure magnitude for a mode (5,5) in the CFM56 geometry at $\omega = 19.2$ and $M_s = -0.5$. Turning points at $X_{t12} = 0.35$ and $X_{t23} = 0.87$.

3.2.4 Application to an engine intake

The ability of the models to capture both resonance and tunnelling phenomena inside real engine geometries is investigated here. To this purpose, we consider the CFM56 engine geometry described in Section 2.3.1.

3.2.4.1 Resonance phenomena

The first case considered is very close to the case 7 presented in [12], with the propagation of a mode $(m, n) = (5, 5)$ and a Mach number at the fan location $M_s = -0.5$. As for the previous test cases, two types of results are presented. First, the pressure maps and the associated projection over Bessel functions for a single frequency are given. This frequency is set to have distant transitions and to be far from an expected resonance phenomenon (which yields a boundary layer thickness estimate of $\epsilon^{-1/3}\omega^{-2/3} \approx 0.20$). This gives $\omega = 19.2$. The associated results are plotted in Figures 3.21 and 3.22. Then, the amplification is computed for a large frequency spectra where double transitions occur. This is plotted in Figure 3.23.

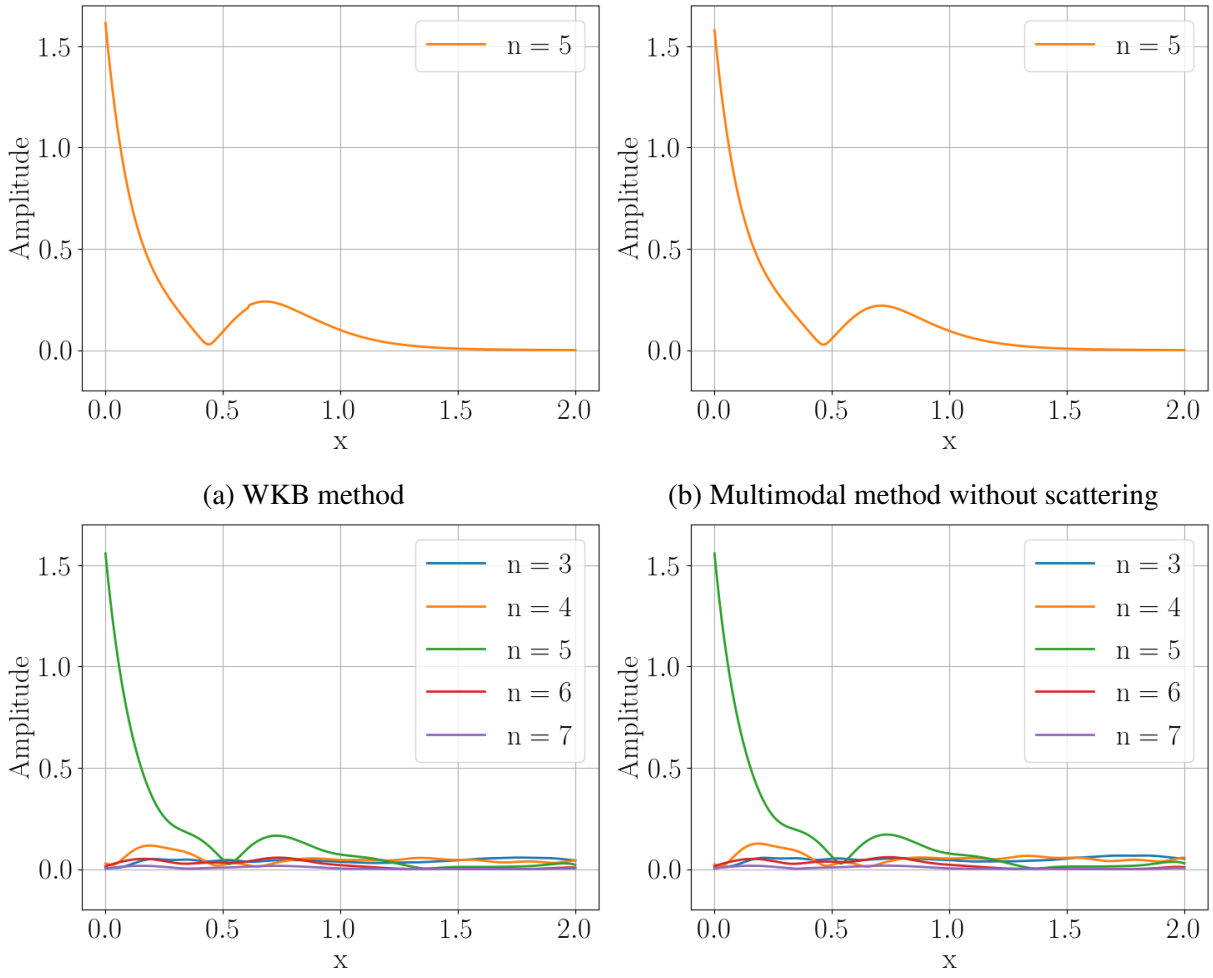

(a) WKB method

(b) Multimodal method without scattering

(c) Multimodal method

(d) Finite element method

Figure 3.22 – Projection over the first four Bessel functions of pressure associated to the injected mode (5,5) in the CFM56 geometry at $\omega = 19.2$ and $M_s = -0.5$. Turning points at $X_{t12} = 0.35$ and $X_{t23} = 0.87$.

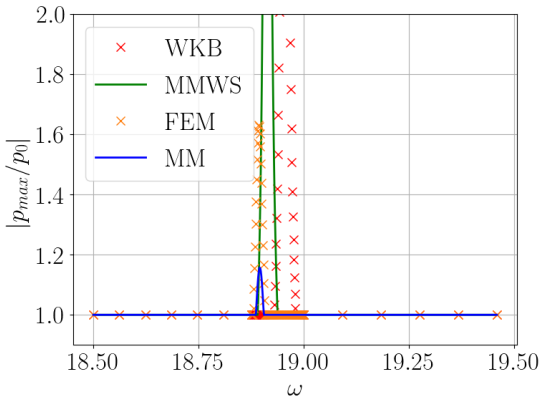

Figure 3.23 – Variation of the amplification with frequency for a mode (5,5) in the CFM56 geometry, $M_s = -0.5$.

For the single frequency, a good qualitative agreement is obtained between both the multimodal method without scattering and WKB and between the multimodal method and the FEM. The differences in the axial amplitude and the position of the lobes for the injected mode between all the models is observed. The differences between with and without scattering methods are explained by an increase of the modal scattering, particularly visible for the radial mode $n = 4$. This was expected because the spinner variation introduces a new scattering mechanism. The differences between the multimodal method without scattering and the WKB come from the fact that we are at the limit of the distant transition hypothesis.

Still, the analysis of the resonance phenomenon displays the presence of an amplification region for $18.8 < \omega < 19.0$. In this region, the match is good between the WKB method and multimodal method without scattering, which both predict a strong amplification but with a frequency shift between them. As for the simplified geometry presented in the Section 3.2.2, there is again a shift between the amplification peaks obtained with the two methods that do not encapsulate the modal scattering phenomenon and the ones obtained with the multimodal method. But, contrarily to these previous results, the peaks appear very attenuated with the FEM and multimodal method. However, the peak is underestimated with the multimodal method. In order to clarify this aspect, it is necessary to recall that the turning points for both cases where a weak amplification is observed are located before $x = 0.84$. The spinner slope variation is high between the turning points, where the multiple reflections occur, leading to important modal scattering phenomena. Consequently, the multiple reflected waves lose significant energy by transferring it to the neighbouring modes, which can become dominant. This prevents the resonance from happening, the impact of double transition is only a finite amplification, and

this strong scattering requires an accurate representation of the flow induced modal scattering. This result is of major importance since most of the parametric studies on resonance [15, 91, 92, 16, 17] are done by neglecting the modal scattering phenomena, which may lead to erroneous conclusions.

3.2.4.2 Tunnelling phenomena

The second case considered is very similar to the case 3 presented in [12] with the propagation of a mode $(m, n) = (51, 2)$. As for the previous test cases made on a simplified geometry, two types of results are presented: first, the pressure maps and the associated projection over Bessel functions for a single frequency, then the evolution of the transmission and reflection coefficients for a large frequency spectrum. Contrary to the resonance study, the frequency variation is not limited to the double transition range but also includes frequencies where the mode is considered cut-on. This is set to understand the impact of other geometric reflection phenomena in non-symmetric geometries. For the single frequency case, ω is taken to ensure that the transitions are at the limit of validity of the distant hypothesis of the WKB model in order to have a visible impact of the second transition. Note that double transition phenomena is not encountered for all the frequencies. Therefore, to apply the WKB model as if, the geometry is truncated at the exit and $x \in [0, 1.8]$. This gives $\omega = 58.3$. This yields a boundary layer thickness estimate of $\epsilon^{-1/3}\omega^{-2/3} \approx 0.09$. The associated results are plotted in Figures 3.24 and 3.25 for the maps of pressure and Bessel's projection respectively. The evolution of the reflection and transmission coefficient with frequency is then plotted in Figure 3.26. The results show a good agreement for the pressure plots and modal projections because the modal scattering is limited. As already observed for the academic test cases (Section 3.2.3), the two modes adjacent to the main one show interaction lobes. Still, there is phase shift between the reflected wave predicted by the WKB model and multimodal method without scattering and the one obtained with the multimodal method and FEM. As for the simplified geometry, the analysis of the tunnelling graph is divided into three parts based on the location of turning points. In the first frequency range, where the main mode encounters two distant turning points, there is an excellent agreement between the multimodal method without scattering and WKB methods. However, the obtained coefficient values are slightly different from the ones of the multimodal method and FEM, which shows a small impact of the modal scattering. In the central region where the main mode experiences collapsing transitions, the conclusions obtained on the simplified test case remain valid. In the last frequency range, where the main mode is cut-on, differences that were not seen in the simplified test case are observed between the multimodal method without scattering and the

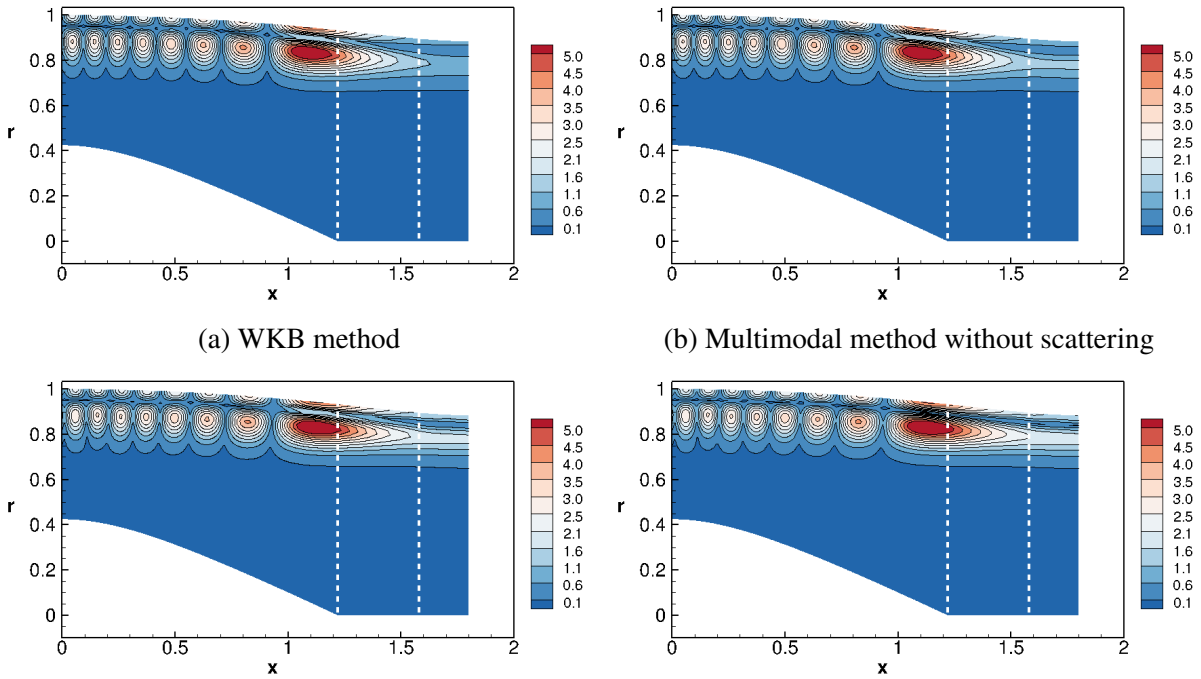

(a) WKB method

(b) Multimodal method without scattering

(c) Multimodal method

(d) Finite element method

Figure 3.24 – Maps of pressure magnitude for a mode (51,2) in the CFM56 geometry at $\omega = 68.5$ and $M_s = -0.5$. Turning points at $X_{t12} = 1.62$ and $X_{t23} = 1.90$.

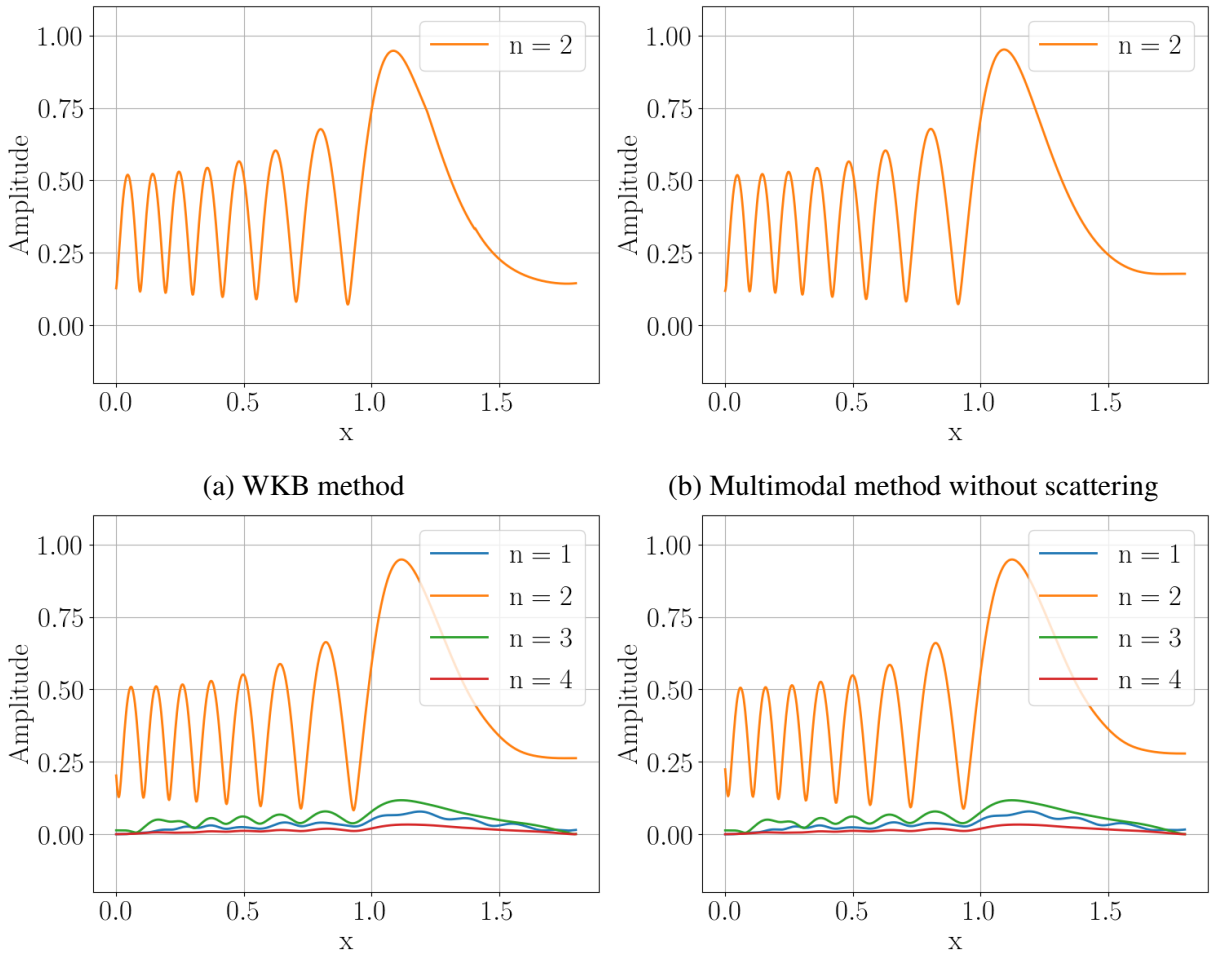

(a) WKB method

(b) Multimodal method without scattering

(c) Multimodal method

(d) Finite element method

Figure 3.25 – Projection over the first four Bessel functions of pressure associated to the injected mode (51,2) in the CFM56 geometry at $\omega = 68.5$ and $M_s = -0.5$. Turning points at $X_{t12} = 1.62$ and $X_{t23} = 1.90$.

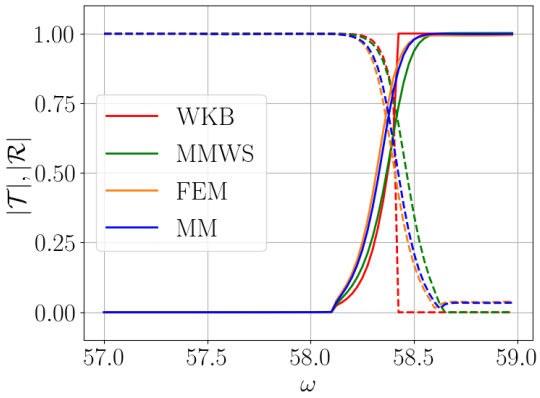

Figure 3.26 – Variation of the amplitude of the reflection (dashed line) and transmission (solid line) coefficients with frequency for a mode (51,2) in the CFM56 geometry and for $M_s = -0.5$.

FEM and multimodal method and highlights the increased impact of modal scattering with this geometry.

3.3 Conclusion

A simplified multimodal formulation when considering a multiple-scale flow has been introduced with the aim of reducing calculation time and isolating scattering phenomena from self-propagation of individual modes. With this approach, all multimodal matrices are a combination of variables that solely vary in the axial direction, multiplied by integrals that remain independent of acoustic, flow, and geometry parameters when the Chebyshev basis is used. This method exhibits particularly favorable performance in proximity to transition phenomena and has been employed to investigate the influence of double transitions on the acoustic field. In scenarios involving such cases, a simplified method based on the WKB ansatz has also been proposed to enhance the analysis and to validate the multimodal method without scattering.

From a physical point of view, it was shown that double turning point can give rise to specific phenomena such as resonance, amplification or tunnelling, that can be captured by both developed models. In the case of a cut-on/cut-off/cut-on transition, tunnelling appears with an attenuation of the wave between the two turning points. If the mode has a non-zero amplitude at the axial location of the second transition, there will be a non-zero transmitted power. In the case of a cut-off/cut-on/cut-off transition, the successive multiple reflections between the two turning points form constructive interference for certain distances. Since the mode is cut-on in this region, these successive reflections do not dissipate energy and can lead to resonance phenomena if no

modal scattering is considered when the mode is trapped between the transitions.

For distant transitions, the agreement between the multimodal method without modal scattering and the WKB model is excellent for both cases. However, the comparison with the simplified multimodal and FEM (which are is close agreement) highlights the inherent limitations of the methods that neglect the modal scattering. For the cut-off/cut-on/cut-off double transition, this limitation is responsible for (1) a small modification of the axial wavenumber, which causes a shift of the amplification peak frequencies and (2) a transfer of the main mode energy over the neighbouring modes which prevents the theoretical resonance from happening. The amplification can even become negligible if the modal scattering mechanism is strong. Then, when one of the neighbouring modes is cut-on, it can carry a non-negligible acoustic power. As for the cut-on/cut-off/cut-on double transition, the improvement gain by adding modal scattering is marginal. In that case, note that even when there are no turning points inside the duct and that the cut-off region vanishes, new geometrical reflections are shown to exist.

In conclusion, the multimodal method with a multiple-scale flow can give accurate results and allows to separate mode propagation from modal scattering. Therefore, it enhances our physical understanding of the phenomena inside the engine and is a valuable way to study modal transitions. In particular, it can be used in a preliminary design of an engine to estimate the frequencies where an amplification only controlled by the geometry occurs and thus to avoid creating resonators that can have dire implications on the sound emission.

CHAPTER 4

FORMULATION WITH MULTIPLE DUCTS AND FREE-FIELD ACOUSTIC RADIATION

In this chapter, the focus is shifted to the computation of the free-field acoustic radiation from an intake. To do so, we propose extending the general multimodal approach developed in Chapter 2. This extension is based on a previous adaptation of the original multimodal method, without flow, to compute the acoustic radiated field [93]. This original method showcased impressive performance, making it well-suited for optimization procedures [50, 49].

This adaptation involves considering an isolated duct surrounded by a notational one with a larger radius and a Perfectly Matched Layer (PML) on its outer boundary [93]. This PML simulates an infinite domain by damping the waves that propagate outwards. The formulation of this problem including the presence of a mean flow is presented in Section 4.1. First, we rewrite the Goldstein propagation equation to account for the presence of a mean flow in a duct when including PML on the "outer wall". Then we show you how the method is applied to compute the mean flow, as done in Section 2.2 for in-duct domains. In Section 4.2, we validate the developed multimodal method to perform radiation calculations against a FEM code, and conduct a parametric study on the impact of the different acoustic parameters on the radiated field to further validate the method.

4.1 Multimodal formulation with multiple ducts

4.1.1 Governing equations in a waveguide with PML

The goal is to simulate the propagation of acoustic waves within an isolated nacelle and their free-field radiation. To achieve this, we use the same idea than the one presented in [93], where the nacelle is surrounded by a duct that has a perfectly matched annular layer to model far-field radiation conditions. The procedure is illustrated in Figure 4.1. The computational domain can be separated into three regions $\mathcal{A}$, $\mathcal{B}$ and $\mathcal{C}$. In the waveguide $\mathcal{A}$, the model is that of a standard

in-duct acoustic propagation, while in the regions $\mathcal{B}$ and $\mathcal{C}$, the propagation occurs in a duct with a PML on the outer wall.

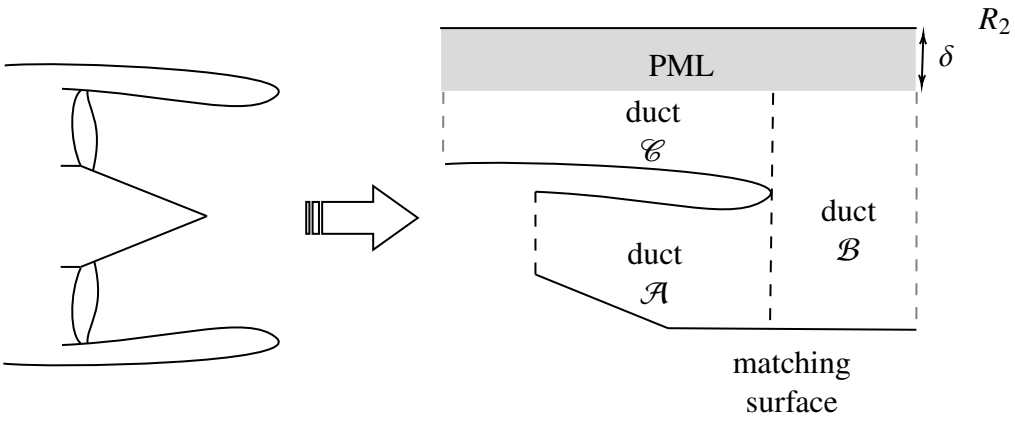

Figure 4.1 – Sketch of a generic turbofan inlet and the associated free-field radiation modelization with the multimodal.

The Equation (1.13) governing the acoustic propagation inside a hard walled duct has been given in section 1.1.3. This equation is now modified to account for a PML. The PML is defined using the function α which aims to modify the radial coordinate r into a stretched radial coordinate $\widetilde{r}$:

$$\widetilde{r} = \int_0^r \alpha(\xi)\mathrm{d}\xi, \tag{4.1}$$

to damp the acoustic waves. It is complex-valued inside the PML and equal to one (such that $\widetilde{r} = r$) elsewhere [94, 95, 96]. The function α is chosen to be:

$$\alpha(\xi) = 1 + 2(\overline{\alpha} - 1)\frac{\xi - (R_2 - \delta)}{\delta}, \tag{4.2}$$

with δ the size of the PML, R_2 the real outer radius and $\overline{\alpha}$ a complex number. When this parameter is used, the stretched radial derivative and the stretched radius can be rewritten: $\partial_{\widetilde{r}} = \alpha^{-1}\partial_r$ and $\widetilde{r} = \beta r$, with:

$$\beta = 1 + (\overline{\alpha} - 1)\frac{(r - (R_2 - \delta))^2}{\delta}. \tag{4.3}$$

With PML, the Goldstein propagation equation (1.13) remains similar, except that all the differential operators are not in the cylindrical coordinate system (x, r, θ), but in the modified coordinate system $(x, \widetilde{r}, \theta)$. With the original operators, the propagation equation to solve

becomes:

$$\begin{aligned}&\alpha\beta\frac{\partial}{\partial x}\left(D\frac{\partial\phi}{\partial x}\right)+\nabla_\perp\cdot(DH\nabla_\perp\phi)\\&-D\alpha\beta\left(\mathrm{i}\omega+U\frac{\partial}{\partial x}+\mathbf{V}_\perp\cdot(L\nabla_\perp)\right)\left[\frac{1}{C^2}\left(\mathrm{i}\omega+U\frac{\partial}{\partial x}+\mathbf{V}_\perp\cdot(L\nabla_\perp)\right)\phi\right]=0,\end{aligned}\tag{4.4}$$

where:

$$H=\begin{pmatrix}\beta/\alpha & 0\\ 0 & \alpha/\beta\end{pmatrix},L=\begin{pmatrix}1/\alpha & 0\\ 0 & 1/\beta\end{pmatrix}.\tag{4.5}$$

As for the boundary conditions, only hard walled are considered (a liner will not bring much since the waves will already be highly attenuated inside the PML). They write:

$$\left(\frac{\partial\phi}{\partial x}\mathbf{e}_x+L\nabla_\perp\phi\right)\cdot\mathbf{n}=0.\tag{4.6}$$

4.1.2 Variational formulation

The in-duct general multimodal method derived in Chapter 2 can be applied in the duct $\mathcal{A}$. We aim to use the same method in the ducts $\mathcal{B}$ and $\mathcal{C}$, but we do not yet have the multimodal equations in the presence of a PML. Therefore, the goal is here to obtain those equations. We begin by writing the weak formulation of the Equation (4.4) over a transverse cross section S bounded by a contour Λ. It writes after some manipulations:

$$\begin{aligned}&\frac{\mathrm{d}}{\mathrm{d}x}\left(\int_S D\alpha\beta(1-M^2)ug^*-\frac{DU}{C^2}\alpha\beta\left(\mathrm{i}\omega+\mathbf{V}_\perp\cdot(L\nabla_\perp)\right)\phi g^*\mathrm{d}S\right)=\\&+\int_S\Bigg[D\alpha\beta(1-M^2)u\frac{\partial g^*}{\partial x}+DH\nabla_\perp g^*\cdot\nabla_\perp\phi\\&-\frac{D}{C^2}\alpha\beta\left(\left(\mathrm{i}\omega+\mathbf{V}_\perp\cdot(L\nabla_\perp)\right)\phi\left(-\mathrm{i}\omega+\mathbf{V}_\perp\cdot(L\nabla_\perp)\right)g^*+Uu\left(-\mathrm{i}\omega+\mathbf{V}_\perp\cdot(L\nabla_\perp)\right)g^*\right.\\&\left.+U\frac{\partial g^*}{\partial x}\left(\mathrm{i}\omega+\mathbf{V}_\perp\cdot(L\nabla_\perp)\right)\phi\right)\Bigg]\mathrm{d}S,\end{aligned}\tag{4.7}$$

where g is a test function.

As in Section 2.1.3, the acoustic variables are represented using a set of linearly independent transverse cross-section functions, denoted $(\varphi_j)_{j\in\mathbb{N}}$. The same basis is used for the test functions

associated to ϕ and u. The Equation (4.7) then becomes:

$$\begin{aligned}
&\frac{\mathrm{d}}{\mathrm{d}x}\left(\int_S D\alpha\beta(1-M^2)\varphi_j\varphi_i^* u_j - \frac{DU}{C^2}\alpha\beta\left(\mathrm{i}\omega + \mathbf{V}_\perp\cdot(L\nabla_\perp)\right)\varphi_j\varphi_i^*\phi_j \mathrm{d}S\right) = \\
&+\int_S\Bigg[D\alpha\beta(1-M^2)\varphi_j\frac{\partial\varphi_i^*}{\partial x}u_j + DH\nabla_\perp\varphi_i^*\cdot\nabla_\perp\varphi_j\phi_j \\
&-\frac{D}{C^2}\alpha\beta\left(\left(\mathrm{i}\omega + \mathbf{V}_\perp\cdot(L\nabla_\perp)\right)\varphi_j\left(-\mathrm{i}\omega + \mathbf{V}_\perp\cdot(L\nabla_\perp)\right)\varphi_i^*\phi_j\right. \\
&\left.+U\varphi_j\left(-\mathrm{i}\omega + \mathbf{V}_\perp\cdot(L\nabla_\perp)\right)\varphi_i^* u_j + U\left(\mathrm{i}\omega + \mathbf{V}_\perp\cdot(L\nabla_\perp)\right)\varphi_j\frac{\partial\varphi_i^*}{\partial x}\phi_j\right)\Bigg]\mathrm{d}S.
\end{aligned} \tag{4.8}$$

This gives one of the new first-order equations needed for the multimodal formulation (which replaces Equation (2.10) of the general multimodal formulation). For the second one, a similar procedure on $u = \partial\phi/\partial x$ gives:

$$\int_S \alpha\beta D(1-M^2)\varphi_i\varphi_i^*\mathrm{d}S\frac{\mathrm{d}\phi_j}{\mathrm{d}x} = -\int_S \alpha\beta D(1-M^2)\varphi_i^*\frac{\partial\varphi_j}{\partial x}\mathrm{d}S\phi_j + \int_S \alpha\beta D(1-M^2)\varphi_j\varphi_i^*\mathrm{d}S u_j. \tag{4.9}$$

As a remainder, the equations governing the axial variation the vectors $\boldsymbol{\phi}$ and $\mathbf{u}$ can be written:

$$\begin{pmatrix} A_{11} & A_{12} \\ A_{21} & A_{22} \end{pmatrix}\frac{\mathrm{d}}{\mathrm{d}x}\begin{pmatrix} \boldsymbol{\phi} \\ \mathbf{u} \end{pmatrix} = \begin{pmatrix} M_{11} & M_{12} \\ M_{21} & M_{22} \end{pmatrix}\begin{pmatrix} \boldsymbol{\phi} \\ \mathbf{u} \end{pmatrix}. \tag{4.10}$$

This gives us access to the matrices A_{11}, A_{12}, A_{21}, A_{22}, M_{11}, M_{12}, M_{21} and M_{22} in the case with PML. The resulting matrices are given in Appendix D. This is the main equation of the problem that is solved in the ducts $\mathcal{B}$ and $\mathcal{C}$ using the multimodal method.

A procedure similar to the one done for in-duct propagation (see Sections 2.1.5 – 2.1.8) is applied to solve this equation. This is done in ducts $\mathcal{B}$ and $\mathcal{C}$ while the general formulation of Section 2.1.3 is solved for duct $\mathcal{A}$. The only step that remains is how the information is exchanged between the three ducts.

4.1.3 Matching procedure

At the junction between the ducts, it is necessary to have connection formula that link the admittance matrix Y and the potential amplitudes $\boldsymbol{\phi}$ of each duct. For the following, the subscripts $\mathcal{A}$, $\mathcal{B}$, and $\mathcal{C}$ indicate that the variables are associated with the ducts $\mathcal{A}$, $\mathcal{B}$, and $\mathcal{C}$ respectively. In the ducts $\mathcal{B}$ and $\mathcal{C}$ admittances $Y_\mathcal{B}$ and $Y_\mathcal{C}$ are found by applying a multimodal method

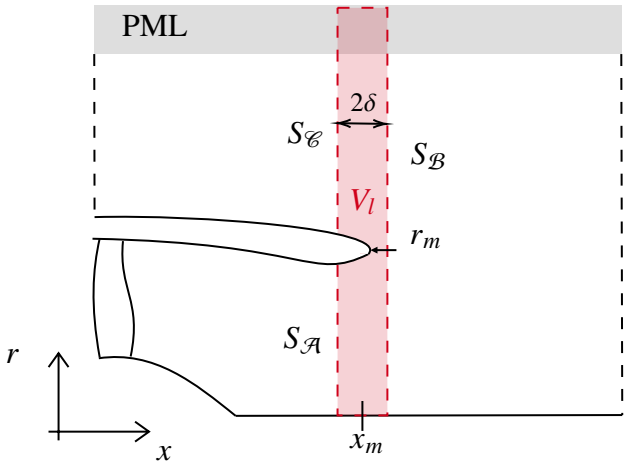

Figure 4.2 – Sketch of a generic matching region at the inlet.

from their initial value at far-field ($x \to \infty$) to the matching region. The connection formula on the admittance therefore writes: $Y_{\mathcal{A}} = Y_{\mathcal{A}}(Y_{\mathcal{B}}, Y_{\mathscr{C}})$. To determine the connection formula, the acoustic potential and velocity are assumed to be continuous at these junctions.

Let us consider the exit of an intake located at (x_m, r_m) such that $x = x_m + \delta$ is in the free-field (duct $\mathcal{B}$) and $x = x_m - \delta$ is located inside the engine. We define a thin volume V_l that goes from $x = x_m - \delta$ to $x = x_m + \delta$, as sketched in Figure 4.2. The computational domain V_l is enclosed by the surfaces S_w, $S_{\mathcal{A}}$, $S_{\mathcal{B}}$, and $S_{\mathscr{C}}$. $S_{\mathcal{A}}$ and $S_{\mathscr{C}}$ are located at $x = x_m - \delta$ inside the ducts $\mathcal{A}$ and $\mathscr{C}$ respectively, while $S_{\mathcal{B}}$ is located at $x = x_m + \delta$ in the duct $\mathcal{B}$.

When $\delta \to 0$, we want the following set of equations to be true in the domain V_l:

$$\begin{cases} u_{\mathscr{C}}(x_m, r) = u_{\mathcal{B}}(x_m, r) \text{ and } \phi_{\mathscr{C}}(x_m, r) = \phi_{\mathcal{B}}(x_m, r) \text{ for } r > r_m, \\ u_{\mathcal{A}}(x_m, r) = u_{\mathcal{B}}(x_m, r) \text{ and } \phi_{\mathcal{A}}(x_m, r) = \phi_{\mathcal{B}}(x_m, r) \text{ for } r < r_m. \end{cases} \tag{4.11}$$

In each duct, these acoustic variables are represented using the functions $\varphi_j^{\mathcal{D}}$, such that:

$$a_{\mathcal{D}} = \sum_j a_j^{\mathcal{D}}(x)\varphi_j^{\mathcal{D}}(x, r, \theta),$$

where $a_{\mathcal{D}}$ is one of the acoustic variables and $\mathcal{D} \in [\mathcal{A}, \mathcal{B}, \mathscr{C}]$.

Equation (4.11) can then be written with the following relations between the acoustic potential

and velocity variables:

$$\begin{aligned}\int_{S_{\mathcal{B}}} \left(\varphi_i^{\mathcal{B}}\right)^* u_{\mathcal{B}} w_{\mathcal{B}} \, \mathrm{d}S &= \int_{S_{\mathcal{A}}} \left(\varphi_i^{\mathcal{B}}\right)^* u_{\mathcal{A}} w_{\mathcal{B}} \, \mathrm{d}S + \int_{S_{\mathcal{C}}} \left(\varphi_i^{\mathcal{B}}\right)^* u_{\mathcal{C}} w_{\mathcal{B}} \, \mathrm{d}S, \\ \int_{S_{\mathcal{A}}} \left(\varphi_i^{\mathcal{A}}\right)^* \phi_{\mathcal{A}} w_{\mathcal{A}} \, \mathrm{d}S &= \int_{S_{\mathcal{A}}} \left(\varphi_i^{\mathcal{A}}\right)^* \phi_{\mathcal{B}} w_{\mathcal{A}} \, \mathrm{d}S, \\ \int_{S_{\mathcal{C}}} \left(\varphi_i^{\mathcal{C}}\right)^* \phi_{\mathcal{C}} w_{\mathcal{C}} \, \mathrm{d}S &= \int_{S_{\mathcal{C}}} \left(\varphi_i^{\mathcal{C}}\right)^* \phi_{\mathcal{B}} w_{\mathcal{C}} \, \mathrm{d}S,\end{aligned} \tag{4.12}$$

where $\varphi_i^{\mathcal{A}}, \varphi_i^{\mathcal{B}}, \varphi_i^{\mathcal{C}}$ are orthogonal with respect to the weights functions $w_{\mathcal{A}}, w_{\mathcal{B}}, w_{\mathcal{C}}$ respectively.

In a matrix form, this writes:

$$\begin{aligned}\boldsymbol{\phi}_{\mathcal{A}} = F_{\mathcal{A}}^{\mathcal{B}} \boldsymbol{\phi}_{\mathcal{B}}, \quad \boldsymbol{\phi}_{\mathcal{C}} = G_{\mathcal{C}}^{\mathcal{B}} \boldsymbol{\phi}_{\mathcal{B}}, \\ \mathbf{u}_{\mathcal{B}} = F_{\mathcal{B}}^{\mathcal{A}} \mathbf{u}_{\mathcal{A}} + G_{\mathcal{B}}^{\mathcal{C}} \mathbf{u}_{\mathcal{C}},\end{aligned} \tag{4.13}$$

where $(F_{\mathcal{A}}^{\mathcal{B}})_{ij} = \int_{S_{\mathcal{A}}} (\varphi_i^{\mathcal{A}})^* \varphi_j^{\mathcal{B}} w_{\mathcal{A}} \mathrm{d}S$ is the transfer matrix from duct $\mathcal{B}$ to duct $\mathcal{A}$ and $(G_{\mathcal{C}}^{\mathcal{B}})_{ij} = \int_{S_{\mathcal{C}}} (\varphi_i^{\mathcal{C}})^* \varphi_j^{\mathcal{B}} w_{\mathcal{C}} \mathrm{d}S$ is the transfer matrix from duct $\mathcal{B}$ to duct $\mathcal{C}$. The admittance at the exit of the duct $\mathcal{A}$ is therefore:

$$Y_{\mathcal{A}} = \left(F_{\mathcal{A}}^{\mathcal{B}} \left(Y_{\mathcal{B}} - G_{\mathcal{B}}^{\mathcal{C}} Y_{\mathcal{C}} G_{\mathcal{C}}^{\mathcal{B}} \right)^{-1} F_{\mathcal{B}}^{\mathcal{A}} \right)^{-1}. \tag{4.14}$$

This formula gives the admittance at the exit of the duct $\mathcal{A}$. This one replaces the original boundary condition, set in Equation (2.15), and is integrated right up to the source. Then, the potential is integrated from the source to the exit of the duct $\mathcal{A}$. This potential is used to find both the "source" potential in the ducts $\mathcal{B}$ and $\mathcal{C}$ using the connection formula:

$$\begin{aligned}\boldsymbol{\phi}_{\mathcal{B}} = \left(Y_{\mathcal{B}} - G_{\mathcal{B}}^{\mathcal{C}} Y_{\mathcal{C}} G_{\mathcal{C}}^{\mathcal{B}} \right)^{-1} F_{\mathcal{B}}^{\mathcal{A}} Y_{\mathcal{A}} \boldsymbol{\phi}_{\mathcal{A}}, \\ \boldsymbol{\phi}_{\mathcal{C}} = G_{\mathcal{C}}^{\mathcal{B}} \boldsymbol{\phi}_{\mathcal{B}}.\end{aligned} \tag{4.15}$$

We can compute the acoustic potential in the ducts $\mathcal{B}$ and $\mathcal{C}$ with these values for the source.

4.1.4 Adaptation for mean flow computation

It was shown that the general multimodal approach of Chapter 2 could also be used to compute the base mean flow in section 2.2. The basic idea is that the equation that governs the acoustic propagation without base flow and at zero frequency is equivalent to the one that governs

the mean flow provided that the density is known. However, the acoustic computation becomes unstable when performed at zero frequency with a complex PML. Therefore, for computing the base flow with the multimodal, the PML is removed and a large outer radius is defined for the surrounding duct so that the flow at its outer wall approximately matches the free-field desired Mach number. The method of Section 2.2 is therefore used as such, except for one point described below.

Enforcing the term $(x_e + c^{\Phi})$ (in Equation (2.37)), which can be seen as the ratio between potential and axial velocity amplitudes associated with the "plane wave", is another issue to consider when dealing with flow computations (see section 2.2). For a single duct, this is not a problem as the potential is defined up to a constant. Thus, imposing this ratio only fixes the potential constant and has no impact on the results. However, in cases where multiple ducts are present, it becomes necessary to enforce this ratio at different axial locations. It must be done in the ducts $\mathcal{B}$ and $\mathcal{C}$ in our case (in order to find $Y_{\mathcal{B}}$ and $Y_{\mathcal{C}}$ at the junction location). While one of the two values can still be freely imposed to fix the potential constant, the other enforces a specific mass flow distribution between the three ducts. We then conduct a convergence process to determine the value of this second potential-to-velocity ratio required to ensure the desired mass flow distribution. One could use a random guess for the initial value, but this would be time-consuming. A good guess for this initial value can easily be obtained because the flow should be constant near the outer wall of the upper duct since we want to represent free-field conditions. Indeed, in the free field, the potential can be written $\Phi_\infty = U_\infty x + b_\infty$ where U_∞ is the free-stream axial velocity (defined by the user) and b_∞ a constant. If the constant is fixed by choosing an arbitrary value for $c^{\Phi}_{\mathcal{B}}$ in duct $\mathcal{B}$, then the initial guess of the potential-to-velocity ratio in duct $\mathcal{C}$ is $(x^{\mathcal{C}}_e + c^{\Phi}_{\mathcal{B}})$. Finally, the convergence process on this second ratio stops when the Mach at the end of duct $\mathcal{C}$ equals M_∞.

4.2 Validation

4.2.1 Engine geometry

The CFM56 engine defined in Section 2.3.1 is used for the validation. However, only the internal part of the nacelle is available, and for performing acoustic radiation calculations, the complete geometry representation is required. This geometry cannot be described as a one-dimensional function as previously. A fictive but realistic nacelle has been designed and is stored on the author's GitHub (https://github.com/brumann/CFM56-geometry). Note that the

internal part of the nacelle respects the 1D function previously given in Equation (2.38) (for the exit of the nacelle piecewise-cubic interpolator matching values and first derivatives were used).

A y-slice of the nacelle is given in Figure 4.3.

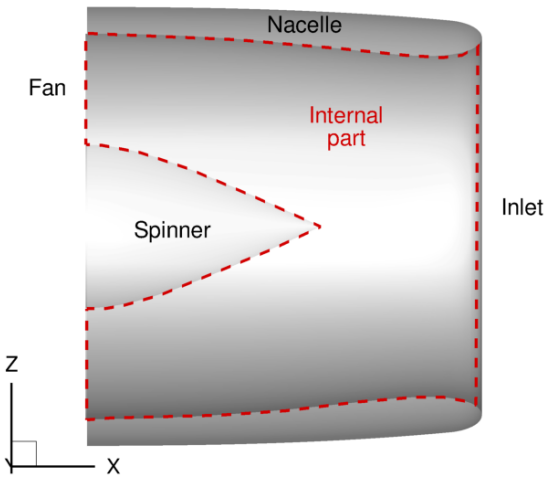

Figure 4.3 – Overview of the nacelle.

4.2.2 Validation methodology

The validation is again done using the FEM (defined in Section 2.3.2) which computes both the steady potential flow and the acoustic field. Note that here, the free-field boundary condition is defined using ray theory approximation [43]. An example of a mesh for a full intake is shown in Figure 4.4.

Regarding the multimodal method, as the problem is axisymmetric, a single Fourier mode in the circumferential direction is used. Chebyshev functions are used in the radial direction. In the axial direction, an axial mesh density equal to 0.5 in the ducts $\mathcal{A}$ and $\mathcal{C}$ is used, and 100 points ($0.25 < D_{ex} < 0.5$ for all cases) are used in the duct $\mathcal{B}$ (where the mesh criterion can be relaxed because there are minor flow changes and no wall variation). The numerical parameters used in all ducts for the mean flow and acoustic computations are summed up in Table 4.1. All the following acoustic computations take between 20 and 60 seconds with these parameters.

The nacelle is placed inside a mean flow with a free-stream Mach number of $M_\infty = -0.2$ and density $D_\infty = 1$, while at the source plane, the Mach number is $M_s = -0.5$. The tip radius of the outer duct is 3 (chosen large enough to ensure that it does not affect the in-duct flow). For all cases studied below, the incident duct mode is defined at the source plane such that the RMS pressure at the injection equals one at the outer wall.

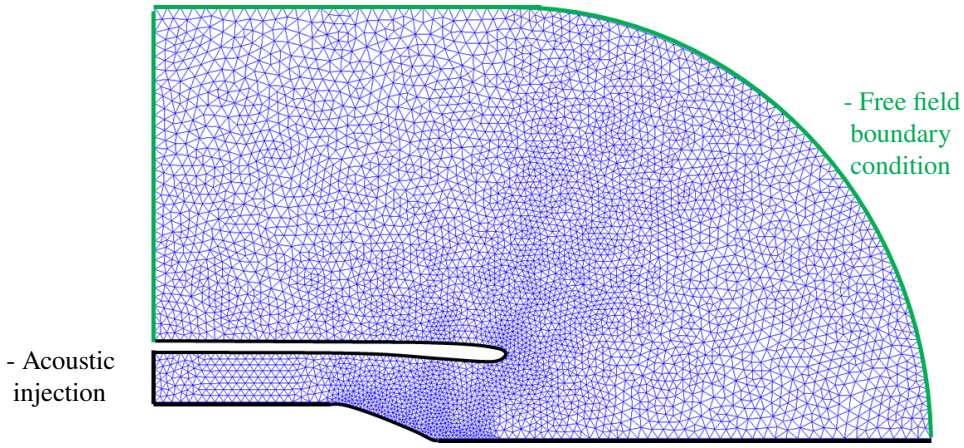

Figure 4.4 – Example of mesh used for free-field computations with the PFE solver (under-meshed for the sake of visibility).

	Duct $\mathcal{A}$	**Duct $\mathcal{B}$**	**Duct $\mathcal{C}$**	**PML definition**
Mean flow	25 polynomials	200 polynomials	25 polynomials	—
Acoustics	50 polynomials	150 polynomials	100 polynomials	$\delta = 0.5,\ \overline{\alpha} = \exp(\mathrm{i}\pi/4)$

Table 4.1 – Summary of the multimodal computation parameters.

4.2.3 Flow results

The computation can be directly carried out using the formulation derived in the section 4.1. However, this does not offer any significant advantage compared to finite element methods. In particular, the flow computation would be time-consuming due to the need for many polynomials in the duct $\mathcal{B}$ to represent the strong velocity gradient near the stagnation point that appears near the nacelle lip. Therefore, the flow is assumed to be incompressible in the duct $\mathcal{B}$, and the admittance does not vary and only needs to be computed at one single axial location (constant cross-section and no density variation). With this hypothesis, the time taken for the flow computation is similar to the one of an in-duct computation.

Three flow computations are conducted, including one with the FEM code and two with the multimodal code. The first multimodal computation is performed without assuming an incompressible flow inside the duct $\mathcal{B}$ to demonstrate the method's ability to compute the precise mean flow. The second one is done with the simplification hypothesis to check its validity. Figure 4.5 displays the axial velocity contours obtained from these three computations.

The small discrepancies between the FEM and exact multimodal computation can be at-

tributed to different definitions of the boundary conditions. In the multimodal method, we assume an hard walled boundary condition at the outer wall, while in the FEM, the velocity value is fixed. The differences between the fully compressible and partially incompressible multimodal computations, only visible in duct $\mathcal{B}$, are minor and are not expected to affect acoustic computations. In contrast, there are major differences regarding the calculation time, with the partially incompressible one running in around 10 seconds while the exact one took around 400 seconds to compute the base flow. Therefore, we only use the flow field resulting from the partially incompressible multimodal computation in the following.

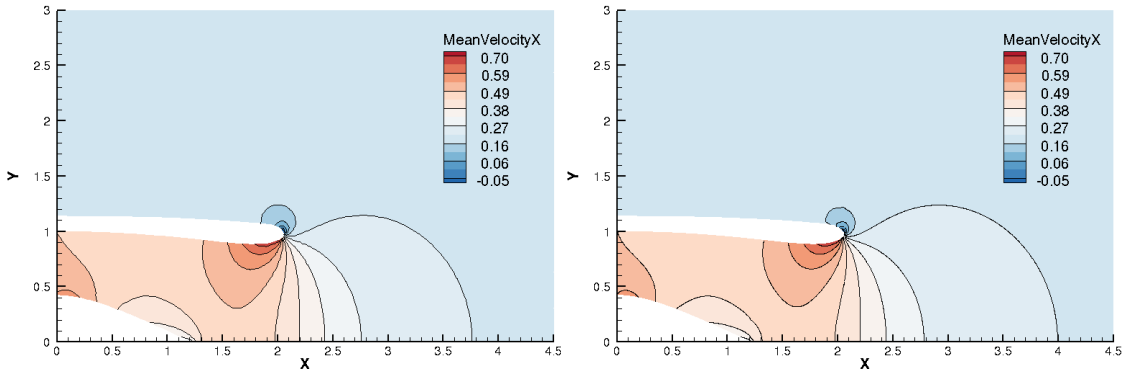

(a) Finite element method

(b) Multimodal

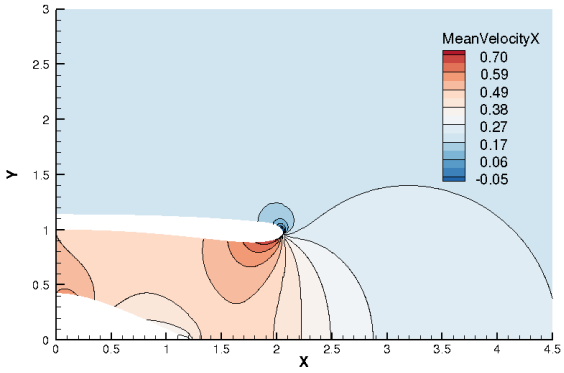

(c) Multimodal with incompressible flow in duct $\mathcal{B}$

Figure 4.5 – Contours of mean axial velocity for $M_s = -0.5$ and $M_\infty = -0.2$.

4.2.4 Acoustic results

Some qualitative acoustic results are given to assess the multimodal method's capability with a PML to represent the radiation condition in the presence of mean flow. The simplified flow is interpolated onto the acoustic grid for multimodal computations. As for the in-duct case in Section 2.3, the axial grid points used in the multimodal calculations of the mean flow differ from those used in the multimodal calculation of the sound field. So, for each duct, the vectors $\mathbf{\Phi}(x)$ and $\mathbf{U}(x)$ are interpolated onto the axial grid points needed for the acoustic calculation. For the FEM simulations which serve as a reference, the same grid is used for the flow and acoustics to avoid errors from grid interpolation.

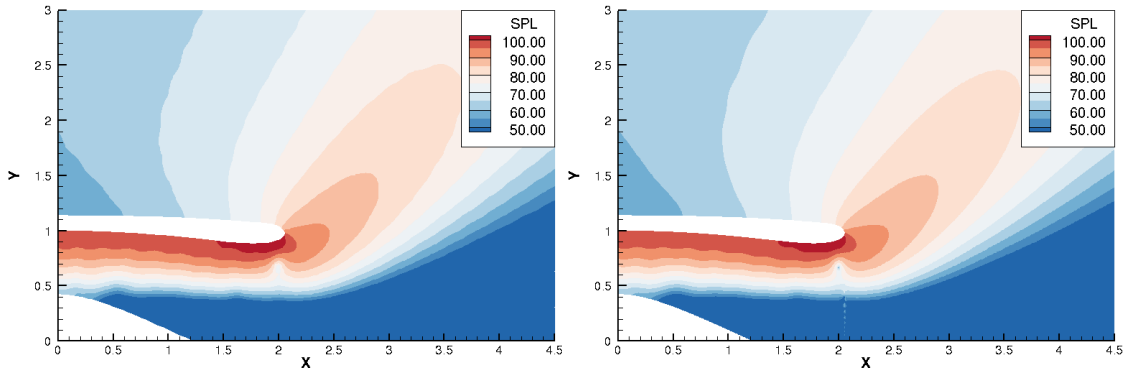

(a) Finite element method (b) Multimodal

Figure 4.6 – SPL pressure field for a mode $(m, n) = (10, 1)$ at $\omega = 15$.

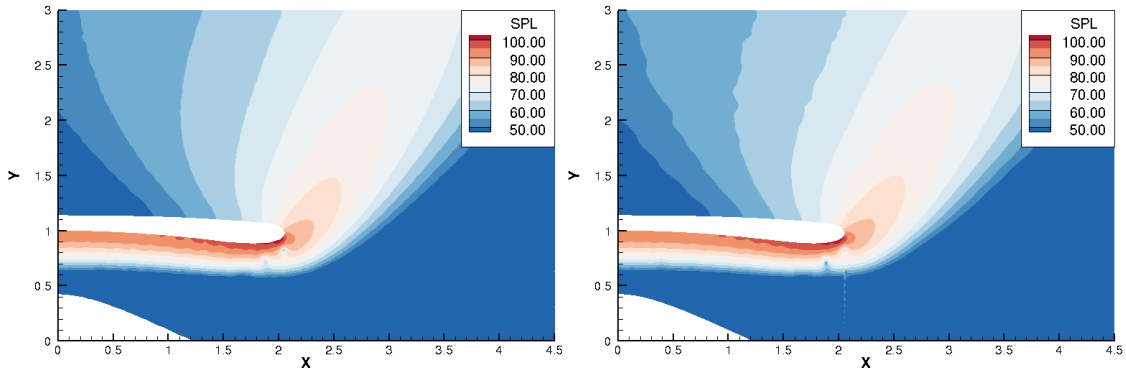

(a) Finite element method (b) Multimodal

Figure 4.7 – SPL pressure field for a mode $(m, n) = (25, 1)$ at $\omega = 30$.

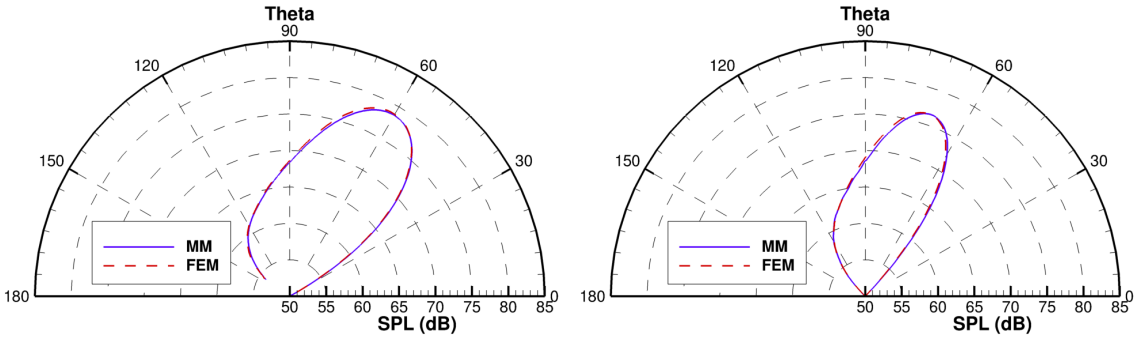

(a) $(m, n) = (10, 1)$ at $\omega = 15$ (b) $(m, n) = (25, 1)$ at $\omega = 30$

Figure 4.8 – SPL directivity for the modes $(m, n) = (10, 1)$ at $\omega = 15$ and $(m, n) = (25, 1)$ at $\omega = 30$.

Figures 4.6 and 4.7 depict the sound pressure level (SPL) in dB for the injected modes $(m, n) = (10, 1)$ at $\omega = 15$ and $(m, n) = (25, 1)$ at $\omega = 30$, obtained using the multimodal method and FEM. The two methods yield similar results. In Figure 4.6, non-physical perturbations can be seen at the junction level ($x = -2.05$). These perturbations arise due to the appearance of high-order modes generated by the poorly conditioned junction matrices. This conditioning issue comes from the weak singularity of the derivative of the radial acoustic velocity at the inlet. However, these spurious fluctuations are quickly attenuated and seem not to propagate.

Figure 4.8 shows the SPL directivity for the two previously studied test cases. The directivity is computed on an arc located at a distance of 2 from the engine exit, with 0° corresponding to the forward direction. We use the term "quiet zone" to refer to the area near the engine axis where the SPL is low (below 50 dB). Despite the flow hypothesis used in the multimodal method, the radiation pattern given by the method is accurate for both modes, which validates the chosen approach. Note that, as expected for modes close to the transition, the radiation pattern presents one main lobe directed towards the forward arc with a large quiet zone (peak radiation near 60° and 70°). Investigating if the method also performs well when different acoustic parameters vary is now necessary.

4.2.5 Parametric study

Extensive work has been done to address the radiation from the engine intake, and several analytical models allow to derive some general trends on the impact of the different acoustic parameters on the radiated field (see for example [97] for cut-on modes and [10] for cut-off modes). In this context, a concise parametric study is conducted to corroborate these analytical

findings and validate the developed method.

4.2.5.1 Cut-on modes

In this section, we study the evolution of the directivity with regards to multiple parameters for injected modes which remain cut-on throughout the whole duct. The parameter study encompasses the variation of the nondimensionalized pulsation ω, the circumferential mode order m, and the radial mode order n. FEM computations are also performed to validate the results.

- **Influence of frequency**

The same mode orders as studied above, $(m, n) = (10, 1)$ and $(m, n) = (25, 1)$, are taken but the frequency is multiplied by 1.5 and 2 to evaluate the developed method for higher frequencies. The results are shown in Figure 4.9. Both methods produce consistent results. Note that the agreement is good for the azimuthal order $m = 10$ at all frequency but some minor differences are observed for the order $m = 25$ at high frequency. From a physical perspective, we observe that the directivity patterns maintain roughly the same peak SPL levels as the pulsation ω increases. But, at low frequencies, the directivity pattern is typically dominated by a single lobe, whereas at higher frequencies, additional lobes appear. This suggests that different radial modes contribute to the radiated field. This phenomenon can be explained by the creation of scattered radial modes within the duct that become cut-on for higher frequencies and thus contribute to the radiated field. Furthermore, we observe that the main radiation lobe is directed towards the forward-arc, which is an expected behaviour given that all modes are cut-on modes. It should also be noted that the size of the quiet zone decreases as the frequency increases, and the angle of the main lobe moves towards the engine axis.

- **Influence of radial order**

We start with both modes studied in the qualitative comparison in Section 4.2.4 and increase the radial order of the injected mode to check how the developed method reacts for high radial orders. For the frequency, a frequency where all the modes are cut-on is kept. We chose $\omega = 30$ for the azimuthal order $m = 10$ and $\omega = 45$ for the azimuthal order $m = 25$ and look at the first three radial orders. The results are shown in Figure 4.10. The results obtained using the proposed method are in good agreement with those obtained using the FEM for all radial orders. The first observation is a decrease in the number of lobes in the radiation pattern as the radial order increases. This result may initially seem counter-intuitive, but it can be explained by considering the distance to modal transition. For instance, for the azimuthal order $m = 10$, when the radial

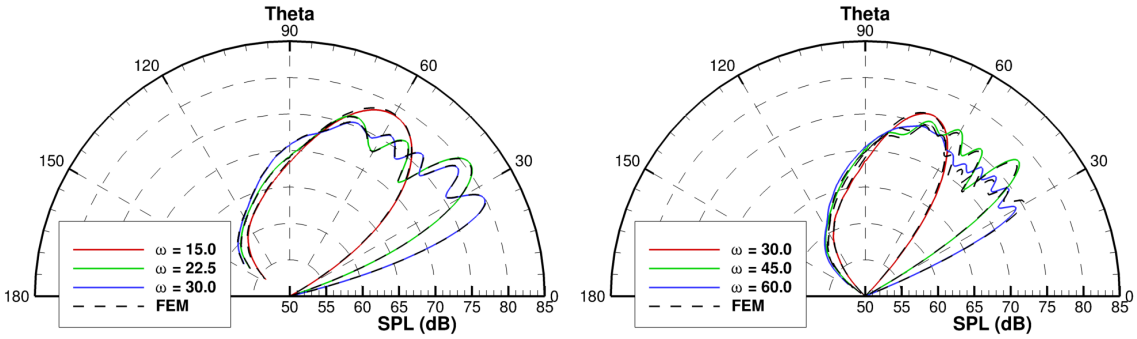

(a) $(m, n) = (10, 1)$ (b) $(m, n) = (25, 1)$

Figure 4.9 – SPL directivity evolution with the increase of the frequency.

order is $n = 3$, the mode is weakly cut-on, which results in a weak modal scattering [98]. As a result, we observe only three lobes in the directivity pattern. On the other hand, when the radial order is $n = 1$, the mode is well cut-on, and there is significant modal scattering inside the duct, which leads to the five observed main lobes. In addition, we note that the pressure levels are higher in the rear-arc for low radial orders. This behaviour can be attributed to the same reason. Indeed, the high-radial order modes generated by scattering mechanisms are weakly cut-on or cut-off, and therefore they tend to have higher levels in the rear-arc [10]. Note that the size of the quiet zone does not vary for the different radial orders.

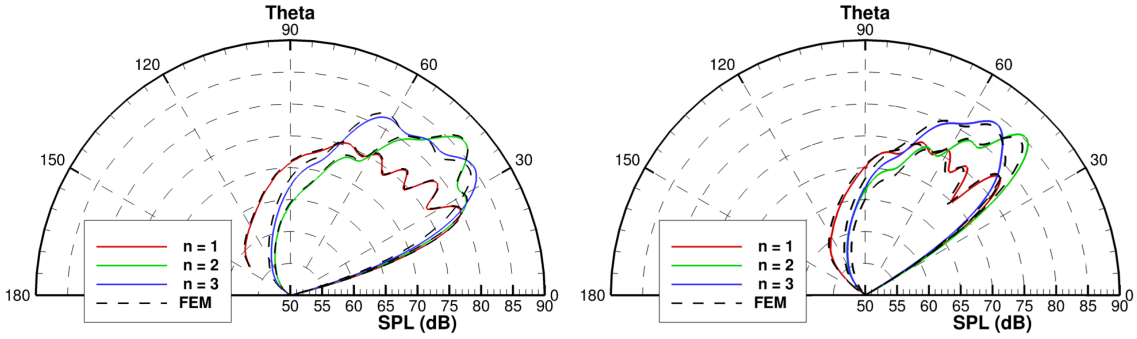

(a) $m = 10$ at $\omega = 30$ (b) $m = 25$ at $\omega = 45$

Figure 4.10 – SPL directivity evolution with the increase of the radial order.

- **Influence of azimuthal order**

The impact of the azimuthal order on how the developed method behaves is evaluated. The

radial order is kept constant and equals one. Three azimuthal orders are considered, $m = 10$, 20, 30 for the pulsation $\omega = 40$. The results are shown in Figure 4.11. Once again, the two methods agree on the directivity patterns. As the azimuthal wavenumber increases, the number of lobes in the radiation pattern decreases. These observations can again be explained by the distance to a modal transition. The further away from it, the more lobes are present in the radiation pattern and the smaller is the angle of the quiet zone. Moreover, as the azimuthal wavenumber order increases, the angle of the main lobe increases. Therefore, the effect of the azimuthal mode order is at the opposite of the one of the frequency.

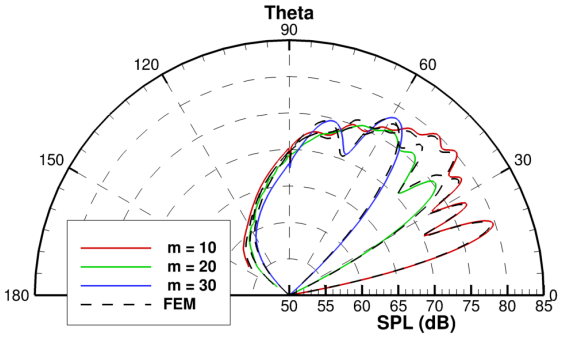

Figure 4.11 – SPL directivity evolution with the increase of the azimuthal order for $n = 1$ at $\omega = 40$.

4.2.5.2 Transition and cut-off modes

Since the injection is moved backward in the FEM computation, cut-off comparisons cannot be made as such. Therefore, the source amplitude is increased in the FEM computations to mitigate the exponential decay in this extended part. Here, various test cases where the mode is cut-off at the injection or encounters a cut-on/cut-off transition are studied. Both radial order and frequency evolutions are examined. The radial test cases are conducted at $\omega = 30$ for the azimuthal order $m = 10$, and the frequency test cases are conducted for a mode $(m, n) = (25, 1)$. First, for the azimuthal order $m = 10$, the studied radial order ranges from $n = 6$ to $n = 8$. $n = 6$ is cut-on while $n = 7$ encounters a double transition (cut-on/cut-off/cut-on) and $n = 8$ is cut-off in the whole duct. Then, for the azimuthal order $m = 25$, three different frequencies are tested: $\omega = 24.5$, 24.7 and 25. At $\omega = 24.5$ the mode encounters a transition at $X_t = 0.59$, for $\omega = 24.7$ at $X_t = 0.67$ and at $\omega = 24$ at $X_t = 0.80$. For these frequencies, the source amplitude is multiplied by 10^5 to avoid low SPL in the radiation pattern. The results are plotted in Figure 4.12. Both methods agree on the directivity pattern for all cases except for the challenging mode $(m, n) = (10, 8)$,

where we are close to the numerical precision. For the radial order evolution, apart from the exponential decay, scattering phenomena cause the injected mode to have almost no impact. The directivity pattern for the modes with radial order $n = 7$ and $n = 8$ is close to that of the mode with a radial order $n = 6$. This suggests that the directivity of transition and cut-off modes is not explicitly dependent on the radial order of the injected mode but rather depends on the closest cut-on mode. Note that this conclusion can be derived analytically for a constant cross-section duct by using the far-field directivity formulation derived by Gabard & Astley [99]. The impact of the frequency is not as clear. Only one lobe is observed in all cases, which comes from the fact that the injected mode radial order is $n = 1$ and that no cut-on mode that could alter the directivity pattern can be excited.

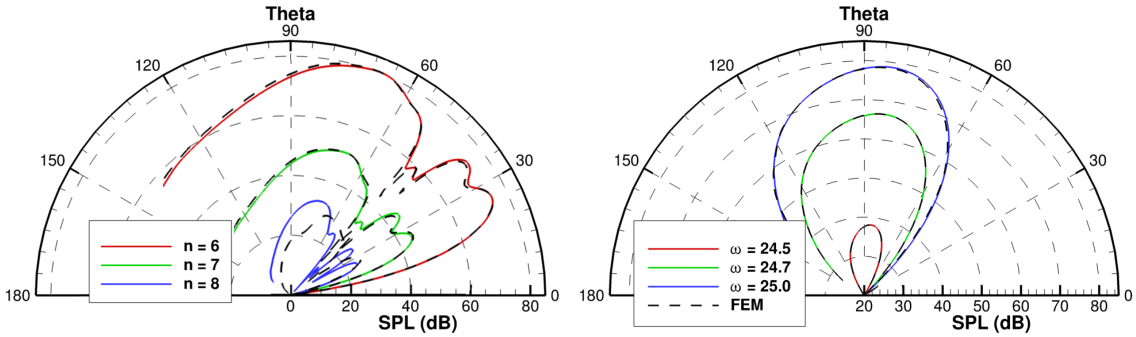

(a) Radial order evolution for $m = 10$ at $\omega = 30$ (b) Frequency evolution for $(m, n) = (25, 1)$

Figure 4.12 – SPL directivity of cut-off modes.

4.3 Conclusion

In this chapter, we have extend the multimodal method of Chapter 2 to compute the mean flow around an engine intake and the acoustic radiation with flow. This was achieved by surrounding the engine with a duct with a perfectly matched layer on the outer wall, rewriting the acoustic propagation equation inside this duct, and using connection formulas between the inner and outer ducts. An incompressible flow hypothesis was added in the free-field to improve the calculation time for the flow computations. This modification reduced by a factor of around twenty the calculation time without significantly impacting the acoustic results. With all of this, the proposed approach enables the efficient calculation of the radiated field. The advantage of the method, when compared to FEM, is not as important as for in-duct computations. Still, the

formulation was validated against FEM results for various frequencies and azimuthal modes and proved accurate in computing the mean flow and acoustic fields.

Chapter 5

Three-dimensional formulation: the impact of flow distortion

Although the general multimodal method developed in Chapter 2 (in-duct propagation) and Chapter 4 (free-field radiation) has previously been validated for axisymmetric flows, its applicability also extends to non-axisymmetric flows. Therefore, this chapter aims to apply it to evaluate the effect of azimuthal flow distortion generated by an angle of incidence on acoustic in-duct propagation and free-field radiation. An analysis of the shape of the azimuthal flow distortion impact is first performed in Section 5.1. Then, the modifications of the general multimodal method are addressed. While for the acoustic computations, the method of Chapters 2 and 4 is directly usable as before with the inclusion of multiple azimuthal modes in the basis functions, adjustments are required in the admittance boundary condition for mean flow prediction. These specificities are addressed in Section 5.2. They impose the use of the free-field radiation multimodal method to correctly represent the distortion generated by an angle of incidence. The method is then validated in Section 5.3. This validation process involves assessing the method for the flow against a finite volume solver that solves the steady Euler equations and for the acoustics against a finite difference solver that solves the linearized Euler equation. Furthermore, a one-dimensional model is introduced to enhance the analysis of the results. Finally, in Section 5.4, the analysis starts by examining the influence of liner effects in a distorted flow. Subsequently, the investigation delves into understanding how changes in engine length, as part of the transition to UHBR engines, impact the distortion's effects on acoustic propagation.

5.1 Description of the flow distortion

The general multimodal method developed in Chapter 2 imposes that the flow is potential. This hypothesis implies that $\nabla \times \mathbf{V} = \mathbf{0}$, and therefore:

$$\frac{\partial W}{\partial x} = \frac{1}{r}\frac{\partial U}{\partial \theta}, \quad \frac{1}{r}\frac{\partial rW}{\partial r} = \frac{1}{r}\frac{\partial V}{\partial \theta}, \quad \frac{\partial U}{\partial r} = \frac{\partial V}{\partial x}. \tag{5.1}$$

In the presence of azimuthal distortion, the term $\partial U/\partial\theta$ is not equal to zero and therefore the term $\partial W/\partial x$ is also non-zero. This implies that the flow needs to be three-dimensional and to vary in the axial direction. The hypothesis of purely axial uniform flow in constant duct formulations [53, 58] is therefore not applicable.

To have a first idea of the axial evolution of such a flow, a simplified flow distortion model is derived hereafter by considering the case of a constant narrow annular duct of radius R. The narrow duct imposes no radial variation of the flow so that the velocity can be simplified to $\mathbf{U} = (U(x,\theta), W(x,\theta))$. Let us assume that any mean flow variables A can be written in the form $A = A_0 + A_1(x)\cos(\theta)$ with $A_1 \ll A_0$. The mass conservation equation and the Equation (5.1) are used to write:

$$\frac{\partial DU}{\partial x} + \frac{1}{R}\frac{\partial DW}{\partial \theta} = 0 \text{ and } \frac{1}{R}\frac{\partial U}{\partial \theta} = \frac{\partial W}{\partial x}. \tag{5.2}$$

Combining both equations gives:

$$\left(1 - \frac{U_0^2}{C_0^2}\right)\frac{\partial^2 U_1}{\partial x^2} - \frac{1}{R^2}U_1 = 0. \tag{5.3}$$

The solutions to this equation are given by:

$$U_1 = \kappa \mathrm{e}^{-kx}, \tag{5.4}$$

where $k^{-1} = \sqrt{1-(U_0/C_0)^2}R$, and κ is a constant. This means that the distortion decreases exponentially inside such a duct under the potential flow restriction. Note that the same solution had already been given by Guérin [7] but no details on the derivation were given.

The transpositions of these observations to a realistic engine geometry are investigated using available RANS simulations of an UHBR engine. The details of this analysis are provided in Appendix E. The numerical simulations demonstrated that the flow rotational is indeed equal to zero outside the boundary layers, which validates the potential flow hypothesis. Moreover, two key findings emerge from this analysis:

— the distortion levels decrease sharply inside the engine (almost exponentially), which is in agreement with the evolution predicted by Equation (5.4);

— the mean flow can be decomposed into a limited number of azimuthal components.

These observations demonstrate that the slowly varying hypothesis for the mean flow of multiple-scale methods is not met and explain why directly applying the general formulation of [66] cannot work.

5.2 Accounting for azimuthal flow distortion in the multimodal method

5.2.1 Specifities for mean flow computation

It has been shown above that the flow distortion varies axially by using both mathematical and empirical analyses. Therefore, for computing the mean flow with the multimodal method, it is not possible to use the classical hypothesis of infinite duct termination with uniform flow by simply imposing a constant c^{Φ} in the term $\mathbf{w}_0^{\Phi}$ (see Section 2.2.2). Two solutions arise to address this issue for in-duct computations.

The first one uses the fact that the distortion decreases exponentially inside the air inlet. Therefore, it can be assumed that the flow becomes 2D at the fan position if the intake is sufficiently long. In that case, the resolution of the flow can be reverted, with the standard admittance condition imposed at the fan plane (step 1 of Figure 2.1). However, as the potential distribution (step 3 of Figure 2.1) has to be specified at the engine exit, a prior knowledge of the distortion shape is required. In addition, this approach can hardly be used for radiation calculation where two potential-to-velocity ratios must be enforced.

For the second solution, adopted in this thesis, a sketch of a generic turbofan and the associated wave-guide problem when there is an incoming flow with incidence is first depicted in Figure 5.1. This solution involves modifying the radial boundary condition of the outer duct to mimic a duct where the flow is under incidence but does not vary axially. To do so, instead of imposing $\nabla\Phi = \partial\Phi/\partial r = 0$ at the outer wall, the condition $\partial\Phi/\partial r = \tan(\alpha_{AoA})\sin(\theta)\partial\Phi/\partial x$ is applied, where α_{AoA} is the angle of attack of the flow. In such a duct $\mathcal{D}$, the potential can be found analytically and is given by:

$$\Phi_{\mathcal{D}}(x, r, \theta) = U_\infty x + \left(r + \frac{R_1^2}{r}\right)\frac{R_2^2}{R_2^2 - R_1^2} U_\infty \tan(\alpha_{AoA})\sin(\theta) + c_{\mathcal{D}}^{\Phi}. \tag{5.5}$$

By projecting this expression onto the Fourier-Chebyshev basis, we obtain the term $\mathbf{w}_0^{\Phi}$ of the admittance at the exit of the duct. This can be performed in both ducts $\mathcal{B}$ and $\mathcal{C}$ with the procedure detailed in Section 4.1.4 to determine the two associated constants $c_{\mathcal{B}}^{\Phi}$ and $c_{\mathcal{C}}^{\Phi}$.

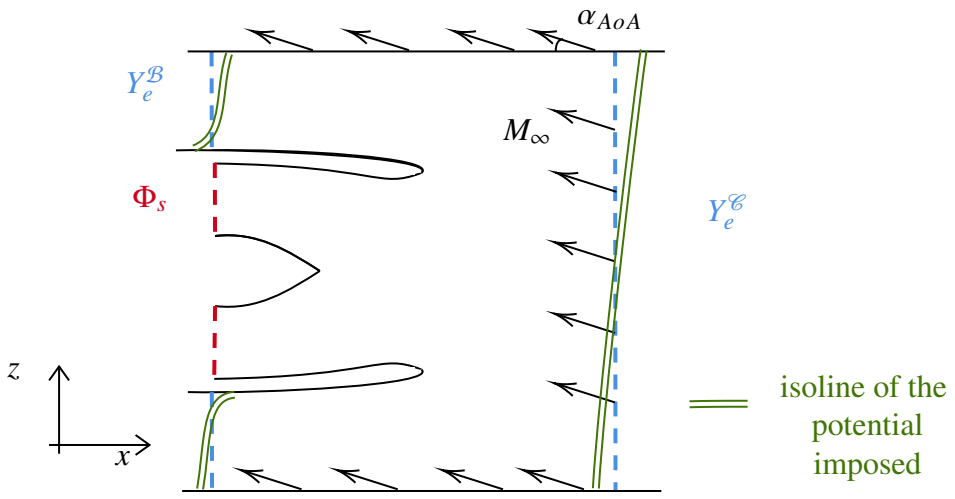

Figure 5.1 – Schematic of the computational domain in a case with distortion.

5.2.2 Coupling between the azimuthal orders

When the general multimodal method was introduced earlier in Chapter 2, the multimodal matrices were derived in a general context (these matrices can be found in Appendix A). A quick focus is made here to understand how they are modified in the presence of distortion, and to see how different azimuthal orders are coupled. Consider for instance the matrix A_{11}, which is expressed as follows:

$$(A_{11})_{ij} = \int_S D(1-M^2)\varphi_j \varphi_i^* \mathrm{d}S. \tag{5.6}$$

For the variables i and j, we associate two sets of variables (m_i, p_i) and (m_j, p_j) respectively such that:

$$\varphi_i = f_{p_i}(r)e^{-\mathrm{i}m_i\theta} \text{ and } \varphi_j = f_{p_j}(r)e^{-\mathrm{i}m_j\theta}, \tag{5.7}$$

where $f_p(r) = \left(\frac{r}{R_2-R_1}\right)^{\min(|m|,1)} T_p\left(\frac{r-R_1}{R_2-R_1}\right)$. The hypothesis that the mean flow can be decomposed into a limited number of azimuthal components is used to express $D(1-M^2)$ as powers of $e^{\mathrm{i}\theta}$, such that:

$$D\left(1-M^2\right) = \left[D\left(1-M^2\right)\right]_{-1}(x,r)e^{\mathrm{i}\theta} + \left[D\left(1-M^2\right)\right]_{0}(x,r) + \left[D\left(1-M^2\right)\right]_{1}(x,r)e^{-\mathrm{i}\theta}, \tag{5.8}$$

where $\left[D\left(1-M^2\right)\right]_{l\in[\![-1,1]\!]}$ are the coefficients of the Fourier expansion. Then, Equation (5.6) transforms into:

$$\begin{aligned}(A_{11})_{ij} = &\int_{r=R_1}^{R_2}\int_{\theta=0}^{2\pi}\left[D\left(1-M^2\right)\right]_{-1}(x,r)f_{p_j}(r)f_{p_i}(r)e^{\mathrm{i}(m_i+1-m_j)\theta}\mathrm{d}S\\ &+\int_{r=R_1}^{R_2}\int_{\theta=0}^{2\pi}\left[D\left(1-M^2\right)\right]_{0}(x,r)f_{p_j}(r)f_{p_i}(r)e^{\mathrm{i}(m_i-m_j)\theta}\mathrm{d}S\\ &+\int_{r=R_1}^{R_2}\int_{\theta=0}^{2\pi}\left[D\left(1-M^2\right)\right]_{1}(x,r)f_{p_j}(r)f_{p_i}(r)e^{\mathrm{i}(m_i-m_j-1)\theta}\mathrm{d}S.\end{aligned} \tag{5.9}$$

This can then be simplified as:

$$(A_{11})_{ij} = \mathcal{D}_{-1}\delta_{m_i m_j-1} + \mathcal{D}_0\delta_{m_i m_j} + \mathcal{D}_1\delta_{m_i m_j+1}, \tag{5.10}$$

where $\mathcal{D}_l = 2\pi\int_{r=R_1}^{R_2}\left[D\left(1-M^2\right)\right]_l(x,r)f_{p_j}(r)f_{p_i}(r)r\mathrm{d}r$ and $l\in[\![-1,1]\!]$. This implies that A_{11} is a block tridiagonal matrix. The off-diagonal terms relate to transfer on adjacent Fourier functions, while the diagonal terms relate to the propagation of a single azimuthal Fourier component. It's worth noting that when $\mathcal{D}_{-1} = \mathcal{D}_1 = 0$, there is no azimuthal transfer and a 2D formualtion is recovered.

5.3 Validation in the presence of azimuthal flow distortion

5.3.1 Engine geometry

The CFM56 engine defined in Section 4.2.1 is used again to validate the mean flow prediction of the multimodal method in the presence of distortion. The same test cases as the ones performed in Section 4.2 are run, but the nacelle is now assumed to be under an incidence of 5° or 10°.

5.3.2 Validation methodology for the mean flow calculations

The FEM solver used up to now is limited to 2D cases. In this chapter, the mean flow is therefore computed using Onera's Computational Fluid Dynamics (CFD) solver *elsA*, which employs a cell-centered finite volume approach on multi-block structured meshes [100]. The solver, operated in Euler mode, solves the steady Euler equations. The fan is not simulated, and the flow is driven by all external boundaries, including total pressure and temperature in the far-field, along with static pressure at the fan plane. A flow angle is also imposed on the

far-field boundary condition. The domain consists of approximately 22 million grid points, and the simulations are run using 200 cores and last for approximately five hours.

For the multimodal solver, the same number of Chebyshev polynomials as for the 2D case is used for the radial discretization (see Table 4.1). In the azimuthal direction, the hypothesis that the mean flow can be decomposed into a limited number of azimuthal components is used such that only the first azimuthal orders ($m = [\![-1, 1]\!]$) are employed. Note that the incompressible flow hypothesis inside duct $\mathcal{B}$ is retained. With these parameters, the flow computations took approximately 150 seconds for each angle.

5.3.3 Mean flow results

Slices of the flow axial velocity predicted by the multimodal method and the CFD solver are illustrated in Figure 5.2 for the large angle of incidence $\alpha_{AoA} = 10°$. The results obtained from both methods exhibit a good similarity, particularly within the duct. The velocity levels and the suction effect of the fan boundary condition are comparable. Furthermore, the incidence of 10° is observed outside the nacelle in both simulations, indicating that the multimodal solver can accurately recover the imposed angle of attack. In terms of flow characteristics, the vertical plane displays a lack of symmetry with regard to the central axis due to the angle of incidence. On the other hand, the symmetry of the flow is successfully recovered in the horizontal plane. However, it is important to note that the agreement between the solvers deteriorates outside the nacelle, as already observed for axisymmetric flow cases (Section 4.2.3). This discrepancy can be attributed to the incompressible flow assumption imposed in duct $\mathcal{B}$.

A more quantitative evaluation of azimuthal flow distortion is performed by computing the axial evolution of the Circumferential Distortion Coefficient (CDC) at different channel heights. This coefficient is defined as:

$$C_{CDC}(x, r) = \frac{\max_\theta(U(x, r, \theta)) - \min_\theta(U(x, r, \theta))}{2 \times \text{mean}_\theta(U(x, r, \theta))}. \tag{5.11}$$

The associated values are given in Figure 5.3, along with those of the 1D model of Equation (5.4) evaluated with R, U_0 and C_0 the radius and azimuthally-averaged flow values along a line at 95% of channel height. The angle of attack $\alpha_{AoA} = 5°$ case is added to strengthen the analysis. An excellent agreement is observed between the multimodal and the CFD simulations. The distortion inside the duct is accurately captured, including its strong variations in the axial direction. It is noteworthy that the exponential decrease is effectively observed. In addition, the 1D model captures the overall decrease of the distortion intensity but tends to overestimate it

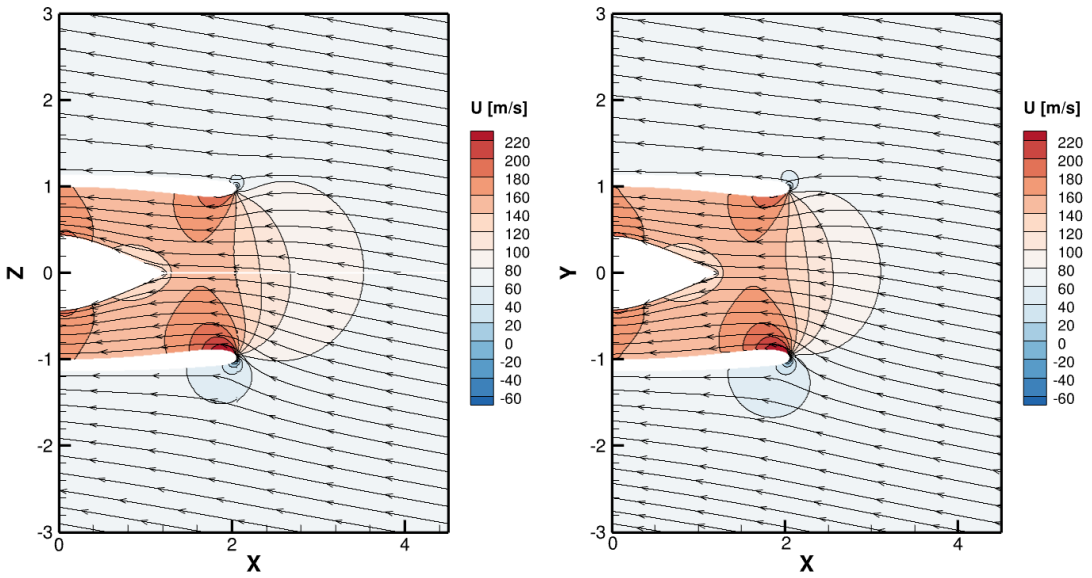

(a) Vertical plane – Multimodal

(b) Vertical plane – CFD

(c) Horizontal plane – Multimodal

(d) Horizontal – CFD

Figure 5.2 – Contour maps of mean axial velocity.

near the exit. In this region, strong flow gradients in the radial direction are present and make the thin annular duct formulation less accurate.

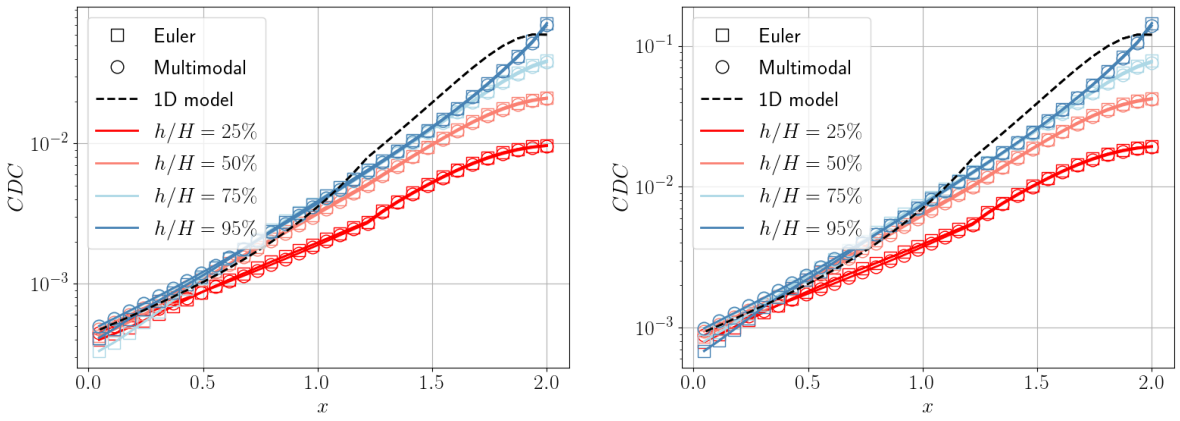

(a) $\alpha_{AoA} = 5°$ (b) $\alpha_{AoA} = 10°$

Figure 5.3 – CDC associated to the axial velocity in the duct intake.

5.3.4 Derivation of distorted mode shapes for low levels of distortion

In order to support the discussion of the acoustic results that will be presented later, we propose an analytical model for predicting the shape of modes in a duct with low levels of distortion.

This extension is based on the analytical solution introduced by Sofrin [53, 54], which examines mode shapes in a thin annular duct with flow distortion. In this model, the distortion does not vary axially, the axial velocity is written $U = U_0 + U_1 \cos(\theta)$ and the density and speed of sound are uniform. The flow is not potential so that Equation (1.11) should be solved. However, as $\nabla \cdot (D\mathbf{v}_r) = 0$, the perturbation velocity potential and vortical parts remain uncoupled and the Goldstein propagation Equation (1.13) can be solved. With the previous formulation of U it writes:

$$-k^2\phi + 2ikM\frac{\partial \phi}{\partial x} + M^2\frac{\partial^2 \phi}{\partial x^2} = \Delta\phi. \tag{5.12}$$

Using an eigenvalue decomposition, Sofrin demonstrated that the transverse distorted modes can be represented using periodic Mathieu's functions $\mathrm{ce}_{2m}(q, \theta/2)$ and $\mathrm{se}_{2m}(q, \theta/2)$, with ce_{2m} and se_{2m} are the even and odd Mathieu's functions of order m respectively, and $q = 4\mu M_1 \Omega_0 R_2^2$, where $\Omega_0 = k - \mu M_0$, $M_0 = U_0/C_0$, $M_1 = U_1/C_0$, and μ corresponds to the axial wavenumber in the absence of distortion. This is consistent with the observation made by Astley *et al.* [58] that the axial wavenumber of modes, modified theoretically by inflow distortion, appears to remain largely unchanged.

In the present work, we propose to reformulate the solution to Goldstein propagation equation

for an annular duct, by considering radial variations in addition to Sofrin's results. We express the acoustic potential as:

$$\phi = T(r,\theta)\,\mathrm{e}^{-\mathrm{i}\mu x}, \tag{5.13}$$

where T is the transverse mode shape. Equation (5.12) is rewritten with the same distorted flow using the cylindrical coordinate as:

$$\frac{1}{C^2}\left(\mathrm{i}\omega + U\frac{\partial}{\partial x}\right)^2 \phi = \frac{1}{r}\frac{\partial \phi}{\partial r} + \frac{\partial^2 \phi}{\partial r^2} + \frac{1}{r^2}\frac{\partial^2 \phi}{\partial \theta^2} + \frac{\partial^2 \phi}{\partial x^2}, \tag{5.14}$$

which can be written:

$$\mathcal{L}(T) = 0, \tag{5.15}$$

where the operator $\mathcal{L}$ is defined by $\mathcal{L} = \left(\Omega^2 - \mu^2\right) + \frac{1}{r}\frac{\partial}{\partial r} + \frac{\partial^2}{\partial r^2} + \frac{1}{r^2}\frac{\partial^2}{\partial \theta^2}$ and $\Omega = k - \mu M$. Since no obvious solution is available, the shape found in the azimuthal direction by Sofrin is used such that acoustic modes can be expressed as:

$$T_m = \mathrm{ce}_{2m}(\theta/2, qr^2)A_m(r), \tag{5.16}$$

where $q = 4\mu M_1 \Omega_0$ and $A_m(r)$ is the radial shape to be determined. We also assume that the distorsion amplitude is low ($C_{CDC} \ll 1$). With these assumptions, we insert the mode shapes (5.16) into Equation (5.15) and expand the terms up to order $O(C_{CDC}^2)$, resulting in:

$$\left(\Omega_0^2 - \mu^2\right)\mathrm{ce}_{2m}A_m + \frac{1}{r}\frac{\partial}{\partial r}\left(\frac{\partial A_m}{\partial r}r\right)\mathrm{ce}_{2m} + 4q\frac{\partial A_m r}{\partial r}\frac{\partial \mathrm{ce}_{2m}}{\partial x_2} - \frac{(2m)^2}{4r^2}\mathrm{ce}_{2m}A_m = O(C_{CDC}^2). \tag{5.17}$$

When $m \gg 1$, $\dfrac{\partial \mathrm{ce}_{2m}}{\partial x_2}/\mathrm{ce}_{2m} \ll 1$ [101] and the equation for A_m simplifies into a Bessel's equation. The same procedure can be applied to the odd Mathieu's function se_{2m}, which yields:

$$T_{mn} = N_m(\mathrm{J}_m(\alpha_{mn}r) + \Gamma_{mn}\mathrm{Y}_m(\alpha_{mn}r))\ (\mathrm{ce}_{2m}(\theta/2, qr^2) + \mathrm{ise}_{2m}(\theta/2, qr^2)), \tag{5.18}$$

with α_{mn} and Γ_{mn} defined in Section 1.3.1.1.

For low levels of distortion and high azimuthal orders, this approximation can be used to estimate the shape of acoustic modes without the need for computationally expensive simulations. However it cannot include axial variations of the geometry nor the flow.

5.3.5 Validation methodology for the acoustic calculations

The only 3D solver able to perform acoustic validations during the thesis is the Onera's in-house code *sAbrinA* [102, 103, 48]. It solves, through finite differences, the linearized Euler equations (1.10) in the time domain on a structured multi-block grid. The modes are injected in the source plane using a source model that allows reflected waves to cross the source [104]. Note that the results from this solver and the ones of the multimodal method are not expected to be in perfect agreement because different equations are solved.

In addition, great care needs to be taken for these time domain simulations, for three general reasons, detailed in [105]. First, when the injected mode at the source plane is close to a cut-off frequency, the response of the overall system is very sensitive to parameter changes. As a consequence, even small numerical errors can have a significant impact on the results, so the mesh needs to be sufficiently refined. Then, when the injected mode encounters a transition inside the intake, the particularly low group velocity of the mode close to its cut-off frequency makes the convergence time very long. Finally, in cases where trapped modes are present, an infinite number of reflections can arise, and the time necessary to get a balance between the right- and left-travelling waves can be huge. For all these reasons, at least 100 periods associated to the source frequency are simulated before extracting the results.

The mesh is designed such that they are at least 15 points per acoustic wavelength in the axial direction. In the azimuthal direction, a minimum of $20 \times m$ points, with m representing the highest anticipated azimuthal order in the calculation, is ensured. To numerically dissipate acoustic waves far from the nacelle, a geometrical progression with a factor of 1.03 is applied on grid size in both the axial and radial directions. In practice, only one mesh is designed that satisfies the most restrictive test case. The number of points is about 140 million cells, and each simulation is run using 800 cores and last several days. For illustration, Figure 5.4 shows longitudinal cuts of this mesh in a mid-nacelle plane. Notably, the figure highlights the local mesh refinements near the nacelle wall.

For the multimodal method, as in Section 4.2.2, an axial mesh density $D_{ex} = 0.5$ in ducts $\mathcal{A}$ and $\mathcal{C}$ is prescribed, while 100 points are used in duct $\mathcal{B}$. In the duct $\mathcal{B}$ and $\mathcal{C}$, 60 polynomials are used in the radial direction, and 20 for the duct $\mathcal{A}$. In the three ducts, 25 Fourier components are used. These parameters are summed up in Table 5.1.

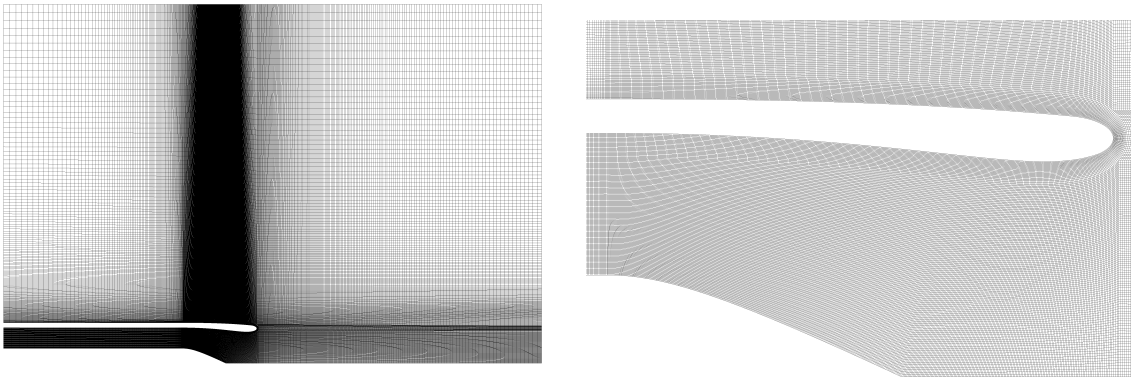

Figure 5.4 – Cuts of the mesh used for the acoustic computations with the *sAbrinA* solver: full mesh on the left, focus around the intake lip on the right.

	Duct $\mathcal{A}$	**Duct $\mathcal{B}$**	**Duct $\mathcal{C}$**
Number of polynomials	20	60	60
Number of Fourier components	25	25	25

Table 5.1 – Summary of the multimodal computation parameters for the distortion case.

5.3.6 Acoustic results

The impact of flow distortion on acoustic radiation is only assessed on the lower incidence case ($\alpha_{AoA} = 5°$). The same test cases as the ones with axisymmetric flow are investigated (refer to Section 4.2).

5.3.6.1 First qualitative observations

Figures 5.5 and 5.6 depict the SPL in dB for the injected modes $(m, n) = (10, 1)$ at $\omega = 15$ and $(m, n) = (25, 1)$ at $\omega = 30$, obtained in the horizontal and vertical planes using the multimodal and the finite difference methods. The overall results are similar and agree on the overall impact of the distortion. The radiation appears to exhibit near-y-symmetry, which can be attributed to the symmetry of the flow over the horizontal plane. However, as the mode rotates, the symmetry is altered, and this is particularly visible for the mode $m = 25$. Conversely, the field is far from z-symmetry because of flow distortion, as the pressure radiation is shifted toward the ground. Discrepancies between the two solvers are observed. Particularly, near the exit of the nacelle, the two solvers exhibit different SPL values. Additionally, in the duct, the FDM solver shows some

high SPL values near the central axis, which are considered numerical errors that the solver fails to dissipate. Regarding the directivity, it appears to be accurate for the case $m = 10$, but significant discrepancies are observed for the case $m = 25$. The main lobe's direction in each slice is identical for the latter, but the lobes appear flattened in the FDM. Two main reasons can explain these differences. Firstly, these modes are close to the transition (radiation towards 90°), which is particularly challenging to compute for the FDM code as mentioned in Section 5.3.5. Then, it should be recalled that the two methods solve different equations (Goldstein propagation equation for the multimodal method, linearized Euler equation for the finite-difference method).

5.3.6.2 Free-field comparisons

More quantitative comparisons are made in Figure 5.7 where SPL directivities of the two modes are plotted. Note that the directivites are provided in both the vertical and the horizontal planes as the axisymmetry is lost. The results in cases where the angle of attack is set to 0° (referred to as multimodal 2D) are also included. Both methods provide consistent results regarding the effects of distortion. First, a change in the angle of the main radiation lobes is observed. This distortion effect is particularly visible on the vertical plane for both cases where the radiation is moved downward with a shift of approximately 10°. Interestingly, a shift is also visible in the horizontal plane for $m = 25$. Despite this, it is observed that the amplitudes of the radiation lobes are close to those of the axisymmetric case over both the horizontal and vertical planes. It is also worth noting that there are more lobes in the upper part, while the lower part tends to have one single lobe.

Two main mechanims explain the tendency of a mode to radiate to one direction or another: diffraction and refraction [32]. A representation of these effects is given in Figure 5.8. Diffraction represents the tendency of an acoustic mode to stick to a solid surface. Refraction denotes the modification of the propagation direction of an acoustic mode caused by mean flow gradients. The modification of the radiation angle in cases with distortion can be easily explained by this flow refraction effect. On the lower part of the nacelle, the intense flow distortion causes higher velocity gradients near the wall. As a result, the propagation speed, which can be approximated by the speed of sound minus the flow velocity, is significantly reduced near the wall. This leads the wavefront to rotate away from the engine axis, causing the radiation to move toward the ground. In the upper part, as the distortion is anti-symmetric, the impact is the opposite and the radiation moves toward the engine axis, which again causes the overall radiation to move toward the ground. This explains the radiation pattern in the vertical plane but ignores that the

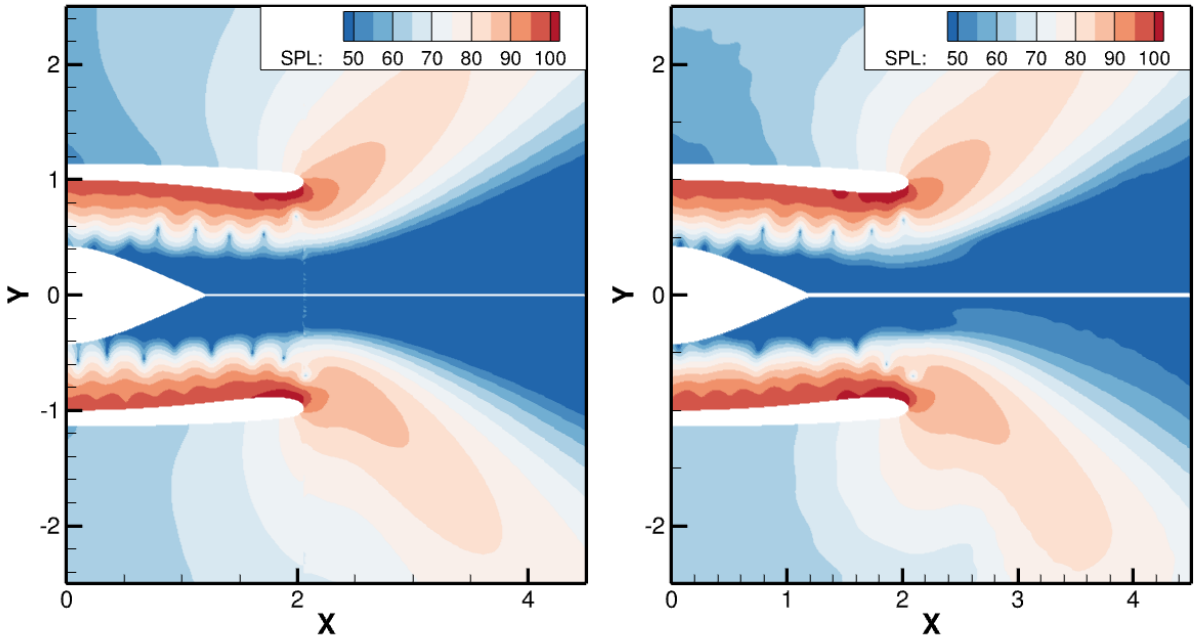

(a) Horizontal plane – Multimodal

(b) Horizontal plane – Finite difference method

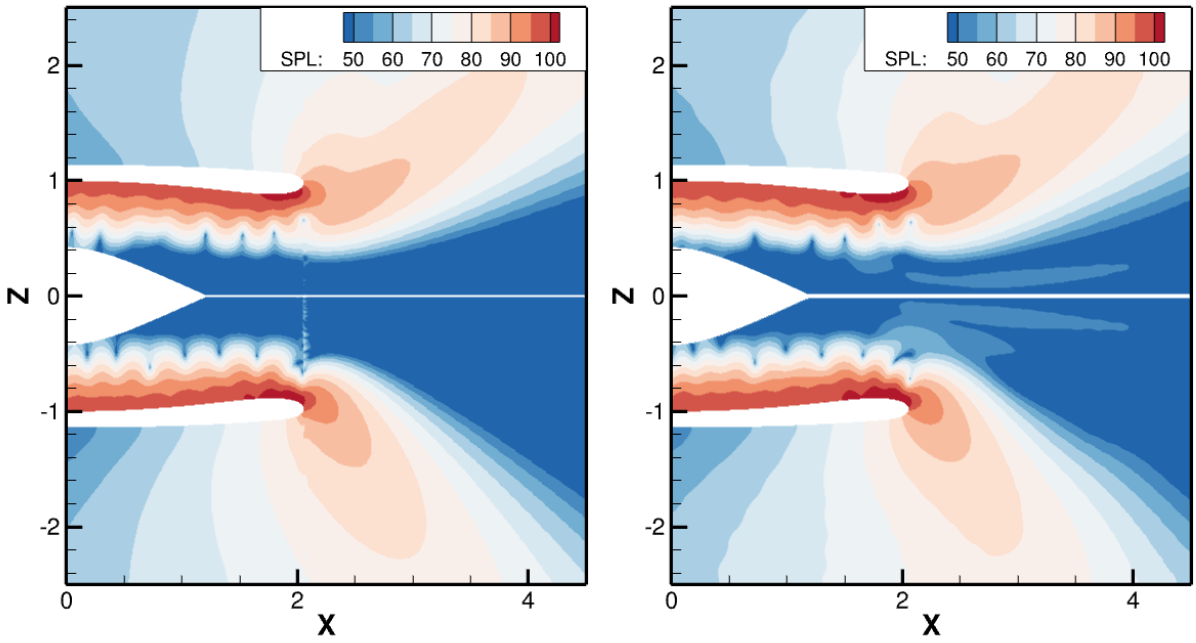

(c) Vertical plane – Multimodal

(d) Vertical plane – Finite difference method

Figure 5.5 – SPL for the mode $m = 10$ for the case $\alpha_{AoA} = 5°$.

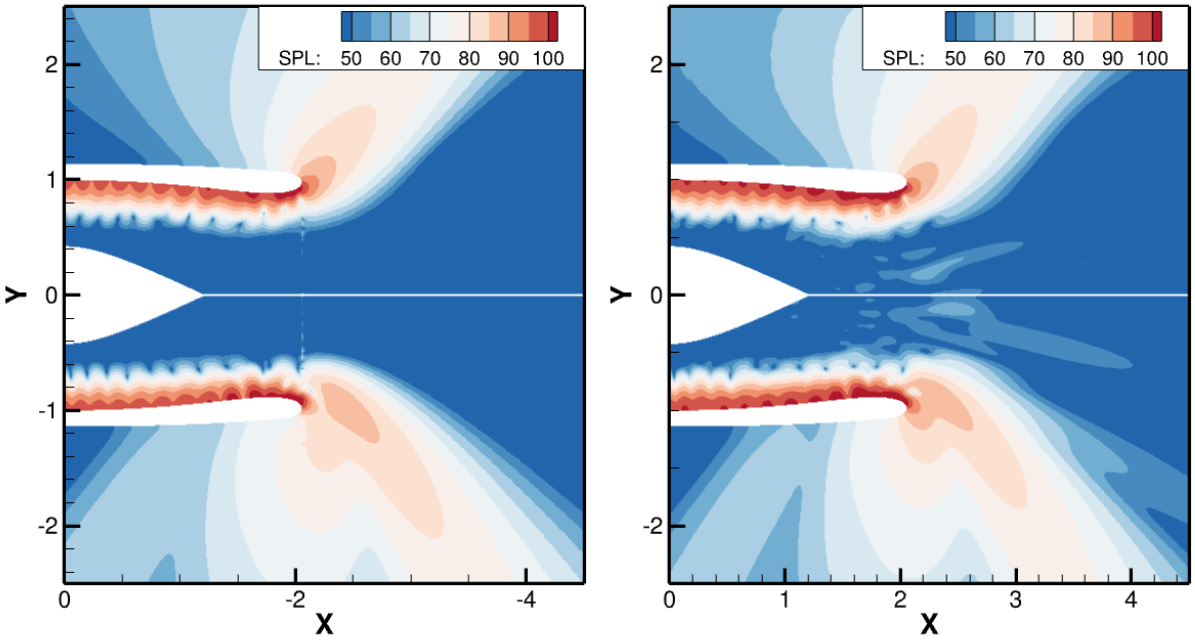

(a) Horizontal – Multimodal

(b) Horizontal – Finite difference method

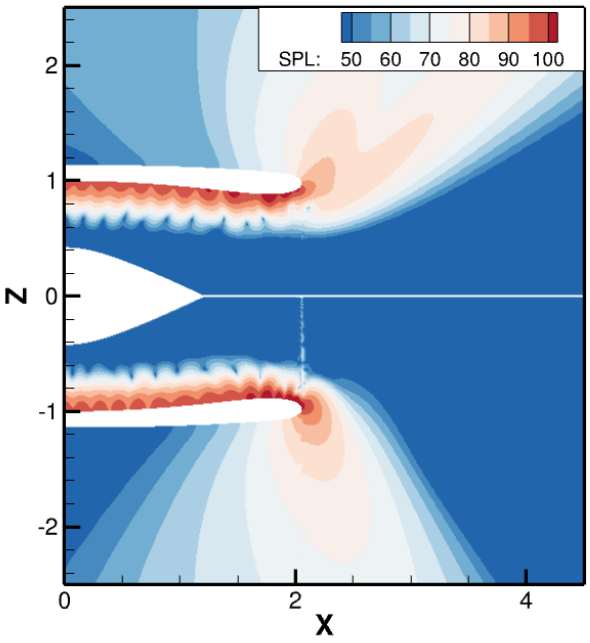

(c) Vertical plane – Multimodal

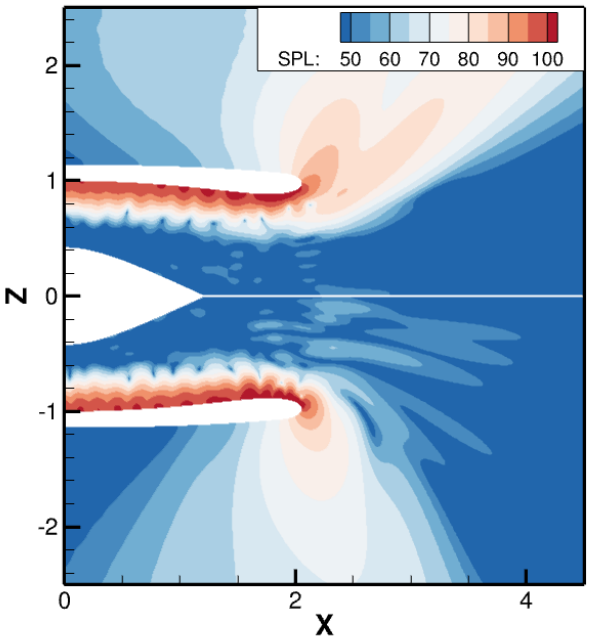

(d) Vertical plane – Finite difference method

Figure 5.6 – SPL for the mode $m = 25$ for the case $\alpha_{AoA} = 5°$.

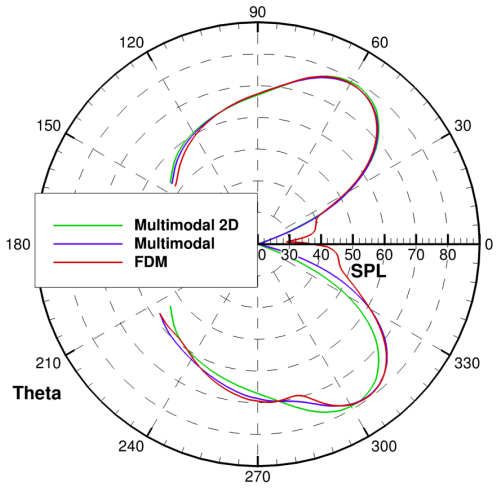

(a) Horizontal – Injected mode $(m, n) = (10, 1)$ at $\omega = 15$

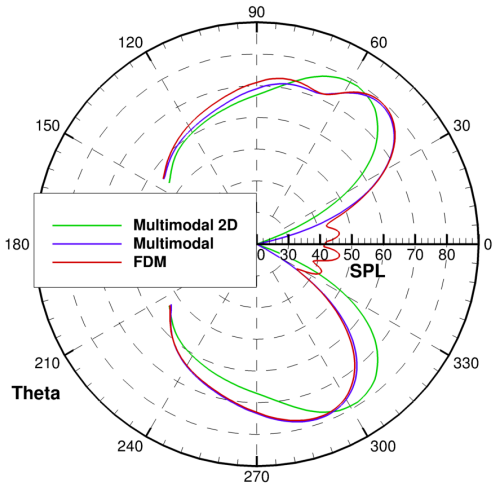

(b) Vertical plane – Injected mode $(m, n) = (10, 1)$ at $\omega = 15$

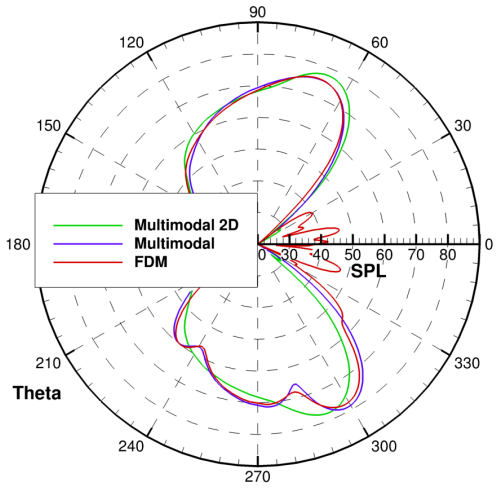

(c) Horizontal – Injected mode $(m, n) = (25, 1)$ at $\omega = 30$

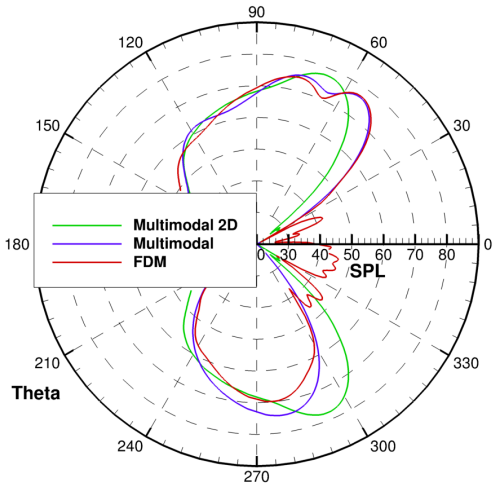

(d) Vertical plane – Injected mode $(m, n) = (25, 1)$ at $\omega = 30$

Figure 5.7 – SPL directivity for the case with $\alpha_{AoA} = 5°$.

tridimensionality of the flow and the rotation of acoustic modes. Indeed, when accounting for, the refraction effect remains valid beyond the vertical plane. If the acoustic mode propagates through a region with higher velocity (lower part of the engine) before radiating outside the nacelle, its directivity therefore shifts away from the engine axis. Conversely, if it propagates in a region with lower velocity (upper part of the engine), the radiation is directed towards the engine axis. This explains the heterogeneous directivity in the horizontal plane. The pressure field in an x-plane near the exit level ($x = 2$) for both modes is depicted in Figure 5.9 to give a more visual understanding of this effect. Outside from the nacelle, the higher pressure values

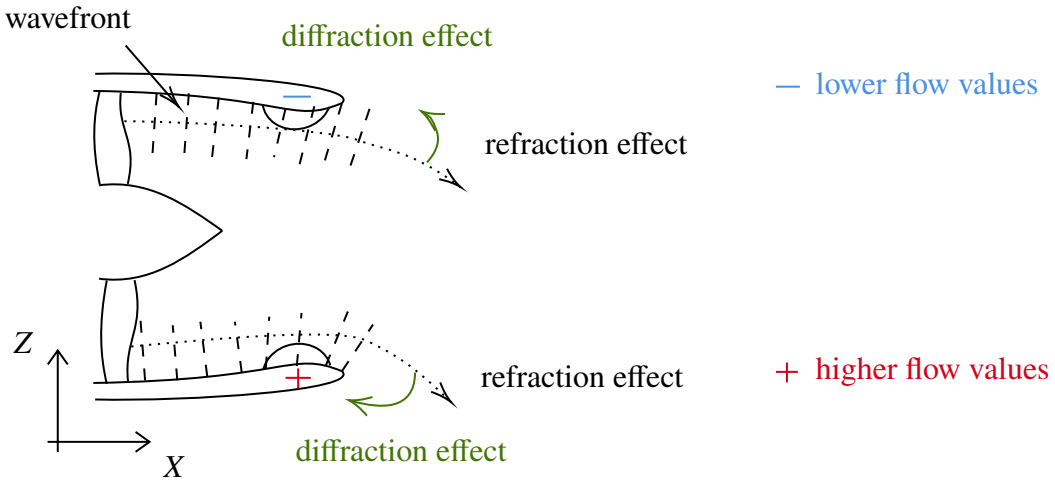

Figure 5.8 – Schematic of the effect of the flow distortion on the radiation pattern.

are observed for negative z- and y-values (yellow rectangles on the figures), which is consistent with the fact that the mode rotates in the counterclockwise direction.

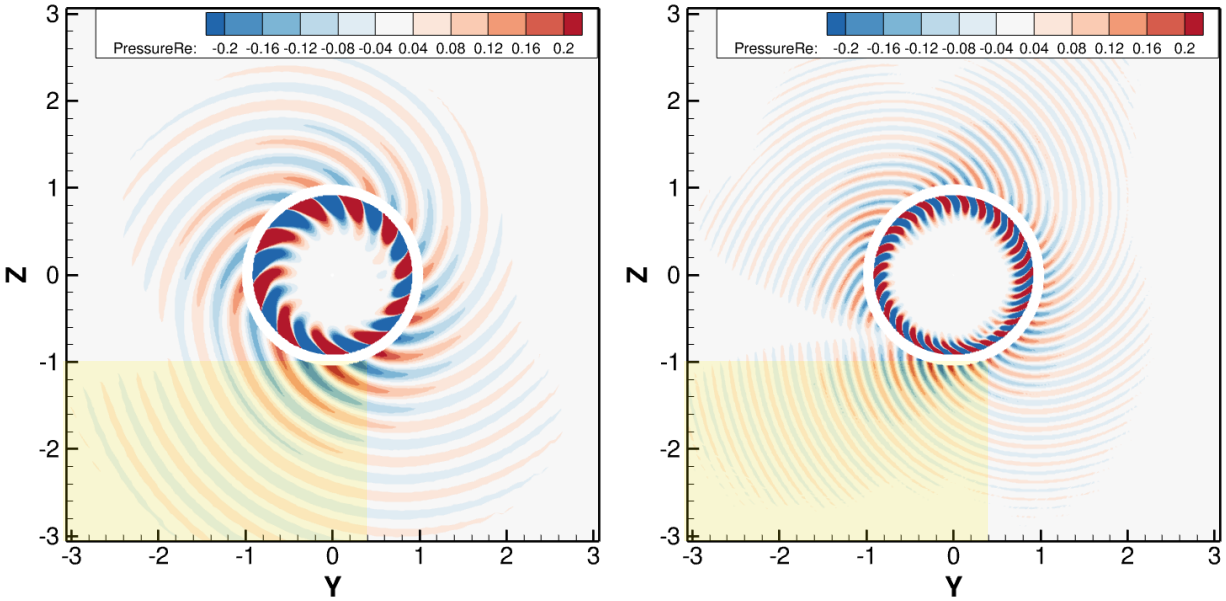

(a) Injected mode $(m, n) = (10, 1)$ at $\omega = 15$ (b) Injected mode $(m, n) = (25, 1)$ at $\omega = 30$

Figure 5.9 – Real part of pressure map at $x = 2$ for the case $\alpha_{AoA} = 5°$. The yellow squares represent the region with the highest pressure levels in the radiated field.

However, while the agreement is satisfactory for the case $m = 10$, significant differences can be found between the finite difference method and the multimodal method for $m = 25$. This is particularly true in the vertical plane near 270°. This suggests a difference in the pressure

distribution inside the duct that needs to be investigated in more detail.

5.3.6.3 In-duct comparisons

To this end, the axial evolution of the Fourier components close to the injected one ($m \pm 2$) at 95% of channel height is presented in Figure 5.10. Overall, the agreement between the multimodal method and the reference method is relatively good . However, slight differences are localized near the exit of the duct. The multimodal method accurately captures the order of magnitude of the transfer on the nearest Fourier components and the reflection on the injected mode. The amplitude of the injected Fourier component decreases as it propagates inside the duct. Additionally, the impact of the distortion is primarily detected on the direct azimuthal neighbours of the injected mode, leading to a transfer happening in cascade: the components $m \pm 1$ appear near $x = 1.5$, then the components $m \pm 2$ appear near $x = 1.75$. Interestingly, the transfer exhibits a close-to-symmetrical pattern on the Fourier components with azimuthal indices of $m \pm k$, where k is a positive integer.

To delve deeper into the cascade transfer of energy onto other azimuthal components, an azimuthal Fourier decomposition on a higher number of modes at 95% of the nacelle height for two axial locations is performed. Specifically, a focus on the axial locations $x = [0, 2]$ is made to capture the significant transfer near the duct exit and the impact of the distortion on the Fourier distribution at the injection position. In addition to comparing the multimodal solver results with the reference solution, the azimuthal decomposition obtained using the analytical solution given by Equation (5.18) with the use of the local flow values is included. Note that the latter cannot predict the absolute amplitude, so the results are adjusted such that the amplitudes of the main azimuthal components ($m = 10$ and $m = 25$) match the ones of the multimodal method. The results are shown in Figures 5.11 and 5.12 for the modes $m = 10$ and $m = 25$ respectively. These figures clearly show the energy transfer across various azimuthal components, highlighting the cascade effect resulting from the distortion in the base flow. For the case $m = 10$, as anticipated based on the preceding results, the multimodal solver accurately captures this transfer phenomenon and shows a close agreement with the FDM solution. The analytical solution also proves to be an excellent estimator of the expected azimuthal distribution. Despite the strong variations in the wall and flow conditions, it provides a reliable estimation of the relative neighbouring mode amplitudes, capturing the correct orders of magnitude. This means that the local level of distortion almost entirely drives the azimuthal shape of the acoustic field, which could be approximated by a single distorted mode. This also suggests that the azimuthal modal scattering is not predominant in this case.

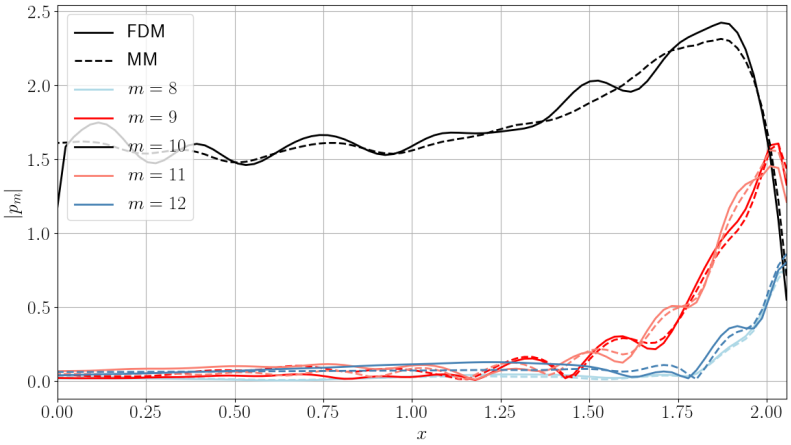

(a) Injected mode $(m, n) = (10, 1)$ at $\omega = 15$

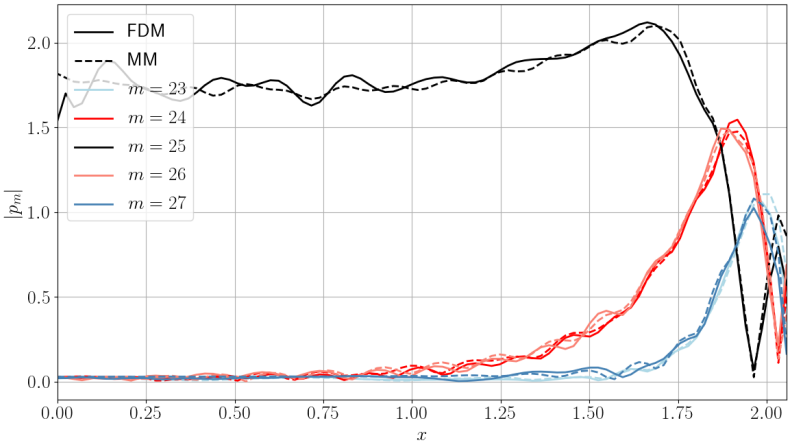

(b) Injected mode $(m, n) = (25, 1)$ at $\omega = 30$

Figure 5.10 – Axial evolution of the azimuthal decomposition of the pressure field at 95% of channel height for the Fourier components neighbouring the injected one.

In the case $m = 25$, both multimodal and FDM agree on the amplitudes of modes for azimuthal orders $20 < m < 30$. However, for higher azimuthal components, the agreement deteriorates, which highlights a significant azimuthal modal scattering. The excellent agreement with the analytical solution in the region $20 < m < 27$ suggests that this scattering has generated a higher-order distorted mode (centered on $m = 31$). Moreover, this mode is not only created, but it also exhibits an amplitude similar to the injected mode, which seems to indicate an amplification mechanism. The privileged explanation of this behaviour is that the newly created mode is trapped.

5.3.6.4 Investigating the presence of trapped mode

The notion of trapped modes has been introduced in Section 3.2 where double transition have been studied using a multiple-scale formulation of the flow. A similar analysis is intended here by examining an equivalent cut-off frequency ω_c that we would have without distortion. It is given by $\omega_c = \sqrt{|C_0^2 - U_0^2|}\alpha$, where U_0 and C_0 are the average value of the mean flow axial velocity and speed of sound at 95% of channel height and α is the radial eigenvalue computed as in the slowly varying formulation (see Section 1.3.3). To consider first-order effects of flow distortion, this equivalent cut-off frequency is also computed using $U(x) = U_0(x)(1 \pm C_{CDC}(x, 0.95R_2))$. The results for modes with an azimuthal order $m = [\![27, 31]\!]$ and a radial order $n = 1$ are plotted in Figure 5.13. We observe that the mode $m = 31$ exhibits a trapped zone within the range $x \in [1.6, 1.9]$. This mode coincides with the one amplified in Figure 5.12.

To confirm this observation, it is useful to check whether the reflection phenomena observed in 1D transitions are still present when the flow is distorted. This is achieved by plotting contour maps of acoustic pressure obtained with and without distortion at a modified frequency $\omega = 25.6$ where the injected mode encounters a transition in the case without distortion. Results at 95% of channel height are given in Figure 5.14. In the case without distortion, destructive interference regions with low-pressure values are observed. This is due to a reflected wave caused by the transition (as seen in Chapter 3). In this case, these zones are located at constant x values. In the case with distortion, these attenuation zones are still observed, but they are now curved due to the inhomogeneity of the flow. This suggests that reflections also occurred in this case, rendering mode trapped by "transitions" still possible.

The emergence of this so-called trapped mode in the multimodal method is investigated more precisely by varying the number of Fourier functions considered in the basis. Computations using $N_m = m \pm k$ Fourier functions, where k ranges from one to ten, are therefore performed. Then, an azimuthal decomposition of the pressure field at 95% of the channel height and at the duct

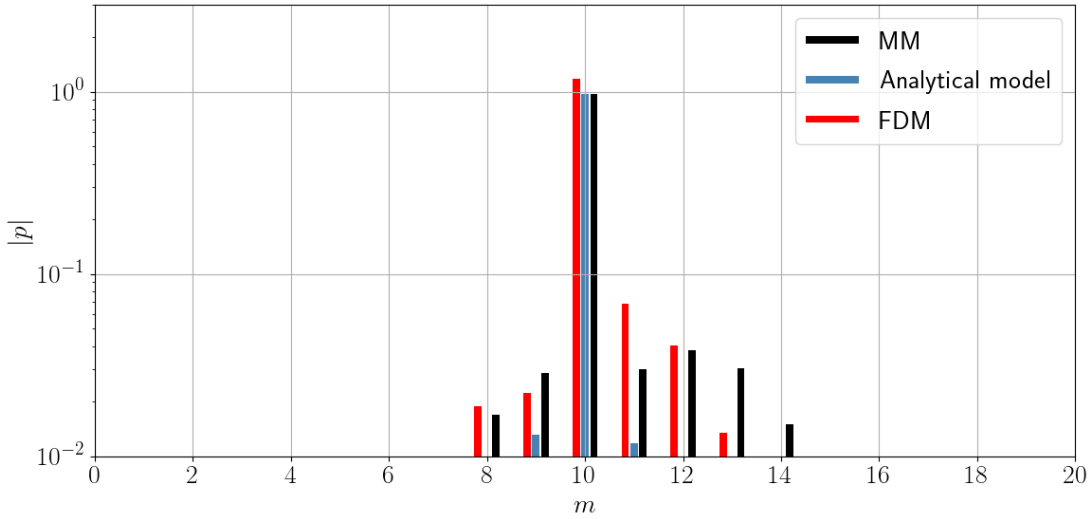

(a) $x = 0$

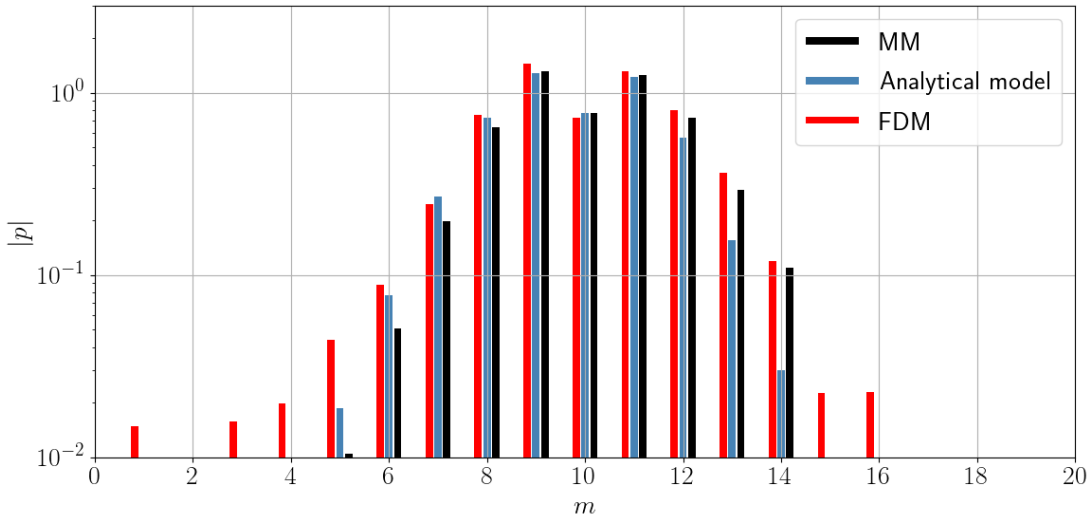

(b) $x = 2$

Figure 5.11 – Azimuthal decomposition of the pressure field at 95% of the channel height, for the injected mode $(m, n) = (10, 1)$ at $\omega = 15$.

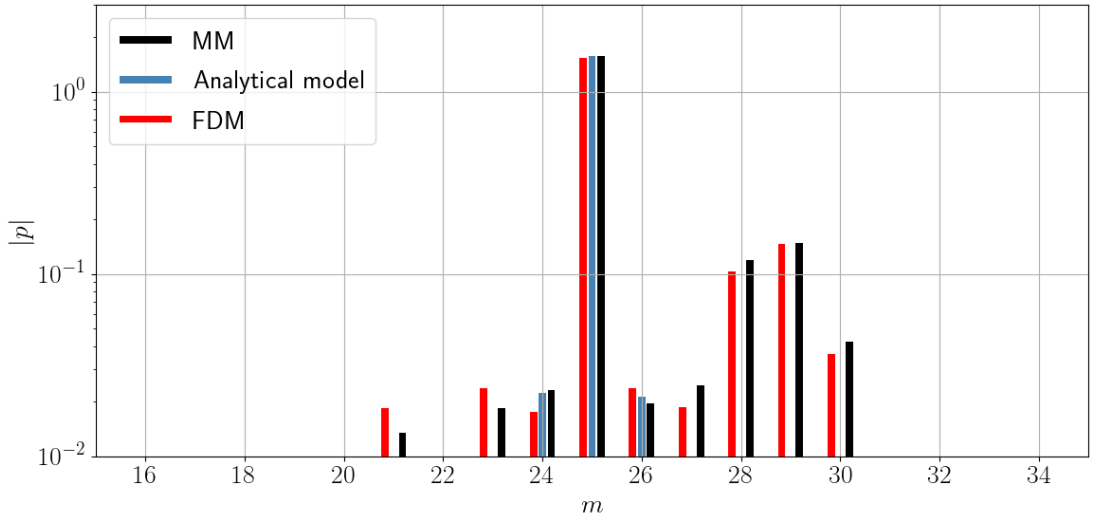

(a) $x = 0$

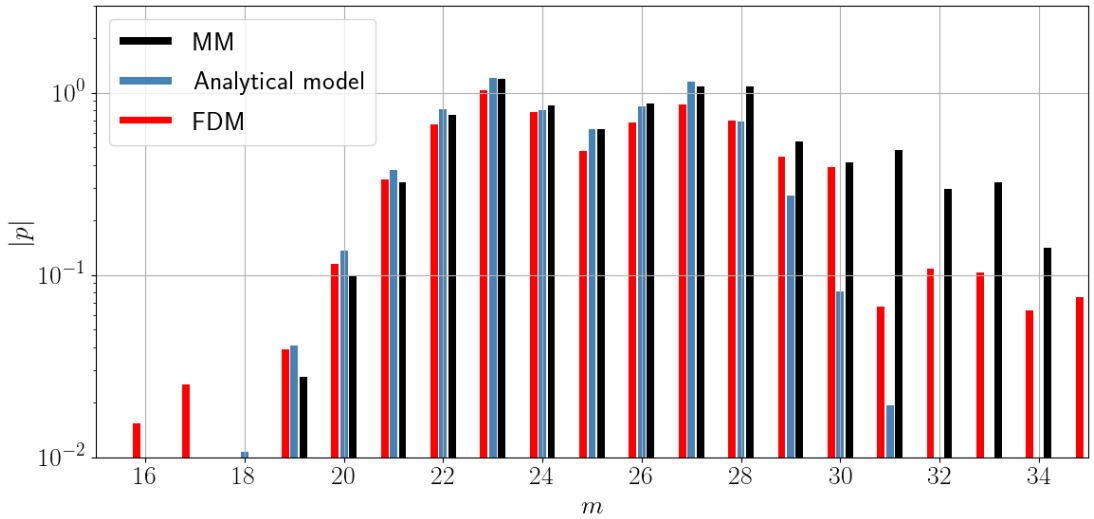

(b) $x = 2$

Figure 5.12 – Azimuthal decomposition of the pressure field at 95% of the channel height, for the injected mode $(m, n) = (25, 1)$ at $\omega = 30$.

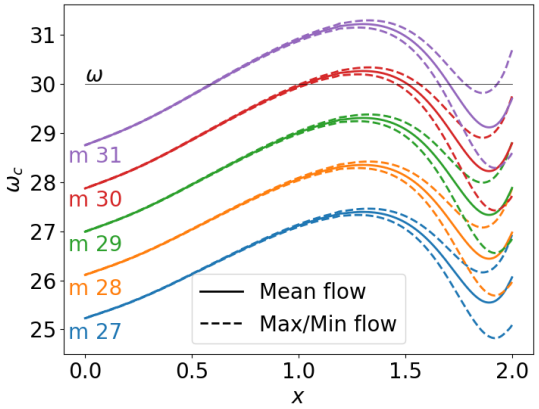

Figure 5.13 – Evolution of the cut-off frequencies for azimuthal modes $m = [\![27, 31]\!]$. The black line at $\omega = 30$ corresponds to the angular frequency used for this test case.

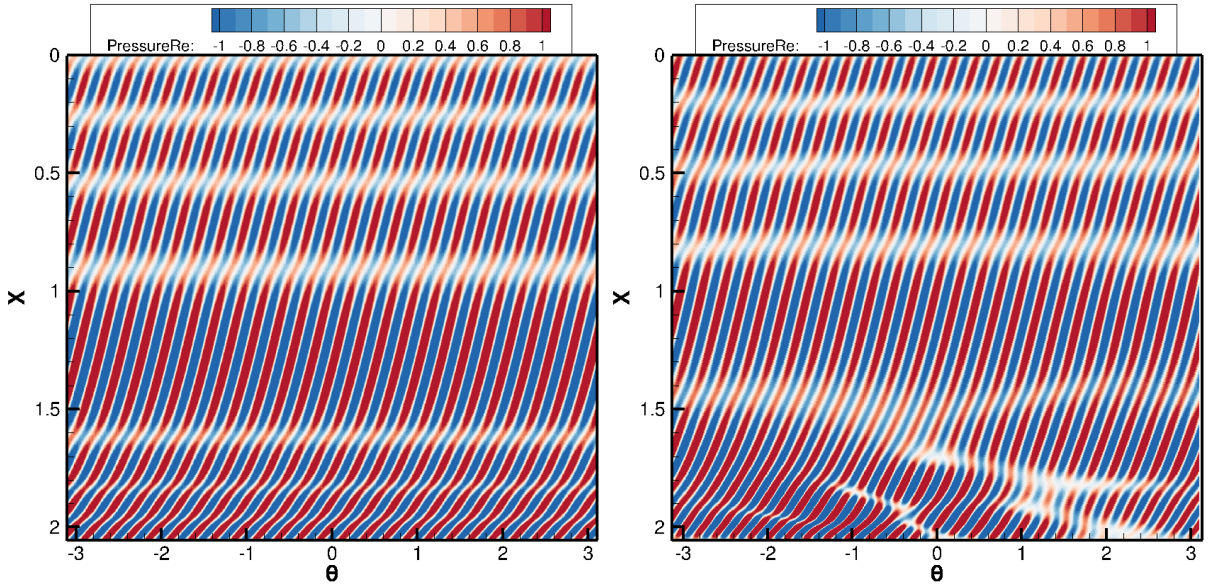

(a) Without distortion

(b) $\alpha_{AoA} = 5°$

Figure 5.14 – Real part of pressure at 95% of the channel height, for the injected mode $(m, n) = (25, 1)$ at $\omega = 25.6$.

exit is repeated for each calculation. The procedure is applied on both $m = 10$ and $m = 25$ cases. The results are presented in Figure 5.15. For the case of $m = 10$, where the comparison with the FDM is better, we can see that when considering $m \pm k$ modes, the transfer is accurately captured up to $m \pm (k - 1)$. Furthermore, with $k = 4$, the results are already excellent, and adding more modes does not significantly improves the precision. This suggests that a single distorted mode represents the overall field correctly. This showcases the method's effectiveness, as it allows for good results at a low computational cost by relaxing the azimuthal discretization. Here, the calculation with $k = 4$ lasted around 100 seconds. In the case $m = 25$, where a trapped mode is suspected, the convergence takes longer. The graph can be divided into two parts. For azimuthal wavenumbers lower than $m = 25$, a good agreement is quickly achieved with a small number of Fourier functions. However, for higher m values, the number of Fourier functions required for getting an accurate solution drastically increases. This confirms the particularity of the Fourier component $m = 31$.

Note that the presence of this trapped mode explains why the comparison with the FDM is degraded as it is associated with many reflections that are difficult to capture accurately with a temporal solver. It also render the multimodal calculation more computationally demanding because of the higher number of required Fourier components (1500 seconds with $k = 10$ in this case).

When the angle of incidence increases, the higher levels of distortion induce a more pronounced cascade transfer on the nearest azimuthal Fourier components and significantly increase the risk of trapped modes. Given the difficulty of accurately validating the developed method with the time-domain FDM in the $\alpha_{AoA} = 5°$ case in the presence of trapped modes, the $\alpha_{AoA} = 10°$ case is not used for validation. Still, first comparisons were performed with $\alpha_{AoA} = 10°$ and can be found in Appendix F.

5.4 Effects of azimuthal flow distortion on acoustic propagation using the multimodal method

During the validation process, initial observations were made regarding the influence of distortion on sound propagation. These observations, which were largely consistent with existing findings, affirmed the model's ability to accurately compute acoustics in the presence of distortion. However, in order to gain a more comprehensive understanding of the effects of distortion on acoustic propagation, additional test cases are being addressed. Specifically, our focus will

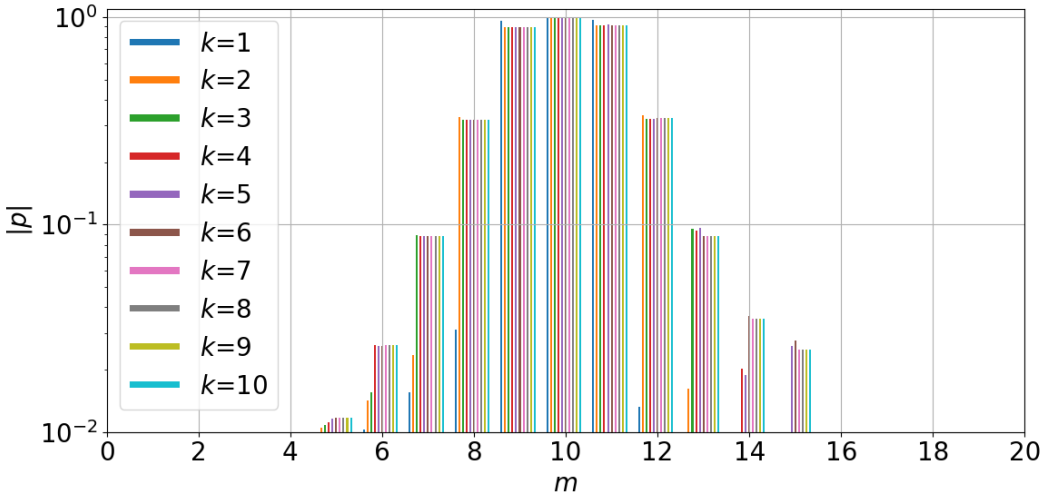

(a) Injected mode $(m, n) = (10, 1)$ at $\omega = 15$

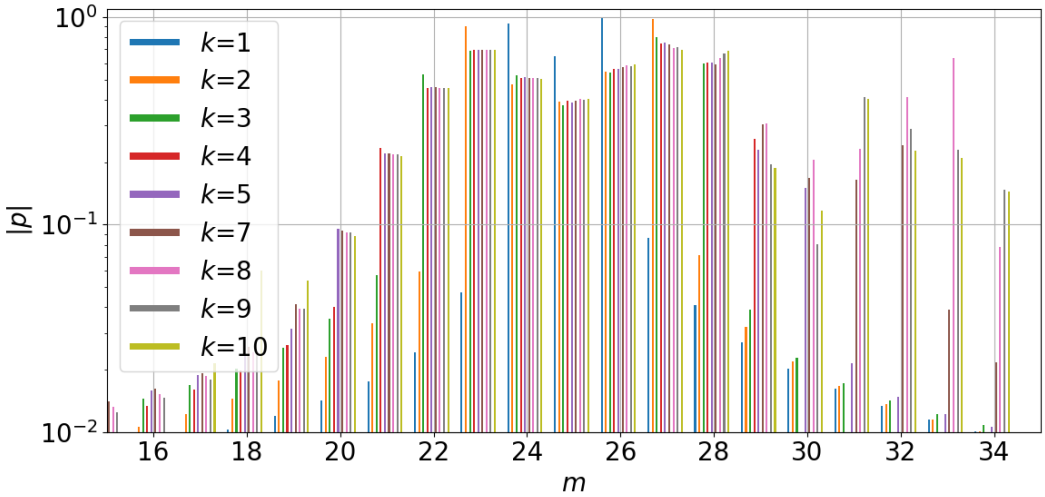

(b) Injected mode $(m, n) = (25, 1)$ at $\omega = 30$

Figure 5.15 – Convergence analysis of the number of azimuthal components based on the azimuthal decomposition of the pressure field at the exit.

initially be on examining the impact of liners in the cases with an azimuthal distortion of the flow. Then, the effect of nacelle shortening on the propagation in the presence of flow distortion is evaluated.

5.4.1 Lined duct with distortion

The same modes as those studied in Section 5.3.6 are considered, but an impedance $Z_2 = 2 - \mathrm{i}$ is applied between $x \in [0.2, 1.8]$ to investigate the effects of liners in the presence of flow distortion. Convergence for the azimuthal number of Fourier components needed is performed for each test case. For the radial discretization, the same number of polynomials as before is used (see Table 5.1). For the two studied modes, the computations are performed with three base flows: one without incidence (referred to as the baseline case), one with a 5° angle of incidence and one with the 10° angle of incidence.

At first, the power attenuation ΔP (see Equation (3.19)) obtained for each calculation is given in Table 5.2. The distortion's impact on the power attenuation is minor for the computed test cases, and it appears that considering the distortion is not necessary to assess acoustic power levels.

Mode	(10,1)			(25,1)		
Angle of incidence	0°	5°	10°	0°	5°	10°
ΔP	41.0 dB	41.1 dB	41.2 dB	64.0 dB	63.8 dB	64.0 dB

Table 5.2 – Summary of the lined test case parameters and associated power attenuations.

The impact of the liner on the radiated field is then investigated by showing in Figure 5.16 SPL directivities over the vertical plane (where significant effect of the flow distortion are observed). The liner strongly modifies the impact of flow distortion on the acoustic field radiated outside the engine. In particular, we observe that the radiated waves going toward the ground are strongly attenuated for both modes in the case $\alpha_{AoA} = 10°$. Note that the downward rotation of the lobes is amplified in the presence of liner. For the mode $m = 10$, a shift of 10° and 20° are observed for the 5° and 10° cases respectively.

To understand these observations, contour maps of acoustic pressure obtained with distortion ($\alpha_{AoA} = 10°$ case) and without distortion are proposed in Figure 5.17 for the mode $m = 10$. When the flow is axisymmetric, the liner is shown to rotate the wavefronts toward the wall. As the distortion levels are higher in this region in cases with incidence, the flow's refraction effect

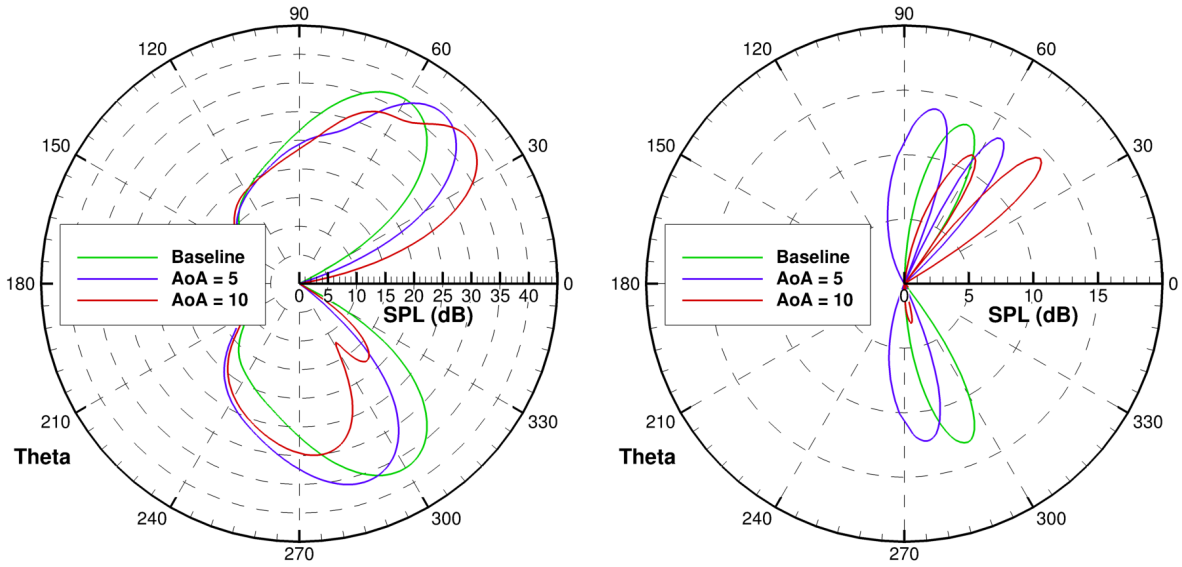

(a) Injected mode $(m, n) = (10, 1)$ at $\omega = 15$ (b) Injected mode $(m, n) = (25, 1)$ at $\omega = 30$

Figure 5.16 – SPL directivity in the vertical plane when a liner $Z_2 = 2 - \mathrm{i}$ is applied between $x \in [0.2, 1.8]$.

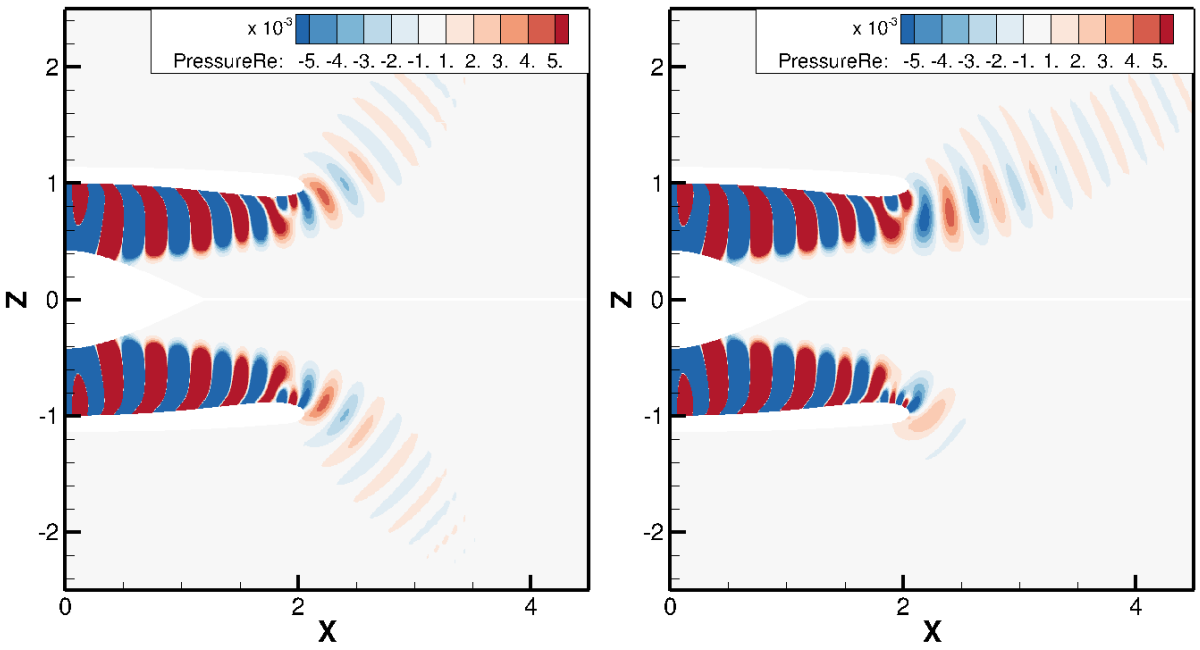

(a) Baseline (b) $\alpha_{AoA} = 10°$

Figure 5.17 – Contours maps of pressure real part over an y-slice, for the injected mode $(m, n) = (10, 1)$ at $\omega = 15$ with a liner $Z_2 = 2 - \mathrm{i}$ applied between $x \in [0.2, 1.8]$.

caused by distortion, described in Section 5.3.6.2, is amplified. The impact of flow distortion on acoustic radiation is higher, thus explaining the increased downward rotation. In addition, the flow's refraction effect caused by distortion in turn cause the wavefronts to rotate downward. As a result, the liner efficiency is increased in the lower part of the nacelle and decreased in its upper part.

These results show the importance of including distortion when evaluating the impact of a liner on the radiated field.

5.4.2 Effect of short intakes

5.4.2.1 Definition of the test cases

Finally, three engine configurations are considered to evaluate the impact of short intakes on noise radiation. These geometries are derived from the original CFM56 geometry described in Section 4.2.1 by considering the evolution of current engines, characterized by a shortening of the inlet. This shortening is characterized by the L/D coefficient, representing the inlet duct length L over the duct diameter D. This coefficient decreases as the architectures evolve from HBR to UHBR.

Some hypotheses are introduced for the design of the three geometries:

— the same section and mass flow at the fan plane are used to have similar flow without distortion;

— the shape for the lip of the nacelle is identical to have similar flow distortions;

— the same hub radius is kept to avoid affecting the radiation pattern.

So, the first engine, referred to as HBR or reference in the following, is very close to the CFM56 defined in Section 4.2.1, but the hub length is slightly reduced. Then, two UHBR engines are designed. The first has an L/D of 0.75, while the second has an L/D of 0.5. The three resulting geometries are shown in Figure 5.18.

5.4.2.2 Flow comparison

The shape of the flow distortion is assessed. This serves a dual purpose: first to ensure similar flow distortion levels at the engine exit; second to determine whether high distortion levels persist at the source's axial location. The latter point is of importance since residual distortion at fan position will generate new acoustic sources (see Section 0.4). These new sources, not considered here, can directly impact the acoustic power and radiation even without considering the impact

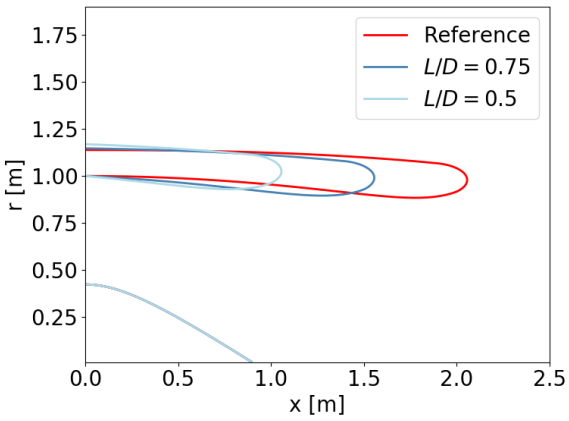

Figure 5.18 – Evolution toward an UHBR geometry.

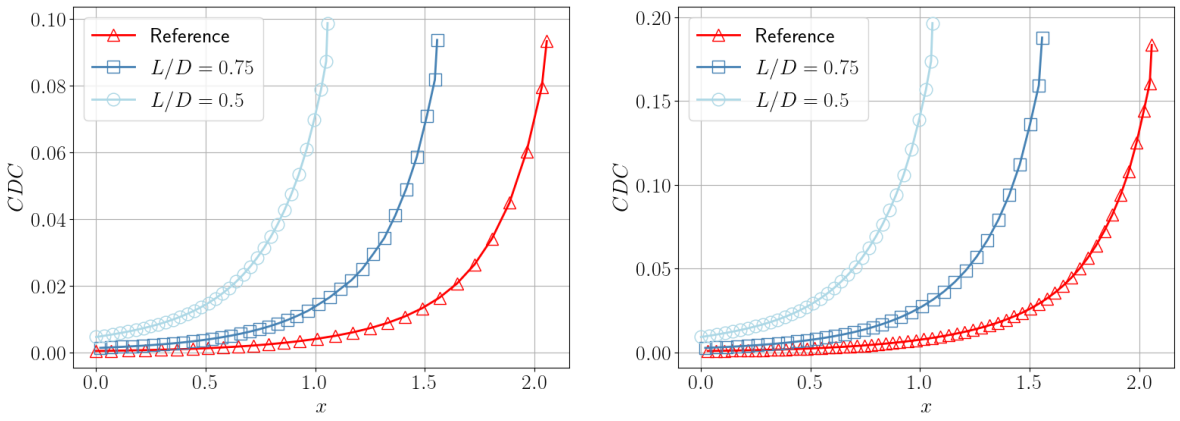

(a) $\alpha_{AoA} = 5°$ (b) $\alpha_{AoA} = 10°$

Figure 5.19 – CDC associated to the axial velocity in the duct inlet for different engine geometries.

of the distortion on the propagation [25]. To this end, the evolution of the distortion coefficient at 95% of the channel height defined in Equation (5.11) is plotted in Figure 5.19 for the three configurations. As expected, the level of distortion at the fan position is higher in the $L/D = 0.5$ and 0.75 configurations than in the reference configuration. However, the exponential decrease of the flow distortion implies that the level of distortion at the fan plane is low so that the impact of the distortion on the acoustic sources can be neglected in this case. Additionally, it is observed that the distortion levels near the inlet are similar. This comes from the tip's shape being the same for the three geometries considered at this axial location.

5.4.2.3 Acoustic comparison

The focus in this section centers on the mode with an azimuthal order $m = 10$. This choice is made to avoid the complications related to the so-called trapped mode observed in the baseline $m = 25$ case. Transition is indeed highly sensitive to variations in both flow and geometry, rendering its inclusion in the analysis quite risky.

In order to check that the geometry modification does not significantly affect the radiation in a case without incidence, the SPL directivity is plotted for all three geometries in Figure 5.20a. As anticipated, the impact of the modification is minor. All three configurations yield the same directivity pattern, with one single lobe radiating around 70°.

With all confounding factors eliminated, the effects of mean flow distortion on acoustic radiation can now be evaluated. Moving forward, we present the directivity pattern obtained with an angle of incidence $\alpha_{AoA} = 5°$ in Figure 5.20b. The impact of the length of the nacelle does not appear to be significant. Still, the longer the intake, the more pronounced is the downward rotation generated by the distortion, and the $L/D = 0.5$ geometry pattern is the closest to axisymmetry. The directivity pattern obtained with a higher angle of incidence $\alpha_{AoA} = 10°$ is shown in Figure 5.20c to have a more pronounced effect of distortion. Indeed, the engine length is here significant. Two main impacts are observed. First, a downward radiation is visible with an approximate 10-degree rotation of the directivity pattern. Then, a decrease in pressure amplitude in the lower part and an increase in the number of lobes in the upper direction are also noticeable. Interestingly, the case with the shortest duct length again exhibits the least distortion impact. This might be counter intuitive but can be explained by the fact that the distance over which the mode propagates in a distorted flow is reduced when the inlet length is shortened. However, this conclusion should be taken with a pint of salt because only propagation effects have been considered. Indeed, the modification of the source due to residual levels of distortion at fan position should also play a significant role.

5.5 Conclusion

The multimodal method has been applied to compute the flow and acoustic fields in the presence of azimuthal flow distortion by considering several Fourier azimuthal components. Only the determination of the initial admittance for computing the mean flow had to be modified to account for the angle of attack of the flow.

The method appears to be well-suited for flow computations. The multimodal method accu-

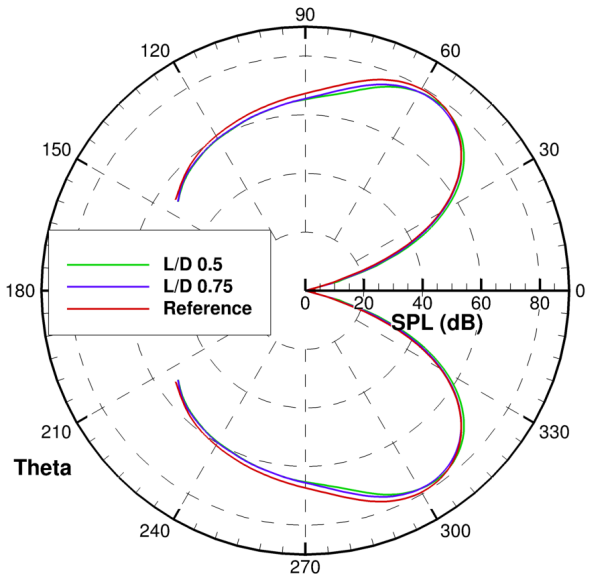

(a) Without distortion

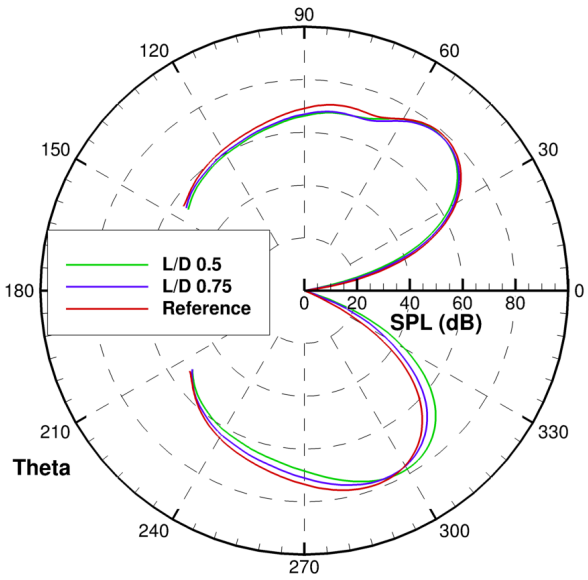

(b) $\alpha_{AoA} = 5°$

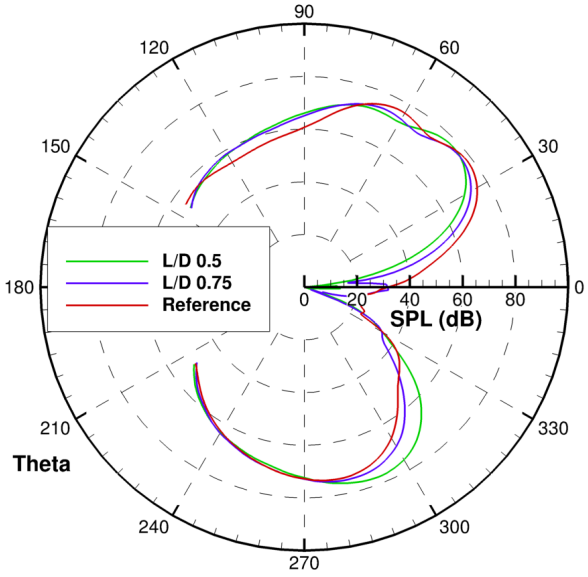

(c) $\alpha_{AoA} = 10°$

Figure 5.20 – SPL directivity in the vertical plane for the injected mode $m = 10$ at $\omega = 15$, for the three engine geometries.

rately captures the exponential decrease in flow distortion inside the intake and compares well against a solver that solves the steady Euler equations. Moreover, the calculation time remained relatively short, typically taking around 100 to 200 seconds, with the hypothesis that the flow in the free-field remains incompressible.

Comparisons with a time-domain solver of linearized Euler equations have been then per-

formed to validate the calculated acoustic field. While the dominant effects were correctly captured, unexplained small differences persisted between the developed admittance multimodal method and the time-domain solver. These errors are believed to arise because different governing equations are considered and because trapped modes have been observed. The latter are particularly challenging for a time-domain solver. Note that these trapping phenomena also increase the computation cost of the multimodal method which then requires more azimuthal Fourier components in the basis. The computation generally took some minutes for weak distortion levels and no trapping. However, when trapped modes appear and the distortion levels are high, the method can take up to an hour to give a result.

The azimuthal flow distortion is found to have two main impacts on the acoustic field. First, the radiation pattern is rotated downward, and then, the number of azimuthal Fourier functions contributing to the acoustic field increases. The shape of the distortion at the end of the nacelle lip is responsible for a rotation of the radiated waves of almost twice the angle of incidence. When the mode propagates over a longer distance in a distorted flow, it becomes more distorted with a cascade transfer on the nearest azimuthal Fourier components. The latter effect is found to significantly increase the risk of trapped modes inside the engine.

Specific investigations on the effect of distortion have then been conducted using only the multimodal method. First, it is found that power attenuation by a liner is not impacted by the flow distortion. However, the attenuation appears to be reduced in the upper part of the engine and increased in its lower part. In addition, including a liner increases the effects of distortion on the radiation field with a greater downward rotation. Finally, the nacelle was shortened to study the influence of short intakes on the radiated field. This leads to higher levels of distortion at the fan position as expected. This would likely impact the acoustic sources, although the thesis did not evaluate this aspect. Surprisingly, with shorter air inlets, the distortion had slightly less impact on the acoustic propagation of a given mode. This is explained by a reduced cascade transfer over neighbouring Fourier components because of the reduced length of the intake.

Chapter 6

Conclusion

6.1 Thesis objectives

This thesis focused on developing improved models to study the noise propagation in modern turbofan engine intakes and on gaining a better understanding of the effects of modal transition and flow distortion on acoustic propagation. Modal transitions are generally ignored because only a few number of modes are concerned in standard geometries. Similarly, flow distortion levels are often assumed to be negligible throughout most of the intake and are, therefore, expected to have a limited impact on the propagation. However, the recent evolution of engines toward ultra-high bypass ratio geometries, particularly the shortening of the nacelle, challenges these assumptions. Concerning modal transition, the nacelle's shortening necessitates the consideration of modes near the cut-off frequency because their attenuation occurs over a limited distance. Being close to their cut-off frequencies, these modes have more chances of facing a modal transition. As for flow distortion, the reduction in nacelle length leads to significant levels of azimuthal flow distortion in the most significant part of the intake. The impact of this evolution on acoustic propagation must be assessed.

6.2 Modelling of acoustic propagation

The primary objective of the thesis work was to develop models for the propagation of noise in modern engine intakes. After briefly describing the equations associated with noise propagation, the first chapter addressed the principles and assumptions necessary for developing duct propagation models. A literature review was conducted, and it was decided to extend the models based on modal approaches that solve the Goldstein propagation equation. In particular, a more in-depth study was conducted on models based on the WKB ansatz and on admittance multimodal formulations.

Throughout the manuscript, the focus was on multimodal methods, and the development of a

general admittance multimodal method formed the core of this work. Since the initial multimodal method was limited to cases without flow or with uniform flow, the development consisted in including a known potential flow in the acoustic propagation equation. The sound field is solved by representing the acoustic variables onto Fourier components and Chebyshev polynomials. This basis proved effective for solving the wall boundary condition problem observed in most multimodal methods and allowed for fast calculations. The polynomial basis exhibits excellent convergence properties for smooth geometries. However, since this basis is not physical, high-order modes are present in the calculation. These modes require increased axial resolution to avoid stability problems. This issue was addressed by modifying the commonly used Magnus–Möbius scheme. This modification is based on a decomposition of the Magnus matrix, to avoid the summation of high and low values associated with non-physical eigenmodes. The formulation avoids the conditioning problems typically observed when using polynomial bases without significantly increasing computational costs and represents one of the major results of the thesis. A formulation was also added to handle liner discontinuities.

Still, there is also a need to access to the potential base flow. In this context, two solutions have been considered. The first one involves using a multiple-scale flow. This allows to distinguish the mode self-propagation from modal scattering and provides a better understanding of the phenomena which are inherently one-dimensional, such as transitions. Still, this method tends to behave poorly far from transitions for high-velocity flows. Then, it was observed that the multimodal method could also compute the mean flow if some adjustments were made. The idea is to do an acoustic calculation at zero frequency and without mean flow. Then, modifying the admittance exit boundary condition and using an iterative procedure on the density allows for the flow field computation. This procedure allowed for flow calculations at a very low cost.

Once these improvements were implemented, the problem of free-field radiation was addressed. The admittance method was adapted to perform such calculation by surrounding the engine with a duct with a perfectly matched layer on the outer wall, rewriting the acoustic propagation equation inside this duct, and deriving formulas relating the admittance and the solution between the inner and outer ducts. Once again, the method can also perform flow computations, but particular care is required for the boundary conditions. All the mentioned developments were validated through comparisons with a finite element solver for the Goldstein propagation equation. It was shown that the developed multimodal method is well-suited for in-duct propagation and free field radiation of acoustic waves. For axisymmetric cases, the method is both fast and accurate.

Finally, the problem of flow distortion was addressed. Generally, the nacelle is designed to

have a uniform flow in front of the fan to maximise engine efficiency. However, during landing or takeoff operations, the aircraft experiences high angles of attack. Consequently, the flow entering the engine is no longer axisymmetric. The developed multimodal method has been applied to compute the flow and acoustic fields in such flows by considering several Fourier azimuthal components in the basis, and by adapting the flow boundary conditions. The flow results were compared against a solver for the steady Euler equations and the method is shown to be fast and accurate. The method was then applied to perform acoustic calculations. The method's validity was initially established for cases with low incidence angles through comparisons with a time-domain solver of the linearized Euler equations. A reasonable but not perfect agreement between the two methods was obtained. The main explanation of these discrepancies is the appearance of trapped modes in the intake, which are challenging to capture with time-domain solvers. Nonetheless, it is worth noting that the primary effects of flow distortion were consistent between the two methods, showing that the multimodal method can describe the impact of azimuthal flow distortion on acoustic propagation.

6.3 Physical insight

Part of this thesis also aimed at improving our understanding of the impact of both modal transitions and azimuthal flow distortion on the acoustic propagation.

A modal transition is inherently one-dimensional and linked to the propagation of a single mode. Therefore, the multimodal method with a multiple-scale flow was used to study the propagation of modes that encounter a double transition phenomenon inside the duct. It was shown that a double turning point can give rise to resonance, amplification or tunnelling. In the case of a cut-on/cut-off/cut-on transition, tunnelling appears with an attenuation of the wave between the two turning points. If the mode has a non-zero amplitude at the axial location of the second transition, there will be a non-zero transmitted power. In the case of a cut-off/cut-on/cut-off transition, the successive multiple reflections between the two turning points form constructive interference for certain distances. Since the mode is cut-on in this region, these successive reflections do not dissipate energy. They can lead to resonance phenomena if no modal scattering is considered. The method also highlights the inherent flaws of models that neglect modal scattering. In particular, it is responsible for a modification of the resonance frequencies and can even prevent the resonances from happening. The amplification can become negligible if the modal scattering mechanisms are strong.

The main effect of the azimuthal distortion inside the duct is an azimuthal transfer on Fourier

components neighbouring the one of the injected mode. When no modes are trapped, this transfer is almost symmetric and happens in cascade. However, even if the shape of the acoustic field is highly modified in the transverse shape, no significant impact on the acoustic power was found. In the free field, two main effects were observed. The refraction effect of the flow distortion tends to rotate the directivity downward of almost the angle of incidence of the engine. On the other hand, the pressure levels radiated toward the ground tend to decrease. Moreover, it is shown that including a liner increases the effect of flow distortion on the propagation. The distortion does not impact the power attenuation by the liner but increases its efficiency in the lower part of the engine and decreases it in the upper part. Finally, the influence of the intake length on the radiated field was assessed. When reducing the inlet length, even if higher distortion levels were observed at the fan plane as expected, the effect of flow distortion on the acoustic field is found to be less pronounced. This can be explained by the shorter distance over which the mode propagates in a distorted flow.

6.4 Future work

Building upon the progress made in this thesis, several avenues for future research have emerged.

The primary challenges remaining are linked to the trapped modes in a flow with an azimuthal distortion. The presence of these modes is difficult to anticipate, and establishing a criterion for detecting their emergence is important. Although the WKB model introduced in the thesis can be used initially, its reliability is not sufficient. Consequently, when using the multimodal method, it is required to manually verify convergence regarding the number of azimuthal Fourier components, which can be time demanding. Furthermore, the code then becomes demanding in terms of memory. Sparse matrix techniques could be used, and some sections of the code should be rewritten to avoid the storage of unnecessary variables, to overcome this limitation. From a physical perspective, the emergence of these trapped modes can strongly alter the directivity pattern in a way not explained by the refraction effect presented in the thesis. No global trends appear for these modes, and improving the understanding of the underlying physical phenomena is necessary.

Another avenue to explore is the improvement of flow computations. While the method developed in the thesis is fast and accurate to compute the mean flow, it relies on assuming an incompressible flow in the free-field. A more accurate flow representation requires removing this assumption. The actual method is computationally too demanding because the improved

Magnus–Möbius scheme developed in the thesis cannot be used to perform the axial integration. It seems that it could be possible to determine the axial evolution of the admittance in the duct $\mathcal{B}$ analytically. This would be the best option since it would mean that the method's computational cost would not be increased, but this analytical formulation is not straightforward.

Then, while this research has improved our understanding of modal transition and flow-induced distortion phenomena in axisymmetric ducts, these models need to be adapted to non-axisymmetric engine configurations. Initial effort can focus on engines with scarfed inlets, followed, if possible, by more complex cases like buried nozzles. Investigating how modal transition and flow distortion are modified in non-axisymmetric ducts would be of interest. Then, the work of this thesis has been restricted to isolated engine configurations. As highly heterogeneous directivities were observed in the presence of flow distortion, including installation effects in the radiation (from the fuselage or wing) is important.

The last study of the thesis has shown a limited impact of the shortening of the intake when only considering the propagation of an individual mode. However residual distortion levels are still visible at the source plane for the shortest configuration. This flow distortion will lead to the appearance of new acoustic sources that have been neglected in this work. Therefore, it would be necessary to complement the thesis propagation model with a model of sources in the presence of distortion thus allowing for a complete analysis of the impact of flow distortion on fan noise.

Finally, this work also demonstrated the capacity of analytical models to capture first order-effects of flow distortion. In particular, when limited modal scattering is present, the analytical model based on Mathieu's functions has shown to accurately recover the azimuthal transfer over the neighbouring Fourier components due to distortion. An analytical formulation of the whole propagation problem seems to be possible. Having such a model would certainly be beneficial as the developed multimodal method can be computationally costly in such cases.

Appendix A

General multimodal matrices formulation

In this Appendix, the matrices defined in Equation (2.11) are detailed:

$$
\begin{aligned}
(A_{11})_{ij} &= (M_{12})_{ij} = \int_S D(1-M_x^2)\varphi_j\varphi_i^* \mathrm{d}S,\\
(M_{11})_{ij} &= -\int_S D(1-M_x^2)\frac{\partial \varphi_j}{\partial x}\varphi_i^* \mathrm{d}S,\\
(A_{12})_{ij} &= 0,\\
(A_{21})_{ij} &= -\int_S \frac{DU}{C^2}\frac{\mathrm{D}_\perp \varphi_j}{\mathrm{D}t}\varphi_i^* \mathrm{d}S - \frac{1}{\mathrm{i}\omega}\int_\Lambda \frac{D^2 V_\tau}{Z}\frac{\mathrm{D}_\perp \varphi_j}{\mathrm{D}t}\varphi_i^* \mathrm{d}\Lambda,\\
(A_{22})_{ij} &= \int_S D(1-M_x^2)\varphi_j\varphi_i^* \mathrm{d}S - \frac{1}{\mathrm{i}\omega}\int_\Lambda \frac{D^2 V_\tau U}{Z}\varphi_j\varphi_i^* \mathrm{d}\Lambda,\\
(M_{21})_{ij} &= \frac{\mathrm{d}}{\mathrm{d}x}\left(\int_S \frac{DU}{C^2}\frac{\mathrm{D}_\perp \varphi_j}{\mathrm{D}t}\varphi_i^* \mathrm{d}S\right) + \int_S D\nabla_\perp \varphi_i^* \cdot \nabla_\perp \varphi_j \mathrm{d}S\\
&\quad - \int_S \frac{D}{C^2}\left(\frac{\mathrm{D}_\perp \varphi_j}{\mathrm{D}t}\left(\frac{\mathrm{D}_\perp \varphi_i}{\mathrm{D}t}\right)^* + U\frac{\mathrm{D}_\perp \varphi_j}{\mathrm{D}t}\frac{\partial \varphi_i^*}{\partial x}\right)\mathrm{d}S\\
&\quad - \frac{1}{\mathrm{i}\omega}\int_\Lambda \frac{D^2}{Z}\frac{\mathrm{D}_\perp \varphi_j}{\mathrm{D}t}\left(\frac{\mathrm{D}\varphi_i}{\mathrm{D}t}\right)^* \mathrm{d}\Lambda + \frac{1}{\mathrm{i}\omega}\frac{\mathrm{d}}{\mathrm{d}x}\left(\int_\Lambda \frac{D^2 V_\tau}{Z}\frac{\mathrm{D}_\perp \varphi_j}{\mathrm{D}t}\varphi_i^* \mathrm{d}\Lambda\right),\\
(M_{22})_{ij} &= -\frac{\mathrm{d}}{\mathrm{d}x}\left(\int_S D(1-M_x^2)\varphi_j\varphi_i^* \mathrm{d}S\right)\\
&\quad + \int_S D(1-M_x^2)\varphi_j\frac{\partial \varphi_i^*}{\partial x}\mathrm{d}S - \int_S \frac{DU}{C^2}\varphi_j\left(\frac{\mathrm{D}_\perp \varphi_i}{\mathrm{D}t}\right)^* \mathrm{d}S\\
&\quad - \frac{1}{\mathrm{i}\omega}\int_\Lambda \frac{D^2}{Z}U\varphi_j\left(\frac{\mathrm{D}\varphi_i}{\mathrm{D}t}\right)^* \mathrm{d}\Lambda + \frac{1}{\mathrm{i}\omega}\frac{\mathrm{d}}{\mathrm{d}x}\left(\int_\Lambda \frac{D^2 V_\tau U}{Z}\varphi_j\varphi_i^* \mathrm{d}\Lambda\right).
\end{aligned}
$$

Appendix B

1D multimodal matrices formulation with the Fourier-Chebyshev basis

In this Appendix, the matrices defined in Equation (3.9) are detailed when a Chebyshev basis is used.

By introducing:

$$I_k(f,g) = \int_0^1 f(r)g(r)r^k \mathrm{d}r, \tag{B.1}$$

and the symbol $'$ to represent the first derivative of the Chebyshev polynomial, the matrices write:

$$\begin{aligned}
(G_0)_{ij} &= 2\pi\left((R_2-R_1)^2 I_3(T_i,T_j) + 3(R_2-R_1)R_1 I_2(T_i,T_j) + 3R_1^2 I_1(T_i,T_j) + \frac{R_1^3}{R_2-R1} I_0(T_i,T_j)\right),\\
(S_0)_{ij} &= 2\pi\left(-\frac{1}{R_2-R1}\frac{\mathrm{d}(R_2-R_1)}{\mathrm{d}X}\mathcal{A}_{ij} - (R_2-R_1)\frac{\mathrm{d}(R_2-R_1)}{\mathrm{d}X} I_4(T_i,T_j')+\right.\\
&\quad \left(4R_1\frac{\mathrm{d}R_1}{\mathrm{d}X} - 3\frac{\mathrm{d}R_2}{\mathrm{d}X}R_1 - R_2\frac{\mathrm{d}R_1}{\mathrm{d}X}\right) I_3(T_i,T_j') - \left(\frac{3R_1^2}{R_2-R1}\frac{\mathrm{d}(R_2-R_1)}{\mathrm{d}X} + 3R_1\frac{\mathrm{d}R_1}{\mathrm{d}X}\right) I_2(T_i,T_j')\\
&\quad \left.-\left(\frac{R_1^3}{(R_2-R_1)^2}\frac{\mathrm{d}(R_2-R_1)}{\mathrm{d}X} + \frac{3R_1^2}{R_2-R1}\frac{\mathrm{d}R_1}{\mathrm{d}X}\right) I_1(T_i,T_j') - \frac{R_1^3}{(R_2-R_1)^2}\frac{\mathrm{d}R_1}{\mathrm{d}X} I_0(T_i,T_j')\right),\\
(S_1)_{ij} &= 2\pi\frac{V^a}{C}\left(\mathcal{A}_{ij} + (R_2-R_1)^2 I_4(T_i,T_j') + 4(R_2-R_1)R_1 I_3(T_i,T_j') + 6R_1^2 I_2(T_i,T_j')\right.\\
&\quad \left.+\frac{4R_1^3}{R_2-R_1} I_1(T_i,T_j') + \frac{R_1^4}{(R_2-R_1)^2} I_0(T_i,T_j')\right)+
\end{aligned}$$

$$2\pi\frac{V^b}{C}\left(I_1(T_i,T_j)+\frac{R_1}{R_2-R_1}I_0(T_i,T_j)+I_2(T_i,T_j')+\frac{2R_1}{R_2-R_1}I_1(T_i,T_j')+\frac{R_1^2}{(R_2-R_1)^2}I_0(T_i,T_j')\right),$$

$$\begin{aligned}(G_1)_{ij}=\frac{2\pi}{R_2-R_1}\Big((R_2-R_1)(1+m^2)I_1(T_i,T_j)+R_1(1+m^2)I_0(T_i,T_j)+\\ (R_2-R_1)(I_2(T_i,T_j')+I_2(T_i,T_j')^*)+2R_1(I_1(T_i,T_j')+I_1(T_i,T_j')^*)+\\ \frac{R_1^2}{R_2-R_1}(I_0(T_i,T_j')+I_0(T_i,T_j')^*)+(R_2-R_1)I_3(T_i',T_j')+3R_1I_2(T_i',T_j')+\\ \frac{3R_1^2}{R_2-R_1}I_1(T_i',T_j')+\frac{R_1^3}{(R_2-R_1)^2}I_0(T_i',T_j')\Big),\end{aligned}$$

when $m \neq 0$ and:

$$(G_0)_{ij}=2\pi\left((R_2-R_1)^2I_1(T_i,T_j)+R_1(R_2-R_1)I_0(T_i,T_j)\right),$$

$$(S_0)_{ij}=2\pi\left(-(R_2-R_1)\frac{\mathrm{d}(R_2-R_1)}{\mathrm{d}X}I_2(T_i,T_j')+\frac{\mathrm{d}\left(R_1^2-R_2R_1\right)}{\mathrm{d}X}I_1(T_i,T_j')-R_1\frac{\mathrm{d}R_1}{\mathrm{d}X}I_0(T_i,T_j')\right),$$

$$\begin{aligned}(S_1)_{ij}=2\pi\frac{V^a}{C}\left((R_2-R_1)^2I_2(T_i,T_j')+2R_1(R_2-R_1)I_1(T_i,T_j')+R_1^2I_0(T_i,T_j')\right)\\ +2\pi\frac{V^b}{C}I_0(T_i,T_j'),\end{aligned}$$

$$(G_1)_{ij}=2\pi\left(I_1(T_i',T_j')+\frac{R_1}{R_2-R_1}I_0(T_i',T_j')\right),$$

when $m = 0$.

Appendix C

Acoustic power for a single mode propagation

In this Appendix, we derive an expression of the acoustic power depending only on acoustic potential terms. The velocity potential ϕ is written for a single mode (m, n) composed of a left and right running wave:

$$\begin{aligned}\phi = Q_0\sqrt{\frac{C_0}{\omega D_0\sigma}}\psi\ \exp\left[\frac{\mathrm{i}}{\epsilon}\int^X \frac{\omega U_0}{C_0^2-U_0^2}\mathrm{d}X\right]\\ \left[\mathcal{D}\ \exp\left[\frac{-\mathrm{i}}{\epsilon}\int^X \frac{\omega C_0\sigma}{C_0^2-U_0^2}\mathrm{d}X\right] + \mathcal{U}\ \exp\left[\frac{\mathrm{i}}{\epsilon}\int^X \frac{\omega C_0\sigma}{C_0^2-U_0^2}\mathrm{d}X\right]\right],\end{aligned} \tag{C.1}$$

where the notation of section 1.3.3 are used.

Developing the expression of the axial component of the time-averaged energy flux (see Equation (1.18)) to the order ϵ gives:

$$\mathbf{I}\cdot\mathbf{e}_x = \frac{D_0\omega}{2}\mathrm{Re}\left(\frac{\omega U_0}{C_0^2}\phi\phi^* - \mathrm{i}\left(1-\frac{U_0^2}{C_0^2}\right)\phi\frac{\partial\phi^*}{\partial x}\right). \tag{C.2}$$

This yields for the acoustic power:

$$\begin{aligned}\mathcal{P} = \frac{Q_0^2\omega}{2}\mathrm{Re}\left[\frac{\sigma^*}{|\sigma|}\left(|\mathcal{D}|^2\exp\left[\frac{2}{\epsilon}\int^X\frac{\omega C_0\mathrm{Im}(\sigma)}{C_0^2-U_0^2}\mathrm{d}X\right]\right.\right.\\ -|\mathcal{U}|^2\exp\left[-\frac{2}{\epsilon}\int^X\frac{\omega C_0\mathrm{Im}(\sigma)}{C_0^2-U_0^2}\mathrm{d}X\right]\\ \left.\left.-2\mathrm{i}\ \mathrm{Im}\left(\mathcal{D}\mathcal{U}^*\exp\left[-2\frac{\mathrm{i}}{\epsilon}\int^X\frac{\omega C_0\mathrm{Re}(\sigma)}{C_0^2-U_0^2}\mathrm{d}X\right]\right)\right)\right].\end{aligned} \tag{C.3}$$

For a cut-on mode, σ is real, therefore:

$$\mathcal{P} \propto |\mathcal{D}|^2 - |\mathcal{U}|^2. \tag{C.4}$$

As for a cut-off mode, σ is imaginary, and we get:

$$\mathcal{P} \propto 2\,\mathrm{Im}\left(\mathcal{D}\mathcal{U}^*\right). \tag{C.5}$$

Appendix D

Multimodal matrices in a duct with PML

In this Appendix, the matrices defined in Equation (4.10) are detailed:

$$
\begin{aligned}
(A_{11})_{ij} &= (M_{12})_{ij} = \int_S D\alpha\beta(1-M_x^2)\varphi_j\varphi_i^* \mathrm{d}S,\\
(M_{11})_{ij} &= -\int_S D\alpha\beta(1-M_x^2)\frac{\partial\varphi_j}{\partial x}\varphi_i^* \mathrm{d}S,\\
(A_{21})_{ij} &= -\int_S \frac{DU}{C^2}\alpha\beta\left(\mathrm{i}\omega + \mathbf{V}_\perp\cdot(L\nabla_\perp)\right)\varphi_j\varphi_i^* \mathrm{d}S,\\
(A_{22})_{ij} &= \int_S D\alpha\beta(1-M_x^2)\varphi_j\varphi_i^* \mathrm{d}S,\\
(M_{21})_{ij} &= \frac{\mathrm{d}}{\mathrm{d}x}\left(\int_S \frac{DU}{C^2}\alpha\beta\left(\mathrm{i}\omega + \mathbf{V}_\perp\cdot(L\nabla_\perp)\right)\varphi_j\varphi_i^* \mathrm{d}S\right) + \int_S DH\nabla_\perp\varphi_i^*\cdot\nabla_\perp\varphi_j \mathrm{d}S\\
&\quad - \int_S \frac{D}{C^2}\alpha\beta\Big(\left(\mathrm{i}\omega + \mathbf{V}_\perp\cdot(L\nabla_\perp)\right)\varphi_j\left(-\mathrm{i}\omega + \mathbf{V}_\perp\cdot(L\nabla_\perp)\right)\varphi_i^* +\\
&\quad U\left(\mathrm{i}\omega + \mathbf{V}_\perp\cdot(L\nabla_\perp)\right)\varphi_j\frac{\partial\varphi_i^*}{\partial x}\Big)\mathrm{d}S,\\
(M_{22})_{ij} &= -\frac{\mathrm{d}}{\mathrm{d}x}\left(\int_S D\alpha\beta(1-M_x^2)\varphi_j\varphi_i^* \mathrm{d}S\right)\\
&\quad + \int_S D\alpha\beta(1-M_x^2)\varphi_j\frac{\partial\varphi_i^*}{\partial x}\mathrm{d}S - \int_S \frac{DU}{C^2}\alpha\beta\varphi_j\left(-\mathrm{i}\omega + \mathbf{V}_\perp\cdot(L\nabla_\perp)\right)\varphi_i^* \mathrm{d}S.
\end{aligned}
$$

Appendix E

Validation of the potential flow hypothesis on an UHBR engine

In this appendix, the RANS computations analyses done to validate the potential flow hypothesis are presented.

E.1 Definition of test cases

The computations are done with the nacelle of the NOVA Onera airplane (side nacelle configuration) [106]. For confidentiality reasons, the spatial dimensions are normalized by the fan radius and velocities by the free-stream velocity. This nacelle is placed inside a mean flow with varying free-stream velocities and an extreme angle of attack of 15° to study the impact of distortion. The scope is here to validate that the potential flow hypothesis is met and that it is reasonable to neglect the vorticity. *Note:* The CFM56 geometry is not used here since we analyse already performed calculations that had been done previosuly on the NOVA engine.

E.2 Mean flow computations

In this study, the mean flow has been computed using Onera's CFD solver *elsA* turned into a RANS mode. The domain comprises around 25 million points, and the simulations are run over 84 processors and last approximately ten hours. Three cases are performed with the nacelle under an incidence of 15° at different free stream Mach number values M_∞.

E.3 Flow analysis

A quick overview of computed mean axial velocity contours provided by the CFD solver at the inlet of the duct is given in Figure E.1. The azimuthal inhomogeneity is visible in all

cases. We observe that the nacelle behaves like an airfoil under incidence, accelerating the flow over the upper lip of the bottom part of the nacelle and decelerating it over the lower lip of the upper part. This causes a difference in velocity between the upper and lower parts of the nacelle, which is responsible for the inflow distortion. Note that the flow is not completely realistic here since no fan was placed in the nacelle. In particular, the two main consequences are that the flow velocities inside the nacelle are moderated, and extremely high inflow distortion levels are obtained.

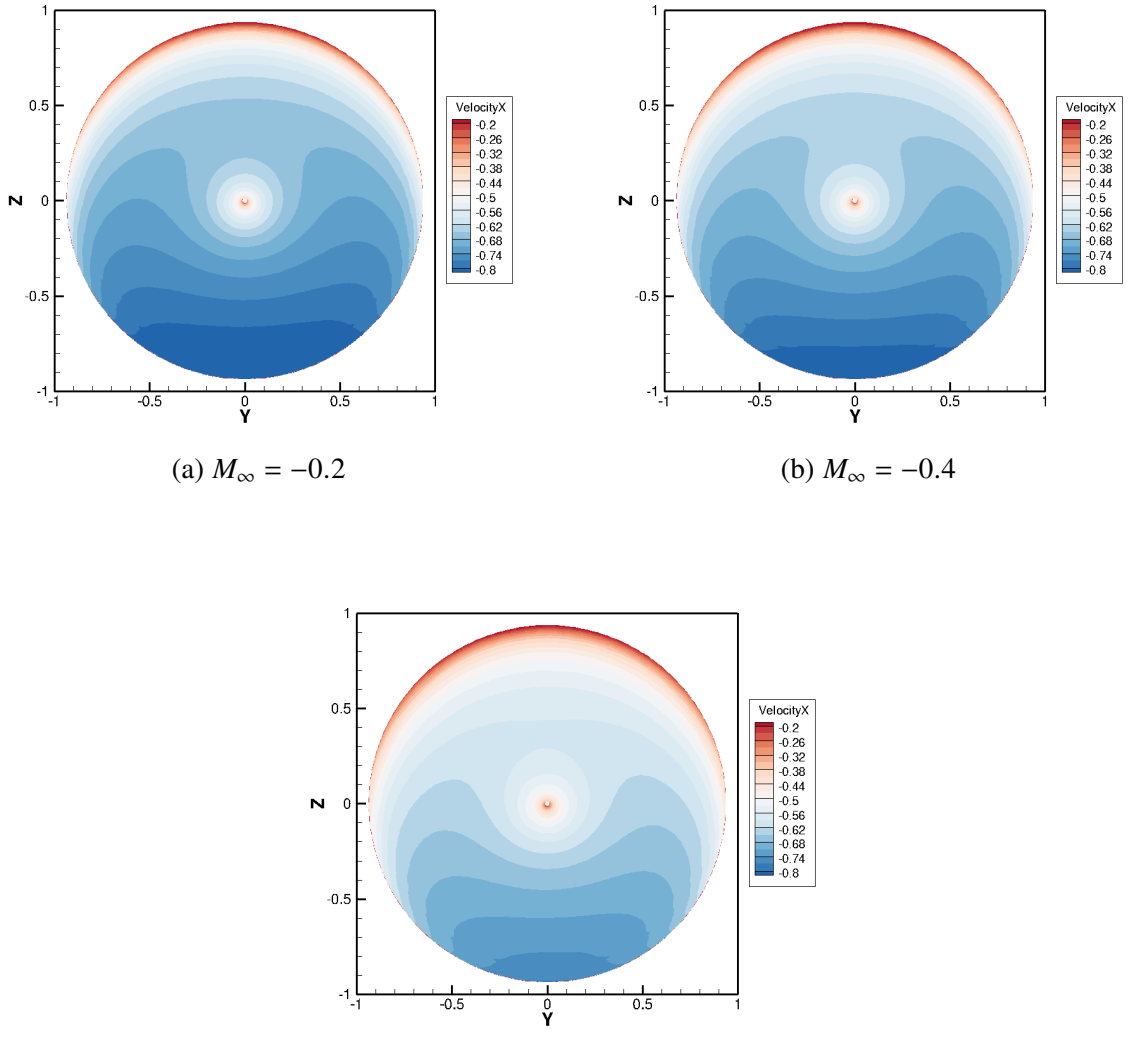

(a) $M_\infty = -0.2$

(b) $M_\infty = -0.4$

(c) $M_\infty = -0.6$

Figure E.1 – Normalized axial velocity contours at the duct inlet.

For the three cases, an angular Fourier transform is performed from the axial velocity maps to get the amplitude of the distortion harmonics. The inflow distortion is also analyzed by computing the axial evolution of the CDC applied to the axial velocity at different channel heights. The associated results are plotted in Figure E.2. It can be seen that the distortion decreases along the duct and that the CDC tends to be independent of the free stream Mach number. However, this decrease depends on the channel height, and the closer to the tip, the higher the attenuation. Near the tip, an exponential decrease is obtained. It also appears that a Fourier superposition of low-order azimuthal components can represent the flow. Considering, only the first two Fourier components for most test cases should be enough to represent the flow correctly. However, this tends to be less true as the Mach number increases.

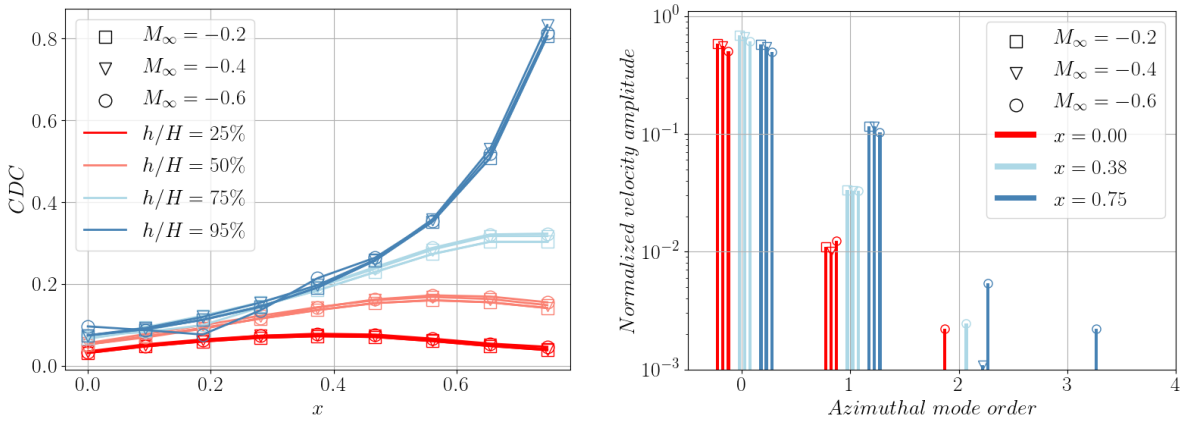

(a) Axial evolution of CDC

(b) Azimuthal Fourier transform harmonics of axial velocity at 95% of channel height

Figure E.2 – Evolution of the azimuthal distortion inside the duct.

Now that the main characteristics of the flow have been presented, let us check that the potential flow hypothesis is realistic. The vorticity magnitude computed by the CFD solver is given at the fan and exit planes for all cases in Figure E.3. The vorticity magnitude is small almost everywhere compared to the distortion levels, and the potential hypothesis is reasonably respected. This hypothesis is not met inside boundary layers. However, their effect on the duct mode propagation is expected to be small (as long as the ratio of the boundary layer thickness is negligible in front of the duct mode wavelength [32]). Note that some non-physical vorticity appears on the mesh junctions (plotted in black) and is caused by numerical interpolations.

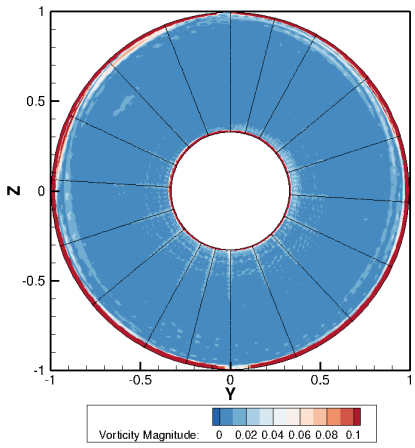

(a) Fan plane. $M_\infty = -0.2$.

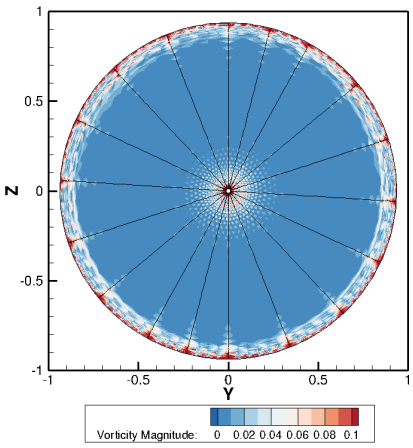

(b) Exit plane. $M_\infty = -0.2$.

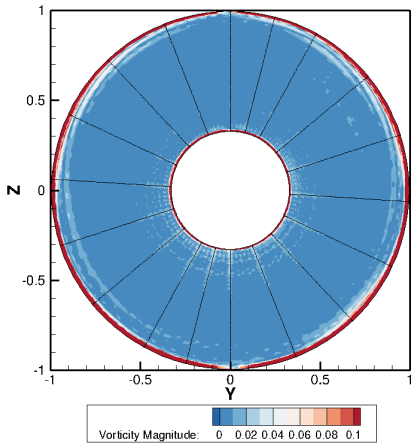

(c) Fan plane. $M_\infty = -0.4$.

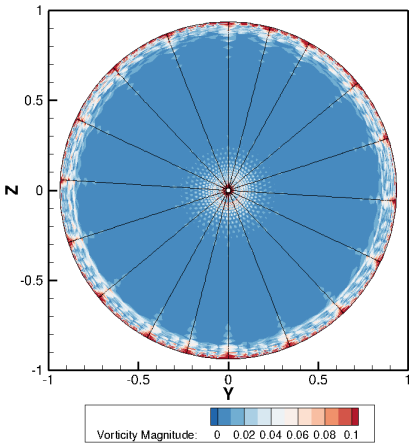

(d) Exit plane. $M_\infty = -0.4$.

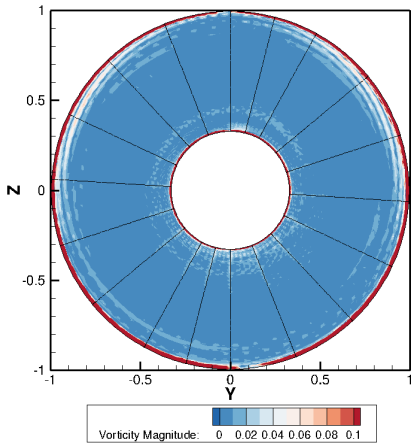

(e) Fan plane. $M_\infty = -0.6$.

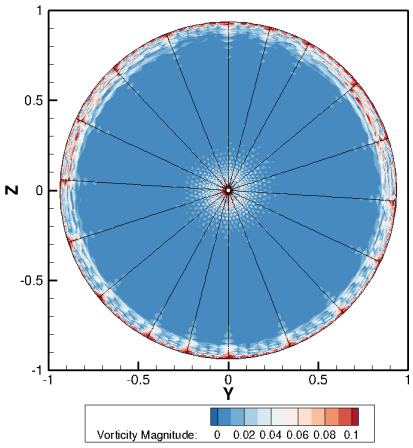

(f) Exit plane. $M_\infty = -0.6$.

Figure E.3 – Normalized vorticity magnitude contours.

Appendix F

First acoustic validations performed for the computations with high levels of flow distortion

In this appendix, the comparisons between the multimodal method and the FDM for the case $\alpha_{AoA} = 10°$ are presented.

The analysis is limited to the injected mode $m = 10$ to avoid requiring huge computational resources for the mode $m = 25$. Figures F.1 present the SPL in dB obtained in the vertical and horizontal planes for this case with the multimodal and the FDM. The two methods agreement is relatively good but some differences are observed between the two methods. Most of the observations made for the case with an angle of incidence of 5° remain applicable (see Section 5.3.6), with a downward rotation of the radiated lobes and an increase in the number of lobes pointing skyward. To assess the validity of the in-duct distribution, we perform a Fourier decomposition at 95% of the channel height and examine the evolution in the axial direction of the azimuthal Fourier components close to the injected one ($m \pm 2$) in Figure F.2. Additionally, we analyze the azimuthal distribution at the exit of the duct, as shown in Figure F.3. Despite the discrepancies observed in the radiated field, the in-duct results match quite well. The cascade diffusion effect remains observable. Due to the higher levels of distortion within the duct, the direct azimuthal neighbors of the injected mode appear sooner inside the duct with respect to the 5° case, with the modes $m \pm 1$ emerging near $x = 1.25$, and the modes $m \pm 2$ appearing near $x = 1.5$. Regarding the azimuthal distribution at the exit, the match is quite good up to $m = 16$ but deteriorates further.

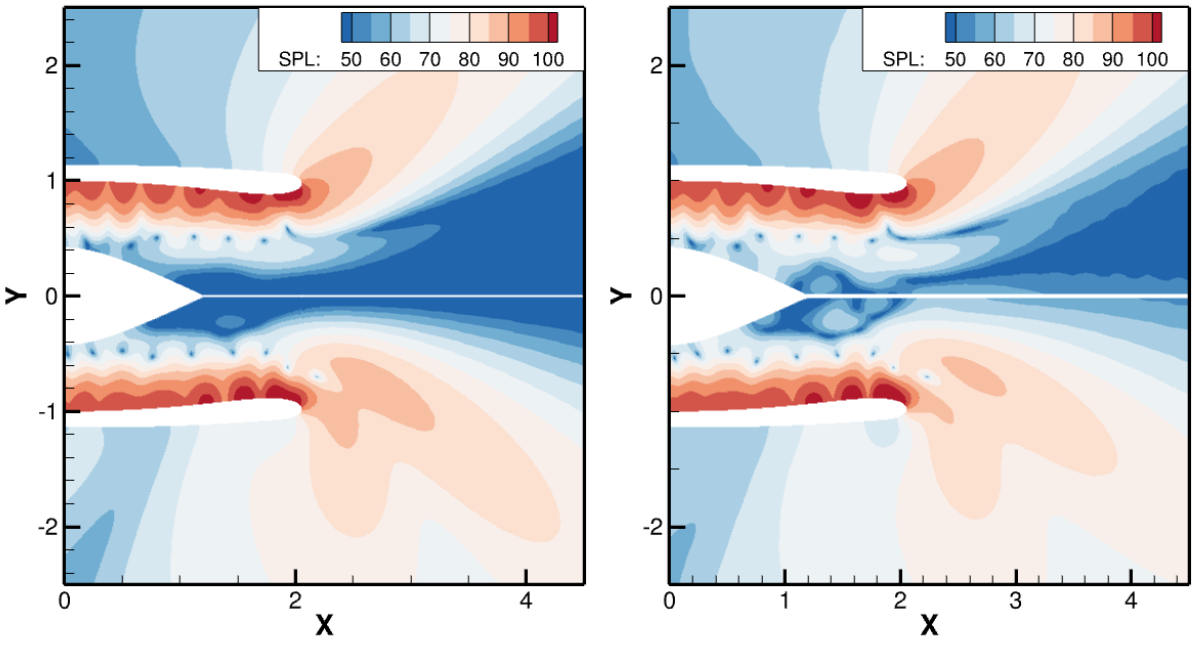

(a) Horizontal plane – Multimodal

(b) Horizontal plane – Finite difference method

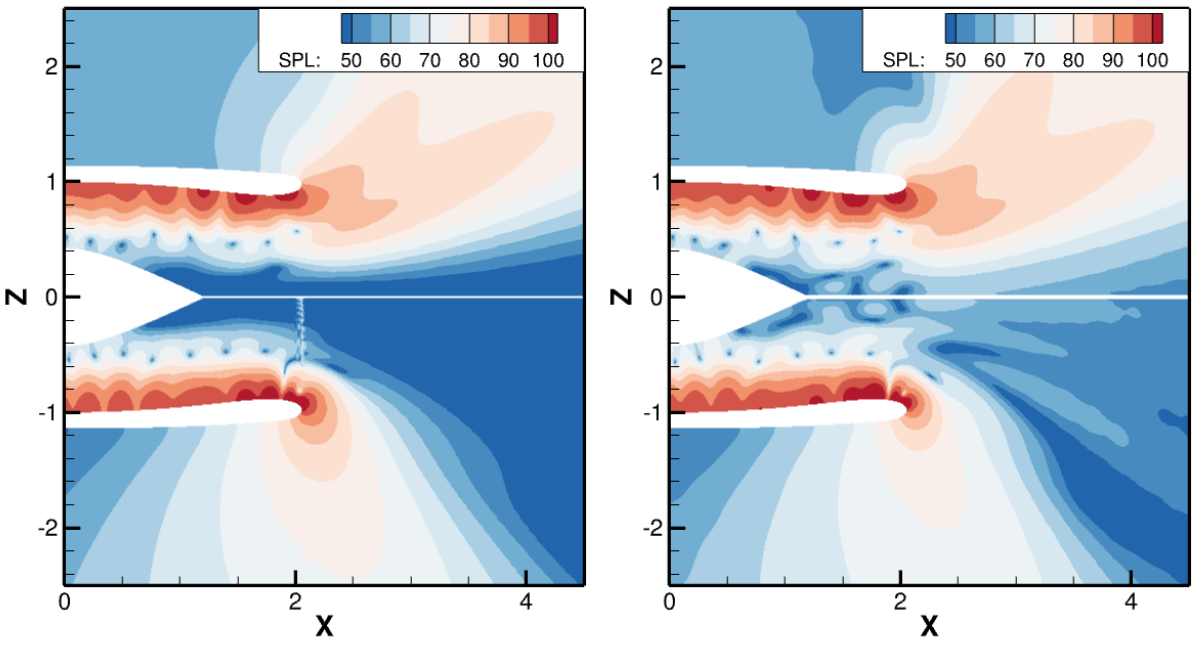

(c) Vertical plane – Multimodal

(d) Vertical plane – Finite difference method

Figure F.1 – Contour map associated to the SPL pressure for the mode $m = 10$ for the case $AoA = 10°$.

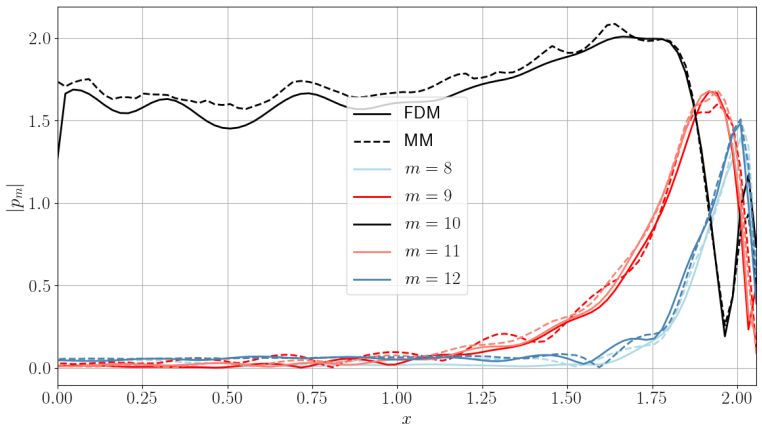

Figure F.2 – Axial evolution of the azimuthal decomposition of the pressure field for the injected mode $m = 10$ at 95% of channel height for the Fourier components neighbouring the injected one.

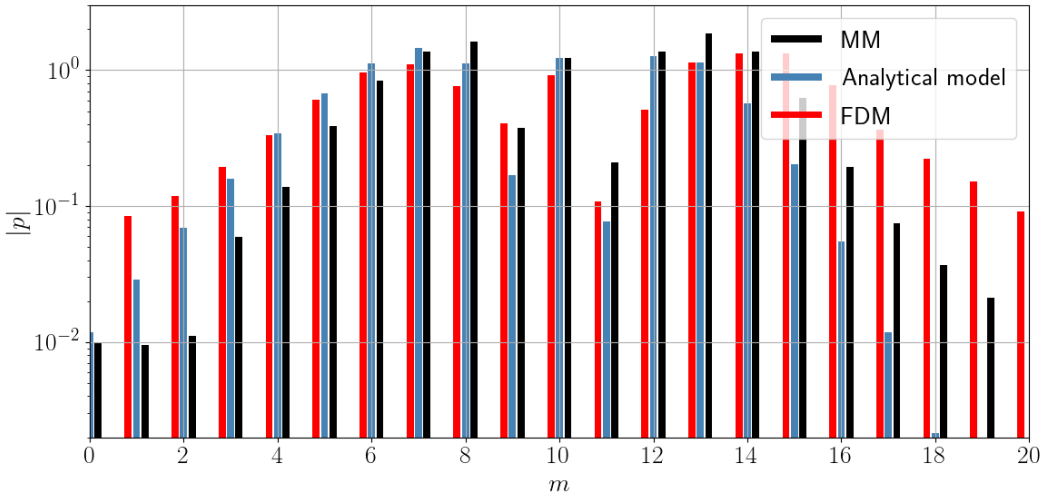

Figure F.3 – Azimuthal decomposition of the pressure field at the outer wall at $x = 2$ for the case $AoA = 10°$.

BIBLIOGRAPHY

[1] S. Delbecq et al. « ISAE-SUPAERO Aviation and Climate: aliterature review ». In: (2022). DOI: 10.34849/a66a-vv58.

[2] BRUIT-PARIF. *Health impact of transport noise in the densely populated zone of Ile-de-France region*. Tech. rep. 2019.

[3] T. Nodé-Langlois. *Aeroacoustics: industrial requirements ISAE - Formation Ingénieur*. Tech. rep. 2019.

[4] I Achunche et al. « Prediction of forward fan noise propagation and radiation from intakes ». In: *15th AIAA/CEAS Aeroacoustics Conference (30th AIAA Aeroacoustics Conference)*. 2009. DOI: 10.2514/6.2009-3239.

[5] L. Neuhaus et al. « Reduction of UHBR fan blade tones by flow induced secondary sound sources ». In: *22nd AIAA/CEAS Aeroacoustics Conference*. 2016. DOI: 10.2514/6.2016-2891.

[6] M. Daroukh. « Effects of distortion on modern turbofan tonal noise ». PhD thesis. Institut National Polytechnique de Toulouse - Université de Sherbrooke, 2017.

[7] S. Guérin, M. Vogt, and A. Holewa. « Multiple scattering of acoustic waves in potential mean flow with circumferential distortion ». In: *23rd AIAA/CEAS Aeroacoustics Conference, 2017*. 2017. DOI: 10.2514/6.2017-3197.

[8] A. G. Prinn, R. Sugimoto, and R. J. Astley. « The effect of steady flow distortion on noise propagation in turbofan intakes ». In: *22nd AIAA/CEAS Aeroacoustics Conference, 2016*. 2016. DOI: 10.2514/6.2016-3028.

[9] S. W. Rienstra. « Sound Propagation in Slowly Varying 2D Duct with Shear Flow ». In: *22nd AIAA/CEAS Aeroacoustics Conference*. 2016. DOI: 10.2514/6.2016-2925.

[10] B. Baddour et al. « Acoustic radiation characteristics of cutoff modes from ducts ». In: *Journal of Sound and Vibration* 541 (2022), p. 117306. DOI: 10.1016/j.jsv.2022.117306.

[11] S. W. Rienstra. « Cut-on, cut-off transition of sound in slowly varying flow ducts, contribution to the David Crighton memorial issue of Aerotecnica Missili E Spazio ». In: 79.3-4 (2000), pp. 93–96.

[12] N. C. Ovenden, W. Eversman, and S. W. Rienstra. « Cut-on cut-off transition in flow ducts: comparing multiple-scales and finite-element solutions ». In: *10th AIAA/CEAS Aeroacoustics Conference*. 2004. DOI: 10.2514/6.2004-2945.

[13] N. C. Ovenden. « A uniformly valid multiple scales solution for cut-on cut-off transition of sound in flow ducts ». In: *Journal of Sound and Vibration* 286.1 (2005), pp. 403–416. DOI: 10.1016/j.jsv.2004.12.009.

[14] A. J. Cooper and N. Peake. « Trapped acoustic modes in aeroengine intakes with swirling flow ». In: *Journal of Fluid Mechanics* 419 (2000), pp. 151–175. DOI: 10.1017/S0022112000001245.

[15] A. J. Cooper, A. B. Parry, and N. Peake. « Acoustic resonance in aeroengine intake ducts ». In: *Journal of Turbomachinery* 126.3 (2004), pp. 432–441. DOI: 10.1115/1.1776586.

[16] N.R. Biggs. « Wave trapping in a two-dimensional sound-soft or sound-hard acoustic waveguide of slowly-varying width ». In: *Wave Motion* 49.1 (2012), pp. 24–33. DOI: 10.1016/j.wavemoti.2011.06.004.

[17] S.N. Gaulter and N.R. Biggs. « Acoustic trapped modes in a three-dimensional waveguide of slowly varying cross section ». In: *Proceedings of the Royal Society* 469 (2013). DOI: 10.1098/rspa.2012.0384.

[18] R. Parker. « Acoustic resonances and blade vibration in axial flow compressors ». In: *Journal of Sound and Vibration* 92.4 (1983), pp. 529–539. DOI: 10.1016/B978-008044396-6/50025-3.

[19] F. Holzinger et al. « Self-excited Blade Vibration Experimentally Investigated in Transonic Compressors: Acoustic Resonance ». In: *Journal of Turbomachinery* 138.4 (2016). DOI: 10.1115/1.4032042.

[20] S. Guérin. « Farfield Radiation of Induct-Cutoff Pressure Waves ». In: *23rd AIAA/CEAS Aeroacoustics Conference*. 2017. DOI: 10.2514/6.2017-4037.

[21] M. Doherty and H. Namgoong. « Impact of turbofan intake distortion on fan noise propagation and generation ». In: *22nd AIAA/CEAS Aeroacoustics Conference*. 2016. DOI: 10.2514/6.2016-2841.

[22] J. Winkler et al. « Inlet and aft tonal noise predictions of a full-scale turbofan engine with bifurcation and inlet distortion ». In: *23rd AIAA/CEAS Aeroacoustics Conference*. 2017. DOI: 10.2514/6.2017-3034.

[23] M. Lorteau and T. Le Garrec. « Numerical assessment of fan noise confinement effects in a closed wind-tunnel ». In: *AIAA AVIATION 2021 FORUM*. 2021. DOI: 10.2514/6.2021-2302.

[24] R. J. Astley, R. Sugimoto, and P. Mustafi. « Computational aero-acoustics for fan duct propagation and radiation. Current status and application to turbofan liner optimisation ». In: *Journal of Sound and Vibration* 330.16 (2011), pp. 3832–3845. DOI: 10.1016/j.jsv.2011.03.022.

[25] S. Guérin and A. Holewa. « Fan tonal noise from aircraft aeroengines with short intake: A study at approach ». In: *International Journal of Aeroacoustics* 17.6-8 (2018), pp. 600–623. DOI: 10.1177/1475472X18789001.

[26] B. Mangin, M. Daroukh, and G. Gabard. « In-duct acoustic and flow computation using the admittance multimodal formulation. Submitted paper ». In: *The Journal of the Acoustical Society of America* (2023).

[27] B. Mangin, M. Daroukh, and G. Gabard. « Propagation of Acoustic Waves in Ducts with Flow Using the Multimodal Formulation ». In: *AIAA JOURNAL* 61.6 (2023). DOI: 10.2514/1.J062659.

[28] B. Mangin, M. Daroukh, and G. Gabard. « An application of the multiple-scales theory to acoustic double transition in ducts with flow ». In: *Journal of Sound and Vibration* 539 (2022). DOI: 10.1016/j.jsv.2022.117252.

[29] B. Mangin, M. Daroukh, and G. Gabard. « Acoustic radiation from an engine intake using an admittance multimodal method ». In: *Inter-noise Chiba, Greater Tokyo*. 2023.

[30] B. Mangin, M. Daroukh, and G. Gabard. « Study of the Impact of Azimuthal Flow Distortion on in-Duct Acoustic Propagation Using a Multimodal Formulation ». In: *33rd Congress of the International Council of the Aeronautical Sciences, ICAS 2022*. 2022.

[31] A.D. Pierce. *Acoustics – An Introduction to its physical principles and applications*. Acoustical Society of America, 1991. DOI: https://www.bibsonomy.org/bibtex/2f50d0733f47ad8409cc2e0e4b2660d70/pagauthier.

[32] C. K. W. Tam et al. « Physical processes influencing acoustic radiation from jet engine inlets ». In: *Journal of Fluid Mechanics* 725 (2013), pp. 152–194. DOI: 10.1017/jfm.2013.181.

[33] M. Daroukh, C. Polacsek, and A. Chelius. « Shock wave generation and radiation from a turbofan engine under flow distortion ». In: *AIAA Journal* 58.2 (2020), pp. 787–801. DOI: 10.2514/1.J058799.

[34] M. E. Goldstein. « Unsteady vortical and entropic distortions of potential flows round arbitrary obstacles ». In: *Journal of Fluid Mechanics* 89 (1978), pp. 433–468. DOI: 10.1017/S0022112078002682.

[35] U. Ingard. « Influence of Fluid Motion Past a Plane Boundary on Sound Reflection, Absorption, and Transmission ». In: *The Journal of the Acoustical Society of America* 31.7 (1959), pp. 1035–1036. DOI: 10.1121/1.1907805.

[36] M. E. Goldstein. *Aeroacoustics*. McGraw-Hill, Inc. New York, 1976.

[37] M. K. Myers. « An exact energy corollary for homentropic flow ». In: *Journal of Sound and Vibration* 109.2 (1986), pp. 277–284. DOI: 10.1016/S0022-460X(86)80008-6.

[38] R. H. Cantrell and R. W. Hart. « Interaction between Sound and Flow in Acoustic Cavities: Mass, Momentum, and Energy Considerations ». In: *The Journal of the Acoustical Society of America* 36.4 (1964), pp. 697–706. DOI: 10.1121/1.1919047.

[39] M. J. Lighthill. « On sound generated aerodynamically I. General theory ». In: *Proceedings of the Royal Society of London. Series A. Mathematical and Physical Sciences* 211.1107 (1952), pp. 564–587. DOI: 10.1098/rspa.1952.0060.

[40] A.J. Burton and G.F. Miller. « The application of integral equation methods to the numerical solution of some exterior boundary-value problems ». In: *Proceedings of the Royal Society of London. A. Mathematical and Physical Sciences* 323.1553 (1971), pp. 201–210. DOI: 10.1098/rspa.1971.0097.

[41] V. Rokhlin. « Rapid solution of integral equations of classical potential theory ». In: *Journal of Computational Physics* 60.2 (2005), pp. 187–207. DOI: 10.1016/0021-9991(85)90002-6.

[42] L. Bertsch et al. « Comparative assessment of aircraft system noise simulation tools ». In: *Journal of Aircraft* 58.4 (2021), pp. 867–884. DOI: 10.1098/rspa.1971.0097.

[43] M. C. Duta and M. B. Giles. « A three-dimensional hybrid finite element/spectral analysis of noise radiation from turbofan inlets ». In: *Journal of Sound and Vibration* 296.3 (2006), pp. 623–642. DOI: 10.1016/j.jsv.2006.03.006.

[44] W. Eversman. « A finite element formulation for aft fan duct acoustic radiation ». In: *3rd AIAA/CEAS Aeroacoustics Conference*. 1997, pp. 506–518. DOI: 10.2514/6.1997-1648.

[45] Y. Zhao and P. Morris. « Inlet and aft tonal noise predictions of a full-scale turbofan engine with bifurcation and inlet distortion ». In: *12th AIAA/CEAS Aeroacoustics Conference*. 2006. DOI: 10.2514/6.2006-2420.

[46] X. Zhang et al. « Computation of fan noise radiation through a realistic engine exhaust geometry with flow ». In: *9th AIAA/CEAS aeroacoustics conference*. 2003. DOI: 10.2514/6.2003-3267.

[47] C. Peyret and P. Delorme. « Discontinuous Galerkin method for computational aeroacoustics ». In: *12th AIAA/CEAS Aeroacoustics Conference (27th AIAA Aeroacoustics Conference)*. 2006, p. 2568. DOI: 10.2514/6.2006-2568.

[48] S. Redonnet and G. Cunha. « An advanced hybrid method for the acoustic prediction ». In: *Advances in Engineering Software* 88 (2015), pp. 30–52. DOI: 10.1016/j.advengsoft.2015.05.006.

[49] T. Guennoc. « Modélisation du rayonnement des guides de forme complexe par une méthode multimodale ». PhD thesis. Le Mans université, 2021.

[50] H. Dong, J. B. Doc, and S. Félix. « Efficient multimodal-based shape optimization of acoustic horns with application to subwavelength perfect transmission ». In: *Journal of Sound and Vibration* 559 (2023), p. 117746. DOI: 10.1016/j.jsv.2023.117746.

[51] E. J. Brambley, M. Darau, and S. W. Rienstra. « The critical layer in linear-shear boundary layers over acoustic linings ». In: *Journal of Fluid Mechanics* 710 (2012), pp. 545–568. DOI: 10.1017/jfm.2012.376.

[52] M. J. King and E. J. Brambley. « Stabilisation of the Hydrodynamic Instability by the Critical Layer ». In: *28th AIAA/CEAS Aeroacoustics Conference, 2022*. 2022. DOI: 10.2514/6.2022-3096.

[53] T.G. Sofrin and D.E. Cicon. « Ducted Fan Noise Propagation in Non-Uniform Flow-Part II: Wave Equation Solution ». In: *11 th Aeroacoustics Conference*. 1987. DOI: 10.2514/6.1987-2702.

[54] T.G. Sofrin and D.E. Cicon. « Ducted Fan Noise Propagation in Non-Uniform Flow-Part I: Test Background and Simplified Model ». In: *11 th Aeroacoustics Conference*. 1987. DOI: 10.2514/6.1987-2701.

[55] C. Canuto et al. *Springer series in computational physics*. Springer, New York, 1988.

[56] P. Moinier and M. B. Giles. « Eigenmode analysis for turbomachinery applications ». In: *Journal of Propulsion and Power* 21.6 (2005), pp. 973–978. DOI: 10.2514/1.11000.

[57] G. Boyer, E. Piot, and J. P. Brazier. « Theoretical investigation of hydrodynamic surface mode in a lined duct with sheared flow and comparison with experiment ». In: *Journal of Sound and Vibration* 330.8 (2010), pp. 1793–1809. DOI: 10.1016/j.jsv.2010.10.035.

[58] R. J. Astley et al. « The effect of steady flow distortion on mode propagation in a turbofan intake ». In: *20th AIAA/CEAS Aeroacoustics Conference*. 2014. DOI: 10.2514/6.2014-3113.

[59] A.G. Wilson. « Propagation of acoustic perturbations in non-uniform ducts with non-uniform mean flow using eigen analysis in general curvilinear coordinate systems ». In: *Journal of Sound and Vibration* 443 (2019), pp. 605–636. DOI: 10.1016/j.jsv.2018.11.023.

[60] M. H. Holmes. *Introduction to Perturbation Methods*. Springer, New York, 1995.

[61] C. M. Bender and S. A. Orszag. *Advanced Mathematical Methods for Scientists and Engineers*. McGraw-Hill, Inc. New York, 1978.

[62] A. H. Nayfeh and D. P. Telionis. « Acoustic Propagation in Ducts with Varying Cross Sections ». In: *The Journal of the Acoustic Society of America* 54.6 (1973), pp. 1654–1661. DOI: https://doi.org/10.1121/1.1914464.

[63] A. H. Nayfeh, J. E. Kaiser, and D. P. Telionis. « Transmission of Sound Through Annular Ducts of Varying Cross Sections ». In: *AIAA Journal* 13.1 (1974), pp. 60–65. DOI: https://doi.org/10.2514/3.49631.

[64] S. W. Rienstra. « Sound transmission in slowly varying circular and annular lined ducts with flow ». In: *Journal of Fluid Mechanics* 380 (1999), pp. 279–296. DOI: 10.1017/S0022112098003607.

[65] A. J. Cooper and N. Peake. « Propagation of unsteady disturbances in a slowly varying duct with mean swirling flow ». In: *Journal of Fluid Mechanics* 445 (2001), pp. 207–234. DOI: 10.1017/s0022112001005559.

[66] S. W. Rienstra. « Sound propagation in slowly varying lined flow ducts of arbitrary cross-section ». In: *Journal of Fluid Mechanics* 495 (2003), pp. 157–173. DOI: 10.1017/S0022112003006050.

[67] E. J. Brambley and N. Peake. « Sound transmission in strongly curved slowly varying cylindrical ducts with flow ». In: *Journal of Fluid Mechanics* 596 (2008), pp. 387–412. DOI: 10.1017/S0022112007009603.

[68] S. W. Rienstra. « Slowly varying modes in a two-dimensional duct with shear flow and lined walls ». In: *Journal of Fluid Mechanics* 906 (2021). DOI: 10.1017/jfm.2020.687.

[69] N. C. Ovenden. « Near cut-on/cut-off transition in lined ducts with flow ». In: *8th AIAA/CEAS Aeroacoustics Conference*. 2002. DOI: 10.2514/6.2002-2445.

[70] R. B. Nielsen and N. Peake. « Tunnelling effects for acoustic waves in slowly varying axisymmetric flow ducts ». In: *Journal of Sound and Vibration* 380 (2016), pp. 180–191. DOI: 10.1016/j.jsv.2016.06.003.

[71] J. B. Doc, S. Félix, and B. Lihoreau. « Coarse-grid computation of the one-way propagation of coupled modes in a varying cross-section waveguide ». In: *The Journal of the Acoustical Society of America* 133.5 (2013), pp. 2528–2532. DOI: 10.1121/1.4799021.

[72] A. Towne et al. « Efficient global resolvent analysis via the one-way Navier–Stokes equations ». In: *Journal of Fluid Mechanics* 948 (2022). DOI: 10.1017/jfm.2022.647.

[73] J. B. Doc et al. « Bremmer series for the multimodal sound propagation in inhomogeneous waveguides ». In: *Wave Motion* 67 (2016), pp. 55–67. DOI: 10.1016/j.wavemoti.2016.07.004.

[74] A. F. Smith, N. C. Ovenden, and R. I. Bowles. « Flow and geometry induced scattering of high frequency acoustic duct modes ». In: *Wave Motion* 49.1 (2011), pp. 109–124. DOI: 10.1016/j.wavemoti.2011.07.006.

[75] V. Pagneux, N. Amir, and J. Kergomard. « A study of wave propagation in varying cross-section waveguides by modal decomposition. Part I. Theory and validation ». In: *The Journal of the Acoustical Society of America* 100.4 (1996), p. 2034. DOI: 10.1121/1.417913.

[76] Ya Yan Lu. « A fourth-order Magnus scheme for Helmholtz equation ». In: *Journal of Computational and Applied Mathematics* 173.2 (2005), pp. 247–258. DOI: 10.1016/j.cam.2004.03.010.

[77] S. Félix and V. Pagneux. « Multimodal analysis of acoustic propagation in three-dimensional bends ». In: *Wave Motion* 36.2 (2002), pp. 157–168. DOI: 10.1016/S0165-2125(02)00009-4.

[78] A. Maurel, J. F. Mercier, and V. Pagneux. « Improved multimodal admittance method in varying cross section waveguides ». In: *Proceedings of the Royal Society A: Mathematical, Physical and Engineering Sciences* 470.2164 (2014). DOI: 10.1098/rspa.2013.0448.

[79] T. Guennoc, J. B. Doc, and S. Félix. « Improved multimodal formulation of the wave propagation in a 3D waveguide with varying cross-section and curvature ». In: *The Journal of the Acoustical Society of America* 149.1 (2021), pp. 476–486. DOI: 10.1121/10.0003336.

[80] J. P. McTavish and E. J. Brambley. « Nonlinear sound propagation in two-dimensional curved ducts: A multimodal approach ». In: *Journal of Fluid Mechanics* 875 (2019), pp. 411–447. DOI: 10.1017/jfm.2019.497.

[81] Q. Li, J. Liu, and W. Guo. « Sound propagation in inhomogeneous waveguides with sound-speed profiles using the multimodal admittance method ». In: *Chinese Physics B* 29.1 (2020). DOI: 10.1088/1674-1056/ab5940.

[82] V. Pagneux. « Multimodal admittance method in waveguides and singularity behavior at high frequencies ». In: *Journal of Computational and Applied Mathematics* 234.6 (2010), pp. 1834–1841. DOI: 10.1016/j.cam.2009.08.034.

[83] W. Eversman. « The boundary condition at an impedance wall in a non-uniform duct with potential mean flow ». In: *Journal of Sound and Vibration* 246.1 (2001), pp. 63–69. DOI: 10.1006/jsvi.2000.3607.

[84] H. Ralph Lewis and Paul M. Bellan. « Physical constraints on the coefficients of Fourier expansions in cylindrical coordinates ». In: *Journal of Mathematical Physics* 31.11 (1990), pp. 2592–2596. DOI: 10.1063/1.529009.

[85] G. Gabard and R. J. Astley. « A computational mode-matching approach for sound propagation in three-dimensional ducts with flow ». In: *Journal of Sound and Vibration* 315.4-5 (2008), pp. 1103–1124. DOI: 10.1016/j.jsv.2008.02.015.

[86] N. Peake and A. J. Cooper. « Acoustic propagation in ducts with slowly varying elliptic cross-section ». In: *Journal of Sound and Vibration* 243.3 (2001), pp. 381–401. DOI: 10.1006/jsvi.2000.3411.

[87] Gwenael Gabard. *PFE Software*. 2021. URL: https://github.com/GwenaelGabard/pfe.

[88] C. Geuzaine and J. F. Remacle. « Gmsh: A 3-D finite element mesh generator with built-in pre-and post-processing facilities ». In: *International journal for numerical methods in engineering* 79.11 (2009), pp. 1309–1331. DOI: 10.1002/nme.2579.

[89] John P. Boyd. *Chebyshev and Fourier Spectral Methods*. Second. Dover Publications, 2001.

[90] J. F. Mercier and A. Maurel. « Improved multimodal method for the acoustic propagation in waveguides with a wall impedance and a uniform flow ». In: *Proceedings of the Royal Society A: Mathematical, Physical and Engineering Sciences* 472.20160094 (2016). DOI: 10.1098/rspa.2016.0094.

[91] Y. Duan et al. « Complex resonances and trapped modes in ducted domains ». In: *Journal of Fluid Mechanics* 571 (2007), pp. 119–147. DOI: 10.1017/S0022112006003259.

[92] S. Hein, W. Koch, and L. Nannen. « Trapped modes and Fano resonances in two-dimensional acoustical duct-cavity systems ». In: *Journal of Fluid Mechanics* 692 (2012), pp. 257–287. DOI: 10.1017/jfm.2011.509.

[93] S. Félix, J. B. Doc, and M. Boucher. « Modeling of the multimodal radiation from an open-ended waveguide ». In: *The Journal of the Acoustical Society of America* 143.6 (2018), pp. 3520–3528. DOI: 10.1121/1.5041268.

[94] J. P. Berenger. « A perfectly matched layer for the absorption of electromagnetic waves ». In: *Journal of Computational Physics* 114.2 (1994), pp. 185–200. DOI: 10.1006/jcph.1994.1159.

[95] F. Collino and P. Monk. « The Perfectly Matched Layer in Curvilinear Coordinates ». In: *SIAM Journal on Scientific Computing* 19.6 (1998), pp. 2061–2090. DOI: 10.1137/S1064827596301406.

[96] P. Marchner et al. « Stable Perfectly Matched Layers with Lorentz transformation for the convected Helmholtz equation ». In: *Journal of Computational Physics* 433 (2021), p. 110180. DOI: 10.1016/j.jcp.2021.110180.

[97] E. J. Rice, M. F. Heidrnann, and T. C. Sofrin. « Modal Propagation Angles in a Cylindrical Duct with Flow and their Relation to Sound Radiation ». In: *17th Aerospace Sciences Meeting*. 1979. DOI: https://doi.org/10.2514/6.1979-183.

[98] S. W. Rienstra and W. Eversman. « A numerical comparison between multiple-scales and finite-element solution for sound propagation in lined flow ducts ». In: *Journal of Fluid Mechanics* 437 (2001), pp. 367–384. DOI: 10.1017/S0022112001004438.

[99] G. Gabard and R. J. Astley. « Theoretical model for sound radiation from annular jet pipes: far- and near-field solutions ». In: *Journal of Fluid Mechanics* 549 (2006), pp. 315–341. DOI: 10.1017/S0022112005008037.

[100] L. Cambier, S. Heib, and S. Plot. « The Onera elsA CFD Software: Input from Research and Feedback from Industry ». In: *Mechanics and Industry* 14.3 (2013), pp. 159–174. DOI: 10.1051/meca/2013056.

[101] M. Abramowitz and S. Irene. *Handbook of Mathematical Functions With Formulas, Graphs, and Mathematical Tables*. National Bureau of Standards Applied Mathematics Series, 1972.

[102] S. Redonnet, E. Manoha, and P. Sagaut. « Numerical simulation of propagation of small perturbations interacting with flows and solid bodies ». In: *7th AIAA/CEAS Aeroacoustics Conference and Exhibit*. 2001. DOI: 10.2514/6.2001-2223.

[103] S. Redonnet and Y. Druon. « Computational aeroacoustics of aft fan noises characterizing a realistic coaxial engine ». In: *AIAA Journal* 50.5 (2012), pp. 1029–1046. DOI: 10.2514/1.J050730.

[104] G. Gabard. « Stochastic sources of broadband noise for time-domain simulations of duct acoustics ». In: *33rd AIAA Aeroacoustics Conference*. 2012. DOI: 10.2514/6.2012-2239.

[105] G. Gabard. « Noise sources for duct acoustics simulations: Broadband noise and tones ». In: *AIAA Journal* 52.9 (2014), pp. 1994–2006. DOI: 10.2514/1.J052739.

[106] L. Wiart et al. « Development of NOVA Aircraft Configurations for Large Engine Integration Studies ». In: *33rd AIAA Applied Aerodynamics Conference*. Vol. 2254. 2015. DOI: 10.2514/6.2015-2254.

DOCTORAT BRETAGNE SCIENCES LOIRE POUR L'INGENIEUR

Le Mans Université

Titre : Modélisation de la propagation acoustique dans l'entrée d'air d'un turboréacteur à l'aide d'une méthode multimodales

Mot clés : Propagation acoustique, Multimodale, WKB, Bruit de soufflante, Transition modale, Distorsion de l'écoulement

Résumé : L'analyse du bruit émis par les parties tournantes des moteurs d'avions comporte trois aspects : la génération des sources acoustiques, leur propagation dans la partie carénée et leur rayonnement en champ lointain. La génération des sources est complexe à estimer, et des calculs coûteux sont généralement effectués. Pour les deux autres aspects, un plus large panel de choix est à disposition. L'accent est mis, dans le cadre de la thèse, sur la propagation à l'intérieur du conduit secondaire d'un turboréacteur et le rayonnement acoustique en champ libre associé. En introduisant quelques simplifications sur la géométrie et l'écoulement, le problème acoustique peut être résolu analytiquement (au moins partiellement), ce qui permet des prévisions très rapides. Ces solutions, semi-analytiques, présentent donc un grand intérêt mais sont naturellement limitées en termes de représentation de la géométrie et de l'écoulement. L'évolution des moteurs vers des géométries à très grand taux de dilution met à mal les hypothèses de ces modèles et introduit des nouveaux défis en terme de modélisation. En particulier, dans ces architectures, le raccourcissement de la nacelle cause une augmentation du nombre de transitions de modes et une distorsion accrue de l'écoulement dans l'entrée d'air qui rendent la propagation particulièrement complexe à calculer. L'objectif principal de cette thèse est de développer des modèles rapides de propagation qui sont capables de prendre en compte ces deux phénomènes. Ceci est réalisé en implémentant une méthode multimodale qui permet de calculer l'écoulement porteur et le champ acoustique sous l'hypothèse d'un écoulement potentiel. Cette méthode est ensuite utilisée pour étudier l'impact de double transitions et de la distorsion azimutale de l'écoulement sur la propagation et le rayonnement acoustique.

Title: Modelling acoustic propagation in modern turbofan intakes using a multimodal method

Keywords: Acoustic propagation, Multimodal, WKB, Fan noise, Modal transition, Flow distortion

Abstract: The analysis of noise generated by the rotating blades of turbofan engines encompasses three aspects: the generation of acoustic sources, their propagation in the intake, and their radiation in the far-field. The generation of these sources is complex to estimate and often requires costly calculations. However, a wider range of options is available for the latter two aspects. In the scope of this thesis, the emphasis is placed on the propagation within the intake of a turbofan engine and the associated free-field acoustic radiation. By introducing some geometry and flow simplifications, the acoustic problem can be solved

analytically. These solutions, known as semi-analytical, hold great interest but are naturally limited in terms of geometry and flow representation. However, the evolution of engines towards configurations with very high bypass ratios challenges the assumptions of these models and introduces new modelling difficulties. Particularly in these architectures, the shortening of the nacelle leads to an increase in the number of modal transitions and to high flow distortion levels in the intake, rendering propagation particularly complex to compute. The main objective of this thesis is to develop propagation models capable of accounting for both phenomena at a low computational cost. This is achieved by implementing a general multimodal method that can compute the mean flow and the acoustic field under the potential flow assumption. This method is then employed to investigate the impact of double transitions and azimuthal flow distortion on acoustic propagation and radiation.